AGH UNIVERSITY OF KRAKOW

FIELD OF SCIENCE
Engineering and Technology

LEADING SCIENTIFIC DISCIPLINE
Automation, Electronics, Electrical Engineering and Space Technologies

DOCTORAL DISSERTATION

Macrospin models: scalable simulations of multilayer spintronic devices

Author: **Jakub Mojsiejuk**

First supervisor: **dr hab. inż. Witold Skowroński**
Auxiliary supervisor: **dr inż. Sławomir Ziętek**

Completed at: **AGH University of Kraków, Institute of Electronics**

Kraków, 2025

AGH

AKADEMIA GÓRNICZO-HUTNICZA
IM. STANISŁAWA STASZICA
W KRAKOWIE

DZIEDZINA
Nauki inżynieryjno-techniczne

DYSCYPLINA WIODĄCA
Automatyka, Elektronika, Elektrotechnika i Technologie Kosmiczne

ROZPRAWA DOKTORSKA

Modele makrospinowe: skalowalne symulacje wielowarstwowych układów spintronicznych

Autor: **Jakub Mojsiejuk**

Promotor rozprawy: **dr hab. inż. Witold Skowroński**
Promotor pomocniczy: **dr inż. Sławomir Ziętek**

Praca wykonana na: **AGH w Krakowie, Instytut Elektroniki**

Kraków, 2025

Abstract

The advances in spintronics enabled technologies such as low-energy non-volatile magnetic memory, sensitive magnetic field detectors, and microwave nano-oscillators. Progress in those areas relied not only on experimental breakthroughs but also on a variety of modelling frameworks that guide material optimisation or clarify mechanisms underlying physical behaviour.

The thesis builds on that tradition by contributing modelling tools tailored to contemporary challenges in the field such as multivariable optimisation of device performance. The first contribution is technical and involves the development of the open source macrospin simulation package called *cmtj* that is used to fit experimental data or prototype new architectures. The package is grounded in modelling frameworks provided by the stochastic Landau-Lifshitz-Gilbert-Slonczewski equation and Smit-Beljers formalism.

As the second contribution, the *cmtj* software is employed in three experimental contexts: (i) numerical modelling of harmonic Hall voltage detection in the Ta/CoFeB sample, (ii) explanation of the multilevel switching phenomenon in a trilayer spin-orbit torque Co/Pt/Co system with strong interlayer exchange coupling and Dzyaloshinskii-Moriya interaction, and (iii) the study of desynchronisation fields in electrically coupled in-series CoFeB/MgO/CoFeB magnetic tunnel junctions. For each, extensive simulations highlight the flexibility of the macrospin model and provide detailed insight into the experimental observations.

Finally, *cmtj* is applied to extrapolate to novel device architectures. Using reinforcement learning, it is demonstrated how a controller can steer an oscillator to synchronise with a desired frequency in a few tuning steps or learn a current impulse shape that leads to magnetisation switching in a simple memory cell model.

Streszczenie

W ostatnich latach postępy w spintronice doprowadziły do powstania niskoenergetycznych pamięci nieulotnych MRAM, czułych detektorów pola magnetycznego oraz nanooscylatorów działających w zakresie mikrofalowym. Rozwój tych urządzeń opierał się w dużej mierze na różnorodnych technikach modelowania, które wyjaśniły mechanizmy leżące u podstaw ich działania lub umożliwiły optymalizację materiałów.

Niniejsza rozprawa wpisuje się w tę tradycję, prezentując narzędzia modelowania dostosowane do współczesnych wyzwań tej dziedziny takich jak optymalizacja układów w przestrzeni wielu parametrów. Pierwszym wkładem rozprawy jest otwarty pakiet symulacyjny *cmtj*, który może być użyty do dopasowywania wyników eksperymentalnych lub prototypowania nowych urządzeń spintronicznych. W ramach pakietu zostały zaimplementowane różne metody numeryczne oparte m.in. na równaniu Landaua-Lifshitza-Gilberta-Slonczewskiego oraz modelach Smita-Beljersa.

Druga część pracy opisuje użycie programu symulacyjnego *cmtj* do zamodelowania trzech zjawisk eksperymentalnych: (i) numerycznego opisu harmonicznej detekcji napięcia Halla w próbce Ta/CoFeB, (ii) wyjaśnienia wielostopniowego przełączania w strukturze Co/Pt/Co z torkiem spin-orbita, silnym sprzężeniem międzywarstwowym oraz interakcją Dzyaloshinskii-Moriya, (iii) opisu mechanizmu pól desynchronizacji w sprzężonych elektrycznie i szeregowo połączonych magnetycznych złączach tunelowych na stacku CoFeB/MgO/CoFeB. W każdym z powyższych przypadków obszerne symulacje makromagnetyczne dostarczają wielu cennych wskazówek ułatwiających interpretację pomiarów eksperymentalnych.

Ostatnia część pracy przedstawia integrację oprogramowania *cmtj* z modelami uczenia ze wzmocnieniem. Zademonstrowano kontroler, który w niewielkiej liczbie kroków automatycznie dostraja oscylator spintroniczny do zadanej częstotliwości oraz kontroler kształtowania impulsu prądu w celu uzyskania przełączenia w układzie ferromagnetyk-metal ciężki lub w złączu tunelowym.

Contents

Dedykacja

Rodzinie, za nieustające wsparcie

Przyjaciołom, którzy odradzali pójście na doktorat

– mieli absolutną rację

Acknowledgements

The author expresses sincere thanks to Dr. Krzysztof Grochot, Dr. Piotr Wiśniowski, Dr. Piotr Rzeszut, and Dr. Piotr Ogrodnik for their support and long discussions. I am immensely grateful to Prof. Tomasz Stobiecki for the charitable counsel provided throughout my PhD and for the perceptive review and critique of this thesis. To my supervisors, Prof. Witold Skowroński, and Dr. Sławomir Ziętek, I thank them for their guidance and comments, because without them I would not have been able to complete this thesis.

Index of terms and symbols

Constants

γ_0	gyromagnetic ratio	$2.208 \times 10^5\,\mathrm{m\,A^{-1}\,s^{-1}}$
$\hbar$	reduced Planck constant	$1.055 \times 10^{-34}\,\mathrm{J\,s}$
μ_0	vacuum magnetic permeability	$1.266 \times 10^{-6}\,\mathrm{N\,A^{-2}}$
e	elementary charge	$1.602 \times 10^{-19}\,\mathrm{C}$
h	Planck constant	$6.626 \times 10^{-34}\,\mathrm{J\,Hz^{-1}}$

Experimental

CIMS	Current Induced Magnetisation Switching
FMR	Ferromagnetic resonance
MTJ	Magnetic Tunnel Junction
PIMM	Pulse-induced Magnetometry
SD	Spin Diode
VSD	Voltage Spin Diode

Interactions and effects

AHE	Anomalous Hall effect
AMR	Anisotropic Magnetoresistance
DMI	Dzyaloshinskii–Moriya interaction
IEC	Interlayer Exchange Coupling
IMA	In-plane magnetic anisotropy
ISHE	Inverse Spin Hall effect
PMA	Perpendicular magnetic anisotropy
REE	Rashba-Edelstein effect

RKKY Ruderman–Kittel–Kasuya–Yosida interaction

SHE Spin Hall effect

SMR Spin Hall Magnetoresistance

SOT Spin Orbit Torque

STT Spin Transfer Torque

VCMA Voltage Controlled Magnetic Anisotropy

Layer types and devices

AFM Antiferromagnet

FM Ferromagnetic layer

HM Heavy metal layer

NM Nonmagnetic layer

SAF Synthetic antiferromagnet

SHNO Spin Hall Nano Oscillator

STO Spin Torque Oscillator

Symbols

α_G	Gilbert's damping parameter	
λ	angular parameter (Slonczewski parameter)	
$\mathbf{m}$	unit magnetisation vector	
$\mathbf{p}$ or $\boldsymbol{\sigma}$	unit spin current polarisation vector	
D	DMI constant	Jm^{-2}
H_{DL}	damping-like torque magnitude	Am^{-1}
H_{FL}	field-like torque magnitude	Am^{-1}
K_u	magnetic anisotropy constant (1st order)	Jm^{-3}
$\mu_0 M_s$	magnetisation saturation	T
ϕ	azimuth angle from + x-axis	rad
θ	polar angle from + z-axis	rad
θ_{SH}	spin Hall angle	
J	IEC constant	Jm^{-2}
j or j_e	charge current density	Am^{-2}

Introduction

If we classify the development of spin devices with respect to their application, several major directions emerge: storage and memory, oscillators and detectors, and methods for efficient computing. Among those, applications in low-power, non-volatile memory have significantly driven interest in spintronics for many years, and much research has been invested in making the designs not only faster and denser, but also more energy efficient. Alternative methods of spin control, notably through spin-orbit torque, have recently gained traction as suitable replacements to spin torque transfer switching, which suffer from excessive Joule heat limiting widespread industrial adoption.

The discovery of new effects in spintronics applicable to spin devices and a deeper understanding of their potential advantages and limitations resulted in emerging branches of research focused on new logic units based on spintronic gates and alternative methods of computing. A representative example of the former has been demonstrated by Zhang et al.[1] where careful manipulation of the gate geometry and spin textures permits a replication of the basic Boolean AND and OR gates. Alternatively, quantum-gate designs have been attempted employing localised electric control to modify spin transport properties, effectively modulating the probability of electron transposition to the receiving electrode[2]. The term 'alternative methods of computing' represents perhaps a broader and more loosely defined front of research, spanning from ideas such as reservoir-like spin wave encoded neural networks[3], through memristors[4], and computation based on nano oscillators[5], to probabilistic computing – where a probabilistic bit, often modelled by a nanomagnet with low energy barrier[6] or a magnetic tunnel junction[7], becomes the primary unit of computation[8]. Generally, the computational aspects of modern spintronics concentrate around neuromorphic computing concepts[9]. Unlike classical neural network architectures, neuromorphic computation primarily relies on temporal integration of incoming impulses and randomly initialised static network graphs known as reservoirs[10].

However, each application needs, at some level, simulation support to iterate on the designs or simply to understand various interactions either present within the device itself or with the external factors. To this extent, both research and the industry employ the help of a multitude of simulation

[1] X. Zhang, Ezawa, and Y. Zhou, "Magnetic skyrmion logic gates".

[2] W. Zhang, "Voltage-driven spintronic logic gates in graphene nanoribbons".

[3] Papp, Kiechle, et al., "Experimental demonstration of a concave grating for spin waves in the Rowland arrangement".

[4] Huang, Xia, et al., "Memristive Artificial Synapses for Neuromorphic Computing"; Chanthbouala, Garcia, et al., "A ferroelectric memristor".

[5] Houshang, Zahedinejad, et al., "Phase-Binarized Spin Hall Nano-Oscillator Arrays"; Torrejon, Riou, et al., "Neuromorphic computing with nanoscale spintronic oscillators".

[6] Nomura, Furuta, Tsujimoto, Kuwabiraki, Peper, et al., "Reservoir computing with dipole-coupled nanomagnets"; Taniguchi, Utsumi, and Imamura, "Thermally activated switching rate of a nanomagnet in the presence of spin torque".

[7] K. Hayakawa, Kanai, et al., "Nanosecond Random Telegraph Noise in In-Plane Magnetic Tunnel Junctions".

[8] J. Kaiser and Datta, "Probabilistic computing with p-bits"; Camsari, B. M. Sutton, and Datta, "p-Bits for Probabilistic Spin Logic".

[9] Torrejon, Riou, et al., "Neuromorphic computing with nanoscale spintronic oscillators"; Kurenkov, Fukami, and Ohno, "Neuromorphic computing with antiferromagnetic spintronics".

[10] Taniguchi, Ogihara, et al., "Spintronic reservoir computing without driving current or magnetic field".

packages that vary in complexity, speed, or degree of fidelity. The situation is not different in spintronics, where there is a selection of methods ranging from ab initio[11], atomistic[12], and micromagnetic[13] to macromagnetic[14,15]. The latter technique is usually not used in the form of an established, usable, and complete simulation package.

Therefore, this thesis demonstrates the relevance of macromagnetic models, emphasising their clarity and effectiveness in solving simplified problems, thus providing valuable insights into real systems. The reduction in complexity and accuracy is offset by the gains in computational speed, ease of prototyping, and iterative simulation improvements. The software flexibility allows the use of a wide selection of tools to analyse the output of those simple models, and when we combine all of that with the experimental data, it turns out that we develop a fairly sound intuition of the investigated phenomenon. Given this versatility of the macrospin modelling, the thesis presents a broad overview of multiple modelling methods. Throughout its course, we discuss various applications such as current-induced magnetisation switching (CIMS), voltage-spin diode (VSD), harmonic Hall voltage detection, coupled oscillators, or noise modelling.

[11] Hafner and Kresse, "The Vienna AB-Initio Simulation Program VASP"; Giannozzi, Andreussi, et al., "Advanced capabilities for materials modelling with Quantum ESPRESSO".

[12] Müller, Hoffmann, et al., "*Spirit*".

[13] M. J. Donahue and D. G. Porter, *OOMMF User's Guide, Version 1.0*; Vansteenkiste, Leliaert, et al., "The design and verification of MuMax3".

[14] Xiao, Zangwill, and M. D. Stiles, "Macrospin models of spin transfer dynamics".

[15] Mojsiejuk, Ziętek, Grochot, et al., "cmtj".

Contents and contributions of this thesis

This thesis makes several distinct contributions to the field. The first contribution is the development of the standardised numerical library CMTJ, which serves as the simulation backbone for the following work. The principal methods implemented in this library are detailed in the first chapter, Numerical methods, including key equations, numerical techniques employed, points of optimisation, and the associated numerical effects. The chapter also provides the theoretical foundation for this thesis. In the second chapter, Modelling spin Hall devices, we use the CMTJ library to explore models that reflect the effects of interfacial asymmetry on spin Hall bars, using experimental data from Co/Pt/Co systems as validation ground. Additionally, we focus on electrical detection techniques, in particular harmonic Hall voltage detection on CoFeB/Ta devices. The following two chapters, Modelling magnetic tunnel junctions and Dynamic control of devices, focus on the role of magnetic tunnel junctions (MTJs) as oscillators and detectors. In Modelling magnetic tunnel junctions, we examine electric coupling and its effect on the synchronisation of the two devices. The simulation results are compared with the available experimental data. Subsequently, we investigate the stochastic behaviour of the MTJs by modelling $1/f^{\alpha}$ noise. The final chapter, Dynamic control of devices, further develops the idea of real-time tuning of the MTJ-based detector to a desired frequency using the reinforcement learning approach. The concluding chapter discusses the potential implications of the proposed solutions and identifies new avenues for future research.

All figures, diagrams, and simulations used in this thesis, unless explicitly

stated otherwise, were created by the author of this thesis, even if they are inserted by citing another publication. For clarity, we map the chapters to relevant publications together with specific contributions from the author of this thesis, indicating that the results presented in this thesis are complementary to the author's published works:

- **Chapter Numerical methods**
  The author created, programmed, packaged, and documented the CMTJ library. The fitting of the experimental data with the simulations was also carried out by the author.[16]

- **Chapter Modelling spin Hall devices**
  The author proposed the model and performed the numerical simulations for asymmetric switching in the Co/wedge Pt/Co sample.[17]
  The author created the model and simulated all the fits to the experimental data for the Ta/CoFeB sample.[18]

- **Chapter Modelling magnetic tunnel junctions**
  The author conducted simulations of the spin-torque oscillators connected in-series. The author also proposed the observation of the desynchronisation based on the analysis of the experimental data.[19]

- **Chapter Dynamic control of devices**
  The author designed the environments and conducted the training of the reinforcement learning algorithms.[20]

[16] Mojsiejuk, Ziętek, Grochot, et al., "cmtj".

[17] Grochot, Ogrodnik, et al., "Influence of ferromagnetic interlayer exchange coupling on current-induced magnetization switching and Dzyaloshinskii–Moriya interaction in Co/Pt/Co multilayer system".

[18] Ziętek, Mojsiejuk, et al., "Numerical model of harmonic Hall voltage detection for spintronic devices".

[19] Rzeszut, Mojsiejuk, et al., "Towards mutual synchronization of serially connected Spin Torque Oscillators based on magnetic tunnel junctions".

[20] Mojsiejuk, Ziętek, and Skowroński, "Reinforcement learning for spin torque oscillator tasks".

The table below summarises the samples, models, and experiments with chapter references for the ease of the reader:

Investigated phenomena	**Sample**	**Type of modelling used**	**Chapter**
Harmonic Hall voltage detection	Ta/CoFeB	SOT-LLGS	Modelling spin Hall devices
FMR	CoFeB/W(wedge)/CoFeB	Smit-Beljers, Bayesian modelling	Modelling spin Hall devices
Multilevel CIMS	Co/Pt(wedge)/Co	SOT-LLGS, Domain Wall motion models	Modelling spin Hall devices
Electric synchronisation of MTJs	CoFeB/MgO/CoFeB	Electric coupling, LLGS	Modelling magnetic tunnel junctions
Noise modelling and reconstruction	Theoretical	STT-sLLGS, $1/f^{\alpha}$ noise modelling, Kasdin noise model, multi-domain noise models	Modelling magnetic tunnel junctions
Real-time control of spintronic oscillators	Theoretical	STT-LLGS, reinforcement learning models	Dynamic control of devices

Publication list

The list below compiles the entire list of articles by the author relevant to the field of spintronics, to date:

1. Skowroński, W., Łazarski, S., **Mojsiejuk, J.**, Chęciński, J., Frankowski, M., Nozaki, T., Yakushiji, K., Yuasa, S., (Aug. 2019). "High frequency voltage-induced ferromagnetic resonance in magnetic tunnel junctions". *Applied Physics Letters* 115.7, p. 072401
   Contribution: Conducted voltage-induced ferromagnetic resonance simulations of MTJs with strong perpendicular magnetic anisotropy.

2. **Mojsiejuk, J.**, Kulig, P., Chęciński, J., Frankowski, M., (Feb. 2020). "Visualization for Micromagnetics With Synchronized Plotting". *IEEE Transactions on Magnetics* 56.2, pp. 1–6
   Contribution: Developed the software and wrote the article.

3. Ziętek, S., **Mojsiejuk, J.**, Grochot, K., Łazarski, S., Skowroński, W., Stobiecki, T., (July 2022). "Numerical model of harmonic Hall voltage detection for spintronic devices". *Physical Review B* 106.2, p. 024403
   Contribution: Conducted the simulations, wrote the article, and performed a formal analysis.

4. **Mojsiejuk, J.**, Ziętek, S., Grochot, K., Skowroński, W., Stobiecki, T., (Apr. 2023). "cmtj: Simulation package for analysis of multilayer spintronic devices". *npj Computational Materials* 9.1, p. 54
   Contribution: Wrote the article and software, and conducted the simulations.

5. Rzeszut, P., **Mojsiejuk, J.**, Skowroński, W., Tsunegi, S., Kubota, H., Yuasa, S., (June 2023). "Towards mutual synchronization of serially connected Spin Torque Oscillators based on magnetic tunnel junctions". arXiv:2306.11608 [physics]
   Contribution: Conducted the simulations, performed formal analysis of the experimental results, and co-wrote the article.

6. Grochot, K., Ogrodnik, P., **Mojsiejuk, J.**, Mazalski, P., Guzowska, U., Skowroński, W., Stobiecki, T., (Apr. 2024). "Influence of ferromagnetic interlayer exchange coupling on current-induced magnetization switching and Dzyaloshinskii–Moriya interaction in Co/Pt/Co multilayer system". *Scientific Reports* 14.1, p. 9938
   Contribution: Conducted the simulations, excluding the spin-wave simulations, and co-wrote the article.

7. Safeer, C., Keatley, P. S., Skowroński, W., **Mojsiejuk, J.**, Yakushiji, K., Fukushima, A., Yuasa, S., Bedau, D., Casanova, F., Hueso, L. E., Hicken,

R. J., Pinna, D., Van Der Laan, G., Hesjedal, T., (Aug. 2024). "Magnetization dynamics driven by displacement currents across a magnetic tunnel junction". *Physical Review Applied* 22.2, p. 024019
Contribution: Conducted micromagnetic simulations. Details in Magnetization dynamics driven by displacement currents across an MTJ

8. **Mojsiejuk, J.**, Ziętek, S., Skowroński, W., (Sept. 2025). "Reinforcement learning for spin torque oscillator tasks". arXiv:2509.10057 [physics] (accepted to *IOP Journal of Physics: Conference Series*)
Contribution: Conducted the simulations, performed the formal analysis, and wrote the article.

9. Cierpiał, M., Maślanka, D., Gubała, K., **Mojsiejuk, J.**, Grochot, K., Wrona, J., Langer, J., Nan, T., Skowroński, W., (Oct. 2025) "Magnetic tunnel junction made of abundant materials for memory and dynamic applications", *Scientific Reports* (accepted)
Contribution: Conducted the simulation parameter fitting.

Numerical methods

This chapter gives a gentle introduction to key numerical techniques that are used implicitly or explicitly throughout the remainder of the work. It presents the base versions of the models later used in experimental reproductions, dynamic control, and parameter fitting.

Landau-Lifshitz-Gilbert-Slonczewski equation

The key equation in spintronics is the Landau-Lifshitz-Gilbert-Slonczewski (LLGS) equation [21] and its variations. The minimal form of the LLGS equation can be derived through standard spin algebra calculations. We begin with a microscopic Zeeman Hamiltonian[22]:

$$\mathcal{H} = -\frac{g\mu_0\mu_B}{\hbar}\hat{\mathbf{S}}\cdot\mathbf{H} = \gamma_e\mu_0\hat{\mathbf{S}}\cdot\mathbf{H} \tag{1}$$

where $\gamma_e = -g\mu_B/\hbar$, and $\hat{\mathbf{S}} = \{\hat{S}_x, \hat{S}_y, \hat{S}_z\}$ is the spin angular momentum operator with 3 components defined in terms of the Pauli matrices $\frac{\hbar}{2}\sigma_i$ with $i = \{x, y, z\}$. However, instead of considering a single spin operator, the introduction of a density operator $\rho = \sum_n p_n|\Psi_n\rangle\langle\Psi_n|, p_n \geq 0, \sum_n p_n = 1$ allows us to write $\langle\hat{S}\rangle$ as a statistical ensemble over local spins:

$$\langle\hat{S}\rangle = \mathrm{Tr}(\rho\hat{S}) \tag{2}$$

Adopting a Heisenberg picture, the time evolution of that ensemble is given by:

$$\frac{d}{dt}\langle\hat{S}\rangle = \frac{i}{\hbar}\langle[\mathcal{H}, \hat{S}]\rangle = \frac{i}{\hbar}\langle[\gamma_e\mu_0\hat{S}\cdot\mathbf{H}, \hat{S}_j]\rangle = \frac{i}{\hbar}\gamma_e\mu_0\mathbf{H}_i\langle[\hat{S}_i, \hat{S}_j]\rangle = \frac{i}{\hbar}i\hbar\gamma_e\mu_0\varepsilon_{ijk}\mathbf{H}_i\langle\hat{S}_k\rangle \tag{3}$$

where we used the fact that ρ is time-independent. ε_{ijk} is the Levi-Civita symbol. The components $\langle\hat{S}_k\rangle, \mathbf{H}_i$ behave as the components of a cross product: $(a\times b)_j = \varepsilon_{jkl}a_k b_l$, hence:

$$\frac{d}{dt}\langle\hat{\mathbf{S}}\rangle = \gamma_e\mu_0\langle\hat{\mathbf{S}}\rangle\times\mathbf{H} \tag{4}$$

If we define magnetisation per unit volume as:

$$\mathbf{M} = \frac{\gamma_e N}{V}\langle\hat{\mathbf{S}}\rangle \tag{5}$$

[21] Landau and Lifshitz, "On the Theory of the Dispersion of Magnetic Permeability in Ferromagnetic Bodies".

[22] Lakshmanan, "The fascinating world of the Landau-Lifshitz-Gilbert equation".

using $\gamma_0 = \mu_0|\gamma_e|$, then the familiar precessional term of the LLG equation emerges:

$$\frac{\mathrm{d}}{\mathrm{d}t}\mathbf{M} = -\gamma_0 \mathbf{M} \times \mathbf{H} \tag{6}$$

To this fundamental equation, Gilbert added a damping term derived from the Lagrangian framework[23]. Finally, Slonczewski and Berger independently calculated the form of the damping and field-like torques[24] that arise from the spin transfer torque (STT) effect. A Landau-Lifshitz (LL) form of the LLGS equation that combines these results is given by[25]:

$$\frac{1+\alpha_G^2}{\gamma_0}\frac{\mathrm{d}\mathbf{m}}{\mathrm{d}t} = -\mathbf{m}\times\mathbf{H}_{\mathrm{eff}} - \alpha_G \mathbf{m}\times(\mathbf{m}\times\mathbf{H}_{\mathrm{eff}}) + a_j\varepsilon\beta\mathbf{m}\times\mathbf{p} - a_j\varepsilon(\mathbf{m}\times(\mathbf{m}\times\mathbf{p})) \tag{7}$$

where we use magnetisation vector normalised by magnetisation saturation, $\mathbf{m} = \mathbf{M}/\mathrm{M_s}$, $\mathbf{H}_{\mathrm{eff}}$ is the effective field term, β determines the field-like to damping-like torque ratio. β is phenomenological and stack-dependent; many simulations set it to 0 or equal to the damping parameter α_G, although sometimes a larger scaling factor is used for the field-like torque[26]. The variable a_j is defined in terms of current density j:

$$a_j = \frac{\hbar j}{e\mu_0 M_s t_{\mathrm{FM}}} \tag{8}$$

e is the electron charge and ε depends on λ, the parameter of the spacer layer derived by Slonczewski, and P, the efficiency of the spin current polarisation ($0 \le P \le 1$):

$$\varepsilon = \frac{P\lambda^2}{\lambda^2+1+(\lambda^2-1)\mathbf{m}\cdot\mathbf{p}} \tag{9}$$

The polarisation vector $\mathbf{p}$ is normalised to have unit length, $|\mathbf{p}| = 1$.

In spin orbit torque (SOT) dominant systems such as heavy-metal/ferromagnet (HM/FM) stacks, the LLGS equation is more naturally expressed by grouping the torque terms under more generic field-like ($\mathrm{H_{FL}}$) and damping-like ($\mathrm{H_{DL}}$) torque magnitudes (here, expressed as effective fields in A/m)[27]:

$$\frac{\mathrm{d}\mathbf{m}}{\mathrm{d}t} = \frac{-\gamma_0}{1+\alpha_G^2}[\mathbf{m}\times\mathbf{H}_{\mathrm{eff}} + \alpha_G\mathbf{m}\times\mathbf{m}\times\mathbf{H}_{\mathrm{eff}}] + \frac{-\gamma_0}{1+\alpha_G^2}[(\mathrm{H_{FL}} - \alpha_G\mathrm{H_{DL}})\mathbf{m}\times\mathbf{p} + (\mathrm{H_{DL}} + \alpha_G\mathrm{H_{FL}})\mathbf{m}\times(\mathbf{m}\times\mathbf{p})] \tag{10}$$

if α_G is sufficiently small, the torque mixing terms can be neglected in favour of the dominant term. See the appendix of Pub. 1: Numerical model for the harmonic Hall voltage detection for derivation of the LL form of the equation for SOT.

Fig.1 shows the idea behind the damping and field-like torques along with the standard effective field precession and damping terms. The contributions from the latter tend to cause the magnetisation alignment along a particular axis, whereas the former produces a precession about the said axis.

[23] Gilbert, "Classics in Magnetics A Phenomenological Theory of Damping in Ferromagnetic Materials".

[24] Slonczewski, "Current-driven excitation of magnetic multilayers"; Berger, "Emission of spin waves by a magnetic multilayer traversed by a current".

[25] We refer to a form of an LLGS equation which does not contain implicit dependency on the $\frac{\mathrm{d}\mathbf{m}}{\mathrm{d}t}$ as the LL-form (Landau-Lifshitz) of the LLGS equation.

[26] Arun, Gopal, et al., "Influence of Field-Like Torque in Synchronization of Spin Torque Oscillators".

[27] Nguyen and Pai, "Spin–orbit torque characterization in a nutshell".

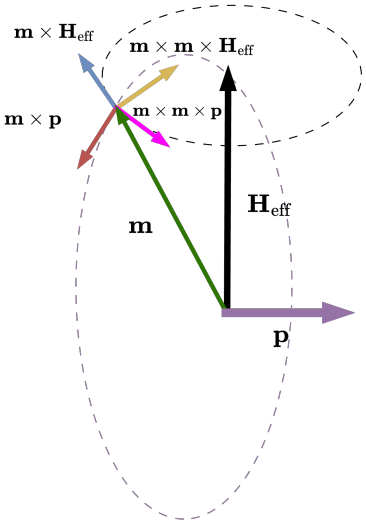

Figure 1: The main idea behind the damping-like and field-like contributions. Here, $\mathbf{m}$ is marked with a green vector, $\mathbf{H}_{\mathrm{eff}}$ is the effective field vector coloured black, and in purple we mark the $\mathbf{p}$ which is the polarisation vector of a reference layer. The dashed lines represent the precession cones about a specific axis designated by $\mathbf{H}_{\mathrm{eff}}$ (dashed black) or $\mathbf{p}$ (dashed purple). In both cases, the precession is produced by the field-like terms (the orange and blue vectors), whereas the damping-like contributions pull the magnetisation vector $\mathbf{m}$, aligning it with the specific axis – again, either $\mathbf{H}_{\mathrm{eff}}$ or $\mathbf{p}$. Those vectors are coloured yellow or pink, respectively.

Energy density contributions

The general effective field term in (7, 10) contains contributions from several physical effects. Some of those, along with their principal forms as fields, are given in the *Methods* section of Pub. 2: Open-source macromagnetic package. Here, we briefly review selected contributions in energy form, suitable for algorithms that directly operate on energy expressions rather than fields. For models that operate on the effective field, the macromagnetic scaling of the effective field is taken to be a functional derivative of the energy density $\mathcal{F}$ with respect to the magnetisation vector:

$$\mathbf{H}_{\text{eff}} = -\frac{1}{\mu_0 \mathrm{M}_s} \frac{\delta \mathcal{F}[\mathbf{m}]}{\delta \mathbf{m}} \tag{11}$$

If we deal with total energy, we also include the volume of the cell, V, in the denominator. For the interaction expressions in $\mathrm{J/m^2}$, we need to rescale $\mathcal{F}$ by the corresponding layer thickness.

Magnetocrystalline anisotropy, henceforth simply referred to as anisotropy, arises because of the preferred alignment of the magnetic moments with the lattice symmetry axes. A single dominant symmetry axis is typically assumed; thus, the anisotropy energy density term is written with respect to some uniaxial anisotropy axis vector $\mathbf{a}$ as:

$$\mathcal{F}_{\mathrm{K}} = -K_1(\mathbf{m}\cdot\mathbf{a})^2 - K_2(\mathbf{m}\cdot\mathbf{a})^4 \tag{12}$$

where K_1 is the first order uniaxial anisotropy constant expressed in $\mathrm{J/m^3}$, K_2 is the second order anisotropy constant, in the same units. Typically, $K_2 < 0$[28]. In certain models, it is convenient to explicitly distinguish the in-plane and out-of-plane (perpendicular) anisotropy axes, as is done, for example, in (34). Notably, distinguishing these axes simplifies interpreting another term, the demagnetisation energy, which has a form that counteracts the perpendicular anisotropy. Shape anisotropy, as is sometimes called, is primarily influenced by the geometry of the sample, specifically the discontinuity at the edges. Macromagnetically, the energy density of the dipole interaction may look like this:

$$\mathcal{F}_{\text{demag/dipole}} = \frac{\mu_0 \mathrm{M}_{\mathrm{s},i} \mathrm{M}_{\mathrm{s},j}}{2} \mathbf{m}_i^T \hat{\mathbf{N}}_{ij} \mathbf{m}_j \tag{13}$$

where the tensor $\hat{\mathbf{N}}$ can be a dipole tensor arising from the interaction with another uniformly magnetised body, or it can also encompass the self-demagnetising field, in which case, for the macrospin, we have $i = j$. Often, for most basic strip geometry, the demagnetising field is approximated using the trivial tensor with 1 in the last place of the diagonal of $\hat{\mathbf{N}}$, which reduces to the z axis component of the magnetisation inducing an internal demagnetising energy. In practice we usually use diagonalised version with off-diagonal elements being zero, allowing the simplified demagnetisation

[28] Strelkov, A. Timopheev, et al., "Stability phase diagram of a perpendicular magnetic tunnel junction in noncollinear geometry".

term to be written as:

$$\mathcal{F}_{\text{demag}} = \frac{\mu_0 \mathrm{M}_s^2}{2} (\mathbf{m} \odot \mathbf{m}) \hat{\mathbf{N}} \tag{14}$$

with $\odot$ as the Hadamard (element-wise) product. We discuss the dipole interaction, that is, the case when $i \neq j$, in the subsequent paragraph.

Another significant term, not explicitly taken into account in the macrospin simulations, is the exchange interaction energy density that is typically given by[29]:

$$\mathcal{F}_{\text{ex}} = A_{\text{ex}} (\nabla \mathbf{m})^2 \tag{15}$$

with exchange stiffness constant $A_{\text{ex}} = \frac{2J_{\text{ex}}}{a}$ where a is the lattice constant and J_{ex} is the exchange integral. Naturally, the value and form of that constant will depend on the crystal lattice itself. The exchange interaction favours alignment of spins, but its nature is short-range. An interesting situation arises when the exchange interaction starts to compete with the dipole interaction (magnetostatic) because the dipole interaction, though weaker, has a longer range, potentially dominating in sufficiently large samples. This competition is, in part, responsible for the magnetic domain configuration. Another use case where dipole interaction plays a major role is when multiple magnetic devices are placed in a close mutual vicinity; we discuss an example of such a circumstance in Dipolar coupling where we measure the synchronisation capacity of two MTJs placed at a sequentially longer distance. In any case, the exact shape of the dipole interaction for an arbitrary system is complicated, but Newell et al.[30] derived the analytical form of the macromagnetic demagnetising tensor. In micromagnetic calculations, when spanned on a regular grid, the demagnetising field can be computed across the entire configuration; there are a couple of efficient methods that reduce the complexity from $\mathcal{O}(n^2)$ to $\mathcal{O}(n \log n)$ by clever use of the Fourier transform, symmetry, and grid padding[31].

In many systems with multiple FM layers, interlayer exchange coupling (IEC) becomes relevant. IEC is a function of the thickness of the nonmagnetic (NM) layer and encompasses both the effects related to the confinement of Fermi surface electrons in the NM itself and the spin-dependent scattering at the FM/NM interfaces[32]. The bilinear constant J_1 can follow the RKKY-like oscillatory behaviour, although due to aliasing the true period may be lost in the experiment. One simple model places the origin of the standard IEC oscillations in quantum wells[33], where the quantum well resonance mode periodically crosses the Fermi energy as the thickness of the spacer layer varies[34]. The so-called quadratic term originates from both intrinsic and extrinsic factors, although the latter is taken to have a more significant influence. Extrinsic factors are typically attributed to interfacial roughness: tiny fluctuations in the thickness of the spacer layer, interfacial defects that become scattering centres, or interfacial atomic mixing. Both bilinear and biquadratic terms are generally combined into the following energy surface

[29] M. Donahue and D. Porter, "Exchange energy formulations for 3D micromagnetics".

[30] Newell, Williams, and Dunlop, "A generalization of the demagnetizing tensor for nonuniform magnetization".

[31] Abert, Bruckner, et al., "A full-fledged micromagnetic code in fewer than 70 lines of NumPy"; Miltat and M. J. Donahue, "Numerical Micromagnetics".

[32] Tsymbal and Žutić, *Spintronics handbook. Volume 2*.

[33] M. Stiles, "Interlayer Exchange Coupling"; Bruno, "Interlayer Exchange Interactions in Magnetic Multilayers".

[34] The electrons reflect from both interfaces in a quantum well – this is the aforementioned model for the confinement of the Fermi surface. Classically, this leads to a standing wave, ergo a resonance mode. Varying the thickness causes a shift in energy and, hence, an oscillatory crossing of the Fermi energy

expression:

$$\mathcal{F}^{*}_{\mathrm{IEC}} = -J_1 \mathbf{m}_i \cdot \mathbf{m}_j - J_2 (\mathbf{m}_i \cdot \mathbf{m}_j)^2 \tag{16}$$

The * denotes that the energy is in $\mathrm{J/m^2}$ and not $\mathrm{J/m^3}$ units, and in macromagnetic models it is rescaled by the FM thickness to arrive at the correct dimensions. We note that (16), or at least its bilinear part, is often applied even when the coupling is of non-oscillatory character and has slightly different origins as those outlined above, yet it follows the dependence on the thickness of a spacer material.

As we discuss later in more detail in Spin-Orbit torque, a broken inversion symmetry at the interface results in the promotion of the spin-orbit interaction, and this in turn may also lead to the emergence of the Dzyaloshinskii–Moriya energy term:

$$\mathcal{F}^{*}_{\mathrm{DMI}} = -\mathbf{D} \cdot (\mathbf{m}_i \times \mathbf{m}_j) \tag{17}$$

where $\mathbf{D}$ is the DMI vector and $\mathbf{m}_{i/j}$ corresponds to the magnetisation sites. If the asymmetry arises exclusively due to the interface, we may talk about the DMI vector pointing in the direction perpendicular to the interface normal. Then, in field terms, the DMI can be modelled as an in-plane field. The sign of the constant $\mathbf{D}$ determines the chirality of the domain wall and the direction of its movement under the SHE field; this concept will be made clearer in the context of the equations discussed in the Domain dynamics section.

Non-conservative torque terms

While static analysis of the LLG equation still plays an important role in determining magnetic parameters from experimental data, the dynamic effects appearing in torque terms are arguably more interesting and broaden the applications of spintronics devices. As previously discussed, two key effects – STT and SOT – appear almost identical within the formulations given by equations: (10) and (7). One can write $\mathrm{H_{DL/FL}}$ amplitudes in terms of the a_j and ε terms and vice versa. However, their origin, mechanics, and consequences for the experimental reality are different and, therefore, require some degree of distinction in the simulation process.

Spin Transfer torque

We start with a discussion of STT as it has been the cornerstone of spintronics devices for almost three decades since it was first described by Slonczewski in 1996[35]. There are two components to understanding the spin transfer torque: one that describes the passing of the spin current through an FM, and another that concerns the behaviour at the NM/FM interface[36] (the following paragraph closely follows Sect. 3 of that work). Mechanically, the idea is simple: an incoming spin current, for example along the $\hat{x}$ axis,

[35] Slonczewski, "Current-driven excitation of magnetic multilayers".

[36] Ralph and M. Stiles, "Spin transfer torques".

causes a torque transverse to the magnetisation of the FM layer, meaning that, to some degree of approximation, there is no transverse angular momentum flowing away from that FM layer. Analysis of the interfacial behaviour reveals that the transverse component of the incoming spin current is absorbed at the interface. In a simple approximation, we may say that the spin coming from NM to FM sees an energy split between the majority and minority bands, which are separated by some energy difference. First, this interfacial band mismatch is responsible for the absorption of the spin-angular momentum component transverse to the FM. Second, because of the exchange energy difference, the spins will oscillate, which in turn leads to dephasing at the interface. The result of that dephasing is that the spin current that leaves the FM is, for the most part, collinear with the FM. The spin current injected into an NM/FM interface is usually achieved by affixing another, preceding FM layer, usually named "a reference layer" with magnetisation pinned by synthetic antiferromagnet (SAF)[37] that, through strong coupling, prevents the reference layer from changing its magnetisation orientation.

[37] SAF is a system created by putting together FM layers with their magnetisations in an anti-parallel alignment, thus mimicking AFM in effect.

Spin-Orbit torque

To introduce the SOT, we first consider the spin Hall effect family, with particular focus on Anomalous Hall Effect (AHE), pure spin Hall effect (SHE) and inverse Spin Hall effect (ISHE)[38]. In heavy metals such as platinum or tungsten, we refer to a "plain" SHE where the transverse spin current arises in the absence of the magnetic field[39]. In contrast to the ordinary Hall effect, SHE does not involve transverse charge accumulation.

[38] Inoue and Ohno, "Taking the Hall Effect for a Spin"; Sinova, Valenzuela, et al., "Spin Hall effects".
[39] Hirsch, "Spin Hall Effect"; Dyakonov and Perel, "Current-induced spin orientation of electrons in semiconductors".

The origin of SHE divides into intrinsic and extrinsic factors. The intrinsic mechanism depends on the band structure and is typically attributed to the deflection caused by the coherence induced by the external electric field. The electrons acquire an additional velocity component, $\frac{d\langle \mathbf{r} \rangle}{dt}$ that depends on the Berry curvature of the Bloch state, $\mathbf{b}_n$, and is perpendicular to that electric field, $\mathbf{E}$:

$$\frac{d\langle \mathbf{r} \rangle}{dt} = \frac{1}{\hbar}\frac{\partial \varepsilon_n(\mathbf{k})}{\partial \mathbf{k}} + \frac{e}{\hbar}\mathbf{E} \times \mathbf{b}_n \tag{18}$$

where $\mathbf{k}$ is the momentum and ε_n is the band energy. The extrinsic mechanisms are usually subdivided into skew-scattering and side-jumping. Skew-scattering, first described by Smit[40], tends to dominate in nearly perfect crystals[41]. The chiral scattering of the electrons from impurities is caused by spin-orbit interaction leading to asymmetric left-handed and right-handed (with respect to the magnetisation) transition probabilities for a scattered electron, resulting in the current flow perpendicular to both the electric field and the magnetisation direction (AHE) or spin current polarisation (SHE).

[40] Smit, "The spontaneous hall effect in ferromagnetics II".
[41] Sinova, Valenzuela, et al., "Spin Hall effects".

However, the side-jumping mechanisms are often defined as the remaining contribution to the SHE/AHE conductivity after the skew-scattering and intrinsic factors have been accounted for. Typically, a semi-classical argument for side-jumping is attributed to Berger[42], and explains how a Gaussian

[42] Berger, "Emission of spin waves by a magnetic multilayer traversed by a current".

wavepacket undergoes a displacement transversal to its momentum upon encountering a potential gradient induced by a spherical impurity. In those cases, the governing spin-orbit Hamiltonian is usually given by[43]:

[43] Sinova, Valenzuela, et al., "Spin Hall effects".

$$\mathcal{H}_{\mathrm{SO}} = \frac{1}{2m^2c^2}\frac{1}{r}\frac{\partial V}{\partial t}S_z L_z \tag{19}$$

where S_z and L_z are the z component of the spin and orbital angular momentum, respectively. In a phenomenological picture, when an in-plane charge current flows in the HM, the SHE generates a transverse pure spin current $\mathbf{j}_s$, which is usually described with the following expression:

$$\mathbf{j}_s = \theta_{\mathrm{SH}}\left(\frac{\hbar}{2e}\boldsymbol{\sigma}\times\mathbf{j}_c\right) \tag{20}$$

where $\mathbf{j}_c$ denotes charge current, $\boldsymbol{\sigma}$ the polarisation of the spin current and θ_{SH} is the spin Hall angle defined as a ratio of spin Hall conductivity σ_{SH} to electrical conductivity σ, $\theta_{\mathrm{SH}} = \frac{\sigma_{\mathrm{SH}}}{\sigma}$. Since SHE leads to a transverse spin current flow, the spin current is absorbed at the HM/FM interface, and its transverse component dephases within the FM, exerting a torque on the FM magnetisation. However, creating an HM/FM interface has the additional effect of breaking the inversion symmetry, which leads to the Rashba-Edelstein effect (REE). REE causes net spin accumulation at the interface and exerts a torque on the FM via the exchange interaction, distinct from the spin-transfer torque, if the net spin polarisation at the interface is misaligned with the FM magnetisation.

In the literature, one frequently associates the damping-like torque with SHE and the field-like torque with REE and, while that is ultimately a good approximation, it presents a somewhat incomplete picture. For example, Amin and Stiles[44] show a HM thickness dependence of τ_{DL}, τ_{FL} torque amplitudes, broken down by the underlying effect (bulk SHE or REE). REE tends to give more or less constant values of both torques, with a dominant contribution from τ_{FL}, excluding very thin HM films. In contrast, when the SHE is the main source of torque, the damping-like part dominates and displays a saturating increase with the HM thickness. At the same time, the field-like torque contributes less, but also increases in magnitude in a similar fashion. Notable are the different signs between the SHE and Rashba contributions for the field-like torque. This has also been experimentally observed for the damping torque and is attributed, for example, to increased oxidation[45], which causes Rashba to dominate over the SHE. The discussion of the differences between SHE and REE and their torque contributions is challenging because existing experiments offer limited means to differentiate these effects clearly. Furthermore, the exact values ascribed to field-like and damping-like, notwithstanding their origin (as they are summed either way in the LLGS model), are also experimentally determined for the most part.

[44] Amin and M. D. Stiles, "Spin transport at interfaces with spin-orbit coupling".

[45] Qiu, Narayanapillai, et al., "Spin–orbit-torque engineering via oxygen manipulation"; An, Kageyama, et al., "Spin–torque generator engineered by natural oxidation of Cu".

Numerical solutions to the LLGS equations

The LLGS equation is typically solved by numerical integration, although there are Monte Carlo solvers for atomistic versions of the equation[46]. In CMTJ, the fixed-step Runge-Kutta 4 (RK4) is the default deterministic solver. Other choices include the Dormand-Prince, DP5(4), method for adaptive step integration, which is a fifth-order method with a fourth-order error estimate[47], and stochastic solvers: Euler-Heun and Heun. For most applications, we stick to fixed-size methods for the following reasons. First, the fixed step makes it trivial to compute the signal spectrum, which is the most common downstream operation performed after the simulation. Second, the accuracy of the solution does not outweigh the increase in computational complexity. If necessary, the step size can be simply reduced in the RK4 method to retain a higher degree of precision.

[46] Evans, Fan, et al., "Atomistic spin model simulations of magnetic nanomaterials".

[47] Dormand and Prince, "A family of embedded Runge-Kutta formulae".

0							
1/5	1/5						
3/10	3/40	9/40					
4/5	44/45	-56/15	32/9				
8/9	19372/6561	-25360/2187	64448/6561	-212/729			
1	9017/3168	-355/33	46732/5247	49/176	-5103/18656		
1	35/384	0	500/1113	125/192	-2187/6784	11/84	
	35/384	0	500/1113	125/192	-2187/6784	11/84	0
	5179/57600	0	7571/16695	393/640	-92097/339200	187/2100	1/40

Table 1: Butcher tableau for Dormand-Prince method.

Higher-order methods are usually given in the form of a Butcher tableau, such as the one we provide for DP5(4) in Tab.1. In this table, the rows are indexed by i, and the columns by j. Leftmost column coefficients are denoted by c_i, the values in the penultimate (second to last) row are referred to as b_i, and the bottommost one as b_i^*. The latter are used for error estimate in the adaptive methods. The slope k_i of an RK method with s stages is defined as:

$$k_i = f(t_n + c_i h, y_n + h \sum_{j=1}^{i-1} a_{i,j} k_j) \tag{21}$$

where $i = 1, ..., s$, f is the differential equation we wish to integrate and h is our step. t_n is the time at nth step and y_n is the value of the integral calculated at nth step. DP5(4) has $s = 7$. The generalised form of the numerical solution is then:

$$y_{n+1} = y_n + h \sum_{i=1}^{s} k_i b_i \tag{22}$$

Consequently, the error estimate would be the difference between two approximations at the same step y_{n+1} and y^*_{n+1}, but y^*_{n+1} is calculated with the b^* coefficients instead of the b coefficients:

$$e_n = y_{n+1} - y^*_{n+1} = h \sum_{i=1}^{s} k_i (b_i - b_i^*) \tag{23}$$

What does the error estimate bring to the table? Apart from some useful knowledge of how well we integrate, it is used to guide step size. For example, in DP5(4), an adjustment ratio to the step size could be of the following form:

$$r = q\left(\frac{1}{\text{err}}\right)^{\frac{1}{5}}, \quad \text{with} \quad \text{err} = \left\| \frac{e_n}{\text{atol} + \text{rtol}\max(|y_n|, |y_{n+1}|)} \right\| \tag{24}$$

where q is the constant safety factor, rtol is the relative error tolerance, and atol is the absolute error tolerance. The update rule is then $h' = \min(h_{\min}, \max(h_{\max}, rh))$ where h is the base step, and we make sure that the new time step is within acceptable limits, $h' \in (h_{\min}, h_{\max})$. The solver also determines whether to accept or reject a step; the step is rejected when $\text{err} > 1$, and the time step is reduced until $h_{\min}$ is reached.

Stochastic forms of Landau-Lifshitz-Gilbert-Slonczewski equation

There are a couple of established methods for solving stochastic differential equations numerically; among the most prevalent are the Euler Heun and stochastic Heun methods, or the Runge-Kutta methods[48]. Many methods cause drift of the magnetisation norm[49], so in our implementations we renormalise the magnetisation vector after each step to enforce $|\mathbf{m}| = 1$. Attempting to solve stochastic LLGS equations with standard methods typically results in an incorrect distribution of the noise (this problem becomes pronounced when simulating the $1/\text{f}$ noise). Specifically from a numerical point of view, because the normal schemes dictate samples to be drawn at each advancement of the time step, while in the stochastic version the sample is drawn once and then shared between intermediate approximations. We further note that in this scheme we can advance our approximations of the stochastic part without having to consider the remaining, coupled layers, as in our setting the noise vector generated in the layer is independent of the one generated for any other. A stochastic formulation of LLGS takes the form of a Stratonovich SDE:

[48] Mackevičius, *Introduction to Stochastic Analysis*; Rößler, "Runge-Kutta Methods for the Strong Approximation of Solutions of Stochastic Differential Equations".

[49] Ament, Rangarajan, et al., "Solving the stochastic Landau-Lifshitz-Gilbert-Slonczewski equation for monodomain nanomagnets".

$$\text{d}X_t = f(X_t, t)dt + g(X_t, t) \circ \text{d}W_t \tag{25}$$

where $f(X_t, t)$ is the deterministic part of the equation and $g(X_t, t)$ is the stochastic part of the equation. $\text{d}W$ is a Wiener increment. The symbol $\circ$ denotes the Stratonovich product, which distinguishes (25) from Ito's SDE. For the Itô integration, coefficients are evaluated at the left endpoint of the interval and in Stratonovich at the midpoint. Unlike classical Riemann integrals, the stochastic integral depends on that choice. In the particular context of the sLLGS equation, it is convenient to define the two parts f and g as operators acting on different terms of the effective field. More specifically, we first define an operator $\tilde{\mathbf{M}}_t$ acting on some field term $\mathbf{H}_t$ as follows:

$$\tilde{\mathbf{M}}_t(\mathbf{H}_t, \eta_1, \eta_2) = \eta_1 \mathbf{m}_t \times \mathbf{H}_t + \eta_2 \mathbf{m}_t \times (\mathbf{m}_t \times \mathbf{H}_t) \tag{26}$$

with η_1, η_2 being the scalar constant that scales the field-like or damping-like portion of the equation. In our case, we will implicitly define $\mathbf{f}_t(\mathbf{m}_t)$ as a proper function acting on the torque and effective fields:

$$\mathbf{f}_t(\mathbf{m}_t) = \frac{-\gamma_0}{1+\alpha_{\mathrm{G}}^2}[\tilde{\mathbf{M}}_t(\mathbf{H}_{\mathrm{eff,t}}, 1, \alpha_{\mathrm{G}}) + \tilde{\mathbf{M}}_t(\mathbf{H}_{\mathrm{torque,t}}, -\eta_{\mathrm{FL}}, \eta_{\mathrm{DL}})] \tag{27}$$

where η_{FL} and η_{DL} play the role of the torque weighting terms, and depend on the LLGS formulation (in the sense of SOT or STT). As a form of notation abuse, we will talk about g as a plain $\tilde{\mathbf{M}}_t$ operator such that we involve the explicit Stratonovich notation: $\mathbf{g}_t(\mathbf{m}_t) \circ \Delta\mathbf{W}_t = \tilde{\mathbf{M}}_t(\Delta\mathbf{W}_t, 1, \alpha_{\mathrm{G}})$. We used the notation involving $\Delta\mathbf{W}$ instead of $\mathrm{d}\mathbf{W}$ to denote the discretised motion. Because of that, we normalise by the integration step in the subsequently described solver schemes.

We will also assume that the samples from the stochastic process, $\Delta\mathbf{W}_t$ contain all the necessary scaling inside, so, for example, the thermal field can be written as:

$$\mathbf{H}_T(t) = \sigma\Delta\mathbf{W}_t = \sigma(t)\sqrt{h}\boldsymbol{\xi}_t \tag{28}$$

where $\boldsymbol{\xi}_t \in \mathbf{R}^3 \sim \mathcal{N}(0, \mathbf{I}_3)$[50] and σ denote the standard deviation of the thermal process[51,52]:

$$\sigma(t) = \sqrt{\frac{2\alpha_{\mathrm{G}} k_B T(t)}{\mu_0 \mathrm{M_s} V \gamma_0}} \tag{29}$$

where V is the volume of the cell (layer) and $k_B T(t)$ is the thermal energy of the system[53]. When this term is multiplied by $\sqrt{\Delta t}$ in the solver, it retains the same units as the non-stochastic terms when they are multiplied by Δt. In the context of $\tilde{\mathbf{M}}_t(\Delta\mathbf{W}, 1, \alpha_{\mathrm{G}})$, the damping term is sometimes discarded, due to its smaller contribution compared to the direct term[54]. In the following, we give a brief description of two methods available in CMTJ for stochastic integration.

[50] a multivariate Gaussian distributed random vector. Here, we make a transition from W being a generalised Brownian process to a Wiener process.

[51] Brown, "Thermal Fluctuations of a Single-Domain Particle".

[52] We cite the standard form here, but the author thanks Professor Jack Sankey for the discussion and the showing how the factor 4, instead of 2, could arise from equipartition derivation.

[53] the time dependence is given here explicitly, as the package allows us to determine the temperature changes over time.

[54] Kubo and Hashitsume, "Brownian Motion of Spins".

Euler-Heun scheme

Aptly named, it combines the first-order approximation (Euler) for the non-stochastic part and the second-order approximation (Heun) for the stochastic part. Following the convention of marking f_t as marking the n^{th} step of the non-stochastic LLGS and g_t to mark the n^{th} step of the stochastic LLGS, we can denote the update scheme as:

$$\mathbf{m}_{t+1} = \mathbf{m}_t + \mathbf{f}_t(\mathbf{m}_t)\Delta t + \frac{1}{2}[\mathbf{g}_t(\mathbf{m}_t) + \mathbf{g}_{t+1}(\hat{\mathbf{m}}_{t+1})] \circ \Delta\mathbf{W}_t\sqrt{\Delta t} \tag{30}$$

where we denoted the integration time step as Δt. Implicitly, both $\mathbf{f}_t$ and $\mathbf{g}_t$ also depend on time due to the presence of drivers controlling various dynamic aspects of the system, but for the sake of notation clarity, we omit that. The intermediate update $\hat{\mathbf{m}}_{t+1}$ is then given by:

$$\hat{\mathbf{m}}_{t+1} = \mathbf{m}_t + \mathbf{g}_t(\mathbf{m}_t) \circ \Delta\mathbf{W}_t\sqrt{\Delta t} \tag{31}$$

Stochastic Heun

Compared to the Euler-Heun scheme, the stochastic Heun adds the second order also to the non-stochastic part of the equation. Concretely, the update is given by:

$$\mathbf{m}_{t+1} = \mathbf{m}_t + \frac{1}{2}[\mathbf{f}_t(\mathbf{m}_t) + \mathbf{f}_{t+1}(\hat{\mathbf{m}}_{t+1})]\Delta t + \frac{1}{2}[\mathbf{g}_t(\mathbf{m}_t) + \mathbf{g}_{t+1}(\hat{\mathbf{m}}_{t+1})] \circ \Delta \mathbf{W}_t \sqrt{\Delta t} \tag{32}$$

with the intermediate estimate:

$$\hat{\mathbf{m}}_{t+1} = \mathbf{m}_t + \mathbf{f}_t(\mathbf{m}_t)\Delta t + \mathbf{g}_t(\mathbf{m}_t) \circ \Delta \mathbf{W}_t \sqrt{\Delta t} \tag{33}$$

Free energy models

In this section, we detour from the LLGS approach to magnetisation dynamics to comment on the techniques that focus on gradient optimisation, particularly the optimisation of the free energy of the system. These methods are also implemented in the CMTJ package and provide an alternative insight into the behaviour of the system, especially in the context of the resonance frequency. Sometimes, avoiding the explicit computation of dynamics and eloping into the energy domain gives numerical benefits such as stability – for example, systems with high IEC would require very small integration steps for dynamics simulation, while the energy model may be less demanding in the optimiser step. Further, visualising energy landscapes, like the one we show in Fig.3 can tell us more about available systems states in general, and the minima indicate stable positions across multiple realisations. Naturally, the energy model comes at the cost of impossibility of simulating interesting phenomena with nonharmonic input such as CIMS. We begin with the introduction of the Smit-Beljers (SB) model and then hint at spherical LLG solutions, which do not require time-dependent integration to obtain the stable state and the resonance frequency of the system. The expression for the free energy of a layer defined as in the SB model[55] is usually given by:

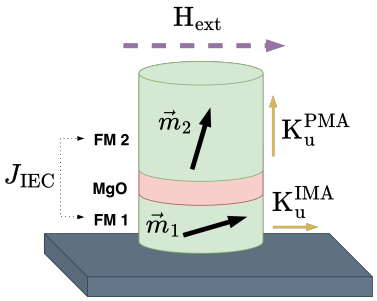

Figure 2: Individual magnetic contributions illustrated on an example MTJ. The anisotropy values are defined per layer, whereas the interlayer exchange coupling is defined per each neighbouring pair of the ferromagnetic layers.

$$\varepsilon_i = -\mu_0 \mathrm{M}_{\mathrm{s},i} \mathbf{m}_i \cdot \mathbf{H}_{\mathrm{ext}} + \frac{\mu_0 \mathrm{M}_{\mathrm{s},i}^2}{2}(\mathbf{m}_i \odot \mathbf{m}_i)\hat{\mathbf{N}}_i - \mathrm{K}_{\mathrm{u},i}^{\mathrm{PMA}} m_{z,i}^2 - \mathrm{K}_{\mathrm{u},i}^{\mathrm{IMA}} (\mathbf{m}_i \cdot \mathbf{K}_{\mathrm{dir},i})^2 \tag{34}$$

where $\mathbf{m}$ is the unit magnetisation vector in the spherical coordinates, $\mathrm{M_s}$ is the magnetisation saturation, $\mathrm{K}_{\mathrm{u}}^{\mathrm{PMA}}$ is the perpendicular anisotropy component, $\mathbf{K}_{\mathrm{dir}}$ is the in-plane direction of the in-plane anisotropy component with a value of $\mathrm{K}_{\mathrm{u}}^{\mathrm{IMA}}$, $\mathbf{H}_{\mathrm{ext}}$ is the applied magnetic field. The total free energy $\mathcal{F}$ is the sum over all layers of N, including the coupling energy between the neighbouring layers, and a simple dipole interaction defined through a tensor $\hat{\mathbf{N}}^{\mathrm{dip}}$:

$$\mathcal{F} = \sum_{i=1}^{N}[\varepsilon_i t_i + \sum_{j,j\neq i}^{N} \frac{\mu_0 \mathrm{M}_{\mathrm{s,i}} \mathrm{M}_{\mathrm{s,j}}}{2} \mathbf{m}_i^{\mathrm{T}} \hat{\mathbf{N}}_{ij}^{\mathrm{dip}} \mathbf{m}_j t_i] - \sum_{k=1}^{N-1}[J_{1,k}(\mathbf{m}_k \cdot \mathbf{m}_{k+1}) + J_{2,k}(\mathbf{m}_k \cdot \mathbf{m}_{k+1})^2 + \mathbf{D}_k \cdot (\mathbf{m}_k \times \mathbf{m}_{k+1})] \tag{35}$$

[55] Baselgia, Warden, et al., "Derivation of the resonance frequency from the free energy of ferromagnets"; Rodríguez-Suárez, Rezende, and Azevedo, "Ferromagnetic resonance investigation of the residual coupling in spin-valve systems".

with t_i denoting the thickness of the i^{th} layer. J_1 and J_2 are the values of the linear and quadratic IEC values between the k^{th} and $k+1^{\text{th}}$ layers. Likewise, $\mathbf{D}_k$ denotes the interlayer DMI vector for the interaction between the same layers[56]. Individual contributions are explained in Fig.2.

As we have mentioned in Energy density contributions, the entire free energy expression (35) can be converted to an effective field that acts on each individual layer, $\mathbf{H}_{\text{eff}}$.

First, the equilibrium state is computed using a gradient descent method, in the form of Adam, a momentum-based optimiser[57]. Then, to compute the ferromagnetic resonance, we construct a dynamical Smit-Beljers matrix with the use of a Hessian matrix:

$$\mathcal{M}_{i,j}(\omega) = \frac{\partial \mathcal{F}}{\partial \mathbf{v}_i \mathbf{v}_j} + \zeta_{\lceil j/2 \rceil}(U_{2N} - L_{2N}) \tag{36}$$

where $\mathbf{v} = [\theta_1, \phi_1, ..., \theta_N, \phi_N]$ is the vector of the spherical coordinates of the N layers. As notation shorthand, we incorporate U_{2N} and L_{2N} matrices, which are upper and lower shift matrices, respectively, constructed as $U_{i,j} = \delta_{i+1,j}$ and $L_{i,j} = \delta_{i,j+1}$ with δ denoting the Kronecker delta. $\zeta_k = \mathrm{i}\frac{\omega}{\gamma}\mathrm{M}_\mathrm{s}^k \sin\theta_k t_k$ is the imaginary factor for the k^{th} layer where ω marks the resonance frequency of the system in radians, t_k is the thickness of the k^{th} layer, and γ is the gyromagnetic factor.

Algorithm 1: High level overview of the algorithm for computing the resonance frequency and the equilibrium position.

Result: $\mathbf{r}$, vector containing the resonance frequencies.
Result: $\boldsymbol{v}^* = \boldsymbol{\Theta}^*, \boldsymbol{\Phi}^*$, equilibrium state for each layer.
Data: $\boldsymbol{v}$ vector of all layers and their parameters
`// Construct free energy vector` $\mathcal{F}$ `using (35).`
`// Find energy minimum using gradient descent`
$\boldsymbol{v}^* = \boldsymbol{\Theta}^*, \boldsymbol{\Phi}^* \leftarrow \mathrm{AdamGradientDescent}(\mathcal{F}(\mathbf{v}), \nabla_\mathbf{v}\mathcal{F}(\mathbf{v}))$
`// Construct dynamical matrix with (36)`
$\mathcal{M}(\omega) \leftarrow \mathrm{ConstructHessian}(\mathcal{F}, \boldsymbol{v}^*)$
`// Perform LU decomposition of the` $\mathcal{M}$ `matrix`
$\mathbf{L}, \mathbf{U}, \mathbf{P} \leftarrow \mathbf{LU}(\mathcal{M})$
`//` $\mathbf{P}$ `is the row permutation matrix`
$\det\mathcal{M} \leftarrow \det\mathbf{P}\det\mathbf{U}$
`// Find roots` $\mathbf{r}$ `of the determinant expression.`
$\mathbf{r} \leftarrow \mathrm{FindRoots}(\det\mathcal{M})$

The real positive roots of the determinant $\det\mathcal{M}|_{\mathbf{v}^*}$ correspond to resonant frequencies for the equilibrium state $\mathbf{v}^*$. We note that for weakly coupled layers, that is, for small values of J_1 (J_2), usually on the order of $\mu\mathrm{J}/\mathrm{m}^2$ or less, (36) can be approximated with a single-layer determinant solution:

$$\left(\frac{\omega}{\gamma}\right)^2 = \frac{1}{\mathrm{M}_\mathrm{s}^2 \sin^2\theta}\left(\frac{\partial^2\mathcal{F}}{\partial\theta^2}\frac{\partial^2\mathcal{F}}{\partial\phi^2} - \frac{\partial^2\mathcal{F}}{\partial\theta\phi}\right) \tag{37}$$

[56] Arregi, Riego, et al., "Large interlayer Dzyaloshinskii-Moriya interactions across Ag-layers".

[57] Kingma and Ba, *Adam*.

This approximation introduces a small error, but vastly improves the speed of computation, especially if the number of layers is large. The pseudocode in Alg.1 outlines the individual high-level steps necessary to calculate the ferromagnetic resonance at a given applied field.

The bulk of the algorithm's time is occupied by two components: computing the determinant and finding the roots of the determinant. The former can be quickly computed by first decomposing the matrix using the LU decomposition[58] and then computing a determinant of the resultant upper triangular matrix. However, finding roots poses a greater challenge. First, for $N \leq 2$, the returned roots are given by analytical formula. For other cases, they are computed numerically using Powell's hybrid method, implemented in the MINPACK library[59] (the SCIPY[60] module uses the same implementation). As it returns only a single root per call, we discretise the search space $[0, f_{\max}]$ into k smaller regions over which the root-finding functions are being called. On the other hand, due to the implementation of the Adam gradient descent algorithm, convergence to the energy minimum is very fast, even for larger N, and the root finding algorithm usually becomes the main bottleneck of the entire procedure. One strategy for physics-guided optimisation is to intentionally decouple selected layers where possible. This means either fixing the direction of the magnetisation vector or setting some of the IEC constants to 0 which eliminates the corresponding off-diagonal (latter) or both diagonal and off-diagonal (former) terms.

To ensure better convergence and to increase the chance of finding the global minimum instead of a local one, the initial magnetisation at the start of the simulation is knocked off the initial condition by a small random perturbation; in dynamical simulation, the same effect can also be achieved by adding some white noise via the temperature field. Yet, reaching global minimum is not guaranteed, as illustrated by the example simulation in Fig.3 – consecutive gradient descent steps are shown for two different starting conditions. Another advantage of this method is rather practical in nature, and when computing the main resonance spectrum or equilibrium, we do not need to be concerned with precise parameter selection, such as the integration step in the dynamics simulation, as the defaults of the computational parameters in CMTJ are suitable for a wide range of systems. Finally, from the point of view of simulation design, the SB model gives a simple way to define the antiferromagnet (AFM) that has a net-zero internal magnetisation. This cannot be done as easily in the dynamics model without modification, as the field contributions, such as interlayer exchange coupling or anisotropy fields, require normalisation by a M_s quantity. Modelling SAF is still possible by setting up two explicit layers of the compensating magnetic moment. Another example of the application of the SB model, this time including the resonance spectra, is described later in Bayesian optimisation.

[58] Boyd and Vandenberghe, *Convex optimization*.

[59] More, Garbow, and Kenneth E. Hillstrom, *User Guide for MINPACK-1*.

[60] Virtanen, Gommers, et al., "SciPy 1.0".

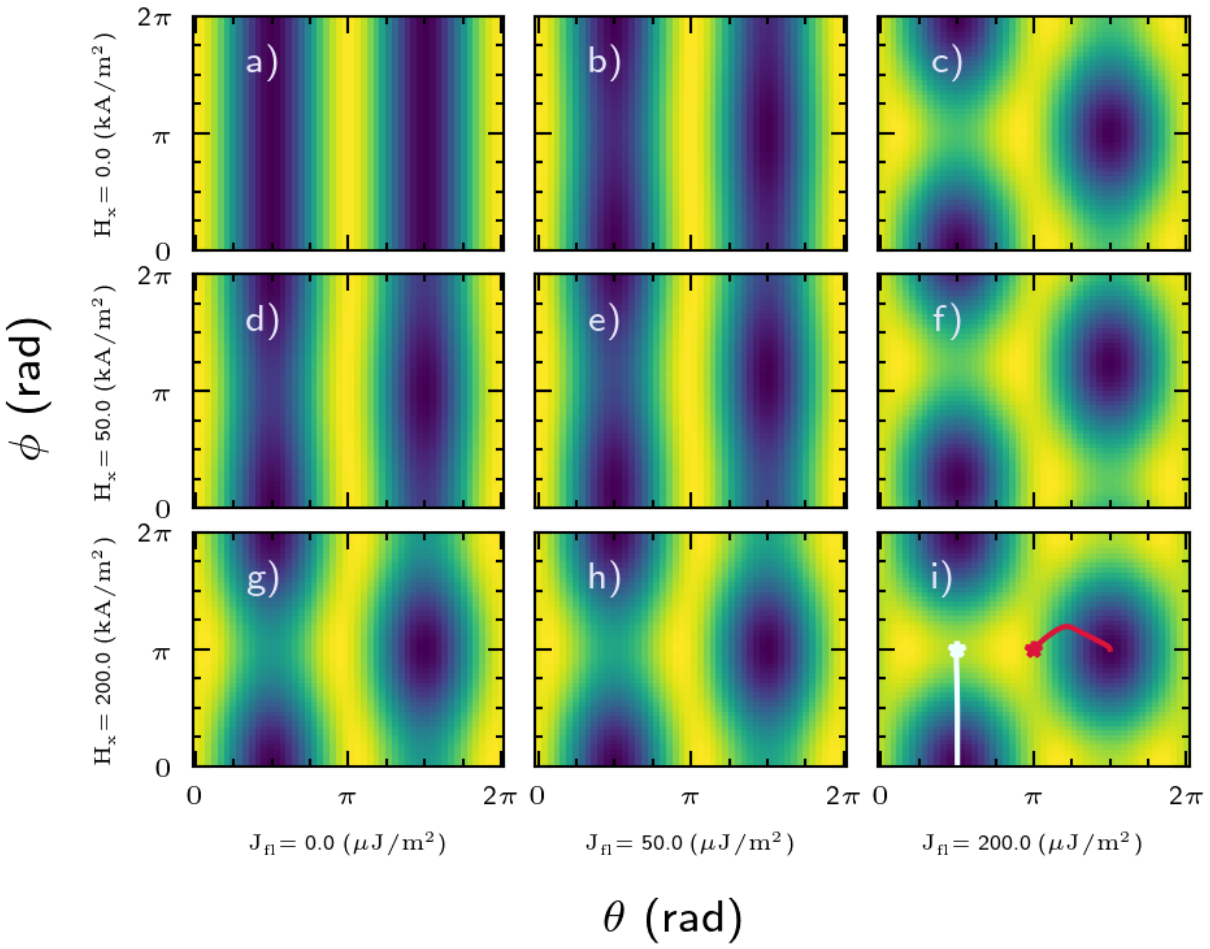

Figure 3: Energy landscapes for different values of the IEC and field magnitudes applied in the x direction for a sample structure with two FM layers. The darker the colour, the lower the value of the energy. The last panel, (i), shows two choices of initial conditions and the resulting gradient descent trajectories which are represented by the white and red lines. The star indicates the starting position. We see that increasing the coupling forces the system to be more stable in the minimum it selects. Increasing the field, as expected, has a similar effect.

Landau-Lifshitz-Gilbert-Slonczewski in spherical coordinates

A result similar to that presented by the SB method can be obtained by expressing the LLG equation using the spherical coordinates given in a general form for N layers as:

$$\mathbf{v} = \frac{\gamma_0}{(1+\alpha_{\mathrm{G}}^2)} \begin{pmatrix} \frac{1}{\mathrm{M}_{s,1}} \left(-\frac{1}{\sin\theta_1} \frac{\partial \mathcal{F}}{\partial \phi_1} - \alpha_{\mathrm{G}} \frac{\partial \mathcal{F}}{\partial \theta_1} \right) \\ \frac{1}{\mathrm{M}_{s,1} \sin\theta_1} \left(\frac{\partial \mathcal{F}}{\partial \theta_1} - \frac{\alpha_{\mathrm{G}}}{\sin\theta_1} \frac{\partial \mathcal{F}}{\partial \phi_1} \right) \\ \cdots \end{pmatrix} + \boldsymbol{\tau} \tag{38}$$

where $\boldsymbol{\tau}$ denotes torque terms. Given the spherical coordinates of N layers, we may find a stable solution by first finding the energy minimum according to the procedure previously outlined for the SB model and then solving the eigenvalue problem for the LLG Jacobian:

$$\mathbf{D}[f(\mathbf{v})] = \omega \mathbf{I} \tag{39}$$

where ω are the eigenvalues and we denoted the RHS of the (38) as $f(\mathbf{v})$. Taking the imaginary part of ω yields the resonant frequencies of the system. An additional advantage of this approach is demonstrated by the possibility of adding torque terms to the RHS of (38). This model was used in[61] where additional torque terms were included in the numerical analysis. In this model, one can also include the VSD computation assuming that under a small oscillating voltage signal $\mathrm{V_{AC}}$, the magnetisation follows and oscillates around the stationary point $\mathbf{v}_0$ with a small amplitude $\delta\mathbf{v}$.

$$(\omega \mathbf{I} - \mathbf{D}_{\mathbf{v}}[f(\mathbf{v}, \mathrm{V_{AC}})])\delta\mathbf{v}(t) = \mathbf{D}_{\mathrm{V_{AC}}}[f(\mathbf{v}, \mathrm{V_{AC}})]\delta \mathrm{V_{AC}}(t) \tag{40}$$

To obtain the linearised solution $\delta\mathbf{v}(t)$ we can invert the LHS matrix:

$$\delta\mathbf{v}(t) = (\omega \mathbf{I} - \mathbf{D}_{\mathbf{v}}[f(\mathbf{v}, \mathrm{V_{AC}})])^{-1} \mathbf{D}_{\mathrm{V_{AC}}}[f(\mathbf{v}, \mathrm{V_{AC}})]\delta \mathrm{V_{AC}}(t) \tag{41}$$

The derivative respective to exciting signal, here the voltage, necessitates that some term in $f(\mathbf{v}, \mathrm{V_{AC}})$ depends on $\mathrm{V_{AC}}$. Usually this is done through a torque with $\boldsymbol{\tau}(\mathrm{V_{AC}})$ term, but it can be placed in the $\mathcal{F}$ term; for example, in voltage-controlled magnetic anisotropy (VCMA) systems, one can set the anisotropy energy dependent as $\mathrm{K_u} + \mathrm{V_{AC}}\delta\mathrm{K_u}$[62].

[61] Ogrodnik, Grochot, et al., "Study of Spin–Orbit Interactions and Interlayer Ferromagnetic Coupling in Co/Pt/Co Trilayers in a Wide Range of Heavy-Metal Thickness"; Ogrodnik, Antonio Vetrò, et al., "Field- and temperature-modulated spin diode effect in a GMR nanowire with dipolar coupling".

[62] Nozaki, Shiota, et al., "Electric-field-induced ferromagnetic resonance excitation in an ultrathin ferromagnetic metal layer".

Domain dynamics

Classically, the dynamics of the domain wall is derived from the Lagrange-Euler (LE) equations, rather than the LLGS equation; this formalism was first introduced by Döring[63] and later expanded with damping dissipative terms by Gilbert[64]. Similarly to the LLGS equation, the Lagrangian formulation is divided into conservative energy and non-conservative (dissipative) terms, wherein the latter is introduced into the picture through the Rayleigh dissipation function $\mathcal{R}$ – in the short derivation that follows we will only include the

[63] Döring, "Über die Trägheit der Wände zwischen Weißschen Bezirken".

[64] Gilbert, "Classics in Magnetics A Phenomenological Theory of Damping in Ferromagnetic Materials".

damping term, but torque from the STT or the SHE are often enclosed in that term as well. The profile of a Bloch domain wall can be represented as the magnetisation angle with respect to the easy axis:

$$\theta(x,t) = 2\arctan\left(\exp\left(-\frac{x-X(t)}{\Delta}\right)\right) \tag{42}$$

where Δ is the width of the domain wall and $X(t)$ is the time-dependent position of the domain wall. However, since for the LE in addition to a position coordinate we need to have a conjugate momentum as well, we use the out-of-plane angle magnetisation $\phi(x,t)$ as such. This quantity is fixed to a domain wall and hence depends only on time $\phi(x,t) = \phi_0(t)$ as the magnetisation precesses. At this point, we are ready to compute the equations of motion for the Lagrangian $\mathcal{L}$ defined as an integral over the entire space of the Lagrangian density $L = K - \varepsilon$:

$$\mathcal{L} = \int \mathrm{d}\Omega\, K - \varepsilon \tag{43}$$

with:

$$K = \frac{\mathrm{M_s}}{\gamma}\dot{\phi}(1-\cos\theta) \tag{44}$$

where we use a dot notation to indicate time-derivative and we include the conservative ε energy terms. These energy terms are of the same type as those described in Free energy models. After defining the aforementioned Rayleigh dissipative equation:

$$\mathcal{R} = \frac{1}{2}\frac{\alpha_\mathrm{G}\mathrm{M_s}}{\gamma}(\dot{\theta}^2 + \sin^2\theta\dot{\phi}^2) \tag{45}$$

The two equations of motion for a 1 dimensional case are then given by the LE application:

$$\frac{d}{dt}\frac{\partial\mathcal{L}}{\partial\dot{q}_i} - \frac{\partial\mathcal{L}}{\partial q_i} + \frac{\partial\mathcal{R}}{\partial\dot{q}_i} = 0 \tag{46}$$

where $q_i = \{X, \phi\}$. As a result, we obtain sets of two equations[65] describing the velocity of the domain wall $\dot{X}$ and the rate of change of the in-domain angle $\dot{\phi}$:

$$\begin{aligned}(1+\alpha_\mathrm{G}^2)\dot{X} &= \Delta(\Gamma_A + \alpha_\mathrm{G}\Gamma_B)\\ (1+\alpha_\mathrm{G}^2)\dot{\phi} &= -\alpha_\mathrm{G}\Gamma_A + \Gamma_B\end{aligned} \tag{47}$$

where Δ is the domain width, Γ_A contains effective field terms and Γ_B contains force dissipation terms:

$$\Gamma_A = \gamma_0\Bigg(-\frac{1}{2}\mathrm{H_k}\sin 2\phi - \frac{\pi}{2}\mathrm{H_y}\cos\phi + \frac{\pi}{2}\mathrm{H_x}\sin\phi + \frac{\pi}{2}Q\mathrm{H_{DMI}}\sin\phi + \frac{2J_\mathrm{IEC}}{\mu_0\mathrm{M_s}\mathrm{t_{FM}}}\sin(\phi-\phi')\Bigg) + \frac{b_j}{\Delta}$$

[65] Thiaville, Rohart, et al., "Dynamics of Dzyaloshinskii domain walls in ultrathin magnetic films"; Martinez, Emori, et al., "Current-driven dynamics of Dzyaloshinskii domain walls in the presence of in-plane fields"; Alejos, Raposo, et al., "Current-driven domain wall dynamics in ferromagnetic layers synthetically exchange-coupled by a spacer"; Yang and S. Parkin, "Novel domain wall dynamics in synthetic antiferromagnets".

$$\Gamma_B = \gamma_0 \left(Q(\mathrm{H_z} + \mathrm{H_{th}} + \mathrm{H_p}) + \frac{\pi}{2} Q \mathrm{H_{SHE}} \cos\phi - \zeta \frac{\pi}{2} \mathrm{H_R} \cos\phi \right) + \zeta \frac{b_j}{\Delta}$$

with $\mathrm{H_R}$ as Rashba term, $\mathrm{H_{SHE}}$ spin Hall term, $\mathrm{H_p}$, pinning field term, $\mathrm{H_{th}}$ thermal field term. b_j is the STT coefficient and ζ is the nonadiabatic parameter of the STT. ϕ' denotes the angle of the domain wall of the other coupled layer. $Q \in \{-1, 1\}$ parameter denotes whether the DW is down-up or up-down, respectively. The schematic distinction between the Bloch and Néel domain walls is shown in Fig.4.

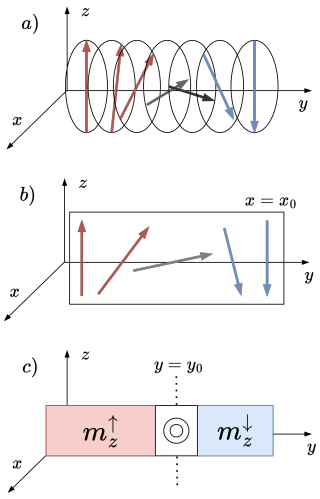

Figure 4: Two different domain wall types. (a) In the Bloch domain wall the rotation of the magnetisation is not constrained by a plane. On the other hand, the Néel domain wall (b) is characterised by a rotation in plane, here $x = x_0$. (c) Schematic view of the Néel domain wall used for simulations, the position of the domain wall is marked by $y = y_0$.

Numerical library design

In this section, we comment on the design principles for the CMTJ library that implements the numerical methods described throughout this section. Modern computing libraries aim to combine speed with a flexible interface. The user or programming interface should be intuitive yet extensible enough to maintain its relevance in a dynamically changing landscape of sprouting programming frameworks, styles, and modules. One great example is the NUMPY library[66] which despite the rapid proliferation of PYTHON retained a widespread influence on computational programming in this language. The success of such libraries stem from their previously mentioned characteristics: speed and flexibility – on the one hand, the underlying code is written in pure C for maximum performance of the vectorised function execution[67], on the other hand, the library exposes `pythonic`[68] interface that feels native to the language. NUMPY has been so effective that numerous other libraries (SCIPY, PANDAS, or TORCH just to name a few) either directly mimic its interface or ensure compatibility with NUMPY objects and functions. The CMTJ is designed in a similar fashion, combining the performance in C and ensuring interoperability with modern PYTHON. The first goal can be achieved via the PYTHON application interface, a relatively low-level interface that exposes C objects directly in PYTHON. However, since it is a basic interface, it introduces significant overhead and tends to insert a PYTHON-specific dependencies into the C code. This makes it challenging to maintain pure C components, resulting in high coupling, and reduced cohesion[69,70]. Another library, PYBIND11, offers much more flexibility and minimises the coupling between C and PYTHON-specific parts. It requires, at minimum, a single additional file in which the C functions and objects are mapped to the PYTHON interface. This approach enabled us to maintain a clear separation, allowing users to import headers directly from C++, or use the PYTHON interface. Additionally, a similar mechanism for exposing the C++ code is provided by the BOOST library[71] – which also supports direct use of NUMPY objects from C++ without implicit conversion. The VISM[72] application utilises the BOOST library and the PYQT[73] interface to visualise magnetic multilayers. The following publication describes in greater detail the physics that can be reproduced by the CMTJ library. Since that publication, the pack-

[66] Harris, Millman, et al., "Array programming with NumPy".

[67] Vectorisation is a method wherein through loop avoidance a sequence of operations can be executed in a wavefront parallel manner as per the single instruction multiple data (SIMD) model.

[68] Although this expression may be considered colloquial, it accurately describes a manner in which code is written. Here, it pertains to the use of native semantics and programming models in PYTHON as opposed to patterns imported from other languages such as C, C++ or JAVA.

[69] Both cohesion and coupling are being used as technical terms from the realm of software engineering, see the reference.

[70] Martin, *Clean code*.

[71] *Boost C++ Libraries*.

[72] Mojsiejuk, Kulig, et al., "Visualization for Micromagnetics With Synchronized Plotting".

[73] *PyQt5 Reference Guide — PyQt Documentation v5.15.7*.

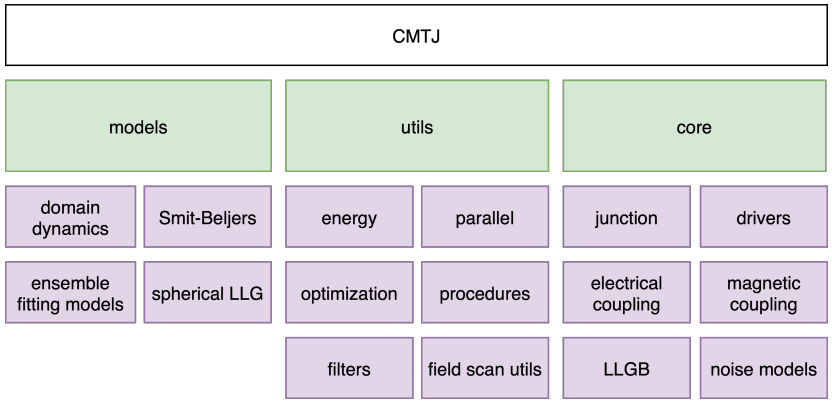

Figure 5: Outline of the CMTJ package library and its decomposition into submodules.

age has been expanded to include the Smit-Beljers models (as described in Free energy models and Landau-Lifshitz-Gilbert-Slonczewski in spherical coordinates), domain wall dynamics (Domain dynamics), Landau-Lifshitz-Bloch, and a variety of optimisation tools pertaining to those described in Bayesian optimisation. Currently, version 1.9.0 of the core library (excluding examples, graphical interfaces, and additional models) contains approximately $\sim$ 5500 lines of PYTHON code and $\sim$ 4600 lines of C++ code. The division of the main library into submodules is given in Fig.5. Additionally, we offer a simple web-based user interface and a large language model agentic system to assist users with simulations. More details in Additional Tools and Interfaces for CMTJ.

Chapter summary

In this chapter, we provided an overview of the numerical techniques implemented in the CMTJ library. The library represents the primary technical contribution of this thesis and offers the spintronics community accessible numerical techniques that do not require a powerful machine to run. Furthermore, the tools described in this section are essential for analysing and interpreting the subsequent results presented in this thesis.

Modelling spin Hall devices

This section introduces general modelling techniques used in the analysis and simulation of spin Hall devices and their associated experimental measurements. Key examples include harmonic Hall voltage detection, current-induced magnetisation switching (CIMS), spin diode ferromagnetic resonance (SD-FMR), pulse-induced magnetometry (PIMM), and R(H) loops. Specifically, the aforementioned techniques can be simulated with the CMTJ package, as detailed in Pub. 2: Open-source macromagnetic package. For experimentalists, the ability to simulate these methods offers valuable insights into observed phenomena and parameter variations, particularly in large-scale parameter scans demonstrated throughout this thesis. The main challenge in reproducing the experimental techniques lies mostly in the complexity of measurement methods, which may involve complex post-processing and filtering procedures.

We begin this section with a brief characterisation of the fabrication process that leads, among other devices, to spin Hall bars. Then, we touch on the spin Hall effects in these devices, expanding the previous discussion from Spin-Orbit torque with details relevant to this particular chapter. The following subsections are arranged into two case studies: we begin by describing FMR spectrum analysis methods and combine them with harmonic Hall detection to investigate the Ta/CoFeB system, as described in Pub. 1: Numerical model for the harmonic Hall voltage detection. We show how, with the use of simulation, we are able to extrapolate the experimental study with insights about the influence of field-like and damping-like torques on the observed harmonic voltage components. In the second part, we combine R(H) loops with CIMS to explain the interesting asymmetry of SOT switching under field reversal in Co/Pt/Co systems. Details of that sample can be found in[74]. For completeness, in Appendix Sample fabrication process we include a description of some of the fabrication processes used in the production of the experimental samples discussed in this and the next chapter.

[74] Grochot, Ogrodnik, et al., "Influence of ferromagnetic interlayer exchange coupling on current-induced magnetization switching and Dzyaloshinskii–Moriya interaction in Co/Pt/Co multilayer system"; Ogrodnik, Grochot, et al., "Study of Spin–Orbit Interactions and Interlayer Ferromagnetic Coupling in Co/Pt/Co Trilayers in a Wide Range of Heavy-Metal Thickness".

Magnetoresistance in spin Hall bars

The key measurable quantities of the device can be described with the most fundamental one, the resistance model. The baseline for the analysis of SHE

devices in this work is established on the grounds of the SMR-corrected equation for the longitudinal R_{XX} and transverse R_{XY} resistance of FM / HM due to Kim et al.[75]:

[75] Kim, Sinha, et al., "Layer thickness dependence of the current-induced effective field vector in Ta|CoFeB|MgO".

$$R_{XX} = R_{xx0} + (\Delta R_{AMR} m_x^2 + \Delta R_{SMR} m_y^2) \tag{48}$$

$$R_{XY} = R_{xy0} + \frac{\Delta R_{AHE}}{2} m_z + \frac{w}{l} (\Delta R_{SMR} + \Delta R_{AMR}) m_x m_y \tag{49}$$

where w is the width of the sample and l is the length of the sample.

As indicated in the above equations, there are contributions of three primary resistance effects: anisotropic magnetoresistance (AMR), spin Hall magnetoresistance (SMR), and anomalous Hall effect resistance (AHE). The AMR arises because of spin-dependent scattering in FM – when the direction of the current is parallel to the magnetisation, the cross-section of spin scattering is the largest. Fig.6 illustrates the effects discussed in Spin-Orbit torque and shows how R_{XX} and R_{XY} are measured.

SMR is a consequence of two effects that manifest in the HM and on the FM/HM interface. First, the longitudinal charge current induces an SHE in the HM. Then, as the transversal current reaches the interface, diffuses through the interface, and exerts a torque on the FM layer if the diffusing spins are perpendicular to the magnetisation or if the spin current carriers are collinear with the magnetisation, it deflects back into the HM. The latter case leads to spin accumulation and ISHE[76] in which the spin current is converted back to the charge current, increasing the total longitudinal current in FM, thereby reducing its longitudinal resistance. In contrast, the former reduces the spin accumulation and thus the charge current, increasing the resistance.

[76] Saitoh, Ueda, et al., "Conversion of spin current into charge current at room temperature".

Finally, AHE was briefly discussed in the Non-conservative torque terms section. As the current flows through the FM layer, the spin-dependent scattering and intrinsic factors lead to transverse spin and charge accumulation, which in ferromagnets is naturally asymmetric because of the imbalance of the majority and minority electrons. The dependence of $m_x m_y$ in transversal expression (49) is often attributed to the mixing of SHE and AHE[77] – initially, the longitudinal charge current in the FM induces the spin current in the direction perpendicular to both the magnetisation and the current itself, that is, $\mathbf{m} \times \mathbf{j}_c$. This spin current then translates into the charge current in the direction $\mathbf{m} \times \mathbf{m} \times \mathbf{j}_c$. At the same time, the transversal spin current (in the z direction) originating from plain SHE in the HM causes the charge current flow in the $\mathbf{m} \times \mathbf{p} \times \mathbf{j}_c$[78]. Therefore, for those accompanying effects to manifest in the transversal magnetoresistance measurement, the magnetisation should have some x and y components such that the entire chain of the described derivative mechanisms takes place. This mixing is of rather small magnitude.

[77] Taniguchi, "Magnetoresistance generated from charge-spin conversion by anomalous Hall effect in metallic ferromagnetic/non-magnetic bilayers".

[78] this expression, assuming a current along x-axis and spin polarisation along y-axis, reduces to $\mathbf{m} \times \hat{\mathbf{z}}$ where $\hat{\mathbf{z}}$ is the unit vector along z axis

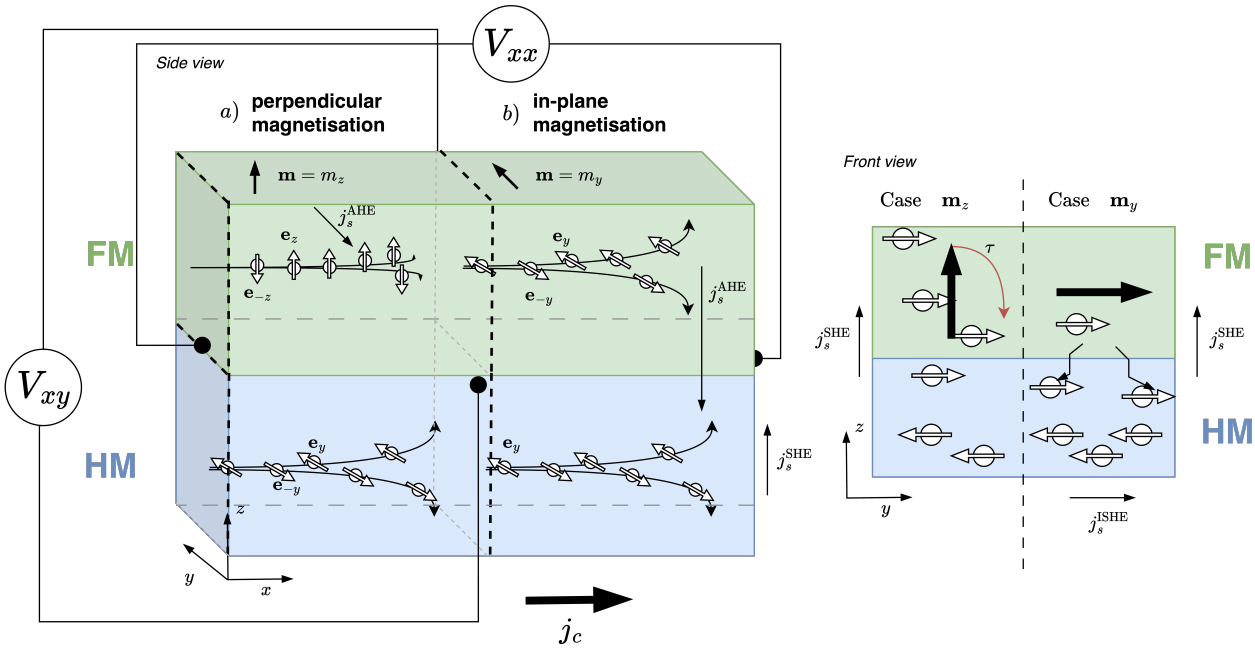

Figure 6: Selected effects in the Hall device for longitudinal V_{xx} and transverse V_{xy} arrangements for the voltage measurement and two cases of the magnetisation m. The charge current flows in the HM (blue). The vertical black dashed line divides the two cases of FM (green) magnetisation – along the z axis (left) and along the y axis (right). Depending on this arrangement, the AHE-induced current can flow into the FM.

Electrical modelling of Spin Orbit Torque Ta/CoFeB bilayer system

Next, we examine FMR by current rectification and harmonic Hall voltage detection methods in the context of the HM/FM bilayer Ta/CoFeB device. Each section includes remarks pertaining to more general cases, in order to show that the outlined simulation methods are widely applicable.

Ferromagnetic Resonance Spectrum Analysis

There are two main methods that are usually used to obtain ferromagnetic resonance spectra[79]: SD measurement or PIMM. Both methods are based on the dynamics of the system, but respond to different excitations. PIMM, in particular, can be viewed as a time-domain impulse response measurement of a spintronic system: the magnetisation vector is rocked out of its equilibrium with a short impulse, effectively a current impulse, but in fact it may happen indirectly through a resulting Oersted field impulse. Excluding the extreme damping cases, the magnetisation vector begins to relax towards the oscillation at natural frequency, which changes with the external field's magnitude or its applied angle. SD is similar in this regard to PIMM, but is typically considered as the frequency-domain method, where the dynamics is forced with the injection of a microwave sinusoidal current. The full spectrum can

[79] Ziętek, Cecot, et al., "Magnetization dynamics of NiFe film and anisotropic magnetoresistance device".

be obtained either by fixing the frequency and sweeping with the magnetic field, or vice versa, i.e. applying a fixed field while varying the generator frequency. The former has an experimental advantage in that the transmittance of the system does not change during the sweep, since the feeding excitation is kept constant (as opposed to continuous or spurious input frequency changes). However, regardless of the method, the final result should be approximately the same: a dispersion relation showing the main modes of oscillation over a range of scanned parameters (for the most part, it is a field magnitude or applied angle).

The basic set of simulated fits related to the VSD simulation has been described in detail for the Ta/CoFeB bilayer for both R_{xx} and R_{xy} configurations in Pub. 1: Numerical model for the harmonic Hall voltage detection, but here we wish to elaborate on the idea mentioned in that work. We aim to solve the inverse problem: identifying the parameters set that reproduce a given experimental line. In our case, we might be interested in reproducing the main resonance lines of some device. To do that, we can perform an iterative procedure in which we make educated guesses about likely parameters that could lead to a particular experimental result. This procedure is manual, but an optimisation technique can be used to automate and speed up the process. We now briefly describe the Bayesian optimisation process and discuss how it can be applied to fitting the spectral data.

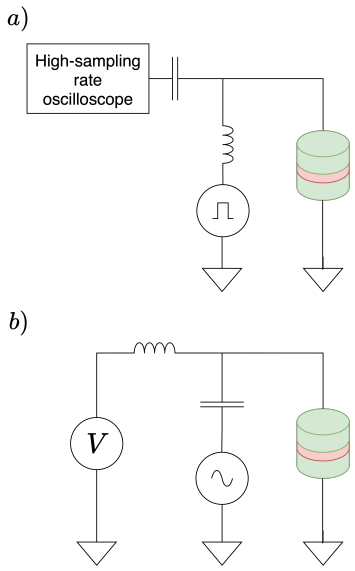

Figure 7: Setups of the experimental methods: schematics of (a) PIMM experiment and (b) the VSD-FMR experiment.

Bayesian optimisation

If the target function is complex and its derivative is not available, then zero gradient optimisation methods can be employed to efficiently find a (near-)global optima. One such method is Bayesian optimisation[80]. Suppose that we wish to find a global minimum of a function f whose explicit form we do not know and which is costly to compute. In Bayesian optimisation, we place a Gaussian process ($\mathcal{GP}$) prior on f and then optimise an acquisition function $\alpha(x)$ built from the posterior predictive to select the next x. Thus, the optimisation will alternate between two steps: (i) fit the $\mathcal{GP}$ to the current observations, (ii) select the next candidate x_c by maximising the acquisition function, and then evaluate $f(x_c)$. The procedure is then repeated with $(x_c, f(x_c))$ added to the observation set $\mathcal{D}$. Sometimes, when the observation of $f(x)$ is noisy, we model the observations as $y(x) = f(x) + \varepsilon$ with $\varepsilon \sim \mathcal{N}(0, \sigma_\varepsilon^2)$. In the case of Bayesian optimisation, the most common choice is to have f sampled from a Gaussian process:

$$f(x) \sim \mathcal{GP}(m(x), k(x, x')) \tag{50}$$

i.e., $\mathcal{GP}$ is a distribution over functions, and for each x it defines the Gaussian parameters: the expected value, $m(x) = \mathbb{E}[f(x)]$, and the variance. Taking the zero mean, $m(x) = 0$, simplifies the downstream expressions and can be achieved by renormalising the data. The kernel $k(x, x')$ defines the covariance

[80] Brochu, Cora, and Freitas, *A Tutorial on Bayesian Optimization of Expensive Cost Functions, with Application to Active User Modeling and Hierarchical Reinforcement Learning*.

between the samples taken from the domain of f and is typically defined on a radial basis, parameterised over $\Theta = (\eta, \lambda)$ such that:

$$k_\Theta(x,x') = \eta \exp\left(-\frac{1}{2}\frac{||x-x'||^2}{\lambda^2}\right) \tag{51}$$

The set of parameters Θ is learnt during the training procedure. We construct the marginal likelihood $p(y|X)$, defined over the observed data y, given the inputs X:

$$p(y|X) = \int p(y,f|X)\,df = \int p(y|f,X)p(f|X)\,df \tag{52}$$

In this expression, we identify the likelihood $p(y|f,X)$ and a Gaussian process prior, $p(f|X) = \mathcal{N}(m(X), \mathbf{K}_\Theta(X,X))$, where $\mathbf{K}_\Theta$ is now a $N \times N$ matrix, with $N = |X|$, $[\mathbf{K}_\Theta]_{ij} = k_\Theta(x_i,x_j)$. The fitting procedure seeks to find:

$$\Theta^*, \sigma_\varepsilon^* = \underset{\Theta,\sigma_\varepsilon}{\operatorname{argmax}}\ \log p(y|X) \tag{53}$$

and is optimised numerically. However, the posterior predictive $f(x)|\mathcal{D}$ for the function values at any point x is also Gaussian, and its two statistics, mean and variance, are computed from closed-form expressions[81]:

[81] Bishop, *Pattern recognition and machine learning*.

$$\mu(x,\Theta) = m(x) + \mathbf{k}_\Theta^{\mathrm{T}}\mathbf{K}_y^{-1}\,\mathbf{y} \tag{54}$$

$$\sigma^2(x,\Theta) = k_\Theta(x,x) - \mathbf{k}_\Theta^{\mathrm{T}}\mathbf{K}_y^{-1}\,\mathbf{k}_\Theta \tag{55}$$

where $\mathbf{k}_\Theta = [k_\Theta(x,x_1),...,k_\Theta(x,x_N)]$, $\mathbf{y} = [y(x_1) - m(x_1),...,y(x_N) - m(x_N)]$ and $\mathbf{K}_y = \mathbf{K}_\Theta(X,X) + \sigma_\varepsilon^2\mathbf{I}$

Fitting a Gaussian process under the set of N observations constitutes the first of two steps of global optimisation of f. In the next step of the procedure, we balance the exploitation of high-confidence regions against the exploration of high-variance regions. Regulating this balance is done via the acquisition functions, of which two are the most common: expected improvement and upper confidence bound (UCB). In our experiments, we predominantly use UCB, but modern methods combine multiple acquisition functions and then maximise over the Pareto front[82]:

[82] Cowen-Rivers, Lyu, et al., *HEBO Pushing The Limits of Sample-Efficient Hyperparameter Optimisation*.

$$\alpha_{\mathrm{UCB}}(x|\mathcal{D}_n) = \mu(x,\Theta) + \sqrt{\beta}\sigma(x,\Theta) \tag{56}$$

where $\mathcal{D}_n$ denotes the dataset observed so far: $[(x_1,y(x_1)),...,(x_N,y(x_N))]$. β parameter controls the trade-off between exploitation and exploration by promoting a large mean or a large variance. The next candidate for the evaluation is thus given by:

$$x_c = \underset{x}{\operatorname{argmax}}\,\alpha_{\mathrm{UCB}}(x|\mathcal{D}_n) \tag{57}$$

When fitting any experimental result, we keep in mind the problem of the multiplicity of solutions. Potentially, the space of systems that have the exact

same set of minima (parameters) is infinite, and similar sets of parameters may lead to the same results. Therefore, to fit a resonance line, we first solve the linear assignment problem per field index H_k:

$$P^* = \min_P \sum_i^{\mathrm{T}} \sum_j^{\mathrm{S}} C_{ij} P_{ij} \quad \text{s.t.} \quad \sum_i P_{ij} = 1, \sum_j P_{ij} = 1, \quad P_{ij} \in \{0,1\} \forall i,j \quad (58)$$

with T as the number of target frequencies and S as the number of candidate frequencies per field index H_k. The cost function is defined as $C_{i,j} = |\mathrm{f_{i,target}} - \mathrm{f_{j,candidate}}|$ and P_{ij} is the assignment of i^{th} target frequency value to j^{th} simulated frequency. For our optimisation metric, we take the maximum error of the optimal assignment for each field index k:

$$\varepsilon_k = \max\{C_{ij} : P^*_{ij} = 1\} \quad (59)$$

This arrangement of the cost function not only makes it a worst-case estimator, but also allows us to avoid having to determine the source of the resonance layer, thus making our system somewhat spatially invariant[83]. The final value of the cost function that enters the Bayesian optimisation is given by mean squared error (MSE):

$$\mathrm{MSE} = \frac{1}{K} \sum_k^K \varepsilon_k^2 \quad (60)$$

where K is the total number of field-scan steps.

This procedure was used in the investigation of the experimental samples of Ta(2)/CoFeB(5)/W(0-10)/CoFeB(1)/MgO(2)/Ta(1) (thicknesses in nm) over a range of W thicknesses. The fitting procedure was first performed under the assumption that there is a transition from the effective in-plane anisotropy of the thinner CoFeB layer to the perpendicular anisotropy as the thickness of the W decreases. The initial set of parameters[84]: $\mathrm{M_s}$, $\mathrm{K_u^{PMA,top}}$, $\mathrm{K_u^{IMA,bottom}}$ and antiferromagnetic coupling constant J parameters, was seeded for the thickest W of 9.74 nm by Bayesian optimisation within reasonable boundary conditions. The fittings for consecutively smaller thicknesses were tuned only in J and $\mathrm{K_u}$, with upper bounds inherited from the system with the next thickest W. The final result of this procedure is shown against the experimental data in Fig.8. The SB model, described in the Free energy models section, is particularly suited for such a fitting, as it is able to give direct frequency values that can be easily inserted into the cost function. In contrast, the dynamic LLGS model would require automatic frequency extraction from the spectrum, which is prone to numerical noise, especially if the spectrum is multimodal. The Bayesian optimisation procedure outlined in this section was used to seed a good initial set of parameters for most of the simulations described in the subsequent chapters.

[83] A simple example of this is to imagine a weakly-coupled system with two FM layers with reasonably different magnetic parameters. We expect 2 frequencies for each field, one per layer. During the simulation, we should also obtain 2 frequencies, provided that they are not degenerate. We need not concern ourselves with the geometry of a system because if the parameters of the upper and lower layers are flipped, the resonance spectrum coming from the simulation would be exactly the same, and so should be the cost function

[84] Here the top layer had a perpendicular anisotropy and the bottom layer had the in-plane anisotropy.

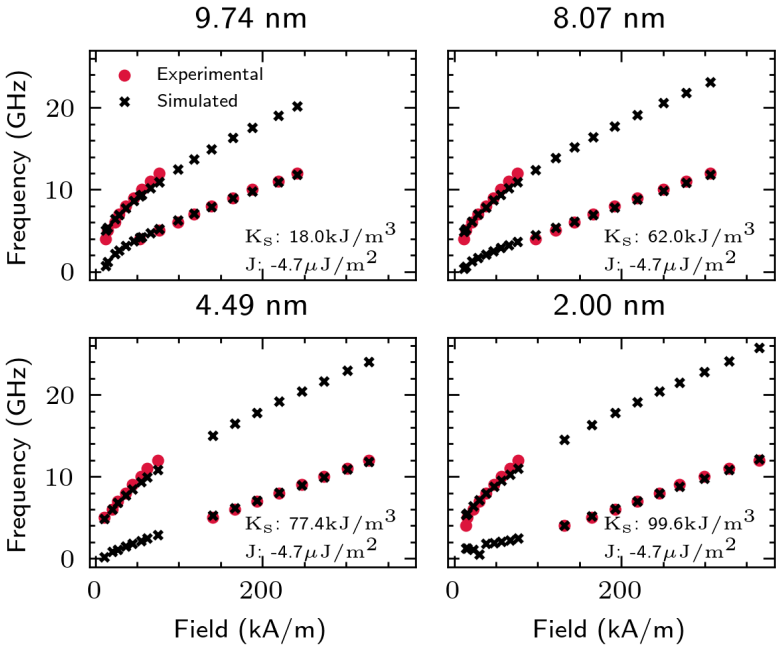

Figure 8: Ferromagnetic resonance fits to the experimental data on Ta(2)/CoFeB(5)/W(0-10)/CoFeB(1)/MgO(2)/Ta(1) wedge samples. The lower resonance line comes from the thinner layer, and it slowly decreases as the thickness decreases; this is primarily caused by the increase of the perpendicular anisotropy component of that layer. Fits were carried out using the SB model.

Harmonic Hall voltage detection

One of the key parameters in optimising SOT devices is the spin Hall angle. The determination of that parameter tells us how well a given system converts the charge current into the spin current, and therefore it is critical for energy-efficient fast memory applications. Switching dynamics is typically driven by extrinsic stimuli, most often current injection. Hence, it must be governed by the torques, both the damping and the field-like. One way to measure the efficiency of both torques occurs through harmonic Hall voltage detection. First, we define two quantities: damping- and field-like spin torque efficiencies (alternatively, effective spin Hall angles), $\xi_{\mathrm{DL/FL}}$ respectively:

$$\xi_{\mathrm{DL/FL}} = \frac{2e\mu_0 \mathrm{M_s}}{\hbar} \frac{\mathrm{t_{FM}} \mathrm{H_{DL/FL}}}{j_c} \tag{61}$$

where $\mu_0 \mathrm{M_s}$ is the magnetisation saturation, t_{FM} is the thickness of the ferromagnetic layer, and j_c is the charge current density flow in the heavy metal. What we ultimately aim to measure are the two quantities, the magnitudes of the torques $\mathrm{H_{DL/FL}}$. These are extracted by fitting the first- and second-harmonic responses of the system under sinusoidal excitation with the current input. Each of these responses is measured in two arrangements, one called longitudinal (L) with the field applied along the direction of the current flow, the x axis, and the other transversal (T) where we apply the field along the y axis (see Fig. 1 in Pub. 1: Numerical model for the harmonic Hall voltage detection). This results in four measurement curves, each of which is used

in the fitting procedure. Specifically, we should fit to the low-field region, where the first harmonic response will have a quadratic form and the second harmonic will have a linear form. Thus, we have the following:

$$\mathrm{H_{DL}} = -\frac{2}{\zeta}\frac{\rho_L \pm 2\kappa\rho_T}{1-4\kappa^2} \tag{62}$$

where κ is the ratio of the planar Hall effect to AHE resistance, $\rho_{L/T} = \partial V_{2\omega}/\partial \mathrm{H}_{\mathrm{ext}}^{L/T}$ and $\zeta = \partial^2 V_\omega/\partial \mathrm{H}_{\mathrm{ext}}^2$. The latter two parameters come from fitting the harmonic response in the process in which we obtain the slope of the linear region and the coefficient of the quadratic function. As noted earlier, the determination of field-like and damping-like torques can be done in a number of other ways, for example through the analysis of the SOT-FMR as in the work of Skowroński et al.[85]. Nguyen et al.[86] provide a good review of the available methods.

The work Pub. 1: Numerical model for the harmonic Hall voltage detection demonstrates an end-to-end process where simulation has been paired with the experiment – starting from magnetoresistance fits, through VSD-FMR fits and culminating with fitting the harmonic Hall voltage detection curves. Finally, the simulation is used to extrapolate the results and present the dependence of the harmonic Hall voltage measurements on the torques: $\mathrm{H_{DL}}$ and $\mathrm{H_{FL}}$, $\mathrm{M_s}$ and the anisotropy constant $\mathrm{K_u}$.

[85] Skowroński, Karwacki, et al., "Determination of Spin Hall Angle in Heavy-Metal/Co − Fe − B -Based Heterostructures with Interfacial Spin-Orbit Fields".

[86] Nguyen and Pai, "Spin–orbit torque characterization in a nutshell".

Electrical modelling of ferromagnetically coupled Co/Pt/Co system

In this section, we continue our study of spin-Hall devices, this time focussing on the trilayer system Co/wedge Pt/Co. The following sections contain selected results from the work Grochot, Ogrodnik, et al. ("Influence of ferromagnetic interlayer exchange coupling on current-induced magnetization switching and Dzyaloshinskii–Moriya interaction in Co/Pt/Co multilayer system") and expand on them. Before that is discussed in detail, we begin with a general overview of R(H) and CIMS methods; in the latter we use, as illustrative examples, an extrapolated numerical sample.

Current Induced Magnetisation Switching

We now give a brief account and a general overview of the CIMS, to form a basis for a later discussion in the context of the perpendicular-magnetised Co/Pt/Co system and its interesting behaviour. In CIMS we attempt to flip the state of the magnetisation along a specific axis, for example, z axis, such that if the initial magnetisation vector was aligned along the $-z$ axis, then after a current impulse it flips to point along the $+z$ axis. The duration and shape of the impulse impact the result; shorter impulses give steep relationships, which have a single maximal (minimal) switching current, whereas longer impulses (in the infinite limit, simply an applied current density) saturate critical current densities at large absolute values of the externally applied

magnetic field. The procedure used to simulate CIMS related phenomena is described in Alg.2.

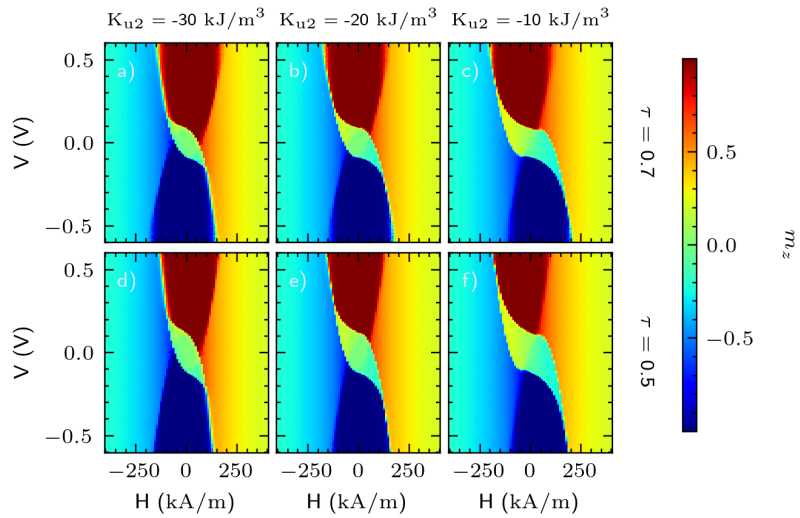

Figure 9: CIMS stability diagrams – an averaged m_z component as a function of torque τ, external magnetic field, applied voltage (current), and K_2, the quadratic anisotropy constant. Top row, $\tau = 0.7$, bottom $\tau = 0.5$, left-to-right has an increase in K_2 which skews, rotates and narrows the region where $m_z = 0$. The plots were produced for the MTJ structure SAF/FeCoB/MgO/FeCoB. Parameters: $\mu_0 M_s = 1.12$ T, and perpendicular anisotropy constant $K_{u,1} = 563$ kJ/m^3. The temperature was set to 300 K and the simulation was averaged over 50 realisations.

The standard stability diagram is produced by averaging the magnetisation component along the switching axis over a fixed time window $[t_{relax}, T]$ after discarding the initial relaxation period, t_{relax} (T is the total simulation time)[87]. We look for the regions of high and low resistance as a function of the current density. In the picture, high-resistance states indicate that the maximum resistance was observed when scanning the current density in one way (from negative to positive values, or vice versa); the converse case applies to low-resistance states. As there is no need to compute a frequency spectrum, calculating the switching diagram is much more efficient with the adaptive step

[87] Strelkov, A. Timopheev, et al., "Stability phase diagram of a perpendicular magnetic tunnel junction in noncollinear geometry"; A. A. Timopheev, Sousa, et al., "Respective influence of in-plane and out-of-plane spin-transfer torques in magnetization switching of perpendicular magnetic tunnel junctions".

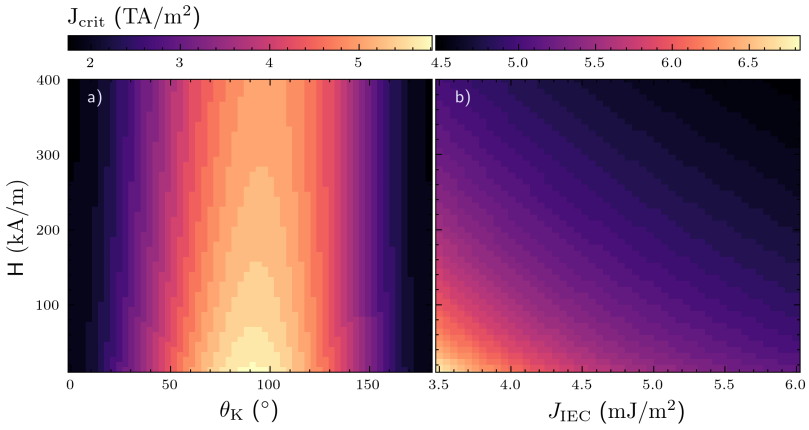

Figure 10: Critical current density as a function of the field vs anisotropy angle (a) and the field vs the IEC constant (b). Figure shown on JEMS 2022.

Algorithm 2: Procedure for simulating CIMS

Result: Steady state resistance vector $\mathcal{R}$
$\mathcal{R} \leftarrow \{\}$
$j_{\min} \leftarrow$ minimum current density
$j_{\max} \leftarrow$ maximum current density
$\mathbf{H}_{\text{ext}} \leftarrow$ external applied field
S $\leftarrow$ ferromagnetic system
T $\leftarrow$ simulation time
for j *in* $[j_{\min}, j_{\max}]$ **do**
  S.setCurrentDensityFunction($j \exp\{-t/\tau_p\}$)
  S.setExternalField($\mathbf{H}_{\text{ext}}$)
  $\mathbf{m} \leftarrow$ S.runSimulation()
  `// Take an average over relaxed` **m** `as a steady state of the magnetisation`
  $\langle \mathrm{R} \rangle \leftarrow$ computeResistance($\langle \mathbf{m} \rangle_{[t_{\text{relax}}, \mathrm{T}]}$)
  $\mathcal{R} \leftarrow \mathcal{R} \cup \langle \mathrm{R} \rangle$
end

methods, as described in Numerical solutions to the LLGS equations. A typical diagram based on sample buffer / SAF / FeCoB(1) / MgO(1) / FeCoB(1.3) / W(0.25)/ FeCoB(0.5)/ cap[88] is shown in Fig.9. Similarly to Strelkov et al.[89], we check the impact of changing the secondary quadratic anisotropy component on the shape of the $m_z = 0$ region. The STT formulation used is a bit different from the one shown in (7), using explicit linear and square voltage dependence in damping-like and field-like torques, respectively:

$$\mathbf{T}_{\text{torque}} = \mathbf{T}_{\text{DL}} + \mathbf{T}_{\text{FL}} = -\gamma a_{\parallel} V \mathbf{m} \times (\mathbf{m} \times \mathbf{p}) + \gamma a_{\perp} V^2 \mathbf{m} \times \mathbf{p} \tag{63}$$

where V is the applied voltage, $\mathbf{p}$ is the polarisation vector and $a_{\parallel}, a_{\perp}$ are the phenomenological transport parameters typically derived from free-electron, tight-binding or first-principles models of the MTJs[90].

Many modern designs favour SOT switching instead of STT switching due to issues connected to Joule heating, and, as we indicated in the earlier chapters, from a simulation point of view, these turn out to be equivalent up to a choice of a parameter. Theoretical aspects of the dependence of switching currents in HM/FM systems are reasonably well understood (Lee et al.[91]), and for instance, for an in-plane field H_x, the critical current threshold is given by:

$$j_c \propto \frac{2e}{\hbar} \frac{\mathrm{M_s t_{FM}}}{\theta_{\text{SH}}} \left(\frac{\mathrm{H_k}}{2} - \frac{H_x}{\sqrt{2}} \right) \tag{64}$$

where $\mathrm{H_k}$ denotes the effective anisotropy field. However, this relation does not hold when there is strong coupling, and thus numerical simulations are required for most cases. To illustrate the point and show how complicated the situation may become under large coupling in Fig.10 which presents an

[88] at the moment of writing, the article is in review
[89] Strelkov, A. Timopheev, et al., "Stability phase diagram of a perpendicular magnetic tunnel junction in noncollinear geometry".

[90] Wilczyński, Barnaś, and Świrkowicz, "Free-electron model of current-induced spin-transfer torque in magnetic tunnel junctions"; Chshiev, Manchon, et al., "Analytical description of ballistic spin currents and torques in magnetic tunnel junctions".
[91] K.-S. Lee, S.-W. Lee, et al., "Threshold current for switching of a perpendicular magnetic layer induced by spin Hall effect".

example trilayer (FM/HM/FM) switching mechanism as a function of the field and anisotropy angle θ_{K_u} (a) or exchange coupling constant between the two layers J_{IEC} (b). Here, particularly for (b), we can deduce, through a mix of parameter fitting and function guessing, that the dependence of the critical current on the system parameters could be proportional to (up to a shared offset constant):

$$j_{crit.} \propto j_0 \exp\{-aJ_{IEC}\sinh(b\mathrm{H}_{ext})\} \tag{65}$$

where j_0, a and b are the fitting constants, dependent on the intrinsic parameters of the system. The expression can be obtained by producing the slices of the map from (b), i.e. $j_{crit}(J_{IEC})$ for all fields and observing a clear exponential and *sinh* behaviour, and the latter can be deduced after plotting the fitting parameter as a function of H_{ext}.

Another non-trivial point is that of geometry. In[92] we investigated a α-W/CoFeB stack where the signs of H_{FL} and H_{DL} could take negative values. When the impulse pulse is sent through the HM layer, the resulting Oersted field can hamper the switching, i.e. increase the magnitude of the critical current. Fig.11 illustrates that classical geometry. However, if the sign of H_{FL} is negative, it effectively aligns with the Oersted field and therefore can result in overall reduced critical currents. We modelled the impact of the Oersted field using a simple relation (orientated along the negative y-axis to comply with the convention in Fig.11):

$$\mathrm{H}_{Oe,-y} = \sigma_{Oe}\frac{j(t)t_{HM}}{2} \tag{66}$$

where j is the current density, t_{HM} is the thickness of the HM layer, and σ_{Oe} is the scaling factor that corrects for the rough macro-spin Oersted field estimate.

In this switching geometry ($y \to -y$) with effective in-plane anisotropy, and no bias field, we require an additional symmetry-breaking term along the x axis; otherwise no stable or deterministic torque will be exerted with current flowing in the x axis (which fixes the polarisation vector along the $+y$ axis, $\hat{\mathbf{e}}_y$). To this end, we use in-plane demagnetisation terms. Starting from the LLG equation in the form of:

$$\frac{\partial \mathbf{m}}{\partial t} = -\gamma\mathbf{m}\times\mathbf{H}_{eff} + \alpha\mathbf{m}\times\frac{\partial\mathbf{m}}{\partial t} - \gamma\mathrm{H}_{FL}(\mathbf{m}\times\hat{\mathbf{e}}_y) - \gamma\mathrm{H}_{DL}\mathbf{m}\times(\mathbf{m}\times\hat{\mathbf{e}}_y) \tag{67}$$

we analyse the stability condition $\frac{\partial\mathbf{m}}{\partial t} = 0$, and compute torque components at equilibrium[93]:

$$0 = \frac{\partial\mathbf{m}}{\partial t} = \mathrm{T}_{eff} + \mathrm{T}_{FL} + \mathrm{T}_{DL} \tag{68}$$

where $\mathrm{T}_{eff} = \mathbf{m}\times\mathrm{H}_{eff}$ contains $\mathbf{H}_{eff} = (-H_d^x, -H_d^y - \mathrm{H}_{Oe}, \mathrm{H}_k - H_d^z)$, with the demagnetisation fields H_d^i for each component x, y, z, the Oersted field H_{Oe}, and the perpendicular magnetic anisotropy field H_k. Using $\mathbf{m} = (\cos\phi\sin\theta, \sin\theta\sin\phi, \cos\theta)$, and observing that switching occurs

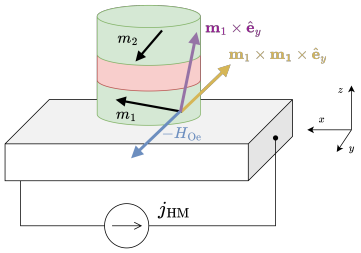

Figure 11: Sketch of a typical switching geometry. Note that H_{Oe} is drawn with the opposite sign to the damping-like torque.

[92] Cierpiał, Grochot, et al., "Spin-Orbit torque in α-W-Based Magnetic Tunnel Junction".

[93] K.-S. Lee, S.-W. Lee, et al., "Threshold current for switching of a perpendicular magnetic layer induced by spin Hall effect".

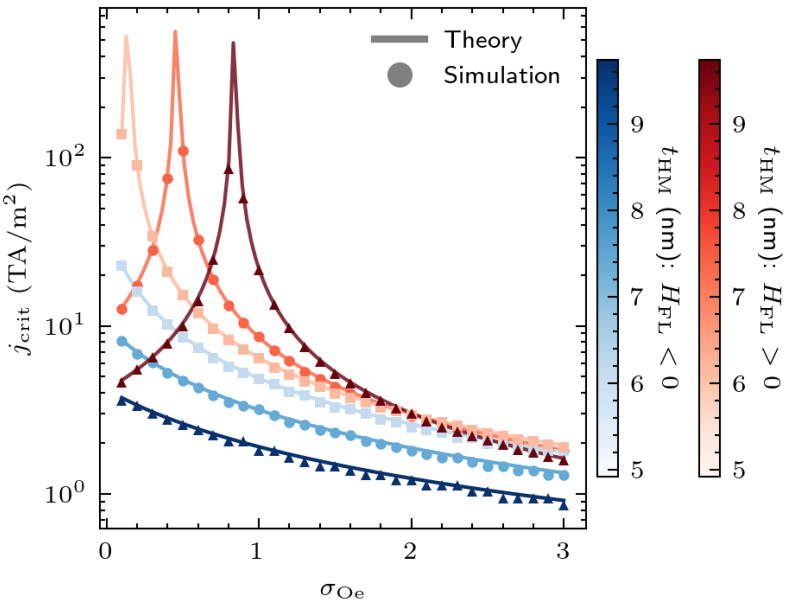

Figure 12: Theoretical (solid line) and simulated (markers) results for three sample thicknesses of W. Blue colour scale illustrates the case when $\mathrm{H_{FL}} < 0$, and red when $\mathrm{H_{FL}} > 0$. Values for j_{HM}, $\mathrm{H_{FL}}$ and $\mathrm{t_{HM}}$ were taken from the experiment. In each case, at $\sigma_{\mathrm{Oe,crit}}$ and $\mathrm{H_{FL}} > 0$, the Oersted field begins to dominate over $\mathrm{H_{FL}}$. Since the Oersted field does not compete with $\mathrm{H_{FL}} < 0$, there is no inflexion point and the current densities are lower overall. The change of peaks depending on W is not always linear, because the increase in the current (and thus the Oersted field) is not linear in the same way as the increase of $\mathrm{H_{FL}}$.

mainly in-plane, that is, $\theta \approx \pi/2$ we arrive at the approximate equilibrium equation:

$$(\mathrm{H_{FL}} + \mathrm{H_{Oe}} + H_d^y)\cos\phi - H_d^x \sin\phi = 0 \tag{69}$$

The damping-like torque is not present in (69), suggesting that the switching in this geometry is driven primarily by field-like torque. After taking the derivative and making trigonometric substitution, we obtain the solution to the quadratic equation for $\sin\phi$:

$$\sin\phi = \pm \frac{H_d^x}{\sqrt{(H_d^x)^2 + (H_d^y + \mathrm{H_{FL}} + \mathrm{H_{Oe}})^2}} \tag{70}$$

Substituting (70) it back into (69), and setting $\mathrm{H_{Oe}} = j\mathrm{H_{Oe}^j}$ and $\mathrm{H_{FL}} = j\mathrm{H_{FL}^j}$, we arrive at the threshold current after solving for $j = j_{\mathrm{th}}$:

$$j_{\mathrm{th}} = \frac{\pm H_d^x - H_d^y}{\mathrm{H_{FL}^j} + \mathrm{H_{Oe}^j}} \tag{71}$$

Clearly, competition arises when the field-like torque in (71) changes sign. In our simple Oersted field model, the inflexion point of this competition occurs at the singularity $\sigma_{\mathrm{Oe,crit}}$:

$$\sigma_{\mathrm{Oe,crit}} = -\frac{2\mathrm{H_{FL}^j}}{t_{\mathrm{HM}}} \tag{72}$$

Fig.12 shows the simulated and computed threshold currents for the competing and non-competing cases of field-like torque, clearly indicating that

a non-competing case of $H_{FL} < 0$ yields order of magnitude smaller critical currents. Three thicknesses of HM were considered, demonstrating the shifting of the critical point, σ_{Oe}.

In the subsequent discussions, we omit the impact of the Oersted field on the switching currents either because of its additive nature (in qualitative sense it compensates the increase or decrease in torques) or because it cancels out in the overall geometry.

R(H) loops

R(H) loops are the most basic tools that provide fundamental insight into the systems. The direction of the applied external field and the resulting shape of the R(H) curve reveal the AMR, AHE and SMR factors, or the magnetic anisotropy energy. In the latter case, if the field is applied along the easy axis, the R(H) curve exhibits a more "square"-like shape. In contrast, a smooth, continuous transition from one boundary-resistance state to another is a testimony to a large anisotropy in that direction. Any horizontal shifts may indicate the presence of some internal bias field, for example, coming from the exchange bias contribution.

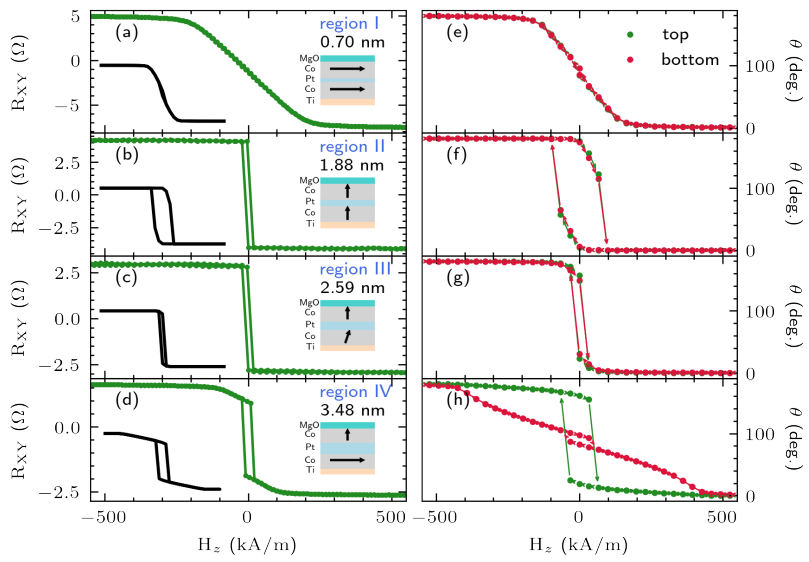

Figure 13: Study of AHE loops for 4 different thickness regions of the Pt (it is given by the inlaid thickness in nm) for the Co(1)/Pt(0-4)/Co(1) sample. Left, (a-d) – black curves in the inset correspond to the simulated results, whereas the green line represents the experimental data. The inset pictures of the Co/Pt stack illustrate the effective anisotropies of each FM layer. A clear transition to strong perpendicular anisotropy of the top Co layer is visible as we move from region I to region III. In region IV the IEC is very weak, almost negligible, so the bottom Co layer, being decoupled from the top one, stays in plane. Right, (e-h) simulation of the θ magnetisation coordinate of the top (red) and bottom (green) layers, corresponding to black insets in (a-d). As the thickness of the Pt spacer increases, the top layer switches with a larger field than the bottom one: the strong coupling field no longer enforces mutual and symmetric switching.

A notable application of R(H) modelling is found in the case of the coupled thin Co layers (each having 1 nm thickness) separated by a Pt spacer that changes from 0 to 4 nm. The detailed description of the fabrication procedure is given in Grochot et al.[94] and Ogrodnik et al.[95] In such a system, the coupling between the two ferromagnets is varied with the thickness of the Pt layer; however, we found also that the anisotropy varies with that thickness, and appears to be crucial components in understanding the phenomenon of

[94] Grochot, Ogrodnik, et al., "Influence of ferromagnetic interlayer exchange coupling on current-induced magnetization switching and Dzyaloshinskii–Moriya interaction in Co/Pt/Co multilayer system".

[95] Ogrodnik, Grochot, et al., "Study of Spin–Orbit Interactions and Interlayer Ferromagnetic Coupling in Co/Pt/Co Trilayers in a Wide Range of Heavy-Metal Thickness".

multilevel switching that we discuss later in the text.

A study of the Co/wedge Pt/Co system begins with the AHE loops, that is, the R(H) loops with the external field applied along the z axis, as they mainly measure the m_z component of the magnetisation; see Eq.(49). We will vary selected parameters to investigate possible explanations for the shape transition of the AHE loops in the second (moderate coupling between to Co layers) and third (weak coupling) regions of the Co(1)/Pt(0-4)/Co(1) sample (thicknesses given in nm); the particular characteristics of each region are given by Ogrodnik et al.[96] First, we present the simulation results for the base case that agree with the observed experimental values, as shown in Fig.13, where the simulated loops are placed as insets. The hysteresis is given for an external perpendicular field, H_z, taken for 4 different thicknesses of Pt. The thicker the Pt layer, the lower the IEC value, which corresponds to the J parameter, which means that the two layers are progressively weakly coupled. Regions II and III are characterised by the largest perpendicular anisotropy in the top layer. Hence, under the large J regime, the two layers will switch simultaneously in fully perpendicular loops.

[96] Ogrodnik, Grochot, et al., "Study of Spin–Orbit Interactions and Interlayer Ferromagnetic Coupling in Co/Pt/Co Trilayers in a Wide Range of Heavy-Metal Thickness".

Fig.13(e-h) also gives magnetisation angles θ of the top and bottom layers for the corresponding AHE loops. The transition from (a-c) to (d) reveals a plausible reason behind the bending of the loop, which may be explained by the difference in switching fields between the top and the bottom layers; this is caused by a much smaller coupling value that no longer enforces symmetric switching. Those results parametrically match the experimental case and will later be used for the CIMS simulations.

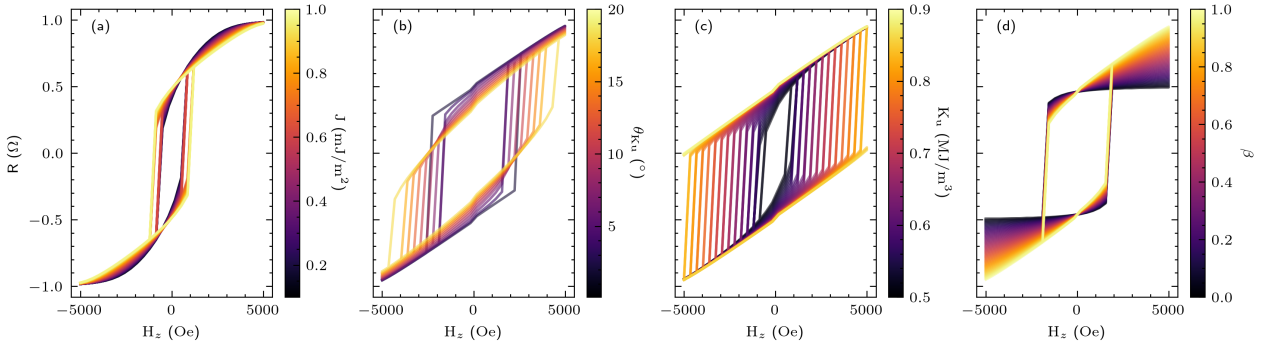

Figure 14: Effects of variation in 4 parameters on AHE loops. (a) IEC constant J, (b) anisotropy axis angle $\theta_{Ku,1}$, of the top layer, c) anisotropy constant $K_{u,1}$ of the top layer and d) the AHE asymmetry parameter β. Relating the behaviour from this plot to Fig.13 we see that there are multiple underlying parameters that could explain the bending of the hysteresis in this system. From Fig.13 (f) we see strong perpendicular anisotropy of the top layer, while the bottom goes strongly in-plane. The widening of the hysteresis can also be explained by larger in-plane anisotropy.

Further investigation of the origins of loop deformation is conducted by varying key simulation parameters, as shown in Fig.14. There, the following parameters were changed: factor β, $K_{u,1}$ (the anisotropy axis), $\theta_{K_{u,1}}$ (the angle of the anisotropy respective to the positive z axis), and J (the IEC

constant). β parameter determines the balance between the top and bottom layers in the resistance summation (75), and its significance is discussed in detail in later section. At first glance, the effects of varying β and J appear similar, but in fact the latter causes the AHE loop to bend more, rather than just rotate. Therefore, the change in shape and bending of the loop near the switching field in region IV may be attributed to a small IEC value. Likewise, a stronger rotation of the same loop may be caused by a greater influence of the interface mixing, leading to greater interfacial asymmetry and hence to a greater β factor.

Multilevel switching in Co/Pt/Co systems: numerical analysis

A phenomenon called multilevel switching (MLS) is observed in Co/wedge Pt/Co thin-wedge systems with strong ferromagnetic interlayer coupling through the Pt layer when subjected to a CIMS experiment[97]. Under certain conditions, such as appropriately large perpendicular anisotropy, the top and bottom layers experience strong opposite spin-orbit torques induced by the current impulse in the heavy metal that separates the two FM layers. If there exists an asymmetry between the two Co layers, for example, due to different interfacial mixing of the heavy metal with the ferromagnets[98], then we may observe a separation of standard CIMS hysteresis. Representative results are shown in Fig.15 (a, d, g); the middle panel is omitted from this discussion for now. The key characteristics of this switching behaviour are as follows:

[97] Grochot, Ogrodnik, et al., "Influence of ferromagnetic interlayer exchange coupling on current-induced magnetization switching and Dzyaloshinskii–Moriya interaction in Co/Pt/Co multilayer system".

[98] Ogrodnik, Grochot, et al., "Study of Spin–Orbit Interactions and Interlayer Ferromagnetic Coupling in Co/Pt/Co Trilayers in a Wide Range of Heavy-Metal Thickness".

1. the decrease in the width of the hysteresis, and so the critical switching currents, with the increase in thickness of Pt,
2. the apparent vertical gap between the hysteresis performed under the positive external applied field and the negative one,
3. the squishing of the hysteresis height (peak-to-peak resistance) with the decrease in thickness of Pt.

To better understand the physical origin of this behaviour, we start with a simplified algebraic model that considers the additive contributions of the top and bottom layer AHE terms. From (49) we exclude the mixing term $m_y m_x$ due to the vanishing amplitude of m_y in the studied system; this also brings more clarity to the consecutive discussion. First, consider the total transverse resistance as the sum of contributions from the top and bottom layers:

$$\mathrm{R_{XY}} = \mathrm{R}^{(1)}_{\mathrm{xy0}} + \mathrm{R}^{(2)}_{\mathrm{xy0}} = \Delta\mathrm{R}^{(1)}_{\mathrm{AHE}} m_z^{(1)} + \Delta\mathrm{R}^{(2)}_{\mathrm{AHE}} m_z^{(2)} \tag{73}$$

with superscripts indicating the top (1) and bottom (2) layer quantities. For a moment, we ignore $\mathrm{R}^{(1,2)}_{\mathrm{xy0}}$ quantities as the present a constant offset irrespective of the magnetisation state. If we start with a standard bilayer hysteresis under the switching current, we can make a symmetric argument that the switching current sweeping from $j_{\max}$ to $j_{\min}$ at H_x is simply a reflection

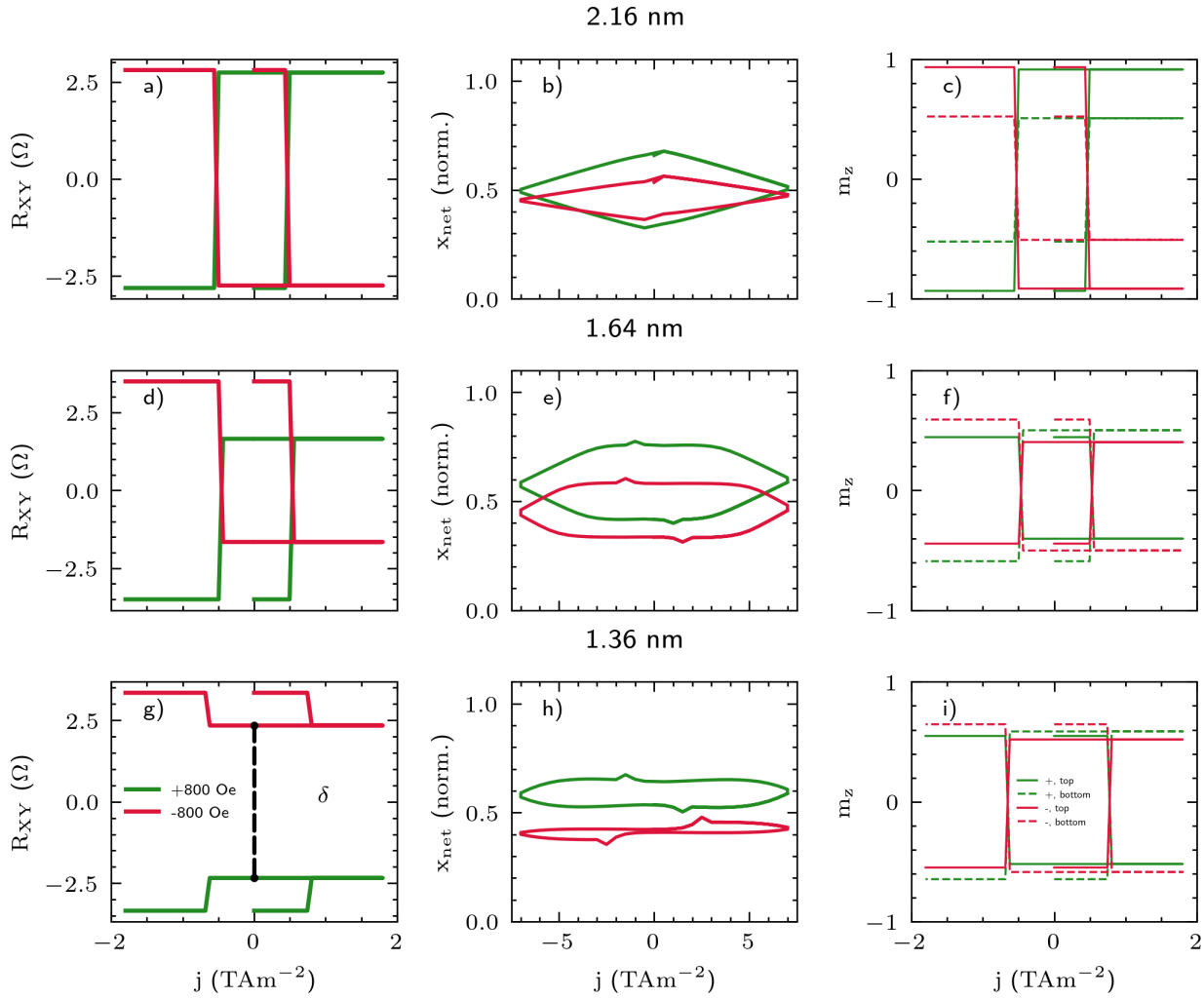

Figure 15: Macromagnetic and domain wall models with asymmetric AHE resistance switching hysteresis $R_{XY}(j)$ under field reversal regime. The left-hand side panel presents the macromagnetic switching model, whereas the middle-panel side model gives the domain wall model simulation, with y-axis denoting the displacement of the domain wall. We see a similar behaviour of state overlap as the Pt thickness decreases (coupling increases) in both cases. The right-hand side panel shows the m_z states during the switching procedure, as shown in (a, d, g). The figure taken from (Grochot, Ogrodnik, et al., "Influence of ferromagnetic interlayer exchange coupling on current-induced magnetization switching and Dzyaloshinskii–Moriya interaction in Co/Pt/Co multilayer system") shows purely simulation results.

with respect to the y axis when we sweep under $-H_x$ and, indeed, that is the case when we inspect the critical current (j_c) behaviour introduced by Lee et al.[99], mentioned earlier. We note that this formula (64) pertains to the bilayer FM/HM systems and hence has a primarily illustrative purpose in this discussion because of the strong coupling field in the system – we indicate this approximation with the use of the $\propto$ symbol. The reason why we roughly hold to that approximation in the subsequent argument is that the experimental critical current thresholds as shown in[100] indeed exhibit a similar switching model, up to a value of the offsetting field, a case that we consider more in detail in a later discussion. Under this symmetric switching argument, we define an MLS gap δ_{MLS} as:

$$\delta_{\mathrm{MLS}} = \mathrm{R}^{+}_{\mathrm{XY}} - \mathrm{R}^{-}_{\mathrm{XY}} = \Delta\mathrm{R}^{(1)}_{\mathrm{AHE}}(m^{(1)}_{z,+} - m^{(1)}_{z,-}) + \Delta\mathrm{R}^{(2)}_{\mathrm{AHE}}(m^{(2)}_{z,+} - m^{(2)}_{z,-}) \quad (74)$$

Here, we denoted $\mathrm{R}^{+/-}_{\mathrm{XY}}$ as the hysteresis resistance under positive field and negative field, respectively. To obtain $\delta_{\mathrm{MLS}} \neq 0$ we have $\Delta\mathrm{R}^{(1)}_{\mathrm{AHE}} \neq \Delta\mathrm{R}^{(2)}_{\mathrm{AHE}}$, since under symmetric j_c we assumed $m^{(i)}_{z,+} - m^{(i)}_{z,-} = 0, i = \{1,2\}$. Note that we inspect the case of field reversal, in which the response is symmetric about the y axis, so there is no change of sign between $m^{(i)}_{z,-}$ and $m^{(i)}_{z,+}$. This suggests that the MLS gap arises from the asymmetries in AHE resistance between layers. To incorporate this into the model, we introduce a weighting factor, β, that captures the imbalance in the interfacial contributions of AHE and / or the electrical connection:

$$\mathrm{R}_{\mathrm{XY}} = \mathrm{R}^{(1)}_{\mathrm{xy0}} + \mathrm{R}^{(2)}_{\mathrm{xy0}} + \frac{1}{2}\kappa\Delta\mathrm{R}_{\mathrm{AHE}}(m^{(1)}_{z} + \beta m^{(2)}_{z}) \quad (75)$$

where the superscript refers to the top (1) or the bottom layer (2). The parameter β ranges from 0 exclusive (asymmetric interfaces) to 1 inclusive for entirely symmetric interfaces. Second, the parameter κ corrects for the amplitude of hysteresis in macromagnetic simulations. Equation (75) is modified from Kim et al.[101] where in the approximation we again neglected $\Delta R_{\mathrm{SMR_{xy}}}$ and $\Delta R_{\mathrm{AMR_{xy}}}$ due to their small values in the experiment. Fig.15 leans on the idea of the AHE resistance asymmetry by introducing the interfacial asymmetry parameter β as outlined above – β approaches one as the Pt layer increases in thickness. Clearly, it can provide an adequate level of agreement with the experiment compared to the experimental data[102]. The estimate for the size of the MLS gap based on the β factor is shown in Appendix Estimate of the MLS gap.

In addition to the AHE asymmetry, another contributing factor is the asymmetry arising from interfacial DMI effects. We mentioned in sections Energy density contributions and Non-conservative torque terms, that strong interfacial asymmetry induces a myriad of effects, one of them being the DMI effect described in an earlier chapter. From the experiment, the measured DMI field in the studied sample appears to be the strongest in the III region, and due to interfacial characteristics, the $\mathrm{H_{DMI}}$ field points along the

[99] K.-S. Lee, S.-W. Lee, et al., "Threshold current for switching of a perpendicular magnetic layer induced by spin Hall effect".

[100] Grochot, Ogrodnik, et al., "Influence of ferromagnetic interlayer exchange coupling on current-induced magnetization switching and Dzyaloshinskii–Moriya interaction in Co/Pt/Co multilayer system".

[101] Kim, Sheng, et al., "Spin Hall Magnetoresistance in Metallic Bilayers".

[102] Grochot, Ogrodnik, et al., "Influence of ferromagnetic interlayer exchange coupling on current-induced magnetization switching and Dzyaloshinskii–Moriya interaction in Co/Pt/Co multilayer system".

x axis, the same as the applied external field. Hence, we could modify our previous expression (64) for the critical current:

$$j_c \propto \frac{2e}{\hbar}\frac{M_s t_{FM}}{\theta_{SH}}\left(\frac{H_k}{2} - \frac{H_x \pm H_{DMI}}{\sqrt{2}}\right) \tag{76}$$

which has the effect of modulating the H_x field depending on the direction of the applied field. Including the DMI asymmetry between the two interfaces modifies the in-plane field, widening or narrowing the hysteresis loop depending on its alignment relative to the applied field. Typically, the DMI values in Co/Pt systems are of the order of 1 mJ/m^2, although there appears to be some variation in reporting these numbers in the literature[103].

[103] Kuepferling, Casiraghi, et al., "Measuring interfacial Dzyaloshinskii-Moriya interaction in ultrathin magnetic films".

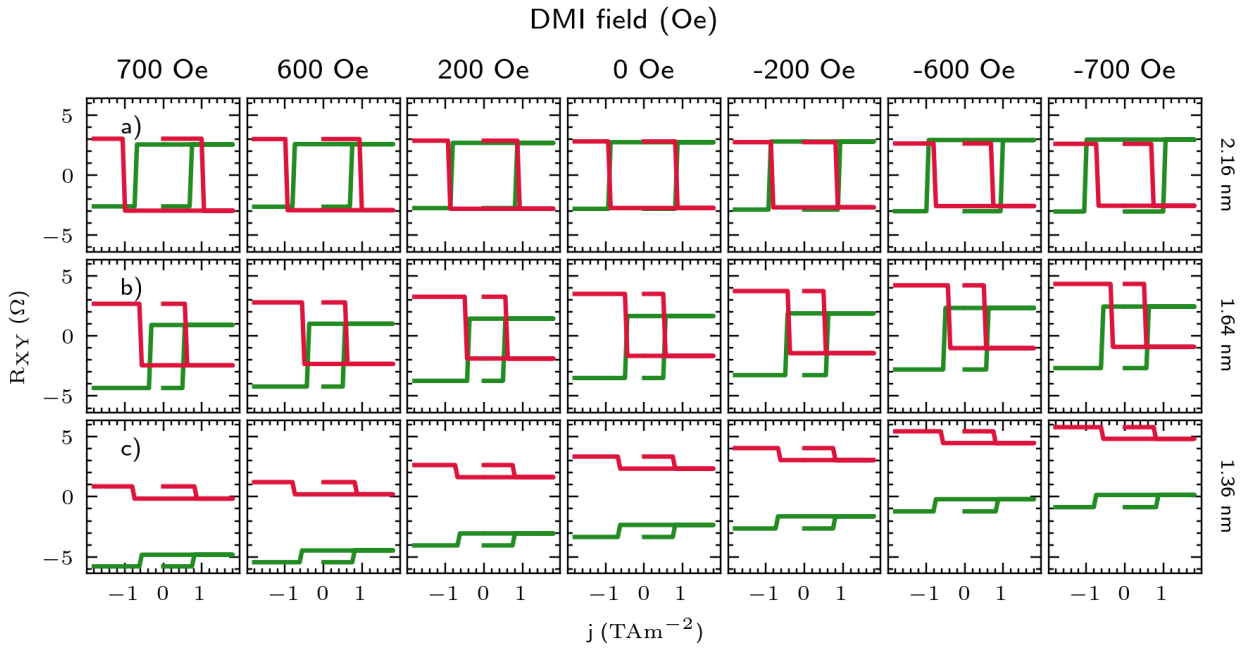

Figure 16: Simulated effect of the DMI field on hysteresis loops at different Pt spacer thicknesses during CIMS. (a) Pt thickness of 2.16 nm, (b) 1.64 nm, (c) 1.36 nm. All parameters, other than the H_{DMI} magnitude along x direction, were kept the same as in the previous simulations. As before, red colour denotes the hysteresis under -800 Oe while the green one under 800 Oe.

In Fig.16, we can observe how the DMI field aids the switching mechanism. If it is in the same (opposite) direction as the applied field, the DMI field facilitates (opposes) switching, which manifests itself with a narrower (wider) hysteresis. There is also the question of the vertical drift of the hysteresis when substantial asymmetry is present; Fig.16(b, c). This drift persists even if we disable m_x, m_y from R_{XY} calculation, suggesting this is solely due to m_z behaviour. In particular, inspecting torque equilibria (68), we notice that H_{DMI} appears in the z component of the torque, as it is set along the x axis. The DMI field will tend to reduce the m_z component if positive, specifically for the bottom layer, which has a much lower perpendicular anisotropy;

the top layer with strong PMA is not affected by the drift. However, when both the R_{XY} of the top and bottom layers are added in series, that small drift is amplified, especially for thinner Pt layers, which are parametrised to weaker PMA in the model.

Altogether, the DMI alone does not influence the gap (see that in Fig.16, at $H_{DMI} = 0$ the gap is still visible, and is unaffected in size otherwise). However, the DMI component does introduce a different type of asymmetry, the asymmetry between the switching currents for the positive and negative fields, but does very little to meaningfully affect the size or the behaviour of the gap.

To account for the MLS gap itself, we consider one more alternative mechanism that bases the existence of the MLS gap on the strength of the coupling field and appropriate relative positioning of $m_z^{(1)}$ and $m_z^{(2)}$, but assumes equal β factors for both layers. The idea here is as follows: in the strong coupling regime, we want the two anisotropy fields to force the z components of the magnetisation close to each other, which maximises the coupling field strength. According to the coupling formula (16), if two z are imbalanced, that is, one is small and the other is large, the product will likely be small, but when those two are of similar magnitude, the coupling field acting on both will be rather large. Therefore, in the simulations we devise the following method to test this hypothesis: we set the coupling high (in the range of $3-6\ \mathrm{mJ/m^2}$) and set the perpendicular anisotropy of the top layer at K_{off}. The bottom layer anisotropy is then defined relative to the top layer anisotropy, such that: $K_{bottom} = K_{off} - \Delta K$, with positive ΔK. Here, we assume, as per the parameters in Ogrodnik et al.[104], that the top layer has strictly perpendicular anisotropy with the bottom layer being much smaller, to the extent that it can be effectively in-plane, if needed. We can now scan with the value of ΔK to obtain Fig.17 and Fig.18. Here, we define the field reversal gap, or shift, as $\delta' = |\min(R_{XY}^{+}) - \min(R_{XY}^{-})|$, which means that if δ' is larger than the height of the hysteresis, then there is no overlap between the two hysteresis loops under field reversal. This is in effect equivalent to δ_{MLS}.

[104] Ogrodnik, Grochot, et al., "Study of Spin–Orbit Interactions and Interlayer Ferromagnetic Coupling in Co/Pt/Co Trilayers in a Wide Range of Heavy-Metal Thickness".

Taken together, our results suggest that both the interfacial AHE asymmetry (through the β factor) and the anisotropy configuration jointly contribute to the emergence of the field-reversal hysteresis gap. In the article, Grochot et al.[105] considered a narrower range of parameters, mainly the variation in the anisotropy, which excluded the latter option, as it requires a larger anisotropy gap between the two Co layers.

[105] Grochot, Ogrodnik, et al., "Influence of ferromagnetic interlayer exchange coupling on current-induced magnetization switching and Dzyaloshinskii–Moriya interaction in Co/Pt/Co multilayer system".

Multilevel switching with domain wall model

The multilevel switching can be reproduced with the domain wall dynamics model we described in Domain dynamics. Because of the large spin-orbit coupling at the interfaces with the HM, there is a reasonably large DMI.

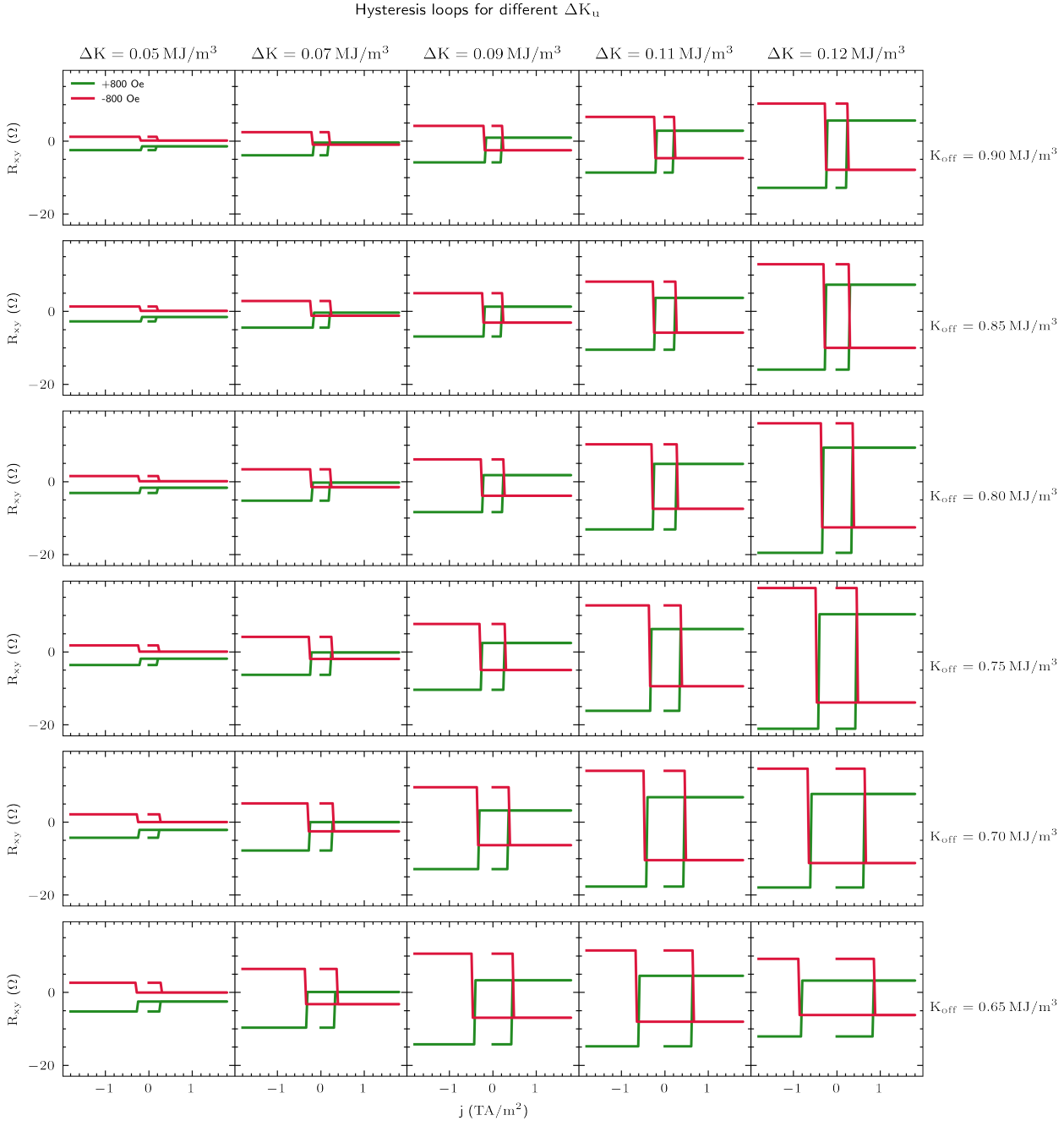

Figure 17: Effect of scanning with ΔK for different values of the top layer perpendicular anisotropy K_{off}. This is an alternative way to achieve MLS, avoiding the introduction of an interfacial asymmetry variable, which was required for Fig.15

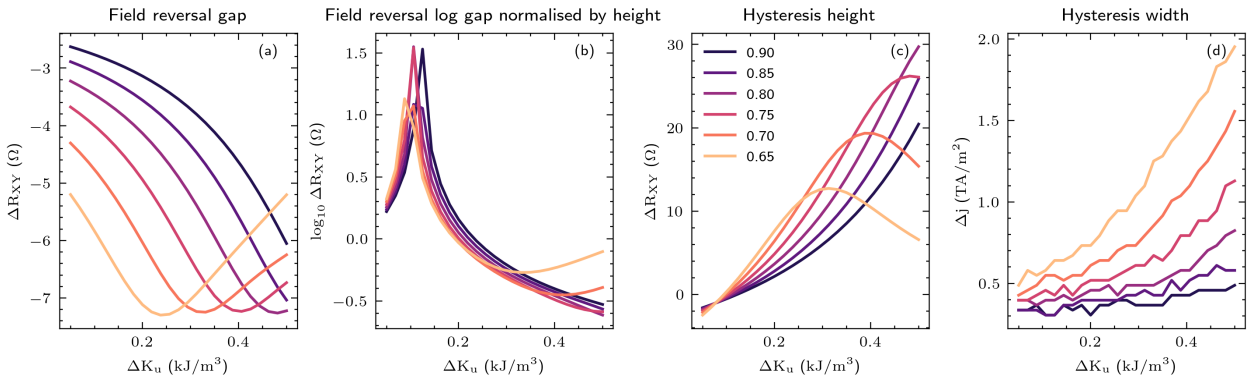

Figure 18: Effect of scanning with ΔK on hysteresis parameters, presented for different values of the top layer perpendicular anisotropy K_{off}. (a) field reversal gap defined as $\left|\min(R^{+}_{XY}) - \min(R^{-}_{XY})\right|$, and normalised by the positive field hysteresis height in (b). (c) hysteresis height (taken from the positive field hysteresis) and d) hysteresis width (taken from the positive hysteresis field). Note that if the field reversal gap is normalised (b), it gives rise to an interesting non-linearity – the magnitude here denotes the effective resolution of the gap, that is, it peaks where the gap is the largest relative to the height of the hysteresis. The wiggly nature of (c) is due to the granularity of the current scan, and hence the switching currents are not always selected with the highest precision.

We now return to the middle side of Fig.15 which presents a side-to-side comparison between the two switching models, where for the domain wall model we used the displacement on the strip of the domain as an indicator of the m_z component, the model derives from (47). Summing the contributions of the two layers, we reproduce the result from the classical macromagnetic simulation. A proper square-like hysteresis loop of the system is possible; however, it requires an additional field component or clipping. When the domain reaches an edge of the device, we have to either numerically clip the x component to contain the domain within the sample or introduce an edge potential that acts as a stopping force as the domain approaches the edge. Only the asymmetric AHE hypothesis was modelled, as other mechanisms are not readily compatible with the domain wall dynamics.

Chapter summary

This chapter summarises the research on spin Hall bars, in particular, a study on two systems: the CoFeB/Ta bilayer device and the coupled HM/FM Co/wedge Pt/Co systems which take advantage of the spin Hall effect and IEC. We presented a wide range of electrical detection techniques, outlining how they were implemented in CMTJ. For the coupled device, we also analysed an interesting phenomenon of the multilevel switching, proposing two viable hypotheses that could explain it, at least numerically: one relies on the asymmetry in the AHE resistance of the two layers, while the other is more organic and arises through the asymmetry in the perpendicular anisotropy of Co layers. Arguably, these two mechanisms may coexist and are indistinguishable in simulation. Regarding the application of multilevel switching,

it could be perceived as a variation of multibit cells, similar to[106], particularly if the gap separation can be controlled through a careful fabrication process. Then, given sufficient resolution between levels (i.e. the gap is wide enough), four resistance states per device could be distinguished. Finally, the phenomenon of multilevel switching warrants supplementary research to determine whether it can be reproduced with different FM and/or HM materials. Similarly, in the simulation domain, the topic could be further explored in a more granular fashion using the micromagnetic approach.

[106] Rzeszut, Skowroński, et al., "Multi-bit MRAM storage cells utilizing serially connected perpendicular magnetic tunnel junctions".

Modelling magnetic tunnel junctions

This chapter focuses on magnetic tunnel junctions, and is structured into two main sections: one addressing the electrical coupling of the in-series connected MTJs, and the other the modelling of $1/f$ noise. After a brief characterisation of an MTJ, we investigate a desynchronisation phenomenon observed experimentally in such systems and discuss how it manifests when there is a notable parameter dispersion between two connected devices. In the second section, we consider MTJs within a stochastic framework, highlighting the capabilities of CMTJ to simulate stochasticity, particularly composite magnetic noise in MTJs. Both sections share a common focus on the device itself and the modelling approach used in CMTJ.

Magnetic Tunnel Junctions

Modern magnetic tunnel junctions are composed of two FM layers, typically made of CoFeB, or Fe layers separated by an oxide, typically MgO. The operation of such a device relies on the quantum-mechanical tunnelling of the electrons from one FM layer to another through the insulating oxide barrier. Tunnelling depends on the matching of the majority and minority bands.

W. Butler showed from DFT calculations[107] how symmetry-dependent spin filtering leads to giant tunnelling magnetoresistance (TMR) along high-symmetry interfaces[108]. In summary, the symmetry group in the Brillouin zone along [001] is 4mm, with the cubic crystal direction [001] denoted as Δ. This group has four representations (two one-dim and two two-dim), of which the symbols of particular significance are Δ_1 (spd)[109], Δ_5 (p_x, p_y, d_{xy}), and $\Delta_2'(d_{xy})$. These form a specific band structure along the Δ line $\Gamma[000] \rightarrow \mathrm{H}[001]$ in which they turn out to be the only bands that cross the Fermi level. In particular, in a spin-resolved band structure, one can see that Δ_1 crosses the Fermi level only for the majority carriers and has the slowest decay rate. Therefore, if two Fe electrodes are in parallel, the majority spin Δ_1 continues through the barrier from one electrode to the other. When the two electrodes are in opposite magnetisation, there are no Δ_1 states available to carry the tunnelling current. This is enough to account for the giant TMR in FM/MgO/FM structures (other bands, Δ_5 and Δ_2 have Tunnelling Density of States (TDOS) that decay orders of magnitude faster in

[107] Butler, X.-G. Zhang, et al., "Spin-dependent tunneling conductance of Fe | MgO | Fe sandwiches".

[108] in the original work it was Fe/MgO [001] which we follow here as well

[109] the brackets indicate the basis

the direction of the opposite electrode). The picture of the highly symmetric crystalline MgO barrier can be contrasted with that of the amorphous one of the Al-O barriers, where other Bloch states also carry the tunnelling current, effectively reducing the total spin polarisation and causing incoherent tunnelling. In fact, some of the first significant TMR ratios at room temperature were demonstrated by Miyazaki and Tezuka[110] on the amorphous barrier junctions $Fe/Al_2O_3/Fe$, and amounted to 18%. In 2004, Parkin et al.[111] and Yuasa et al.[112], independently, replaced that amorphous barrier with magnesium oxide and showed TMR ratios of 220% in Fe/MgO/Fe MTJs at room temperature. Later, in 2008, Ikeda et al. reported a record-breaking TMR ratio of 604% at room temperature for the CoFeB/MgO/CoFeB pseudo-spin valve structure[113].

[110] Miyazaki and Tezuka, "Giant magnetic tunneling effect in Fe/Al2O3/Fe junction".
[111] S. S. P. Parkin, C. Kaiser, et al., "Giant tunnelling magnetoresistance at room temperature with MgO (100) tunnel barriers".
[112] Yuasa, Nagahama, et al., "Giant room-temperature magnetoresistance in single-crystal Fe/MgO/Fe magnetic tunnel junctions".
[113] Ikeda, J. Hayakawa, et al., "Tunnel magnetoresistance of 604% at 300K by suppression of Ta diffusion in CoFeB/MgO/-CoFeB pseudo-spin-valves annealed at high temperature".

Drawing from the conclusions above, we would ideally like any tunnel barrier to be as thin as possible, which would mean the strongest tunnelling current and the smallest resistance due to the higher Δ_1 TDOS at the opposing electrode. However, when we make the barrier too thin, we at the same time remove the symmetric bands, which perform spin filtering, i.e. the discrepancy between the majority Δ and minority Δ, meaning the majority spin carriers and the minority spin carriers; existence of which is indispensable to the TMR effect.

An important trend in modern MTJ design tends to lean towards fabrication of the perpendicular anisotropy MTJs[114]. In a general case, we have two components of the magnetisation energy representing the interplay between the magnetic anisotropy energy and the demagnetisation energy. We could write it down in a simplified form as[115]:

$$E = -N\frac{M_s^2}{2\mu_0}V + K_{perp}V \tag{77}$$

[114] Ikeda, Miura, et al., "A perpendicular-anisotropy CoFeB–MgO magnetic tunnel junction"; Yakata, Kubota, et al., "Influence of perpendicular magnetic anisotropy on spin-transfer switching current in CoFeB/MgO/CoFeB magnetic tunnel junctions".
[115] Igarashi, Jinnai, et al., "Temperature dependence of the energy barrier in X/1X nm shape-anisotropy magnetic tunnel junctions".

with M_s expressed here in Tesla, V as the volume, N being the demagnetisation factor (in a simplified expression of that of (34)), and K_{perp} denoting the perpendicular magnetic anisotropy energy density, expressed in J/m^3. Given the expression (77), we can also consider the stability of MTJ. The energy barrier between the parallel and antiparallel states, which keeps the magnetisation in a given state, is given by $\Delta = E/k_bT$, where k_b is the Boltzmann constant, and T is the temperature. The reason why perpendicular MTJs are desired is that there exists an asymmetry between the energy barrier that keeps the state stable, E_b^{stab} and the barrier that is required during current-induced switching, the switching current being proportional to a switching energy barrier E_b^{sw}: $I_c \sim \alpha E_b^{sw}$[116]. In the in-plane case, the in-plane magnetic anisotropy is the stabiliser of the state, whereas the demagnetisation energy is the one that has to be overcome for switch. On the other hand, in the perpendicular case, the demagnetisation and magnetic anisotropy energy work along the perpendicular direction, so $E_b^{sw} = E_b^{stab}$. The critical current for switching the in-plane case is thus larger than the one usually required to switch a

[116] J. Hayakawa, Ikeda, et al., "Current-Driven Magnetization Switching in CoFeB/MgO/CoFeB Magnetic Tunnel Junctions".

perpendicular junction. How can we achieve a perpendicular junction experimentally? It turns out that making the FM layers (CoFeB) thinner orients the magnetisation from the in-plane to the out-of-plane (perpendicular) direction, but only to some extent[117]. However, making the layers too thin may eventually result in a superparamagnetic state. Depending on whether the sample was deposited and annealed (1.65 nm - 1.52 nm), mid-range thicknesses appear adequate. As seen in (77), the magnetic anisotropy energy can also be regulated by volume; thus, the diameter of the junction plays a crucial role in the thermal stability of the perpendicular MTJ[118]. With that, we can manipulate the demagnetisation energy by engineering an adequate demagnetisation tensor, rather than simply manipulating the interfacial, i.e., perpendicular anisotropy[119]. Here, the problem is that if we make the diameter smaller, the interfacial anisotropy term drops (assuming that the demagnetisation stays the same), and the barrier decreases. Therefore, we have indeed achieved better switching at the cost of lower stability. However, one can engineer the demagnetisation tensor differently by adjusting the thickness-to-diameter ratio, which, when done properly, maintains low switching currents and a larger energy barrier.

[117] Ikeda, Miura, et al., "A perpendicular-anisotropy CoFeB–MgO magnetic tunnel junction".

[118] Igarashi, Jinnai, et al., "Temperature dependence of the energy barrier in X/1X nm shape-anisotropy magnetic tunnel junctions".

[119] Jinnai, Watanabe, et al., "Scaling magnetic tunnel junction down to single-digit nanometers—Challenges and prospects".

There is yet another flavour of MTJs, the stochastic MTJs (sMTJs), where one tunes the energy barrier to achieve fast fluctuation switching and small relaxation time, which translate to fast computation. Kanai et al.[120] showed that having in-plane MTJs (IMA-MTJs) as opposed to perpendicular MTJs (PMA-MTJs) seems beneficial for probabilistic bit (pbit) applications, because the time constants of the in-plane can be two orders of magnitude lower than for PMA-MTJs, although the energy barrier was set to be the same for those two. This is because in PMA-MTJs $\Delta \propto H_k^{\text{eff}}$[121] with a trade-off of $\nabla E \propto H_k^{\text{eff}}$, while in IMA-MTJs $\Delta \propto H_{k,in}$[122] but $\nabla E \propto H_k^{\text{eff}}$, with H_k^{eff} being the effective anisotropy field. ∇E denotes the energy gradient as a function of spatial coordinates. For the PMA-MTJs, we make a trade-off between setting the barrier high and making an easy path between two states, while in IMA-MTJs those two can be set independently.

[120] Kanai, K. Hayakawa, et al., "Theory of relaxation time of stochastic nanomagnets".

[121] effective perpendicular anisotropy

[122] in-plane anisotropy

In one of the following sections we discuss MTJs operating as spin-torque oscillators (STOs). To achieve stable auto-oscillation of the magnetisation in an MTJ, the current applied to the junction needs to be below the switching threshold but above a current value where the damping is compensated. If this condition is met, the resulting stable auto-oscillation of magnetisation induces resistance oscillation, and the system can act as an AC voltage signal generator in a GHz regime. Typically, STOs require the presence of the external magnetic field to tilt the free layer magnetisation relative to the magnetisation of the polarising (reference) layer, but zero-field operation is also possible as shown by Skowroński et al.[123] (canted PMA in the free layer, IMA reference layer) or Fang et al.[124] (IMA free layer and PMA reference layer). The critical current threshold for auto-oscillation in STOs with a PMA free layer, in the absence of field-like torque, can be given after Taniguchi et

[123] Skowroński, Stobiecki, et al., "Zero-Field Spin Torque Oscillator Based on Magnetic Tunnel Junctions with a Tilted CoFeB Free Layer".

[124] Fang, Feng, et al., "Zero-field spin transfer oscillators based on magnetic tunnel junction having perpendicular polarizer and planar free layer".

al.[125]:

$$j_c = \frac{4\alpha e \mathrm{M_s t_{FM}}}{\hbar P \lambda}(\mathrm{H_{appl}} + \mathrm{H_{K,eff}}) \tag{78}$$

where $\mathrm{t_{FM}}$ is the thickness of the free layer and $\mathrm{H_{appl}}, \mathrm{H_{K,eff}}$ are the external magnetic field applied along the z-axis and the effective PMA field, respectively.

[125] Taniguchi, Arai, et al., "Theoretical Study of Spin-Torque Oscillator with Perpendicularly Magnetized Free Layer".

Electrical coupling

Introduction to inter-device coupling

The coupling of spintronic devices is one of the fundamental mechanisms through which computation is carried out in a spintronic system. Commonplace methods include coupling via the electrical connection of the MTJs, static coupling due to dipolar interaction, and coupling mediated through the propagation of the spin waves.

Electrical coupling has been extensively explored in a myriad of applications. First, Tsunegi et al.[126] experimentally scaled electrically coupled oscillators, demonstrating that networks of up to 8 STOs exhibit increased emitted power and Q factor. They also showed that the coupled STOs retain in-phase synchronisation over longer time scales, proving the robustness of the synchronised state against thermal fluctuations. In 2021, Sharma et al. demonstrated a series and a parallel STO array and proposed their use for WiFI band transmission and energy harvesting[127]. Gibeault et al. presented the programmable electric coupling between stochastic MTJs[128] while Romera et al.[129] showed a practical implementation of electrically coupled STOs for a classification task.

[126] Tsunegi, Taniguchi, et al., "Scaling up electrically synchronized spin torque oscillator networks".

[127] Sharma, Mishra, et al., "Electrically connected spin-torque oscillators array for 2.4 GHz WiFi band transmission and energy harvesting".

[128] Gibeault, Adeyeye, et al., "Programmable electrical coupling between stochastic magnetic tunnel junctions".

[129] Romera, Talatchian, et al., "Binding events through the mutual synchronization of spintronic nano-neurons".

Another class of solutions uses VCMA to control the strength of the coupling. Yun et al.[130] have designed a device based on the Pt/Co/GdO stack, where a gating region (a cobalt layer exposed to GdO) had a tunable anisotropy through oxygen ion migration in GdO. Such a mechanism has effectively coupled the competition between DMI (when the gated region is in-plane, causing the neighbouring regions with PMA to exhibit chiral texture) and tunable exchange coupling to the anisotropy of that gated region. The authors showed that it is possible to construct an Ising machine based on such a device.

[130] Yun, K.-J. Lee, and Lim, "Critical switching current density induced by spin Hall effect in magnetic structures with first- and second-order perpendicular magnetic anisotropy".

The dipolar coupling, being a static interaction, is primarily dependent on the distance between the devices. Still, we can control how much it affects each device by manipulating with other field terms in the effective field. First, Kanao et al.[131] demonstrated a basic case of reservoir computing with nanomagnets. The array of STOs connected to a linear layer with trainable weights was shown to perform simple short-term memory and parity check tasks. Nomura et al.[132] included the VCMA control in a similar array of STOs, which opened the way to computing simple logic operations: AND/X-OR/OR.

[131] Kanao, Suto, et al., "Reservoir Computing on Spin-Torque Oscillator Array".

[132] Nomura, Furuta, Tsujimoto, Kuwabiraki, Peper, et al., "Reservoir computing with dipole-coupled nanomagnets"; Nomura, Furuta, Tsujimoto, Kuwabiraki, Samura, et al., "Randomly generated node-state-update procedure for dipole-coupled magnetic reservoir computing with voltage control of the magnetism".

Electrical coupling – experimental setup and observations

In this section, we explore the concept of electric coupling primarily within a simulation context, with a slight experimental backdrop. The discussion draws heavily from the work by Rzeszut, Mojsiejuk, et al. ("Towards mutual synchronization of serially connected Spin Torque Oscillators based on magnetic tunnel junctions"), originally published in 2023, but substantially revised thereafter. Relevant passages from that work are cited verbatim when appropriate; however, readers are encouraged to consult the original text for detailed implementation information.

Our study begins with an experimental setup of a basic injection locking system through an external generator signal. The sample is an MTJ Si /SiO_2 / buffer / (4) Ru / (6) IrMn / (2.5) CoFe / (0.8) Ru / (2.5) CoFeB / (1) MgO / (1.8) CoFeB / (1) MgO / (3) Ru / (5) Ta / (2) Ru / (3) Pt with bracketed thicknesses expressed in nanometers. The presence of Ru indicates that the reference CoFeB layer is strongly pinned to the SAF, as well as the MgO cap, which is known to enhance perpendicular magnetic anisotropy[133]. A similar structure has been shown to produce a decent STO in the work of Skowroński et al.[134]

First, the ability of the MTJ to synchronise needs to be validated. Therefore, junction parameters are fitted to the experimental FMR spectrum following the procedure described in Bayesian optimisation – result of that fit is presented in Fig.19a). Then, the same junction is synchronised to half of the generator frequency, which, following the experiment, was also 4 GHz – as per Fig.19b). The ratio $\Delta j / j$, that is, the ratio of AC density to DC density, plays a significant role in the injection locking simulation. As shown in Fig.20 the increase in the locking range correlates with the increase in that ratio. The minimal current modulation ratios required for injection locking (0.1-0.2) agree with theoretical observations[135]. Having verified the basic synchronisation case, we are now ready to discuss the electric coupling where we will compare the numerical modelling with the experimental result. In contrast to dipole-based coupling, no magnetic effects participate in the coupling mechanisms of the oscillators that are electrically coupled. Although that dipole interaction is typically considered long-range separating the two oscillators apart with a distance of a couple µm is usually sufficient to isolate them magnetically – in the experiment it was taken to be at least 600 µm. A typical schematic illustrating possible electrical connections of the MTJ (both in series and in parallel) is given in Fig.21. From now on, given an in-series connection of two MTJs, we will refer to the first MTJ in the connection as *L* (left), and the second as *R* (right). Fig.22(a-c) illustrates the spectrum generated by *L* (a) and *R* (b) individually, when they were disconnected, and (c) shows their joint signal collected when measured in series. All subplots (a-c) share the same power scale. First, comparing (a) and (b), *L* has a much narrower oscillation linewidth than *R* throughout the external field scan. Second,

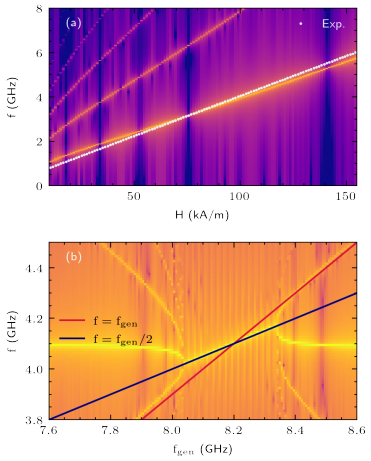

Figure 19: Simulation of the injection locking to the external generator signal. (a) Approximate fit to the experimental FMR. (b) The locking spectrum of the same MTJ. Synchronisation occurs at half the generator frequency.

[133] Kubota, Ishibashi, et al., "Enhancement of perpendicular magnetic anisotropy in FeB free layers using a thin MgO cap layer"; Dieny and Chshiev, "Perpendicular magnetic anisotropy at transition metal/oxide interfaces and applications".

[134] Skowroński, Chęciński, et al., "Microwave magnetic field modulation of spin torque oscillator based on perpendicular magnetic tunnel junctions".

[135] Slavin and Tiberkevich, "Nonlinear Auto-Oscillator Theory of Microwave Generation by Spin-Polarized Current".

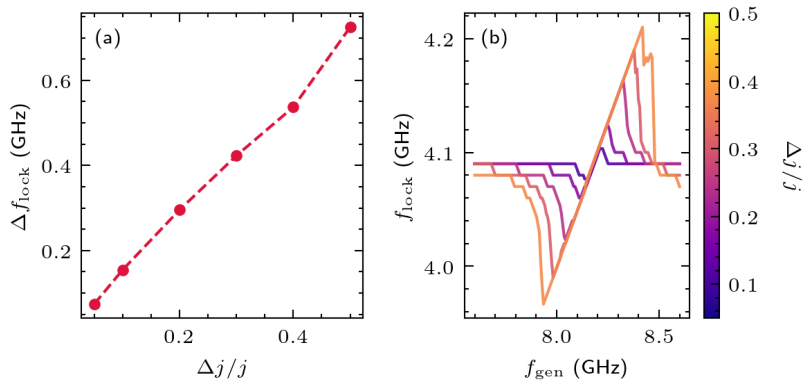

Figure 20: Dependency of the locking range on the amplitude of the excitation. The MTJ simulated here is the same as the one optimised in Fig.19. (a) Locking range bandwidth depending on the $\Delta j/j$ ratio. (b) Line of maximum resonance under different excitation amplitude $\Delta j/j$.

in the spectrum of *R* there is a well-defined oscillation line starting at 3 GHz at 80 kA/m.

This broad auto-oscillation pattern of *R* is retained in the in-series configuration *S*, shown in (c), although it becomes noticeably narrower compared to (b). In addition, the thin oscillation line starting at 3 GHz from (b) also appears in (c). Moreover, a distinct narrow spectral line emerging near 130 kA/m is observed in panel (c), which is absent in both individual spectra of *L* (a) and *R* (b).

Fig.22d) shows the lines of maximum power for each of the spectra, with an additional synthetic line created by averaging individual signals of *L* and *R* (grey line). In the region starting at about 135 kA/m *L* and *R* start to diverge strongly and at that point *S* closely follows *R* up to approximately 145 kA/m, beyond *S* diverges both from *R* and *L* (blue), as well as from their averaged signal (grey).

To clarify the relationship between *L*, *R* and *S* we fitted a trend line to *L* signal in Fig.22d), as it is the least affected by the in-series connection. A linear trend line is defined as: $f = kH + H_0$, where k is the slope, and H_0 is the intercept. Using that trend line, we subtract it from each of the main oscillating frequency lines in Fig.22d). The resulting characteristics visible in Fig.22e) are:

1. two points of divergence occur where *R* deviates from *L*, i.e. the red line moves away from zero. The first occurs at about 90 kA/m; a second, larger divergence appears at 130 kA/m, preceded by a brief synchronisation. This demonstrates that, individually, *R* and *L* do not oscillate with the same nominal frequencies in ranges (90, 125) and (130, 155) kA/m.

2. at 145 kA/m lines move further away from *L*-trend line (blue), including the signal S - (L+R)/2. This means that beyond 145 kA/m the maximum power signal of the in-series configuration no longer aligns with the individual or averaged responses of *L* and *R*.

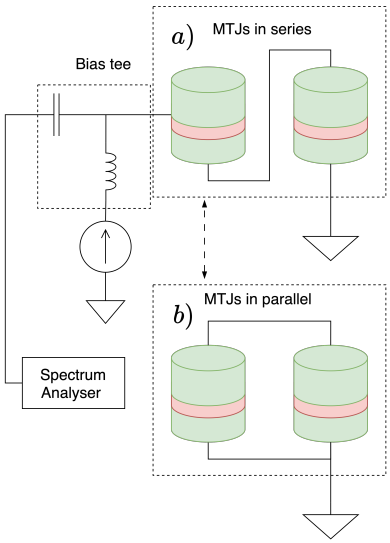

Figure 21: Measurement setup and available arrangements for electric coupling: (a) in-series coupling, and (b) parallel connection coupling.

Given these experimental observations, we can proceed to the numerical analysis of some of the synchronisation aspects observed in Fig.22.

Numerical modelling of electrical in-series coupling

The numerical reproduction of this experimental outcome derives from the work of Taniguchi et al.[136] where the authors introduce a simple model for electrical synchronisation in two configurations: in series and parallel. The total current fed to consecutive junctions $i+1$ depends on the free magnetizations $\mathbf{m}$ and the reference layers $\mathbf{p}$ of the i_{th} and $i+1_{th}$ junction:

$$j_c(t) = j_0(t) + \chi j_0(t)(\mathbf{m_i} \cdot \mathbf{p}_i + \mathbf{m}_{i+1} \cdot \mathbf{p}_{i+1}) \quad \text{(series)} \tag{79}$$

$$j_c(t) = j_0(t) + \chi j_0(t)(\mathbf{m_i} \cdot \mathbf{p}_i - \mathbf{m}_{i+1} \cdot \mathbf{p}_{i+1}) \quad \text{(parallel)} \tag{80}$$

where $j_0(t)$ is the value of the uncoupled current density and χ is the unitless coupling strength. Typically χ is constrained within the (0, 1) interval[137]. In our simulations, we usually fix it to $\chi = 0.3$, but show that it can be as low as $\chi = 0.1$ under certain values of β (see the later discussion and Fig.26 for more details on the impact of χ and β). The situation originally considered in equation (79) supposes that j_c is the total current flowing in the circuit and j_0 is simply a theoretical baseline current. However, in the experiment, the voltage source response is not instantaneous as a result of the parasitic capacitance and inductance. Therefore, in the following analysis we assume that $j_c(t)$ is the current induced in the second (R) STO, while the input to the first MTJ, (L), is kept at $j_0(t)$. For completeness, we show in the Appendix, Coupled current for the in-series configuration of STOs, that this assumption does not impact, up to a choice of constant χ, the result of the subsequent analysis. According to our assumption, as illustrated in Fig.23b,e,g), the peak associated with the first MTJ in the connection remains fixed while the resonance of the second junction is pulled toward it. This behaviour is the archetypal of injection locking scenarios. As a point of further note, we observe in Fig.23f) that the phase difference between two oscillating junctions seems to be approaching $\Phi_{\text{diff}} = 180$, indicating that $\chi > 0$ leads to in-phased synchronisation, while $\chi < 0$ aligns the frequencies, but causes out-of-phase oscillation. This is in contrast to the in-phase synchronisation shown in panel (c).

After examining a simple base case, we proceed to more complex conditions illustrated in Fig.22. The two MTJs of a connected pair are not identical, although they might have come from the same wafer. Therefore, in our discussion below, unlike prior studies[138], we assume that the connected devices are not identical and vary the anisotropy constant and magnetisation saturation to model the parameter dispersion. Taking anisotropy as an example: we denote the anisotropy of the left MTJ and the right MTJ by $K_{u,L}$, and $K_{u,R}$, respectively. The $K_{u,R}$ is then parametrized with a ΔK (a variation in

[136] Taniguchi, Tsunegi, and Kubota, "Mutual synchronization of spin-torque oscillators consisting of perpendicularly magnetized free layers and in-plane magnetized pinned layers".

[137] Arun, Gopal, et al., "Influence of Field-Like Torque in Synchronization of Spin Torque Oscillators"; Taniguchi, Tsunegi, and Kubota, "Mutual synchronization of spin-torque oscillators consisting of perpendicularly magnetized free layers and in-plane magnetized pinned layers".

[138] Arun, Gopal, et al., "Influence of Field-Like Torque in Synchronization of Spin Torque Oscillators"; Taniguchi, Tsunegi, and Kubota, "Mutual synchronization of spin-torque oscillators consisting of perpendicularly magnetized free layers and in-plane magnetized pinned layers".

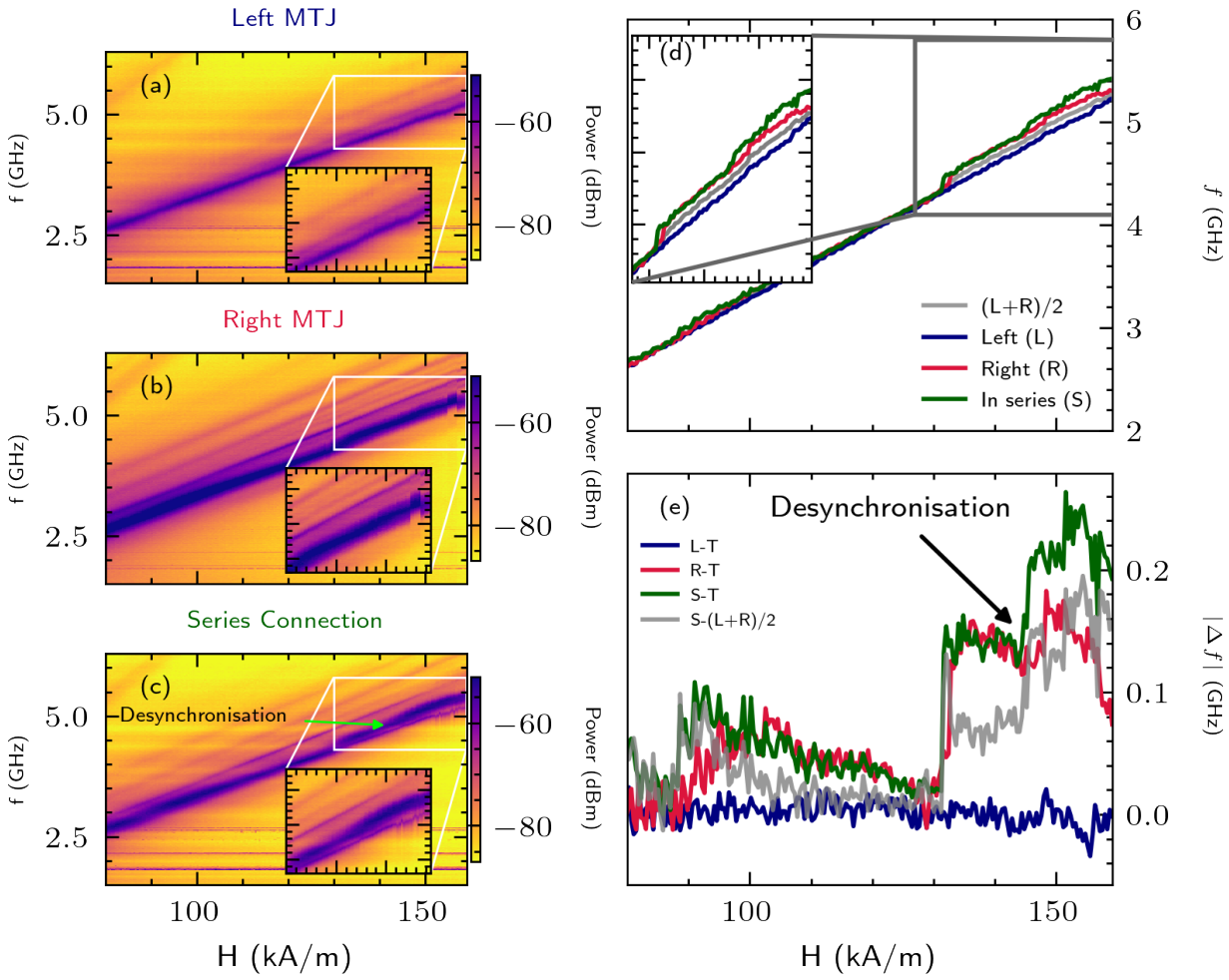

Figure 22: Experimental electrical frequency synchronisation and desynchronisation of two serially connected MTJs. The individual spectrum of left *L* (a), right *R* (b) MTJ individually and when connected in-series (c). (d) Main oscillating frequency of the *L*, *R* and in-series systems, with a zoom of the desynchronisation region. (e) the synchronisation and desynchronisation ranges of *L* and R and in-series (*S*) signal respective to the trend line (T) fitted to the *L* signal. *L* signal should, in theory, be least affected by the in-series electrical connection, and therefore is used as a reference. The arrow marks the spot where the *R* signal diverges from *L*, and *S* diverges both from *L* and *R*. As shown, up to about 145 kA/m, the *S* signal follows *R* closely and then settles to oscillate with its own distinct frequency. In the (d) and (e) panels, we include an average of *L* and *R* signals, (L+R)/2, for reference. In (e) that signal is subtracted from (*S*) for comparison. The figure and caption were adapted from Rzeszut, Mojsiejuk, et al. ("Towards mutual synchronization of serially connected Spin Torque Oscillators based on magnetic tunnel junctions").

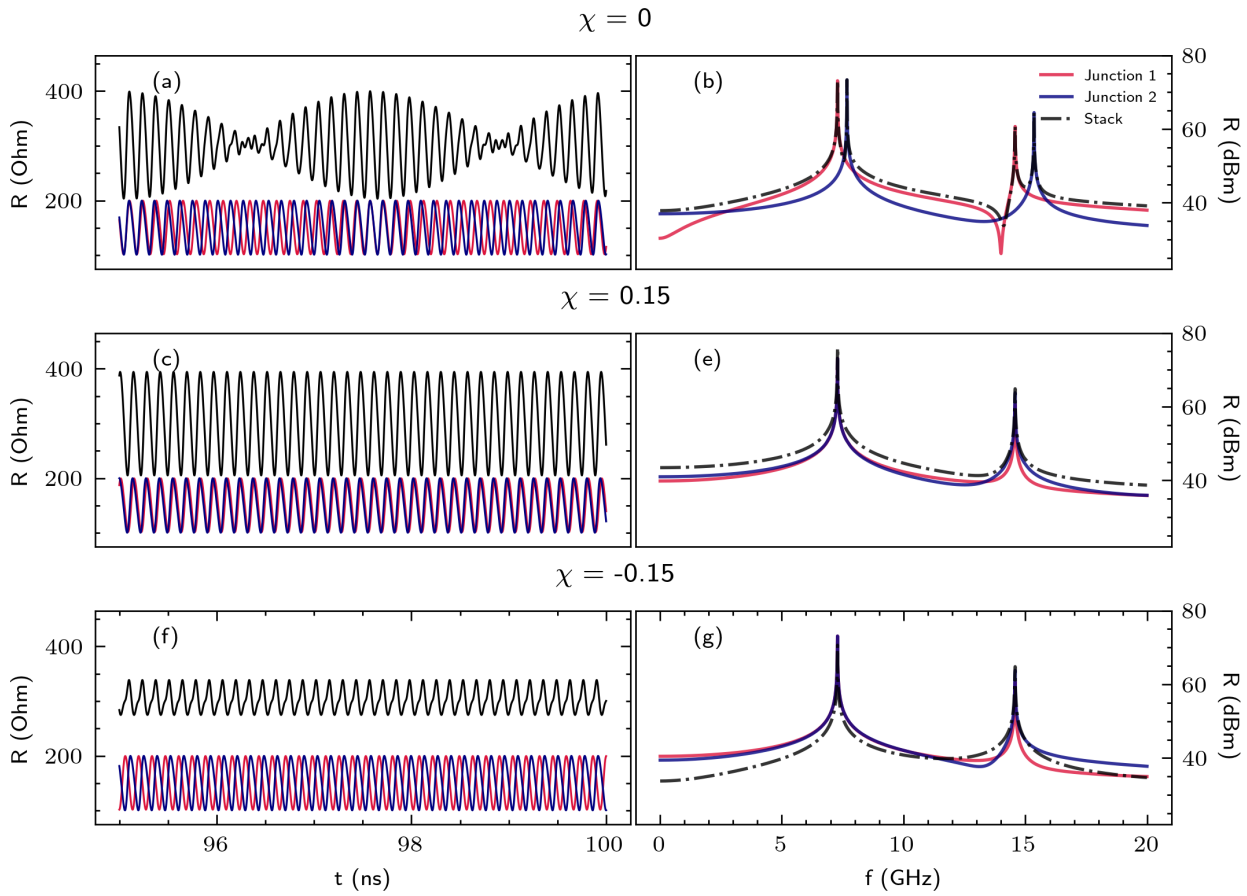

Figure 23: Three different coupling values for the in-series electric coupling. The left column shows the time series of serially connected MTJs and their individual time series. The right column presents the resonance spectrum of the stack and individual MTJs up to 20 GHz. Negative coupling causes phase synchronisation to settle at $\phi_{\text{diff}} = 180°$, which may not be desirable, and the resulting resistance decreases. Comparing (b) with (e) and)g) we see that the blue spectrum of the second MTJ is *pulled* towards the resonance mode of the first MTJ which stays fixed. In that sense, electric coupling can be thought of as a case of injection locking.

magnetic anisotropy) parameter such that:

$$\mathrm{K_{u,R}} = \mathrm{K_{u,L}}(1 + \Delta\mathrm{K}/100) \tag{81}$$

where the relative change in anisotropy ΔK is expressed in percentages and is allowed to vary between $(-10\%, 10\%)$. In other words, we keep the anisotropy of L fixed, and allow the anisotropy of R vary up to 10% respective to L. For assessing synchronisation quality, we use three metrics:

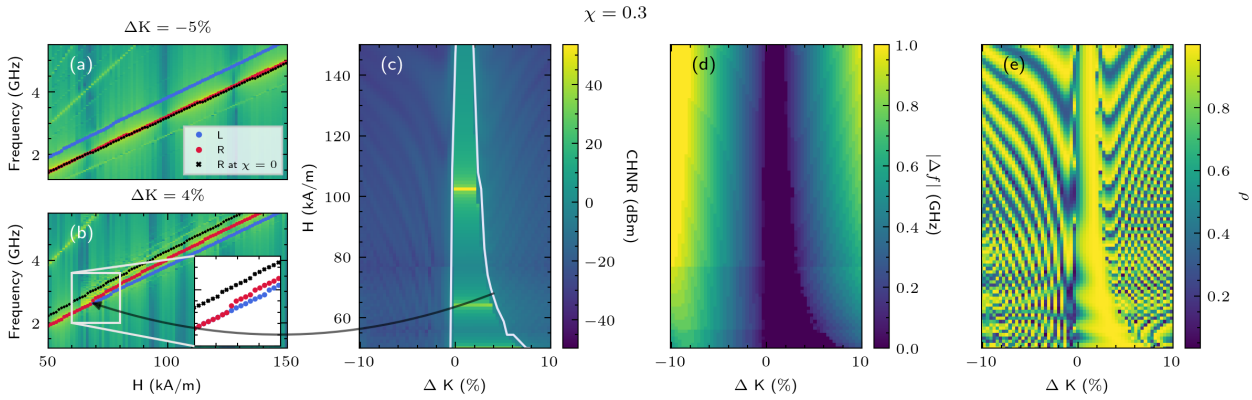

Figure 24: Simulated desynchronisation of serially coupled MTJs in function of the anisotropy change ΔK of the (R) MTJ in-series. Panels (a) and (b) show two sample spectra for R junction taken at $\Delta\mathrm{K} = -5\%$ (a) and $\Delta\mathrm{K} = 4\%$ (b). The arrow leads from the desynchronisation boundary at $\approx$ 68 kA/m and $\Delta\mathrm{K} = 4\%$ in (c) to a precise place of desynchronisation in the spectrum of (b), with the desynchronisation moment placed in zoom in (b). (a-b) The blue marker follows the line of the main oscillating frequency of L, and the red marker tracks the one for R. The black dots show the main oscillating frequency line of R when the two MTJs are decoupled, i.e. $\chi = 0$. Otherwise, simulations performed assuming $\chi = 0.3$ and $\beta = 0.5$. (d) Frequency difference in (GHz) between the L and R junctions. For $\Delta\mathrm{K} > 0$, i.e. $\mathrm{K_{u,R}} > \mathrm{K_{u,L}}$ there is a desynchronisation boundary where the L and R junctions start to fall out of synchronisation, i.e. leave the dark blue region (white line in (c) denotes that desynchronisation boundary H_{thres}). (c) illustrates that the dark-blue region from (d) is characterized by a large CHNR, supporting the evidence for strong synchronisation. The asymmetry between the frequency de-synchronisation fields for $\Delta\mathrm{K} > 0$ and $\Delta\mathrm{K} < 0$ arise from the particular arrangement of the (L) and (R) MTJs in-series, and is a direct consequence of smaller frequency changes due to current change. High order parameter values (e) confirm a good degree of synchronisation within the desynchronisation boundary. The figure and caption were adapted from Rzeszut, Mojsiejuk, et al. ("Towards mutual synchronization of serially connected Spin Torque Oscillators based on magnetic tunnel junctions").

1. the cross-Harmonic-to-Noise (CHNR) ratio measuring spectral overlap between the two oscillating MTJs. The cross-Harmonic-to-Noise ratio is defined as:

$$\mathrm{CHNR} = \frac{\sum_{\forall n>0, n\in\mathbb{Z}} A^{\mathrm{R}}_{nf_{\mathrm{L}}}}{\sum_{f'\neq k f_{\mathrm{L}} \forall k>1, k\in\mathbb{Z}} A^{\mathrm{R}}_{f'}} \tag{82}$$

   where f_{L} is the primary oscillating frequency of the first MTJ in-series. $A^{\mathrm{R}}_{f_i}$ denotes the values taken from the frequency spectrum of the second MTJ in-series, that is, the amplitude at a frequency f_i.

2. the order parameter, which also quantifies the phase alignment. It serves as an additional measure of uniformity of synchronisation and is defined by the following equation[139]:

$$\rho = \frac{1}{2}\left|\sum_{i}^{2} \frac{c_i}{|c_i|}\right| \tag{83}$$

[139] Kanao, Suto, et al., "Reservoir Computing on Spin-Torque Oscillator Array"; Acebrón, Bonilla, et al., "The Kuramoto model".

where $c_i = m_x^i - i m_y^i$ with m_x and m_y as the x and y components of the magnetization. The closer ρ approaches 1, the better the order of synchronisation.

3. and the absolute frequency difference between the dominant peaks of the two STOs: $|f_L - f_R|$

Having two junctions connected in-series, the magnetic field angle is set at $\theta = 25^\circ$, the same as in the experiment. For every field magnitude and ΔK value, we note the frequency difference of the primary modes between the first and second MTJ, which results in Fig.24d).

We observe that synchronisation occurs more easily when the anisotropy of the second MTJ is slightly larger ($\Delta K > 0$). However, beyond a threshold, increasing ΔK leads to desynchronisation, with the desynchronisation boundary influenced by the coupling constant χ. A similar desynchronisation boundary occurs if we move vertically, increasing the field. At some H_{thres}, marked with a white line in Fig.24c), there is a transition from the synchronised state to the desynchronised state. Fig.24c) shows the CHNR where the transition to the desynchronised state is connected with an abrupt nonharmonic oscillation of the second MTJ, which results in frequency splitting similar to the signal observed experimentally in Fig.22(c-d) – numerical equivalent presented in Fig.24b). As in the experiment, the main oscillating mode follows neither L nor R modes exactly. Finally, the order parameter is shown in Fig.24e), where for the synchronised region, we clearly observe swaths of large ρ values close to 1, which is in agreement with the results in Fig.24(c-d).

Following the analysis first shown for identical junctions by Arun et al.[140], we also investigate the influence of the field-like torque β scaling in the field-like torque term in our notation: $a_j \beta \tilde{\mathbf{M}}_t(\mathbf{p})$. Consistently with the aforementioned work, we observe that the presence of the synchronised state is essentially dependent on the strength of the β scaling. Fig.26 demonstrates how the desynchronisation threshold shifts for $\Delta K > 0$ both with the coupling strength χ and the field-like torque scaling β. There are two key observations from that figure: the first is that the induction of a larger field-like torque works in a similar fashion as increasing the coupling strength, i.e., it facilitates synchronisation, which results in broadening of the synchronised region, both across the field range (vertically) and also across the ΔK (horizontally), suggesting that one could be potentially compensated by the other. Secondly, we see that there is a distinct peak when β, which means that the largest field locking range does not need to occur at $\Delta K = 0$, which is when the two junctions are identical.

As evident from the discussion in Introduction to inter-device coupling, VCMA seems to be an overarching mechanism to enhance coupling dynamics. Inspired by this, we used the existence of the desynchronisation threshold at a particular $K_{u,R}$ to induce the synchronised and desynchronised state be-

[140] Arun, Gopal, et al., "Influence of Field-Like Torque in Synchronization of Spin Torque Oscillators".

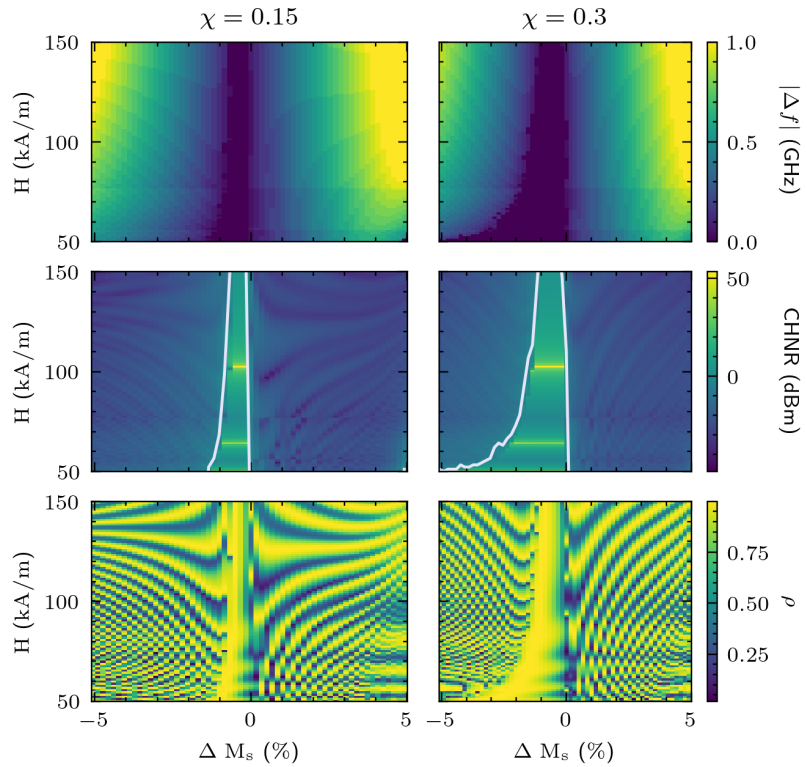

Figure 25: The impact of varying M_s and the coupling χ parameter. The synchronisation region grows with larger χ, but also expands for lower ΔM_s variations respective to L, as it has the exact opposite effect as increasing ΔK_u. ΔM_s is defined analogously to ΔK_u. The figure and caption were adapted from Rzeszut, Mojsiejuk, et al. ("Towards mutual synchronization of serially connected Spin Torque Oscillators based on magnetic tunnel junctions").

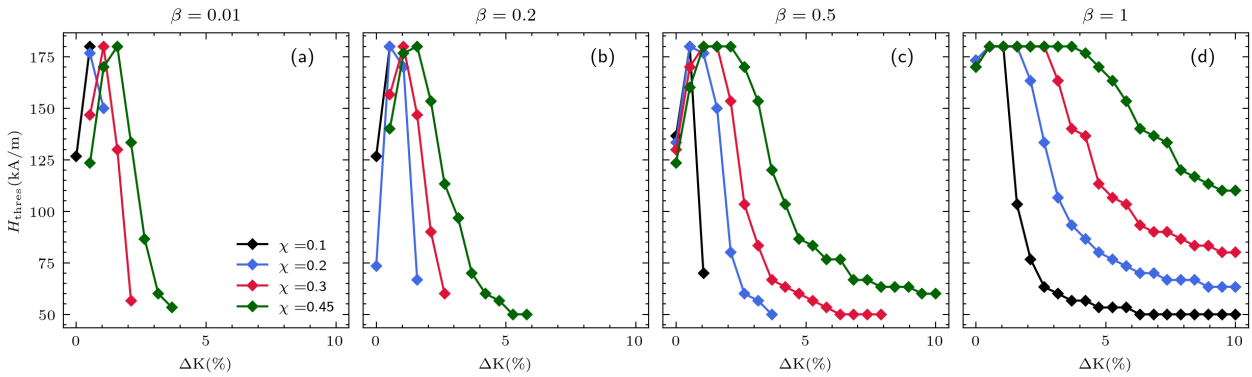

Figure 26: Effect of field-like torque scaling β and the magnitude of the electric coupling χ on the desynchronisation threshold H_{thres} in function of the anisotropy change ΔK of the (R) MTJ in-series. Case (a) corresponds to $\beta = \alpha_G$. A larger β widens the synchronisation range, similar to the effect of increasing the coupling constant χ. The external field range is capped at 175 kA/m. Plotted points denote only states that were synchronised at some field, a lack of a marker means that the state either did not start in a synchronised state at lower field values or it has already desynchronised. The figure and caption were adapted from Rzeszut, Mojsiejuk, et al. ("Towards mutual synchronization of serially connected Spin Torque Oscillators based on magnetic tunnel junctions").

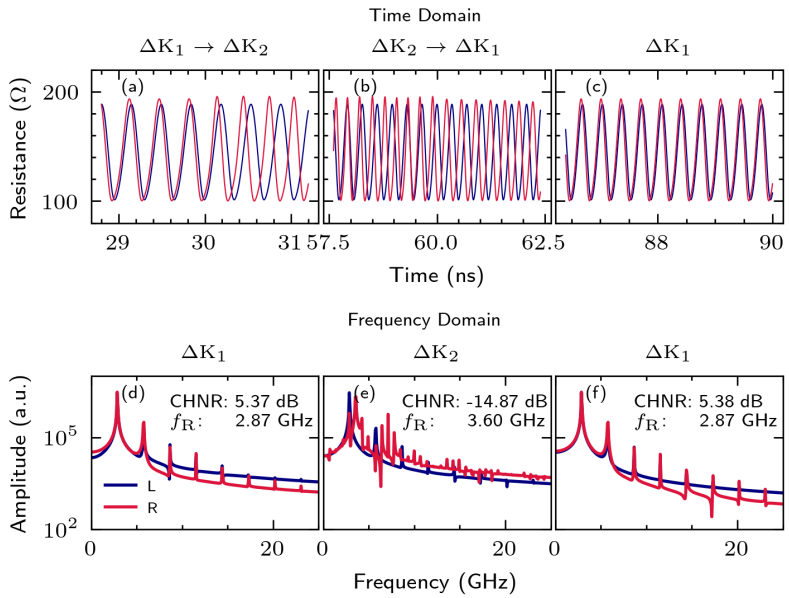

Figure 27: Simulated VCMA-controlled synchronisation of and in-series MTJ system. The VCMA controller switches from ΔK_1 to ΔK_2 first, then back to ΔK_1. (a) shows the magnetoresistance during transition at 30 ns from ΔK_1 to ΔK_2, (b) at 60 ns from ΔK_2 back to ΔK_1 and (c) gives last couple nanoseconds from a synchronised state in ΔK_1 after the final switch. Frequency spectra corresponding to states ΔK_1, ΔK_2 and ΔK_1 (after the transition from ΔK_2) are shown in (d-f) respectively. Simulated for $\chi = 0.15$, $\Delta K_1 = 4\%$, $\Delta K_2 = 20\%$, $H_{ext} = 80$ kA/m. The figure and caption were adapted from Rzeszut, Mojsiejuk, et al. ("Towards mutual synchronization of serially connected Spin Torque Oscillators based on magnetic tunnel junctions").

tween two STOs coupled in the in-series configuration. Fig.27 illustrates this mechanism: the increase in anisotropy of the (R) MTJ from ΔK_1 to ΔK_2 causes the two STOs to desynchronise, but reverting the anisotropy back to ΔK_1 leads to a synchronised state again. Although the synchronised signal is easily detectable electrically because of an increase in amplitude, and a relatively small voltage is sufficient to switch the pair out of the synchronised state, the practical implementation of VCMA-based synchronisation control presents several challenges. The proposed structure is viable when the magnetisation dynamics is driven by a spin current that originates from spin-orbit coupling (SOT) rather than spin filtering (STT)[141]. In this configuration, an additional gate can be used to modulate the magnetic anisotropy via VCMA. Although devices based on ionic migration can exhibit significant VCMA[142], they are limited by a lower modulation speed and degradation over time. In contrast, devices based on MgO/FM can operate at a rate below 1 ns[143].

Dipolar coupling

Another mode of interdevice coupling is due to dipolar coupling, which we indirectly compare to electrical coupling. As mentioned above, dipolar coupling is frequently the main mechanism used for simulation in reservoir computing[144]. In those applications, a nanomagnet array is subjected to remagnetisation programming, often via setting the anisotropy. Then, the calculation is conducted after connecting the digitised magnetisation outputs with a synthetic neural network. For complex device geometries the dipolar interactions must be computed micromagnetically (Dipolar coupling), but for

[141] Liu, Pai, et al., "Magnetic Oscillations Driven by the Spin Hall Effect in 3-Terminal Magnetic Tunnel Junction Devices".

[142] Bauer, Yao, et al., "Magneto-ionic control of interfacial magnetism".

[143] Shiota, Nozaki, et al., "Induction of coherent magnetization switching in a few atomic layers of FeCo using voltage pulses"; Skowroński, Nozaki, et al., "Perpendicular magnetic anisotropy of Ir/CoFeB/MgO trilayer system tuned by electric fields".

[144] Nomura, Furuta, Tsujimoto, Kuwabiraki, Peper, et al., "Reservoir computing with dipole-coupled nanomagnets"; Kanao, Suto, et al., "Reservoir Computing on Spin-Torque Oscillator Array"; Nomura, Tsujimoto, et al., "Reservoir computing with two-bit input task using dipole-coupled nanomagnet array".

point dipoles we can use a macromagnetic approximation as an illustrative means of comparison with the electric coupling:

$$\mathbf{H}_{\text{dipole}} = 3\frac{\mathbf{r}(\boldsymbol{\mu}\cdot\mathbf{r})}{|\mathbf{r}|^5} - \frac{\boldsymbol{\mu}}{|\mathbf{r}|^3} \tag{84}$$

where $\mathbf{r}$ is the distance vector spanning from the one device to another (centre to centre), $|\mathbf{r}|$ is its length and the quantity $\boldsymbol{\mu}$ is defined by the magnetisation $\mathbf{m}$

$$\boldsymbol{\mu} = \mu_0 \mathrm{M_s} V \tag{85}$$

where V is the volume of the ferromagnetic layer in the device.

In CMTJ, two devices can be coupled by any distance-based interaction function with the *GroupInteraction* class. For convenience, the library provides the basic dipolar approximations by estimating the dipolar tensor based on the device arrangement in space, but the user may define their custom interaction function.

For comparison with the electric coupling, we create two simulation setups using the same device parameters as the ones used for discussing electrical coupling. In the first setup, called *symmetric excitation*, the DC current is supplied to both STOs that differ slightly with the parameters. In the second, called *asymmetric excitation*, the current is supplied only to the STO (source), which allows us to observe the spectrum of the other MTJ undisturbed by its own auto-oscillation. Fig.28 presents the results of the symmetric and asymmetric excitation simulation setups as a function of the distance between two STOs and temperature. By comparing symmetric and asymmetric excitation, we observe additional frequency peaks permeating the spectra of both STOs when excited asymmetrically, in particular at $d = 100$ nm. At 300 nm, the unexcited MTJ practically loses the frequency component coming from the source. When the two STOs experience symmetric excitation, the frequency alignment is stronger and aligns the auto-oscillations of both STOs, even across the th second harmonic at 150 nm. In both cases, we also run a temperature simulation with $T = 300$ K, averaged over 50 runs to see how selective the dipole excitation is when noise is present. The differences turn out to be relatively minor, with the exception of the spectra between $d = 100$ and $d = 150$ nm. In those two cases, we see that the further harmonics in *symmetric excitation* cease to appear in both STO spectra, while for *asymmetric excitation* the temperature eliminated the back-coupling of higher harmonics of the unexcited MTJ from the source spectrum. Another pronounced effect of temperature shows at $d = 300$ nm, *symmetric excitation*, where otherwise strong synchronisation would occur, but it diminishes completely at $T = 300$ K. Note that at a very close range, the system becomes stiff as the dipole excitation dominates, and the supplied current is no longer sufficient to excite neither of the junctions, cf. Fig.28 ($T = 0$ K at 50 nm for symmetric and asymmetric excitations). However, the introduction of temperature $T = 300$ K allows for a faint spectrum signal.

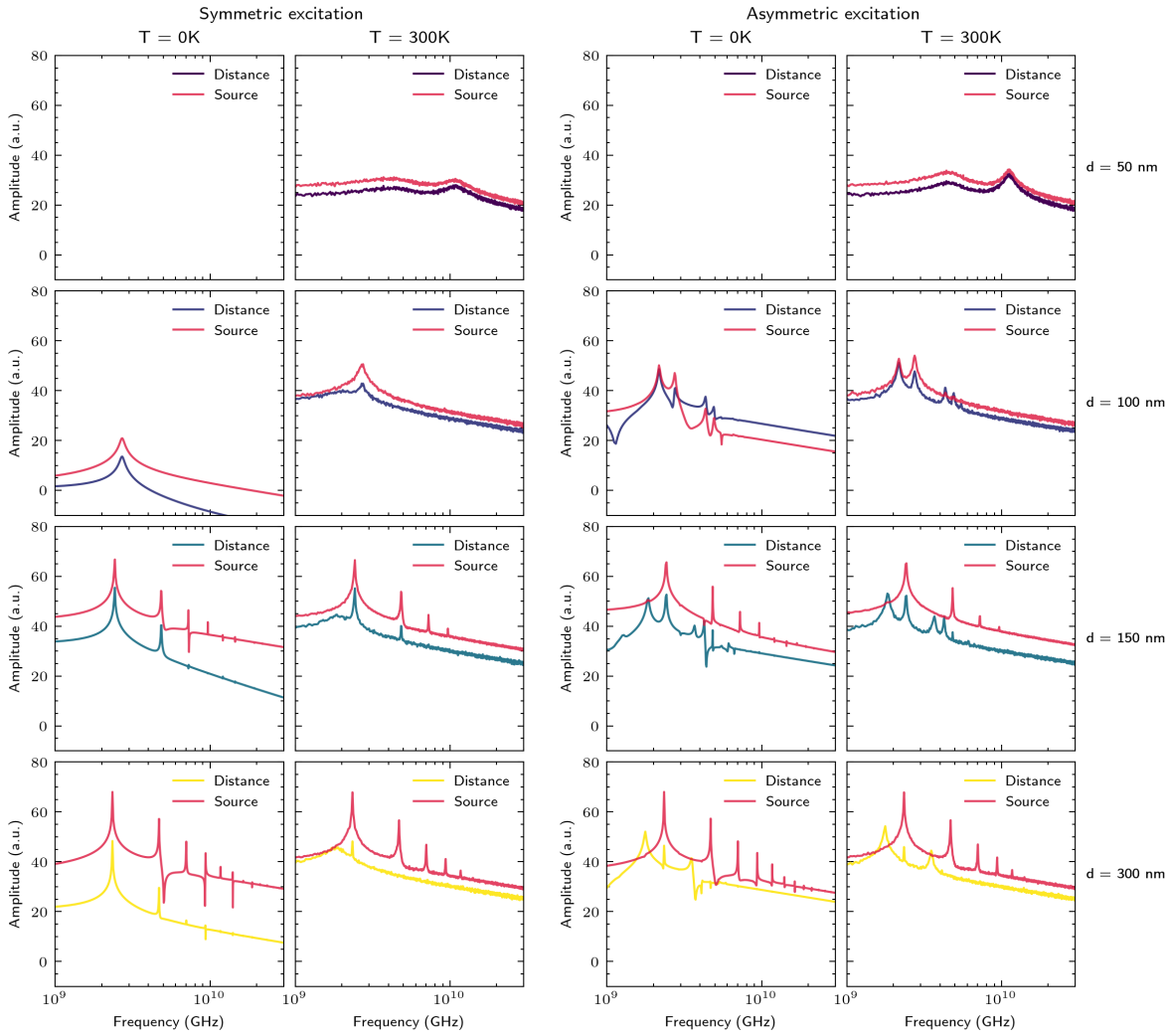

Figure 28: Comparison of dipole excitations as a function of temperature and distance. In symmetric excitation (left panel), the same current is supplied to both STOs. In asymmetric excitation (right panel) the current is supplied only to the first (source) STO. The source and distance STO differ with the anisotropy constant with the following relation $K_{dist} = 0.85K_{source}$. Note that at 50 nm and 0 K there is no effective excitation due to a very strong dipole coupling, which stiffens the systemm hence no spectrum is present.

Modelling correlated noise

Approaches to noise modelling

In addition to applications in storage and as oscillators, MTJs are widely used in sensing. We can construct TMR-based field sensors by leveraging two facts: (i) the magnetoresistance depends on the relative magnetisation angle between two layers, which is typically nonzero in the low-field regime, and (ii) the resistance-field relation, R(H), is often linear in that low-field regime. Thus, in sensor development, achieving a high sensitivity is paramount. The voltage sensitivity in TMR sensors is typically defined as:

$$S = I_b \frac{d\mathrm{R}}{d\mathrm{H}} \tag{86}$$

where I_b is the bias current, and R is the measured resistance. Unfortunately, in the low-field regime, magnetic noise dominates electronic noise, the latter remaining relatively constant regardless of the applied field magnitude. Furthermore, this magnetic noise consists mostly of the $1/\mathrm{f}$ type of noise which overpowers the noise coming from the thermal fluctuations in the low-frequency regime. The subject of magnetic noise in the sensor is a rapidly developing domain. Chęciński et al. demonstrated through a fitting procedure based on stochastic signal generation[145] that, to a good degree of precision, explains the RMS and the amplitude of composite white plus $1/\mathrm{f}$ noise. However, in that work, the noise generator was used as an extrinsic signal and was not inserted into a magnetic simulation model. The question of direct inclusion of $1/\mathrm{f}$ noise into a simulation warrants a discussion on practical application in numerical solvers such as those described in Stochastic forms of Landau-Lifshitz-Gilbert-Slonczewski equation. Those schemes require a particular set of conditions for the stochastic part, specifically the samples drawn for $\Delta\mathbf{W}_t$. In classical examples $\Delta\mathbf{W}_t$ is drawn from the normal distribution and models the independent Brownian motion specifically. One, given that the $1/\mathrm{f}^{\alpha}$ noise, where $\alpha = 0$ describes uncorrelated white noise and $\alpha = 2$ describes Brownian noise, we may argue that the process of generating the $1/\mathrm{f}^{\alpha}$ noise is only different in the scaling of the multidimensional noise vector, but the underlying distribution still relies on initial sampling from $\mathcal{N}(0, \mathbf{I})$, as will be shown later. There is limited literature on $1/\mathrm{f}$ noise applications as we attempted here, but there was some exploration in the context of the influence of such noise on the solutions of differential equations[146]. We will only offer an empirical result arising from the implementation of the $1/\mathrm{f}$ procedural generation into the magnetic solvers and consequently show that the resulting distributions of magnetisation under such inserted noise are indeed, to a large degree, consistent with the experimental observations (up to some scaling factor). Secondly, we want to touch on a point of physics, namely the assumption that the Wiener processes leading to the noise in separate layers are not correlated with each other. This becomes, in fact, a very

[145] Chęciński, Wiśniowski, et al., "Magnetic Noise Prediction and Evaluation in Tunneling Magnetoresistance Sensors".

[146] Stoyanov, Gunzburger, and Burkardt, "Pink Noise, 1/f noise, and their effect on solutions of differential equations".

convenient assumption, since correlated processes demand a different numerical treatment involving the correlation matrix[147]. The locality of such a noise process may not be of extremely high concern in the macrospin perception of MTJs where a relatively thick oxide layer separates the two layers and thus the interlayer or magnetic coupling is weaker, but definitely requires further inspection if the algorithms described here were to be applied to the microspin simulations.

[147] Sauer, "Computational solution of stochastic differential equations".

Empirical sensor field noise models were proposed in works by Jiang et al.[148], Nowak et al.[149] or Ozbay et al.[150] and provide a good baseline for experimental fits for the composite noise (white + 1/f):

[148] Jiang, Nowak, et al., "Low-frequency magnetic and resistance noise in magnetic tunnel junctions".

[149] Nowak, Weissman, and S. S. P. Parkin, "Electrical noise in hysteretic ferromagnet–insulator–ferromagnet tunnel junctions".

[150] Ozbay, Gokce, et al., "Low frequency magnetoresistive noise in spin-valve structures".

$$S_v = \frac{(\alpha_{\text{mag}}\text{MSP} + \alpha)V_b^2}{\Omega f^\beta} + \mathcal{W} \tag{87}$$

where S_v denotes the voltage noise power, α is the electronic noise with units of m^3, α_{mag} is the normalised 1/f magnetic noise, V_b is the bias voltage applied to the sensor, Ω is the volume of the sensing layer and f^β is the frequency exponentiated to a spectral component (we show the effect of having different exponents in the following sections). $\mathcal{W}$ represents the white noise component. The quantity $\text{MSP} = \frac{\Delta R}{R^2}\frac{dR}{dB}$ is called the magnetoresistance sensitivity product. The values of the α parameters are obtained through a fitting procedure. In the following paragraphs, we will consider only the effects of the magnetic noise, discarding the electrical noise components.

Simple model of 1/f *noise*

Egelhoff et al.[151] attributed the existence of magnetisation hopping of domains between metastable states. In other words, the 1/f magnetic noise could be thought of in terms of multiple small magnetic domains fluctuating at relatively low frequencies. In contrast, thermal noise is white in nature, which means that its amplitude is constant for the entire spectrum of frequencies. A micromagnetic approach to white noise requires one seed and one random unit of vector sampling per magnetic site. But a similar approach for the 1/f noise would be more costly due to additional local computation, as will become evident from the algorithms that describe its procedural generation. Therefore, in lieu of the micromagnetic approach we will now entertain this idea of fluctuating domains in purely mathematical simulation, and by avoiding any computation of the sLLGS we hope to gain some insight into potential magnetic origins of the 1/f noise. Following Egelhoff's hypothesis, we first devise a randomly generated magnetic surface, that is, we create a set of magnetic domains of various sizes sampled from a distribution. The choice of the distribution is dictated primarily by a physical picture, domain imaging experiments often show not a uniform, but more of a gamma distribution of domain areas, which means skewing towards smaller domain areas[152]. However, ignoring this fact and selecting a uniform distribution of areas still produces the same result. After creating the magnetic structure, we now move

[151] Egelhoff, Pong, et al., "Critical challenges for picoTesla magnetic-tunnel-junction sensors".

[152] Egelhoff, Pong, et al., "Critical challenges for picoTesla magnetic-tunnel-junction sensors".

on to selecting the metastable oscillation patterns. In the simple model we discuss here, we pretend that all the magnetic contributions at play in the real device, i.e. the exchange, demagnetising, and anisotropy energies, lead to the result that the domains randomly change their orientation with some predefined period. Our previous assumption about the domain distribution proves to be convenient, as we are now able to posit that perhaps larger domains should be more stable than the smaller ones, hence having longer fluctuation periods than their smaller neighbours. In our model, this statement can take a functional form where $\tau_i \approx \lambda / \mathcal{A}_i$ which denotes a switching period τ_i of a domain i inversely proportional to its area $\mathcal{A}_i$ with a constant λ. Given the gamma distribution of $\mathcal{A}_i$, we also produce a somewhat inverted gamma-like distribution of τ_i. The constant λ here is only for the purpose of scaling the frequencies to the range that we can see in the final spectrum or in the time series. Having almost all pieces assembled, we discuss the simulation, where at each simulation step t we will check τ_i and for all domains for which we have $0 \equiv t \mod \tau_i$, we will generate a random Gaussian vector $\zeta \sim \mathcal{N}(0, \sigma^2)$ where σ is some positive constant. It turns out that this procedure will result in a 1/f-like noise and Fig.29 gives the simulated picture.

In contrast, Fig.31 shows the experimental values obtained from the real sensors. From Fig.31 we also notice an extra factor at play, namely the characteristic corner point where the dominant 1/f noise transitions into the dominant white noise in the power spectrum. In our simple model, this can be accounted for in two ways. One is simply to generate a background white noise distortion for each site at each timestep, sampled similarly from a zero-mean Gaussian with σ' standard deviation $\nu \sim \mathcal{N}(0, \sigma'^2)$. The ratio of σ' to σ and any additional scaling in ν determine whether the corner point moves up or down the spectrum. In the experiment, the simplified rule on how the corner sensor behaves for a sensor with strong perpendicular anisotropy is that the higher the sensitivity, the more the corner moves towards higher frequencies. For MTJ-based sensors with CoFeB electrodes, these relationships translate to anisotropy in an inverse way; a larger perpendicular anisotropy implies a lower sensitivity[153]. Thus, for larger anisotropies, we may expect the corner point to be located at lower frequencies. A further point is the variability of the metastable switching. In the model, we can assume small random phase shifts, which can be summarised with a modification of the switching rule: $0 \equiv t \mod (\tau_i + \delta_{i,t})$ where $\delta_{i,t}$ is a random instantaneous disturbance to the switching of the domain i at time t. We keep it small and on the order of 3-5. Yet another way to have a corner in the spectrum is to generate a set of background domains wherein each oscillates with a high frequency, or a frequency selected from uniform range. So, as shown in Fig.30 using the first of the solutions mentioned, we achieve the corner in the output spectrum, which brings us closer to the experimental result.

What we have essentially shown by this simple exercise is that the necessary components for 1/f noise originate in i) adequate modelling of the

[153] Wisniowski, Dabek, et al., "Effect of CoFeB electrode compositions on low frequency magnetic noise in tunneling magnetoresistance sensors".

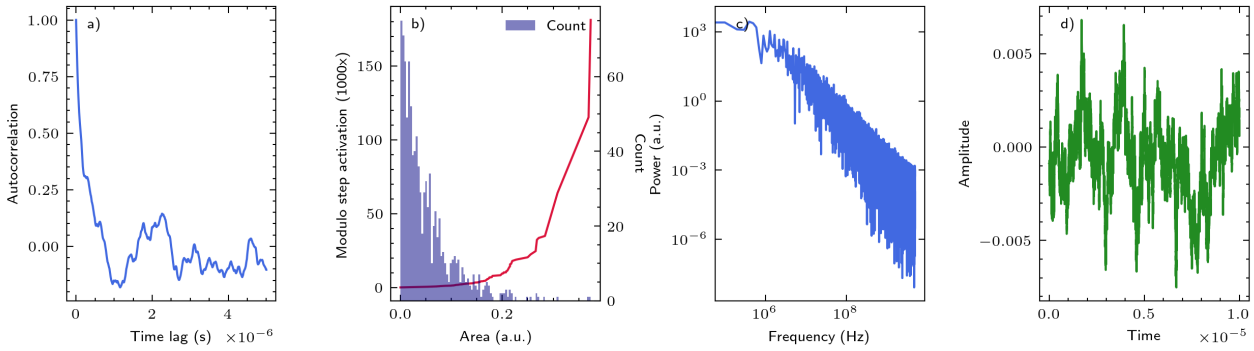

Figure 29: Result of the simplistic approach to simulating the domains. The behaviour of the autocorrelation (a) and $S(f)$ (c) strongly resembles what can be seen in the experiment. (b) the purple histogram denotes the distribution of the domain areas $\mathcal{A}_i$ in a sample, drawn from a Gamma distribution with parameters $a = 1, b = 0.05$ and the red line in the (b) modulo step denotes the activation period, which follows the inverted rule: $\tau_i \sim \lambda / \mathcal{A}_i$.

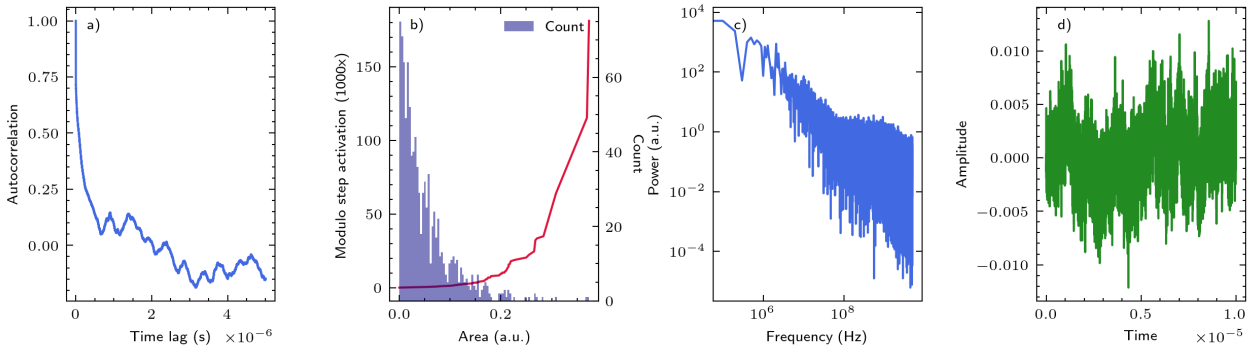

Figure 30: Result of the simplistic approach to simulating the domains, this time with the inclusion of the white noise. Specifically, (c) has the correct corner where the $1/f$ noise transitions into the white noise. Explanations of the panels follow from Fig.29. Noteworthy: even though we see the same distribution of the domains as in Fig.29, their volumes and their metastable switching periods (b), the autocorrelation drops and becomes less oscillatory (looses its detail and succumbs to dominant frequency).

metastable switching and ii) the thermal nature of the metastable fluctuation. This does not mean that the thermal effects themselves are directly responsible for the metastable switching of the domains, if that metastable switching indeed takes place, but rather that the mathematical nature of that fluctuation is similar.

Advanced algorithms for $1/\mathrm{f}$ *reproduction*

We now discuss two known techniques that produce decent quality $1/\mathrm{f}$ noise; most notably: the Voss-McCartney-Trammel (VMT)[154] algorithm and the Kasdin algorithm[155]. The reason why we opt for an established algorithm in lieu of the procedure outlined in a paragraph above is that they reproduce a similar behaviour but with fewer parameters and have better properties in the time-domain, meaning that the samples produced by them yield more realistic autocorrelation.

[154] Voss, "'1/f noise" in music".

[155] Stoyanov, Gunzburger, and Burkardt, "Pink Noise, 1/f noise, and their effect on solutions of differential equations"; Kasdin, "Discrete simulation of colored noise and stochastic processes and 1/f^alpha power law noise generation".

Starting with the VMT algorithm, we define the three-dimensional random field:

$$\mathbf{H}_{1/\mathrm{f}} = k\eta_{VMT}\mathrm{d}W \tag{88}$$

where k is the scaling factor, and $\mathrm{d}W$ is the random Gaussian unit vector. η_{VMT} will come from the VMT algorithm with the steps outlined in Alg.3.

The state vector is laid out such that the first element is the highest frequency noise component, n, the second appears with the probability p, at np, the third with p^3 at np^3 frequency, and so on. If p increases, then the frequencies are more clustered. A natural course of optimisation is to observe that in the second loop we need only to iterate over the unique realisations of the $T^{(k)}$ vector, which reduces the length of the subsequent inner loop, and hence the number of new pseudo-samples drawn diminishes. This is especially the case if $p > 0.5$. Otherwise, the cost of sorting may exceed the cost of a simple iteration. Furthermore, the probability that S_0 will change at each step i when the *else* statement omitted is still rather large, so skipping this clause may save extra time without the loss of generalisation.

Unlike the VMT algorithm, the Kasdin algorithm allows estimating $1/\mathrm{f}^{\alpha}$ in the full range $\alpha \in [0,2], \alpha \in \mathcal{R}$. It can be elegantly described with a Z-transform system functional:

$$H^{\alpha}(z) = \frac{1}{(1-z^{-1})^{\alpha/2}} \tag{89}$$

which can be rewritten using the fractional differencing theorem[156] to see the linear system:

[156] Hosking, "Fractional differencing".

$$H^{\alpha}(z) = \sum_{k=0}^{\infty} (-\alpha/2)_{(k)} (-1)^k z^{-k} \tag{90}$$

where $(-\alpha/2)_{(k)}$ is the falling fractional. We can convert it to the rising fractional using the identity $(-\alpha/2)^{(k)} = (-\alpha/2)_{(k)}(-1)^k$ leading to:

$$H^{\alpha}(z) = \sum_{k=0}^{\infty} (\alpha/2)^{(k)} z^{-k} \tag{91}$$

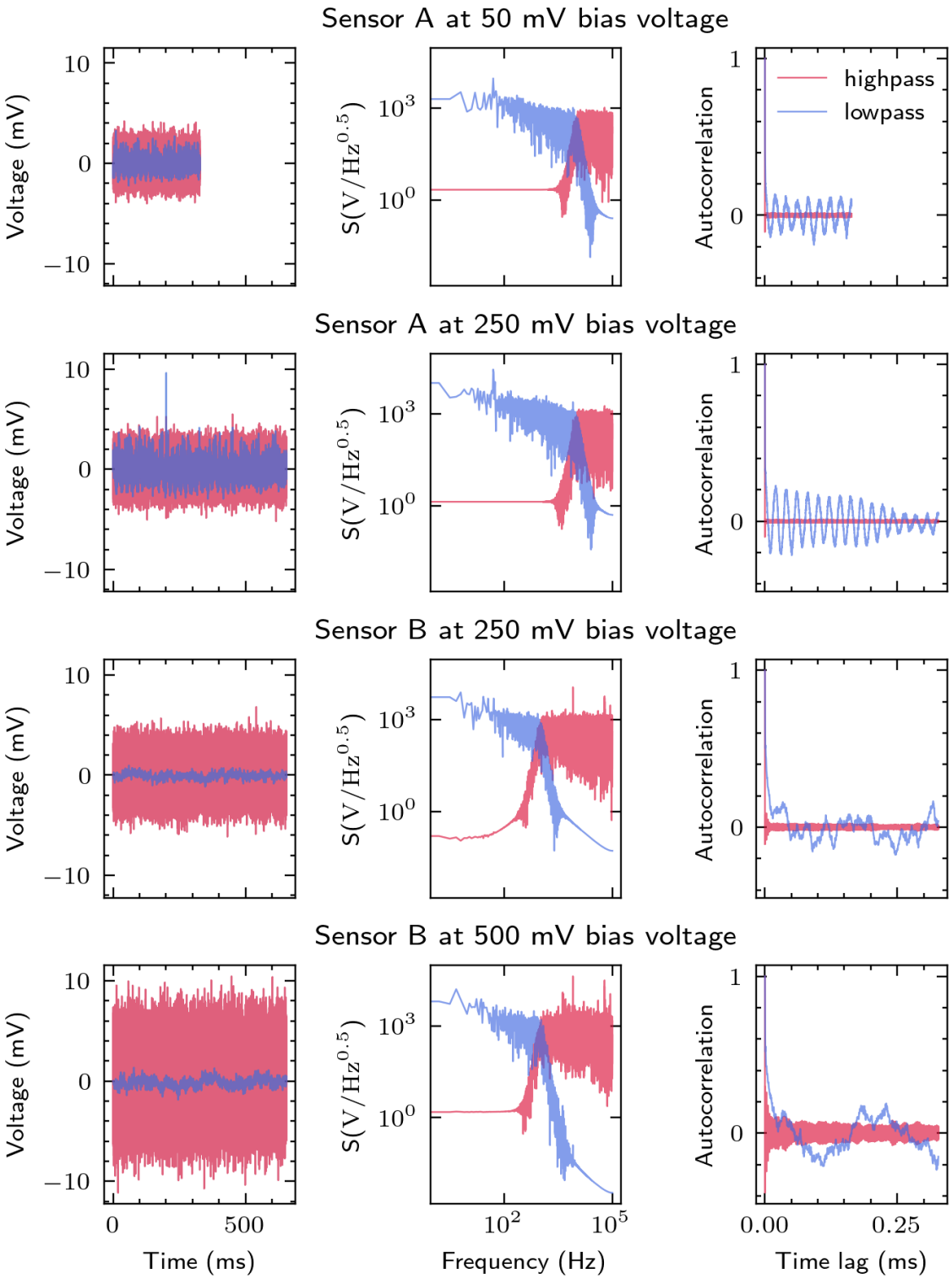

Figure 31: Experimentally measured noise time series and spectrum from two sensors, each with two different applied voltages. The sensors do not exhibit the VCMA effect under voltage change, but the two sensors have two different nominal perpendicular anisotropies. We can deduce from the placement of the characteristic 'corner' point, i.e. the point where the white noise starts dominating over $1/f$ noise, that the sensitivity of the sensor whose corner point is in the higher frequency is lower, thus its anisotropy is larger than the one of the second sensor. The strong oscillating autocorrelation in the first-top panels suggests a large, also strongly oscillating domain in the signal. The red colour denotes the data filtered with the Butterworth 6-th order high-pass filter, and the blue colour marks the signal after it has been filtered with the Butterworth 6-th order low-pass filter. The cut-off point for sensor A was 10 kHz, and for sensor B, 1 kHz; these values were selected so that they separate white noise and $1/f$ at the characteristic 'corner' point. Data were measured by Dr. Piotr Wiśniowski's laboratory and made accessible for analysis to the author. The first sensor time series was measured for a shorter time compared to others.

Algorithm 3: VMT 1/f noise generation

Result: η_i^{VMT}, noise amplitude for each step i.
$k \leftarrow$ number of sources
$p \leftarrow$ probability of success for $\mathcal{B}$, the Bernoulli distribution.
$N \leftarrow$ number of steps
$i \leftarrow 0$
$S^{(k)} \leftarrow$ state vector of length k
$S_i \leftarrow \mathcal{U}(0,1), i = 1...k$ initialise
while $i < N$ **do**
    // $T^{(k)}$ is a vector of size k, sampled from the Bernoulli distribution
    $T^{(k)} \sim \mathcal{B}(p)$
    for s *in* $T^{(k)}$ **do**
        if $s < k$ **then**
            // generate a new sample for that source
            $S_s \sim \mathcal{U}(0,1)$
        else
            // S_0 is the most frequently changing source
            $S_0 \sim \mathcal{U}(0,1)$
        end
    end
    $\eta_i^{\mathrm{VMT}} \leftarrow \sum_j^k S_j$
    $i \leftarrow i + 1$
end

From that form, we can see that the system consists of a series of infinite 1-delay blocks weighted by an appropriate binomial coefficient. Expanding the rising fractional, we can obtain an iterative implementation viable for algorithmic generation:

$$\sum_{k=0}^{\infty}(\alpha/2)^{(k)} = 1+\alpha/2+\frac{\alpha/2(\alpha/2+1)}{2!}+\frac{\alpha/2(\alpha/2+1)(\alpha/2+2)}{3!}= \\ = 1+\sum_{k=1}^{\infty} w_{k-1}\frac{\alpha/2+k-1}{k} \tag{92}$$

where $w_0 = 1$. This finally gives:

$$H(z) = 1+\sum_{k=1}^{\infty} w_{k-1}\frac{\alpha/2+k-1}{k}z^{-k} \tag{93}$$

Further optimisation occurs by observing that consecutive terms diminish

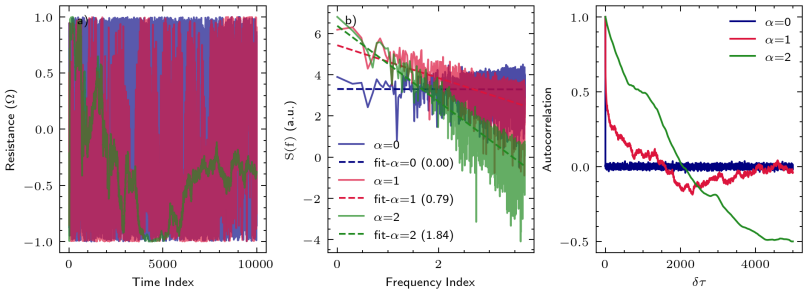

Figure 32: Three values of α corresponding to white ($\alpha = 0$), pink ($\alpha = 1$) and brown ($\alpha = 2$) noise spectra. Panel (a) shows an artificial magnetoresistance computed based on the samples drawn from a given noise distribution (not simulated). (b) The result of computing an FFT on that magnetoresistance time series. The fits, although imperfect, illustrate the increasing α parameter. (c) autocorrelation of the time signal for each of the noise types. Generated based on the Kasdin algorithm.

rapidly (for $\alpha/2 \leq 1$), and thus we can truncate the series to $k = N$, with an error term of $\mathcal{O}(N+1)$. It is worth noting in (93), when we have $\alpha = 2$, the weight term $w_k = 1, \forall k$. In the next step, we compute the FFT of the vector H^N and a vector of samples of normal distribution $\mathcal{N}(0,\sigma)$. After that, the two resultant complex vectors are multiplied and run through IFFT. Finally, we return the real part of the signal. In practice, batching might be required in some cases because, at low frequencies, we require long simulation times, often of the order of µs. This causes large buffer sizes and, more importantly, increases the size of the array based on which we compute the FFT, which, in case it grows too large, makes the computation infeasible. However, such an optimisation may lead to small continuity errors occurring at the buffer boundaries and to the destruction of the longer-scale correlation.

From now on, we will prefer the Kasdin algorithm for noise generation, as it offers greater flexibility. Fig.32 presents the spectra for three values corresponding to white, pink, and brown noise. One crucial feature of $1/f^{\alpha}$ noise is that it becomes increasingly more correlated in the time domain as α increases. Panel c) of Fig.32 shows the smallest autocorrelation values for white noise and the largest for brown noise, which is consistent with the

[157] Carpena and Coronado, "On the Autocorrelation Function of 1/f Noises".

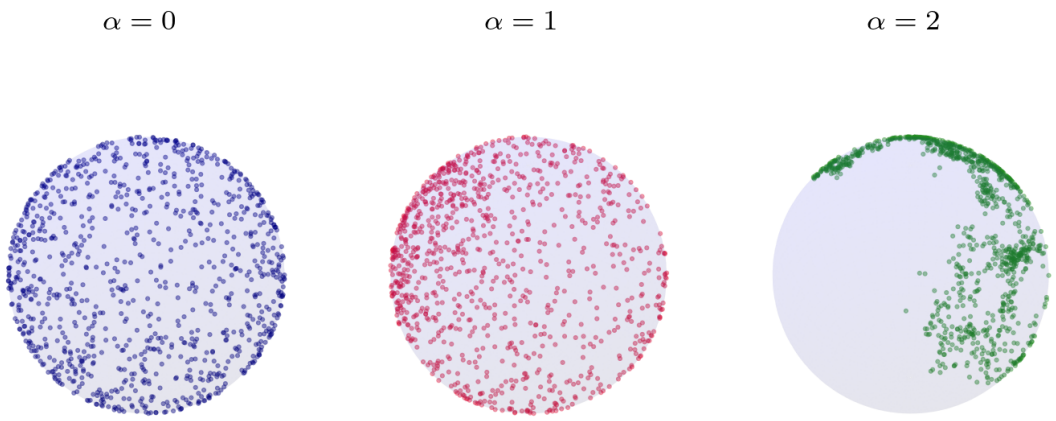

Figure 33: The noise vectors samples for different values of α demonstrating different correlation scales for $\alpha = 0, 1, 2$. The increase in correlation as α grows corresponds to the tendency of the samples to localise in a particular region of the sphere.

theoretical expectation[157]. A similar picture emerges from Fig.33 where the dots on the sphere represent the vector samples drawn from a single buffer of the noise generated by the Kasdin algorithm, again for three different values of α. In subsequent macrospion simulations, this vector will be inserted in place of $\Delta\mathbf{W}$ at each step. In the package, the vector has each component sampled from the $1/f^{\alpha}$ distribution and then normalised. The user can then

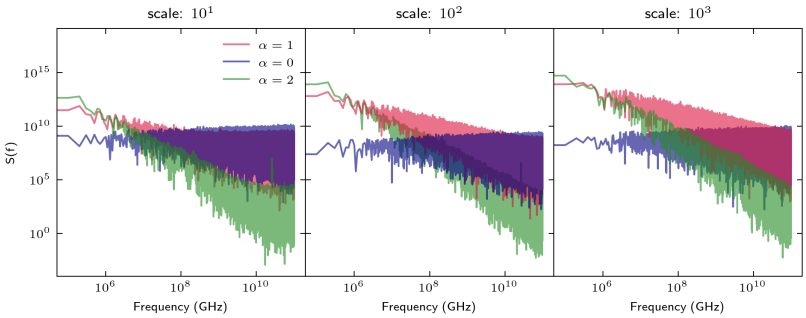

Figure 34: Effect of the $1/f^{\alpha}$ scaling on a sample MTJ with strong perpendicular anisotropy. Although white noise appears to be unaffected, the precise frequency at which other types of noise are overcome with white noise changes depending on the scale. Note that even though the simulation ran for a 10 µs, the low frequency part of the spectrum still received a low number of samples.

define the scaling factor, k, which needs to be determined experimentally. The effect of scaling is shown in Fig.34, where we simulate an example MTJ with a strong perpendicular anisotropy for 10 µs. In addition, we also see a potential effect of noise aliasing on a lower scale, where the typical slope of the noise is disturbed at higher frequencies.[158]

We can now investigate a couple of basic behaviours that arise from the presence of different kinds of noise. First, we return to the theoretical exer-

[158] Kirchner, "Aliasing in 1 / f α noise spectra".

cise from the beginning of this subsection and attempt to reproduce it with LLGS-simulated curves. The setup is nearly identical to the mathematical model, but the purely theoretical assumptions are made more physical. As before, we only assume thermal (white) noise generated in the system, for that we use samples drawn from normal distribution according to thermal equation. The same can be repeated by drawing the Kasdin algorithm; however, the domain methodology allows us only to replicate $\alpha \sim 1$, because the correlation length in the simulation is one, as memory persists only from a previous step. For the sample MTJ, we set $M_s = 1.5$ T, effective perpendicular anisotropy, and measure the response to noise along the z axis. Following our earlier findings, we sample the N domains (here, 1000), with the anisotropy constant of each drawn from a Gamma distribution. The final spectrum is computed with respect to the normalised volume, i.e., each domain's contribution to the spectrum $\mathcal{S}(\omega)$ is proportional to its size and its size is proportional directly to the anisotropy:

$$\mathcal{S}(\omega) = \sum_{i}^{N} w_i \mathcal{S}_i(\omega) \tag{94}$$

where $\mathcal{S}_i(\omega)$ is the spectrum of the particular domain, and w_i is the weight corresponding to the volume. In that way, we reprise the earlier conclusion that we can somewhat reproduce the $1/f$ noise characteristics using only white noise and the assumption that there are a lot of small domains of relatively small anisotropies and few domains with much larger anisotropy.

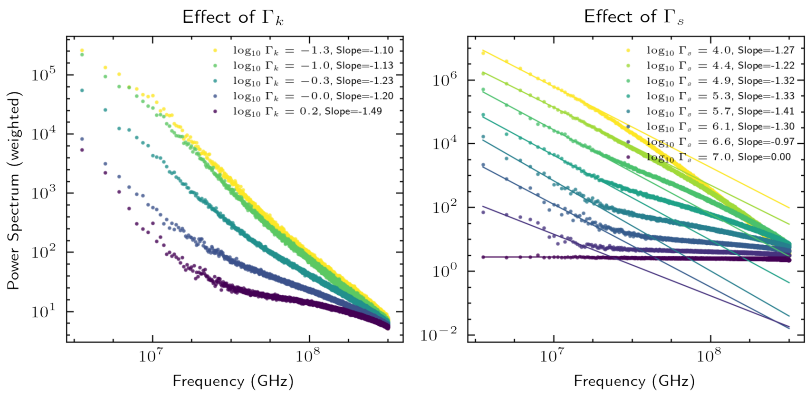

Figure 35: Effect of the scale and k parameter of the Γ function on the $1/f$ spectra produced by synthetic aggregation of multi-domain ($N = 1000$) white noise responses.

Fig.35 shows the sample spectrum in a range of Γ distribution parameters. It shows how the distribution of domains and therefore their anisotropies affects the corner noise, but not as much the effective slope of the $1/f$ distribution and that the slope does not vary with neither Γ_k nor Γ_s. However, the behaviour observed mimics the noise of $1/f$ and gives some strength to the argument that the noise of $1/f$ could be understood as a composite of white noise, gated by a varying response from different domains. In conclu-

sion, from our simulations, the key components for the reproduction of the approximate $1/f$ noise are:

1. Magnetic memory, which in simulation is ensured as the magnetisation from time t is carried over to the next step, $t+1$ and then modified. This memory functions as a correlation component.

2. Randomly sampled thermal sample generators; the domain acts as such generators, given that T is set sufficiently high to overcome stiffness due to effective anisotropy.

The choices of distributions over the anisotropies we tested were the normal distribution, the gamma distribution, and the uniform distribution. We note that, as before, the Γ distribution is not critical to the reproduction of the linear slope, nor is the weighting by domain size, and those conditions were chosen for a closer physical reproduction of magnetic domain structures.

In the second example, we inspect two examples based on a plain MTJ oscillator with a perpendicular anisotropy, excited by a constant current density bias j_b. In Fig.36 we present such an MTJ with 0.15 kJ/m^3 anisotropy constant and in Fig.37 an equivalent MTJ but with a larger anisotropy of 150 kJ/m^3. The scale of the noise, though slightly exaggerated to make a point, was kept constant for both runs. As expected, increasing the anisotropy improves the resistance to noise, which is clear both in the time domain and in the frequency domain. Inspecting the magnetoresistance shows a range of aharmonic contributions for the white noise, and less so for the $\alpha = 1$. Noise $1/f^2$ appears to induce a more regular disturbance, which is a particular hazard for devices that operate as frequency detectors. When $\alpha = 2$ we can observe that an additional frequency peak emerges in a frequency bin below the main resonance frequency, and so in a significant magnitude. The ratio of that peak to the main resonance peak A_0/A_{noise} is subject to particular realisation, which means that it fluctuates heavily due to the stochastic nature of the noise. Despite a large standard deviation across all realisations, there is a slight tendency for the A_0/A_{noise} ratio to increase along with an increase in the perpendicular anisotropy constant. These results seem to be in line with similar experimental findings showing that MTJs with larger perpendicular anisotropy are more robust to $1/f$ noise.[159]

Finally, for completeness, Fig.38 is analogous to Fig.28, this time reproduced with $1/f$ noise instead of pure thermal noise. The characteristics of peak deterioration are different from the thermal noise for both $\alpha = 1$ and $\alpha = 2$, and $1/f$ noise seems to have a strong impact, even at a lower amplitude parameter k. Furthermore, the correlation component of the noise affects the ability of two MTJs to synchronise, but in asymmetric and the symmetric excitation cases.

[159] Wisniowski, Dabek, et al., "Effect of CoFeB electrode compositions on low frequency magnetic noise in tunneling magnetoresistance sensors".

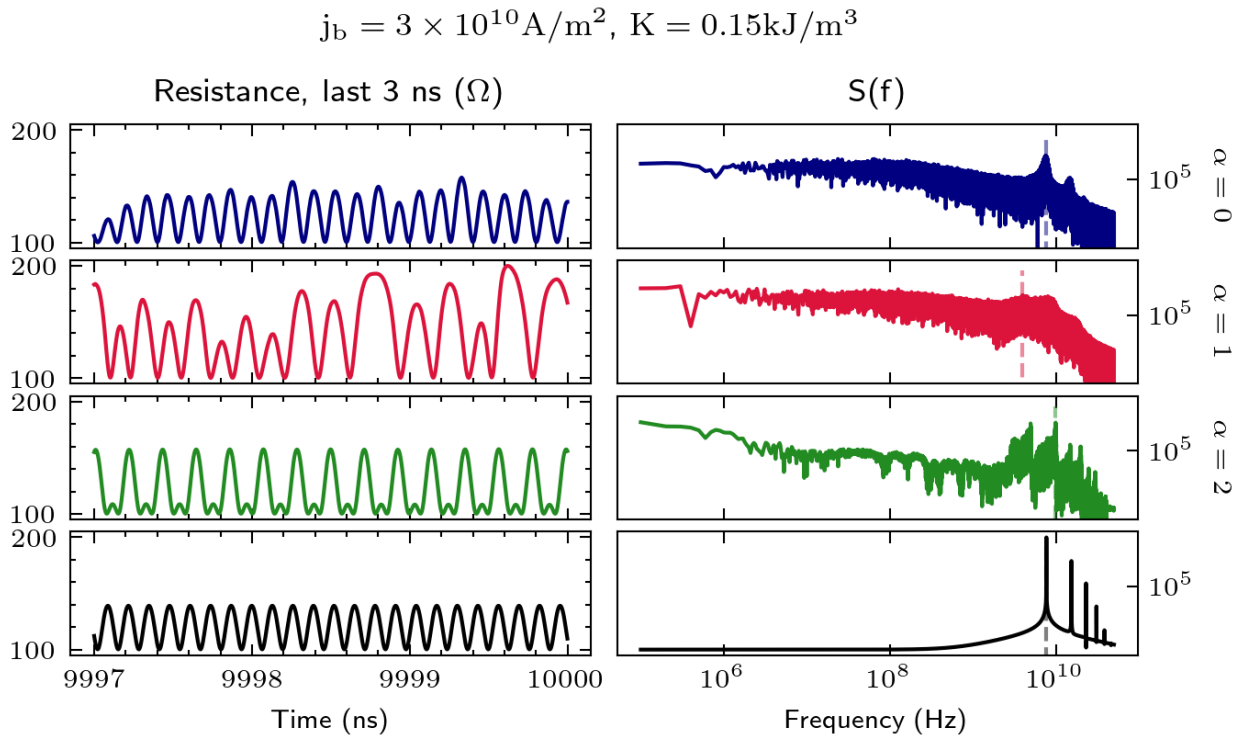

Figure 36: The spectrum for smaller anisotropy constant of 0.15 kJ/m^3.

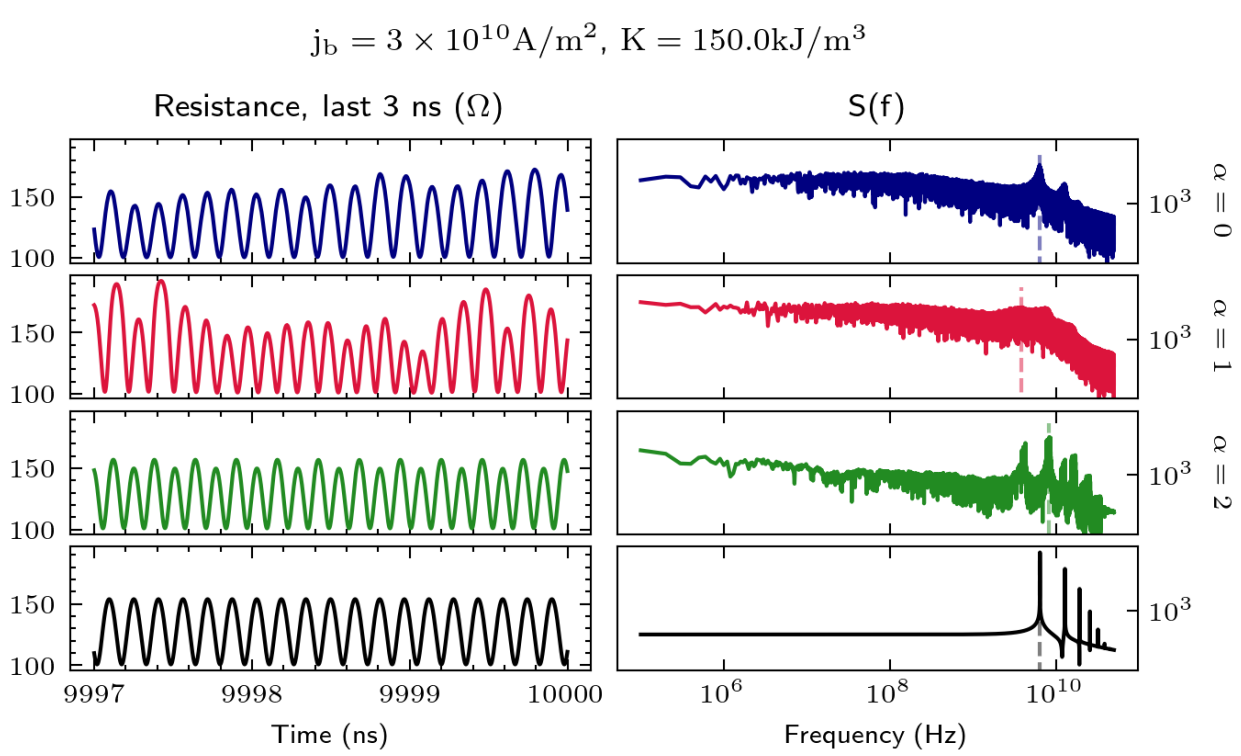

Figure 37: The spectrum for the MTJ with a larger anisotropy of 150 kJ/m^3, 100 times larger than in Fig.36. Compared to lower anisotropy, the peaks at $\alpha = 2$ are much more separated and thinner. In the case of $\alpha = 1$, the noise still covers the oscillation peaks.

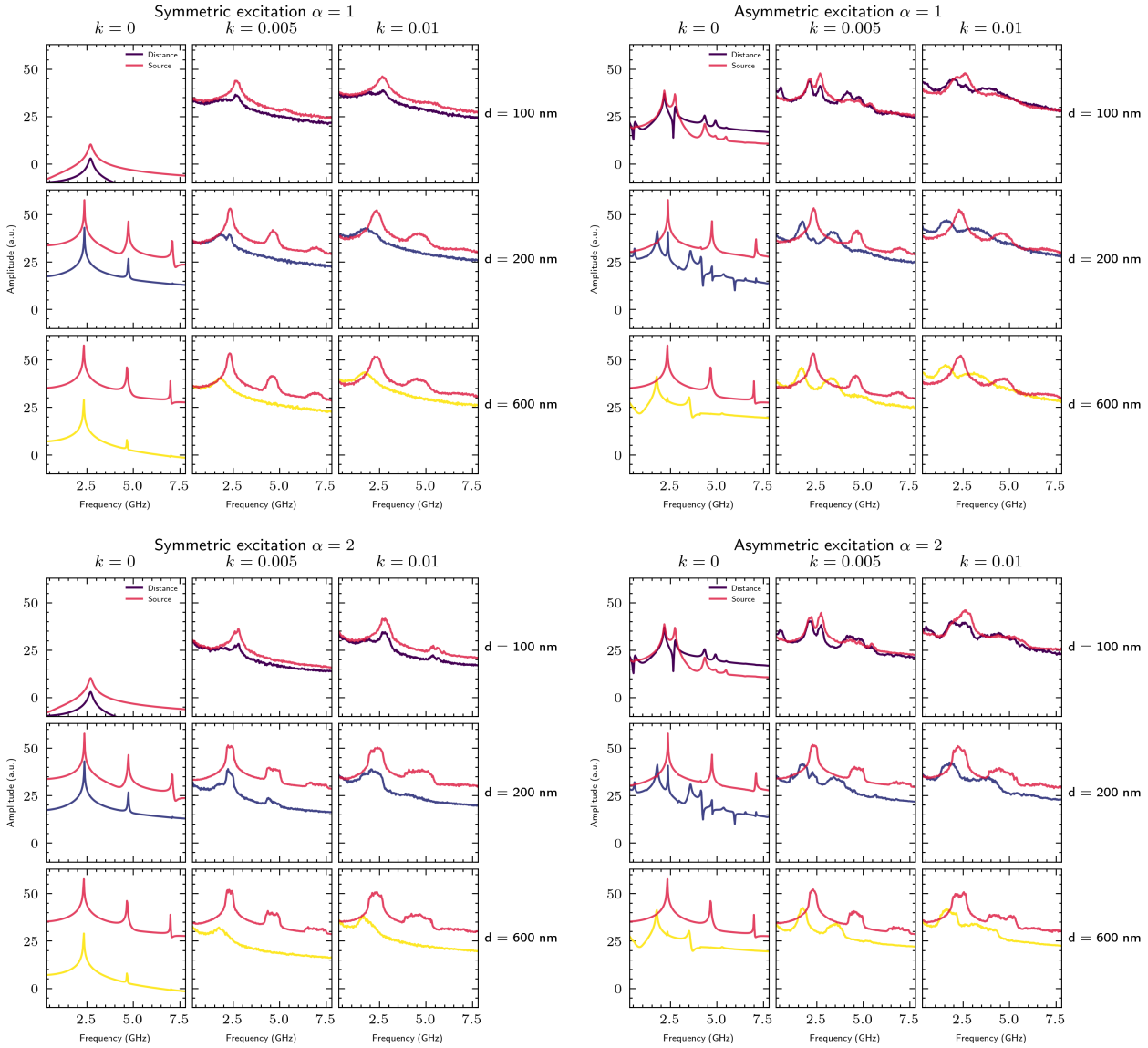

Figure 38: Dipole interaction over $\alpha = 1$ (top row) and $\alpha = 2$ (bottom row) $1/f^{ff}$ noise. Below 50 nm the system becomes too stiff to be excited. $\alpha = 2$ show faster peak deterioration than $\alpha = 1$, both with distance and with noise amplitude. However, for symmetric excitation, the synchronisation peak seems to be retained in $\alpha = 2$, but it disappears when $\alpha = 1$. k is the $1/f^{ff}$ noise scaling factor.

Chapter summary

In this chapter, we discussed selected applications of the MTJs. Electrical coupling, though difficult to achieve, presents a promising direction for different computing applications. Adequate modelling of 1/f noise can improve sensor design that retains its robustness in the high-sensitivity regime or can cleverly balance the trade-off between field noise, range, and sensitivity. Our simulations demonstrate how an ensemble of thermally activated domains can lead to primitive 1/f characteristics. Furthermore, similarly to the experimental findings, the simulated effect of 1/f noise on the resulting spectra diminishes with increasing perpendicular anisotropy or with increasing junction size. As a closing word to this chapter, we touch on potential areas of improvement. First, while we can create complex simulations of electrically coupled junctions, we still have little understanding of the relationship between the quantity of theoretical coupling χ and its experimental realisation. Resolving this could lead to less frustration in attempting to fabricate MTJs that synchronise at near frequencies easily – and the difficulty of achieving this has been noted in detail in[160]. Second, we would like to have a more definitive answer to the origin of 1/f noise. In Modelling correlated noise we propose, using a mathematical toy model, several hypotheses that reproduce the experimental behaviour, yet the real answer will probably reveal itself in the process of observing the sensor noise under optical magnetic imaging over long acquisition times. This is again not a trivial experimental setup and remains to be implemented. Finally, a numerical issue is: How can we simulate micromagnetically 1/f noise in a reasonable time, in terms of computational efficiency. The simple toy model we presented at the beginning of the Modelling correlated noise is a reflection of a micromagnetic world, but it needs to be sufficiently distilled so that a full-scale simulation with LLGS dynamics would be possible.

[160] Rzeszut, Mojsiejuk, et al., "Towards mutual synchronization of serially connected Spin Torque Oscillators based on magnetic tunnel junctions".

Dynamic control of devices

The meteoric rise of machine learning methods in recent years has had a profound impact on the perception of what an optimal way to approach a given problem should be. In previous chapters, an example of automatic parameter fitting was demonstrated, which eliminated the need for manual tweaking; here, we present a compelling case for a related technique: the dynamic control of various types of spintronic devices.

After a brief theoretical introduction to reinforcement learning, we propose a control problem based on a spintronic oscillator as an example. This serves as a motivating example for the reinforcement learning (RL) methods that are subsequently employed to solve it. Finally, other spintronic applications of RL are discussed.

Introduction to reinforcement learning

Recent model-free reinforcement learning algorithms fall into two broad categories: policy optimisation methods and Q-learning, with some methods combining the two. Policy, typically denoted as $\pi_\theta(a|s)$[161], is a set of rules that dictates the actions of the agent in a given environment. The algorithms that perform policy optimisation explicitly represent the policy and learn an optimal policy via direct updates. In addition, the actions the agent performs are sampled from some policy; that is, $a_t \sim \pi_\theta(\cdot|s_t)$. On the other hand, Q-learning methods rely on learning a function approximator for the action-value function, $Q_\phi(s,a)$. In Q-learning, the optimal policy is not learnt directly, but through optimisation of the Q_ϕ function. The actions can be selected by following a greedy policy:

$$\pi_{\text{greedy}}(s) \in \arg\max_a Q_\phi(s,a) \quad \text{s.t.} \quad a_t = \pi_{\text{greedy}}(s_t) \tag{95}$$

There is a further distinction between on-policy and off-policy learners. On-policy algorithms use the data collected while acting with the policy to update the very same policy. Conversely, off-policy methods learn from past examples through replay, meaning they update the policy based on past experiences collected when the actions were selected using a different (a past version of) policy. Typically, off-policy algorithms are more sample-efficient because the same collected sample can be reused to improve many

[161] $\pi_\theta(a|s)$ represents the probability of selecting an action given that the agent has observed a state s. θ denotes policy parameters.

future versions of the policy (experience replay). This comes at the cost of stability, as the examples collected in earlier versions of the policy may not reliably guide the policy gradient updates into stable optima. Sample efficiency becomes critical when the environment is costly. Simulations are quick to run, but on-device experiments are much slower, and therefore off-policy learning is important.

In this chapter, we limit ourselves to three algorithms that yielded the best results for the environments considered in our work: Soft Actor-Critic (SAC)[162], Twin Delayed Deep Deterministic Policy Gradient (TD3)[163] and Proximal Policy Optimisation (PPO)[164]. The first two are off-policy actor-critic methods that combine off-policy temporal-difference (TD) learning[165] of Q_ϕ with policy optimisation employing the actor network (learning $\pi_\theta(a|s)$) and two critic networks estimating $Q_\phi(s,a)$[166]. Fig.39 schematically illustrates the architecture of the actor-critic pair, specifically its SAC flavour. The reasoning behind using two critic networks instead of one is that in the past iterations of actor-critic methods, the critic network had a tendency to overestimate the Q-value. Thus, in the twin-critic version, the minimum of the two is taken for the gradient update step. After the agent has been trained, only the actor part is deployed. Discarding the critic is possible only because the state-action value is not used directly when selecting actions, only for the policy improvement step during learning. Such an approach, combined with the simulated pretraining, was effectively demonstrated in many real-world applications from the physics domain, for example, recently in the magnetic control of a tokamak plasma during the fusion process[167].

[162] Haarnoja, A. Zhou, et al., *Soft Actor-Critic*.

[163] Fujimoto, Hoof, and Meger, *Addressing Function Approximation Error in Actor-Critic Methods*.

[164] Schulman, Wolski, et al., *Proximal Policy Optimization Algorithms*.

[165] R. S. Sutton and Barto, *Reinforcement learning*.

[166] Here, we separately denote actor and critic parameters as θ and ϕ respectively.

[167] Degrave, Felici, et al., "Magnetic control of tokamak plasmas through deep reinforcement learning".

SAC combines techniques from algorithms such as Trust Region Policy Optimisation (TRPO)[168] and PPO, characterised by stochastic on-policy learning, stability, and low sample efficiency, with methods such as the Deep Deterministic Policy Gradient (DDPG)[169] or TD3 characterised by a deterministic policy, relative instability, and the use of a replay (experience) buffer, which leads to good sample efficiency. Here, stability means that the convergence of the algorithm is not overly sensitive to the choice of hyperparameters. SAC also introduced a soft learning objective that maximises both the reward and the entropy:

[168] Schulman, Levine, et al., *Trust Region Policy Optimization*.

[169] Lillicrap, Hunt, et al., *Continuous control with deep reinforcement learning*.

$$\pi^*_\theta = \underset{\pi_\theta}{\operatorname{argmax}} \sum_t \mathbb{E}_{(s_t,a_t)\sim\pi_\theta}[\gamma^t\,(r(s_t,a_t) + \alpha\mathcal{H}(\pi_\theta(\cdot|s_t)))] \tag{96}$$

where γ is the discount factor, and $\mathcal{H}(\pi_\theta(\cdot|s_t))$ represents the policy entropy, α determines its weight. In practice, this objective is rewritten in terms of an optimisation constraint on the lower bound of the entropy, some $\mathcal{H}_0$. Intuitively, the entropy term should not converge to 0, as that would mean a fully deterministic policy, yet the goal of the SAC is to balance the stochasticity of the policy while maximising the reward. Since the original release of the SAC, the maximal entropy target has been used to augment other algorithms as well. This stochasticity is evident in Fig.39, the actor predicts $\mu_\theta, \sigma_\theta$ that parametrise a Gaussian $\mathcal{N}(\mu_\theta, \sigma_\theta)$ from which the actions are drawn. tanh

squashing is then applied to bound the action values.

On the other hand, PPO is an on-policy optimisation algorithm, which maximises a surrogate objective function. This surrogate function indicates how much the performance objective will change as a consequence of the update. In the **PPO-CLIP** variant, the algorithm attempts to limit the amount that each policy update drifts away from the old policy, improving stability and convergence. The policy update rule is given by:

$$\theta_{k+1} = \underset{\theta}{\operatorname{argmax}} \frac{1}{|\mathcal{D}_k|T} \sum_{\tau \in \mathcal{D}_k} \sum_{t=0}^{T} \min \left(\frac{\pi_\theta(a_t|s_t)}{\pi_{\theta_k}(a_t|s_t)} A^{\pi_{\theta_k}}(s_t,a_t), g(\varepsilon, A^{\pi_{\theta_k}}(s_t,a_t)) \right) \tag{97}$$

where θ_{k+1} denotes the policy parameters in step $k+1$, $\mathcal{D}_k$ is a set of trajectories τ obtained from running π_{θ_k} (old policy) in the environment, T is the duration of a particular trajectory, g is defined as[170]:

[170] Schulman, Moritz, et al., *High-Dimensional Continuous Control Using Generalized Advantage Estimation*.

$$g(\varepsilon, A) = \begin{cases} (1+\varepsilon)A & \text{if } A \geq 0, \\ (1-\varepsilon)A & \text{if } A < 0. \end{cases} \tag{98}$$

Finally, the advantage function A is defined as:

$$A^\pi(s,a) = Q^\pi(s,a) - V^\pi(s) \tag{99}$$

with the value function $V^\pi(s) = \mathbb{E}_{\tau\sim\pi}[R(\tau)|s_0 = s]$, the state-action value function $Q^\pi(s,a) = \mathbb{E}_{\tau\sim\pi}[R(\tau)|s_0 = s, a_0 = a]$ and $R(\tau) = \sum_{t=t_0}^{\infty} \gamma^t r(s_t,a_t)$ is the discounted return of the trajectory. The advantage function measures whether the action taken is better than the policy's default behaviour.

For all experiments in this chapter, we benefit from the implementations of the baseline algorithms provided in the Stable Baselines 3 repository[171]. The reader is also referred to[172] for pseudocode on practical implementation of the policy and Q-function updates for all algorithms discussed in this section.

[171] Raffin, Hill, et al., "Stable-Baselines3: Reliable Reinforcement Learning Implementations".

[172] Achiam, *Spinning Up documentation*.

Spintronic oscillator environment

Introduction to the problem

Suppose that we are faced with the relatively simple problem of tuning an oscillator to some desired frequency f^*. To arrive at this frequency, we can adjust two control parameters: the first regulates the DC current, and the other modifies the external magnetic field. For a human, the procedure could probably look like this: the user first observes a frequency f, in some initial configuration of the current and field gauge. Then they pick one of the inputs and adjust it, resulting in a new frequency reading denoted as f'. If the resulting change, that is, $\Delta f = f' - f$ is positive and brings the system closer to the target frequency f^*, such that the error $\varepsilon = |f^* - f|$ decreases, then they would try turning the same gauge in the same direction again. In any other case, they would either change the turning direction of the same gauge

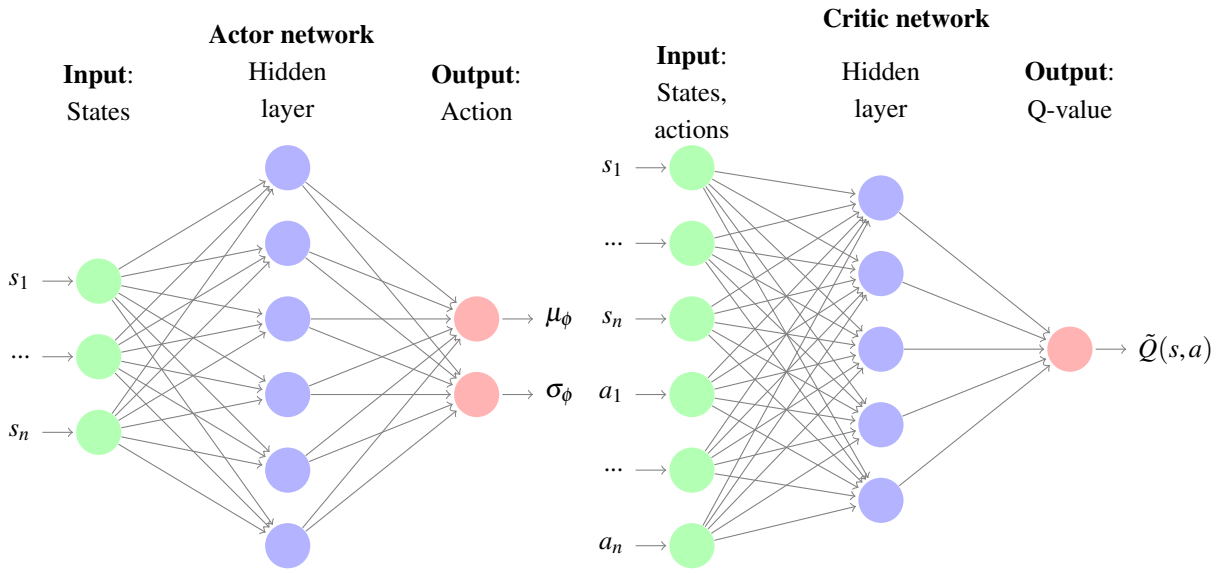

Figure 39: Actor and critic network generic architecture. TD3 introduced two critic networks to reduce the overestimation bias. In SAC the actor networks returns μ_ϕ and σ_ϕ, the mean and the standard deviation vectors representing the action vector which are then squished with either tanh or RELU. Both tanh and RELU are activation functions and the latter stands for *Rectified Linear Unit*.

or pick another gauge to test. The act of turning up or down the same gauge is called *exploitation* and the action of changing a gauge, or a direction of regulation introduces an element of *exploration*, where the user anticipates that changing the method of adjustment could lead to quicker or more precise convergence. A human agent may only require a few attempts to get a good grasp of the dependence $\frac{\mathrm{d}f}{\mathrm{d}j}$ or $\frac{\mathrm{d}f}{\mathrm{d}h}$, that is, the change in frequency with respect to the current or field. Content with an easy success, we may decide this is a non-problem, but in real life setup, there are just a few modifications that make the problem extremely difficult and prohibitively time-consuming for the human user. Firstly, we should observe that the dependence of frequency on current and/or on the field is often a nonlinear one, wherein one range of currents/fields yields distinctly different behaviour from some other range. Second, if the task is to be repeated for different types of oscillator, or even for oscillators of the same type that differ as a result of the fabrication process, we quickly find that there is a latent dependency on the intrinsic oscillator parameters that makes it difficult to carry over the process of tuning one oscillator to another. Finally, tying back to the issue of optimal control, we may wish to complete the task in the shortest possible manner, i.e. have an optimal procedure for going from initial state to synchronised state. In conclusion, the control problem for the simplest oscillators becomes nontrivial if we constrain the time and allow the intrinsic parameters to vary more or less freely. Conservative solutions from control theory toolboxes such as PIDs controllers[173] or LQRs[174] can help in a limited way, but fail in cases where the environment conditions change spuriously, as would be the case

[173] Proportional Integral Derivative
[174] Linear Quadratic Regulator

with varying parameters of the oscillator. However, such a problem turns out to be well-posed for a reinforcement learning setup, especially the one where the agent learns to be more adaptive to the environment. Reinforcement learning, although known for a relatively long time – a popular textbook by Sutton and Barto originally published in 1998[175] – lives through its renaissance, benefiting from tremendous progress made in effective training and design of deep learning models. In fact, those algorithms are known for integrating the aforementioned *exploration* and *exploitation* concepts into their learning mechanism.

[175] R. S. Sutton and Barto, *Reinforcement learning*.

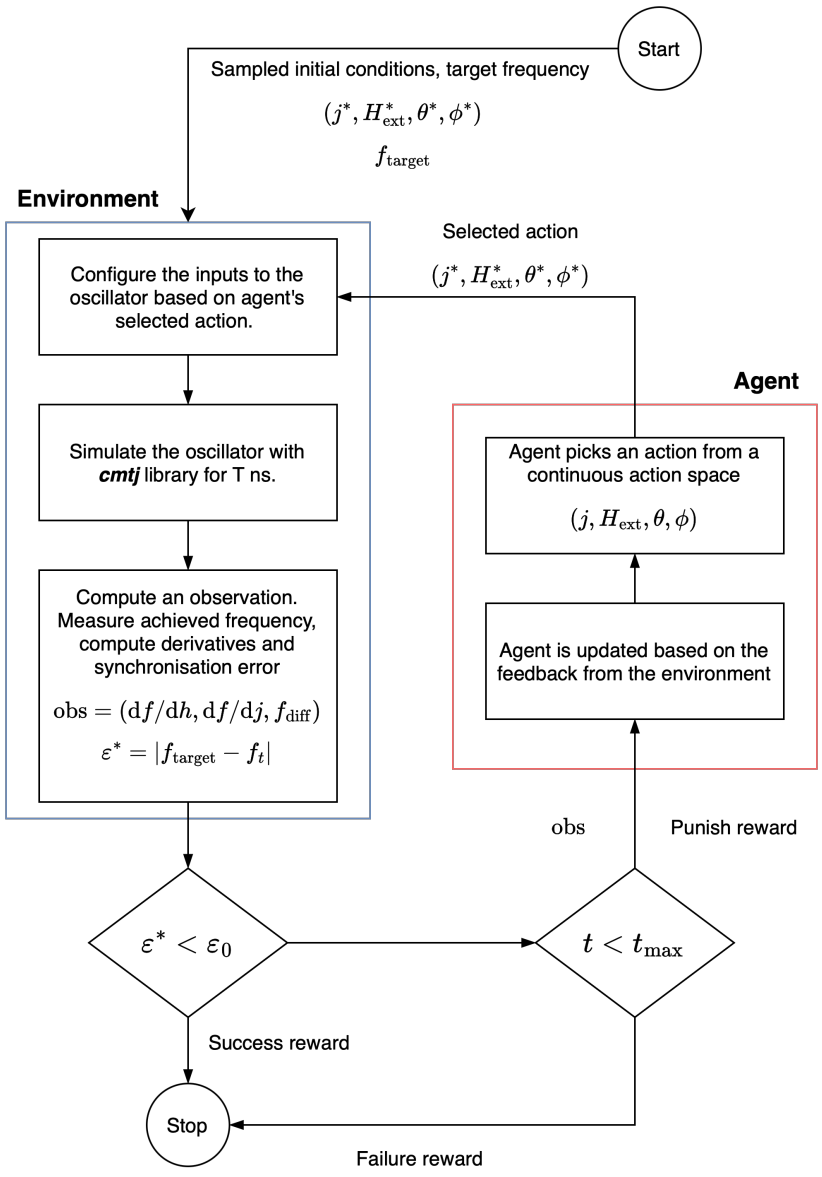

Figure 40: A schematic of a training and decision loop representing agent and environment design parts.

Implementation details

The work Pub. 3: Reinforcement learning for spintronic oscillator application outlines the implementation details for the RL-controlled environment of a spintronic oscillator. A simplified training loop schematic illustrating the setup is shown in Fig.40. The RL controller attempts to manipulate the input current and the applied external field such that the STO oscillates with a target frequency. The target frequency, starting control values, and magnetic parameters (K_u and M_s) are randomly assigned at each step, so the RL agent must be able to complete the task under varying conditions and in a fixed number of steps. The reward system has been engineered to ensure fast, but smooth synchronisation, and higher Q-factor of oscillations. The reader is referred to Pub. 3: Reinforcement learning for spintronic oscillator application for more details on the implementation of the environment design, the reward shaping, and the parameter used. Expanding on the *Reward shaping* section of that work, we stress that the design of the reward system is critical to learning behaviour and the convergence trajectory of the reinforcement learning agent. The primary objective of the agent is to reach a synchronised state, defined by a maximum synchronisation error ε^* (the difference between the desired and current frequency). Upon reaching this threshold, the agent receives a large success reward. At the same time, we want the agent to achieve the synchronisation as quickly as possible; therefore, we define a relatively small penalty applied at each step taken that does not result in synchronisation. If this signal is shaped, that is, is directly proportional to the synchronisation error ε^*, then the convergence to a good success rate is faster, and the mean path to synchronisation is shorter, as shown in Fig.41. The simulation is limited to 100 steps to ensure computational efficiency, enough to achieve synchronisation from any initial state. This truncation also helps formalise the terminal condition of the episode, although it does not affect the underlying Markovian nature of the environment.

Each time an additional reward component is introduced, the challenge of properly adjusting the reward weights ζ resurfaces. Unfortunately, resolving this issue requires trial-and-error experimentation. As the complexity of the reward system grows, the task of tuning becomes increasingly tedious. For example, if excessive weight is given to the error-shaping component relative to the action magnitude control term, the agent may learn to disregard the latter entirely. Similarly, assigning too large a weight to the Q-factor reward function overshadows the primary objective of achieving synchronisation, leading to much lower success rates. Furthermore, the time horizon over which the rewards are evaluated has a significant influence on the agent's behaviour. Consider a two-component reward system, with the reward for achieving the synchronised state ($\hat{\mathcal{R}}_{\text{synch}}$) and the punishment relative to the synchronisation error ε^* ($\mathcal{R}_{\delta \text{f}}$). Suppose that the agent reaches a state s_1 where it receives a small penalty $\mathcal{R}_{\delta \text{f}} = 0.1$. The agent can choose to stay

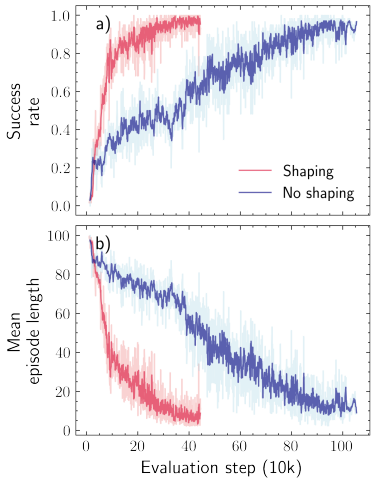

Figure 41: Impact of shaping on the success rate convergence speed and mean number of steps required for synchronisation. Making a part of the reward proportional to the synchronisation error ε^* (red) significantly improves the speed of training over a reward system where there is only a reward for achieving synchronisation (blue). The graph presents results averaged over 4 runs per each reward system.

in this state s_1, for the remainder of the simulation, over 10 steps, which yields an expected return proportional to a discounted sum of $\mathcal{R}_{\delta \mathrm{f}}$ over these steps. If some trajectories from s_1 to some other state s_2 produce a temporarily larger $\mathcal{R}_{\delta \mathrm{f}}$, but ultimately achieve synchronisation, it is essential that the final reward for achieving the synchronised state does not vanish over the discounted sum in the expected reward. Otherwise, the agent may prefer suboptimal but locally rewarding behaviour. In other words, the magnitude of $\hat{\mathcal{R}}_{\mathrm{synch}}$ must be sufficiently large compared to $\mathcal{R}_{\delta \mathrm{f}}$ and the expected number required for synchronisation, to ensure that its signal is not lost in the cumulative return estimate.

Impulse shaping

CIMS is another strong application use case for RL. Ender et al. focused on reducing SOT-MRAM failure rates, employing reinforcement learning to adjust the time and amplitude of the two current impulses necessary for a single memory write operation[176]. In that work, the authors assumed a step of variable duration and amplitude, but in this section we explore the possibility of learning the impulse shape itself. Two switching configurations are considered, as shown in Fig.42, one using the STT mechanism (a) and the other using the SOT mechanism (b).

The impulse shaping simulation is composed of many meta-steps, where each meta-step itself consists of multiple LLG simulation steps. Depending on the configuration, we adjust the meta-step simulation size and the number of LLG steps inside, but we keep the integration parameters constant. The agent can only set the controls at the meta-step level, and their values are considered constant for the duration of that meta-step. To improve sensitivity to change and decrease learning time while increasing the final success rate, the current is controlled through its exponent $j_t = \mathrm{sgn}(a_t^j) 10^{\max(a_t^j + j^0, j^{\max})}$ $\mathrm{A/m^2}$ where sgn is the signum function, j^0 is the offset of the exponent and $j^{\max}$ is the absolute maximum bound on the exponent. a_t^j corresponds to the unnormalised current density component of the controller action. This setup comes at the cost of some precision control and the lowest exponent should be treated as an effective zero signal. The observation space includes a z component of magnetisation, m_z, averaged over several last simulation steps of the meta-step, and its change over the duration of the meta-step, $\partial_t m_z$ and j. During our experiments, increasing the observation space with the remaining components did not significantly impact the learning process. Each episode has two stages: the control stage where the control input affects the simulation and the evaluation stage where the controller is disconnected. The evaluation stage only considers the alignment reward, and its role is to ensure that the magnetisation remains in a stable target state.

The baseline reward system is simple and focuses on rewarding the persis-

[176] Ender, De Orio, et al., "Improving failure rates in pulsed SOT-MRAM switching by reinforcement learning"; Ender, Lacerda De Orio, et al., "Reinforcement learning to reduce failures in SOT-MRAM switching".

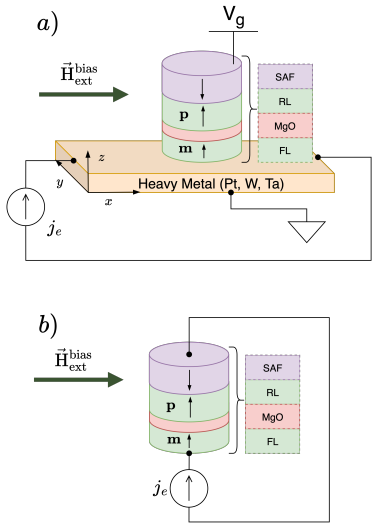

Figure 42: Proposed setups for RL impulse control in CIMS. (a) SOT configuration with optional VCMA control, (b) STT configuration. A small external applied magnetic field is needed to break the symmetry in this geometry.

tent and accurate alignment of the m_z component with the target state m_z^*:

$$\mathcal{R}_t = \zeta_{\text{energy,j}}|a_t^j|^2 + \zeta_{\text{align.}}|m_z^* - m_{z,t}|^2 + \hat{\mathcal{R}}_{\text{term.}} \tag{100}$$

where ζ denote weights of each reward component (they can be negative), and $\hat{\mathcal{R}}_{\text{term.}}$ is a terminal reward which is awarded during the evaluation stage, after completing k control meta-steps. $\hat{\mathcal{R}}_{\text{term.}}$ is positive if the magnetisation remains stable in the target state and becomes negative if the target has not been achieved within a small error $\varepsilon = 0.05$.

To conduct the simulation for a given meta-step, we use the standard LLGS equation, depending on the configuration: STT (7), or SOT (10). In STT configuration, the following parameters are fixed $\lambda = 0.69, P = 1.0$, in SOT we set $\theta_{\text{SH}} = 0.35$, utilising the following torque scaling of the damping-like torque ($\text{H}_{\text{FL}} = 0$ in the experiments)[177]:

$$\text{H}_{\text{DL,t}} = \frac{\hbar\theta_{\text{SH}} j_t}{2e\text{M}_\text{s}\text{t}_{\text{FM}}} \tag{101}$$

where t_{FM} is the thickness of the free FM layer. In both configurations, $\alpha = 0.035$, $\text{t}_{\text{FM}} \sim (1, 1.5)\,\text{nm}$, $\text{M}_\text{s} \sim \left[(1-\vartheta)\text{M}_\text{s}^0, (1+\vartheta)\text{M}_\text{s}^0\right]$, $\text{K}_\text{u} \sim \left[(1-\vartheta)\text{K}_\text{u}^0, (1+\vartheta)\text{K}_\text{u}^0\right]$[178] where ϑ is the dispersion, usually between 2% and 15%, $\text{M}_\text{s}^0 = 0.95\,\text{T}$, $\text{K}_\text{u}^0 = 0.95\,\text{MJ}\,\text{m}^{-3}$.

Fig.43 illustrates a set of trajectories obtained from sample models trained in each of the configurations. In SOT switching, the agent clearly prefers to induce short-term current bursts and attempts to align them adequately to quickly maximise the $|m_z^* - m_z|$ component.

In our simulations, we observed that both the meta-step duration, operational current range, and parameter dispersion strongly affect the models ability to learn successful switching control. The dispersion of the parameters, that is, the thickness ranges, M_s and K_u, has a strong impact on both the final success rate and the learnt amplitude of the impulse. Since the model has no access to the underlying magnetic and dimensional parameters of the device during the control stage, the only cue that it can use is the response of the magnetisation at a given current impulse. As the model is punished for superfluous application of current, it does not have a 'probing' stage where it would attempt to triage the device parameters. Instead, the model opts for global optimisation (i.e. across various device realisation) of the current impulse, which yields maximal average success rate, and thus mostly chooses to operate with timed-short impulses of large amplitude and, if necessary, delivers secondary impulse of lesser amplitude to correct the trajectory. The latter strategy is highlighted in Fig.44, and we note that this approach to switching is learnt at random by selected models. Intuitively, the expectation could be that the model learns some sort of oscillatory pattern to improve switching rates and efficiency, but that requires a setup where the model has an option to probe or judge the parameters – this could either happen by a delivery of an additional observation entry or, through, as mentioned before,

[177] K.-S. Lee, S.-W. Lee, et al., "Threshold current for switching of a perpendicular magnetic layer induced by spin Hall effect".

[178] Here, the values were uniformly sampled from a given interval.

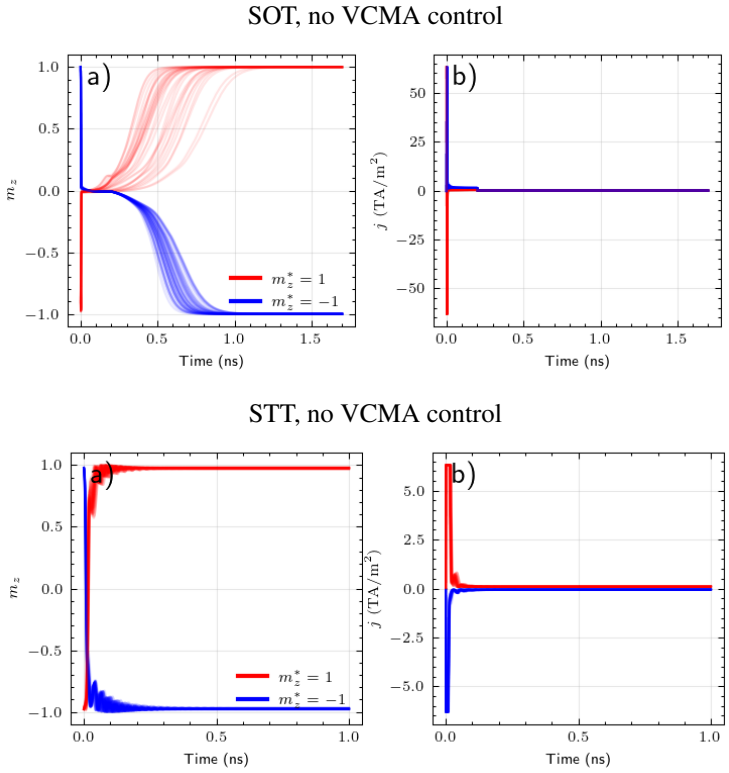

Figure 43: Overall comparison 100 assembled trajectories of the SOT and STT configurations. Magnetisation state over the switching period is shown in (a) and the corresponding current densities in (b). In the SOT configuration, the controller opts for two-stage current impulse to speed up magnetisation alignment with the target state. In the STT configuration, the model learns a single impulse, but of more shaped structure. Note that the current scales and time scales are different in each configuration. $\vartheta = 0.1$

a 'probing' stage preceding the control stage. Furthermore, as we mentioned, the duration of a metastep and the controller current density range also play an important role in the learning process. From an energy perspective, for successful switching, enough energy must be supplied to the system, not only exceeding the critical current, but also the minimal duration of the impulse. If the number of meta-steps is large, but they are short, the complexity of the problem for the model increases, and it is only aggravated by the increase in the controllable range of the current. Suppose a theoretical current threshold of 80% of the maximum range $j_c = 0.8 j_{\max}$, a minimum pulse duration of 0.2 ns. Given a metastep of 1 ps, the model needs to learn to more or less consecutively apply the current at least above threshold for 200 steps in a row. The number of possible combinations becomes enormous if we additionally take into account the variation in magnetic parameters. In conclusion, we find that for the STT configuration, a meta-step duration of 0.8 ps, and a current exponent $x \in (10, 12.9)$ yield repeatable learnable models. In the SOT setup, the polarisation vector is set along the y direction, which necessitates that the current density drops nearly to 0 so that the magnetisation can relax to a stable state. Because of that, the relaxation seems to also take longer, which necessitates slightly longer meta-simulation steps. Therefore, we use $x \in (11, 13.8)$ and, at minimum, 0.8 ps. We note that the temporal resolution is impractical in the real world, but it represents the *lower bound* of what the control algo-

rithms presented in this section can handle. For real-world application two sets of critical values must be established: (i) the controller resolution, that is, the minimal interval between successive control inputs (for example, the minimal time between a registered change in current from j_t to $j_{t+\Delta t}$), and (ii) the minimal resolution of the output quantity, in this case the resistance or voltage. Optionally, to keep the two timescales at comparable levels, one could take the maximum of (i) and (ii), and apply an estimator to the quantity with a finer resolution, for example by averaging the signal. Reward shaping

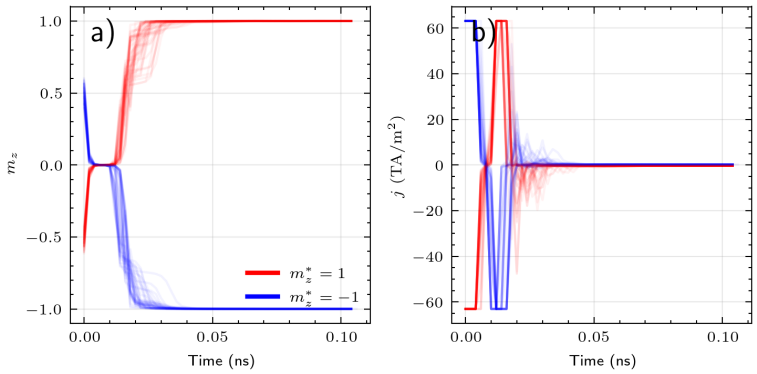

Figure 44: Sample trajectories from a controller that learnt a double impulse strategy for switching.

poses another challenge in this environment. Unlike the spintronic oscillator environment, the standard shaping signal, the alignment component of (100) is a weak signal during control stages due to general bistability of the system, and the terminal reward dominates. As mentioned in the previous subsection, good shaping speeds up training and can potentially improve stability. We tested two strategies that aim to increase the learning speed: directional current reward and progress reward. The former rewards the model for applying the current in the correct direction (positive or negative) given the target state. The progress reward applies a small positive reward each time the magnetisation is pushed towards the target state which depends on the change in the distance to the target:

$$\mathcal{R}_{\text{prog.}} = \zeta_{\text{prog.}} \left(|m_z^* - m_{z,t-1}| - |m_z^* - m_{z,t}| \right) \tag{102}$$

However, neither of those strategies caused any substantial increase in training speed. Instead, we continuously keep a N-element buffer of metastep errors, and if all elements fall within ε_0, the evaluation period is initiated, which shortens the reward horizon, but disadvantages the model in learning to zero the current output after observing a successful switch. Contrary to what we observed in the spintronic oscillator environment, the PPO algorithm yielded a faster convergence to a good success rate and produced stable switching results. There are two potential reasons for this behaviour: one, the PPO should converge faster than SAC because of its direct policy optimisation focus in the environment where sample efficiency is not that relevant. Second, the

CIMS environment has a much narrower space of successful trajectories, and the reward landscape is rather sparse. Therefore, entropy-driven exploration of SAC and off-policy learning offer no advantage and may actually slow down the learning process.

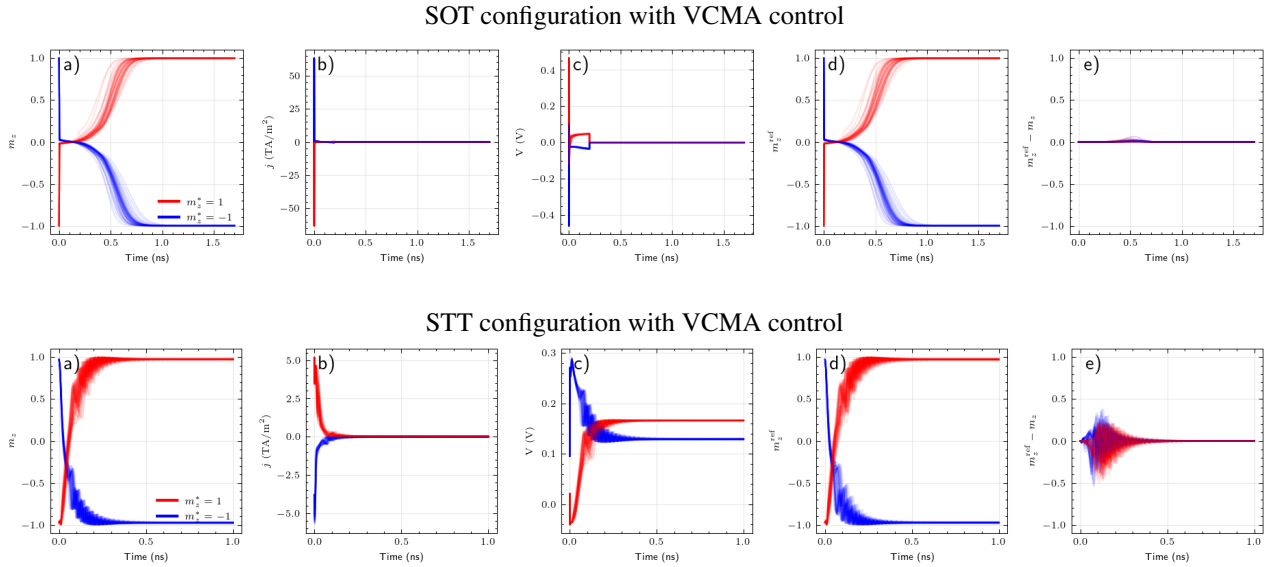

Figure 45: Overall comparison 100 assembled trajectories of the SOT and STT configurations, with additional VCMA control. The magnetisation state over the switching period is shown in (a) and the corresponding current densities in (b). $\vartheta = 0.1$ and δK is linear in V. The first column (a) presents the m_z trajectory with VCMA on, the second, (b) shows the current applied by the controller, and the third, (c), the voltage. The fourth column (d) shows the trajectory of a reference device that does not use VCMA, but was simulated under the same current trajectory as the VCMA device, and the last panel (e) shows the difference between the m_z trajectory of the reference device and the VCMA device.

Having studied the base case, we move on to the VCMA control which we will apply to both our configurations. We note that independent, simultaneous voltage and current control is not practically possible in the STT setup, yet as a means of comparison, it is included in the simulated cases. In the SOT configuration, we anticipate, based on (64), that the controller should prefer to apply the maximum possible voltage to lower the anisotropy, thus reducing the theoretical critical current. To our baseline reward from (100), we add the term linearly dependent on the voltage change that represents the current flow:

$$\mathcal{R}_t = \zeta_{\text{energy,j}} |a_t^j|^2 + \zeta_{\text{energy,V}} (a_{t-1}^V - a_t^V) + \zeta_{\text{align.}} |m_z^* - m_{z,t}|^2 + \hat{\mathcal{R}}_{\text{term.}} \quad (103)$$

where a_t^V is the voltage action component of the controller at time t. If, instead, it is preferred to avoid large voltage values, not just change, then the term $\zeta_{\text{energy,V}} (a_{t-1}^V - a_t^V)$ can be substituted with the component analogous to the current control: $\zeta_{\text{energy,V}} |a_t^V|^2$. The result of learning with the VCMA control is shown in Fig.45. While for the SOT configuration there is no visible advantage to learning with V control, the STT setup slightly benefits

by reducing the current density impulse amplitude. This is probably due to the agent having difficulty in properly learning VCMA application in a timely fashion, that is, lowering the anisotropy barrier before initiating the impulse current rather than attempting both at the same time.

When comparing both the VCMA control and the baseline, the agent prefers to induce short-term current bursts, which in effect resembles the standard impulse excitation used in CIMS. The short time scale is due to the macrospin assumption, which underestimates current densities, but is not uncommon in similar modelling scenarios involving microspin approaches[179]. Additionally, the RL agent autonomously learns to set both the voltage and the current to 0 after having observed that the target position has been attained. This behaviour is achieved by balancing the energy and the alignment reward.

[179] Ender, Lacerda De Orio, et al., "Reinforcement learning to reduce failures in SOT-MRAM switching".

Chapter summary

The chapter introduces the field of reinforcement learning with specific applications to spintronic devices. Fast simulation times enabled by efficient implementation in CMTJ offer tremendous opportunities to facilitate this kind of research. The examples given so far are based on the simulation alone, but further research should focus on the on-hardware implementation of the trained agents, with potential prior fine-tuning. Designing more intelligent devices can shorten the time to market of potential spintronic devices, for example, via efficient optimisation of the input controls, which we have shown with the synchronisation example. In terms of simulation, the next step could concentrate on optimising micromagnetic models such that they too could be easily integrated into the RL training procedures; at the moment, this is computationally challenging, as such training requires thousands, if not millions, of simulations per training run. Additionally, more effort can be directed towards creating more realistic simulations by taking into account device and measurement limitations with a greater degree of fidelity. For instance, during our simulations, although we include a relatively small parameter dispersion, little to none experimental noise is assumed. Those assumptions can be addressed in the RL context as well, but require meticulous revision when discussing a specific experimental setup.

Summary and outlook

This thesis presents contributions to the large-scale modelling of multilayer spintronic devices. With a rapid increase in general-purpose computational power, we anticipate that the methods discussed in this thesis will soon become computationally feasible on personal computers also in the micromagnetic setting. However, at present, our focus is on providing tools and techniques to help the community achieve faster device design iterations, simplify parameter fitting, and streamline the theoretical workflows required to reproduce experimental results. This goal is particularly evident in the first two contributions: Mojsiejuk, Ziętek, Grochot, et al. ("cmtj") and Ziętek, Mojsiejuk, et al. ("Numerical model of harmonic Hall voltage detection for spintronic devices"), which open-source the simulation software and provide easy-to-use recipes for reproducing various numerical models corresponding to known experiments. The utility of these solutions was then demonstrated and elaborated in subsequent chapters, notably in Modelling spin Hall devices and Modelling magnetic tunnel junctions, highlighting the explanatory capabilities of the methods when applied to numerically complex systems.

Another exciting research direction emerges from the final contribution that employs methods developed within reinforcement learning to spintronics. As outlined in the chapter Dynamic control of devices, automating processes via real-time control of multiple device implementations may facilitate their industrial adoption, addressing a persistent challenge common to various scientific disciplines.

The subchapter of Modelling magnetic tunnel junctions discusses 1/f noise with a similar intention. Capturing the nature of this noise numerically has a broader potential, as identifying operating points with optimal signal-to-noise ratios has been an ongoing difficulty for nearly a century in classical electronics. The ability to incorporate the noise as an extra field contribution may lead to more realistic and accurate device simulations.

Appendix

Estimate of the MLS gap

To complement the simulation-based discussion on the introduction of the β parameter, we now derive a semi-analytical calculation for the bounds of the non-zero δ_{MLS} gap. In a numerical sense, the asymmetry is defined as a discrepancy between the AHE resistances between two Co-Pt interfaces that make up the structure. As per the diagram in Fig.46, we denote a state $s_{XY}^{+/-}$ as a state of m_X on the Y side of the hysteresis, because we are concerned only with the edge states (left, right) for both magnetisations. We compute the resistance (R_{XY}) of the hysteresis in the state of the left or right edge (the leftmost and rightmost value) as: $R_L^+ = s_{00}^+ + \beta s_{10}$ and $R_R^+ = s_{01}^+ + \beta s_{11}$ respectively, for the positive field (the negative field has the same, but we swap the superscript $+ \to -$).

For state separation δ_{MLS}, we are concerned only if the left (right) state in positive $\mathrm{H_{ext}}$ is above the left (right) state in negative $\mathrm{H_{ext}}$. Alternatively, we are allowed to swap the inequality, saying that the state at the left (right) state at the positive field is below that at the negative field. Assume that the positive field hysteresis is to be above the negative field hysteresis:

$$R_L^- < R_L^+ \wedge R_R^- < R_R^+$$
$$\text{starting with: } R_L^- < R_L^+$$
$$s_{00}^- + \beta s_{10}^- < s_{00}^+ + \beta s_{10}^+$$
$$s_{00}^- - s_{00}^+ < \beta (s_{10}^+ - s_{10}^-)$$
$$\text{which produces:}$$
$$\beta > \frac{s_{00}^- - s_{00}^+}{s_{10}^+ - s_{10}^-}, \text{ if } (s_{10}^+ - s_{10}^-) > 0$$
$$\beta < \frac{s_{00}^- - s_{00}^+}{s_{10}^+ - s_{10}^-}, \text{ if } (s_{10}^+ - s_{10}^-) < 0$$

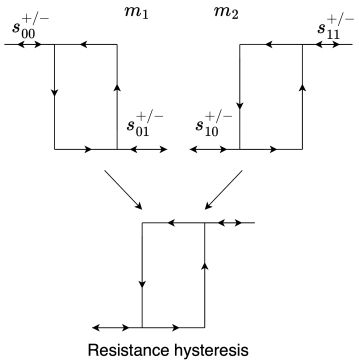

Figure 46: Diagram of switching. The top two hysteresis are magnetisation trajectory switching for each current density that composes the final resistance hysteresis. The picture is given for a specific value of $\mathrm{H_{ext}}$. Arrows indicate the current sweep direction.

likewise, for $R_R^- < R_R^+$:

$$
\begin{aligned}
s_{01}^- + \beta s_{11}^- &< s_{01}^+ + \beta s_{11}^+ \\
s_{01}^- - s_{01}^+ &< \beta (s_{11}^+ - s_{11}^-) \\
\beta &> \frac{s_{01}^- - s_{01}^+}{s_{11}^+ - s_{11}^-}, \text{ if } (s_{11}^+ - s_{11}^-) > 0 \\
\beta &< \frac{s_{01}^- - s_{01}^+}{s_{11}^+ - s_{11}^-}, \text{ if } (s_{11}^+ - s_{11}^-) < 0
\end{aligned}
$$

The reverse condition (i.e., where the negative-field hysteresis exceeds the positive) can be derived by inverting the inequality signs. The state separation

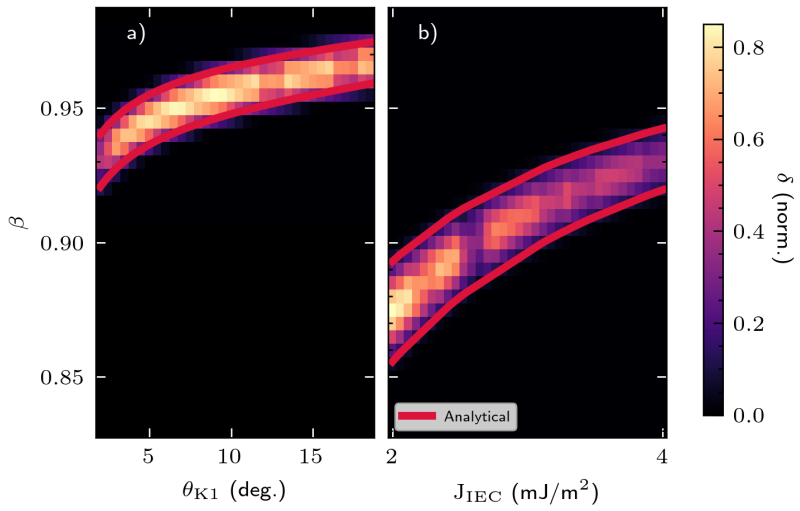

Figure 47: Solid red line follows analytical determination of β (AHE asymmetry) from conditions on $\delta_{\text{MLS}} > 0$. (a) state separation according to the anisotropy polar angle θ_{K1} and β, (b) state separation as a function of J_{IEC} and β. The δ_{MLS} is normalised respective to a maximum value. There is a clear gap size divergence from the centre of the gap interval – the gap gets smaller as it nears the red analytical line.

is thus defined as:

$$
\delta_{\text{MLS}} = \min\{R_L^+ - R_L^-, R_R^+ - R_R^-\} \tag{104}
$$

subject to constraint above on β. The existence of state separation will depend on the fact that β can be found such that it satisfies the condition for $R_L^- < R_L^+ \wedge R_R^- < R_R^+$. Fig.47 depicts ranges of β, θ_{K1} (a) and β, J_{IEC} (b) producing non-zero δ_{MLS}. The red line comes from the analytical calculation of δ_{MLS} given a set of $(m_{z+}^{(1)}, m_{z+}^{(2)}, m_{z-}^{(1)}, m_{z-}^{(2)})$ states, with the subscript denoting positive or negative H_{ext}.

Coupled current for the in-series configuration of STOs

In our research, we have considered two models: one as discussed in Numerical modelling of electrical in-series coupling, and the other where the current strictly follows Kirchoff's current law (KCL) and is the same for both MTJs, that is,

$$j_{\text{total}} = j_0 + j_0\chi(\mathbf{m}_{\text{L}} \cdot \mathbf{p}_{\text{L}} + \mathbf{m}_{\text{R}} \cdot \mathbf{m}_{\text{R}}) \tag{105}$$

where j_0 is the baseline current and j_{total} is the current flowing in the circuit. Generally, after assuming (105), the simulation results are qualitatively the same, and for comparison, we show the reproduction of Figs.24 and 27; see Figs.48 and 49, respectively. In those figures, we only modified the value of χ so that the synchronisation regions have a size similar to that in Fig.24.

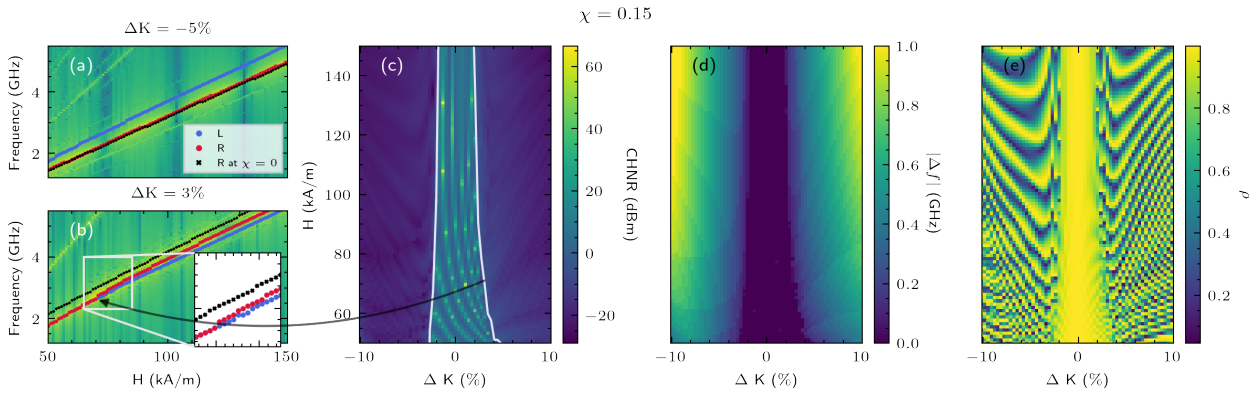

Figure 48: Reproduction of Fig.24 from the manuscript with j_{total}. The $\chi = 0.15$, a smaller value than the one in the manuscript to bring the regions to a scale similar to that in the original figure. (b) panel has also been adjusted to show the desynchronisation field at $\Delta K = 3\%$. The remaining parameters are preserved exactly as per Fig.24.

The major difference is the smaller asymmetry towards larger ΔK which is directly related to the fact that the oscillation mode of L stays fixed, and thus the order of MTJs in the in-series configuration plays a more significant role. However, in the case presented here, the asymmetry is still visible, especially if we enlarge the regions by increasing χ, and it is similarly skewed towards positive ΔK. Regardless of the specific details of the coupling mechanism, the key factor behind the proposed *desynchronisation* still lies in the asymmetry in magnetic parameters between the two coupled oscillators, a condition that remains the same in both cases discussed.

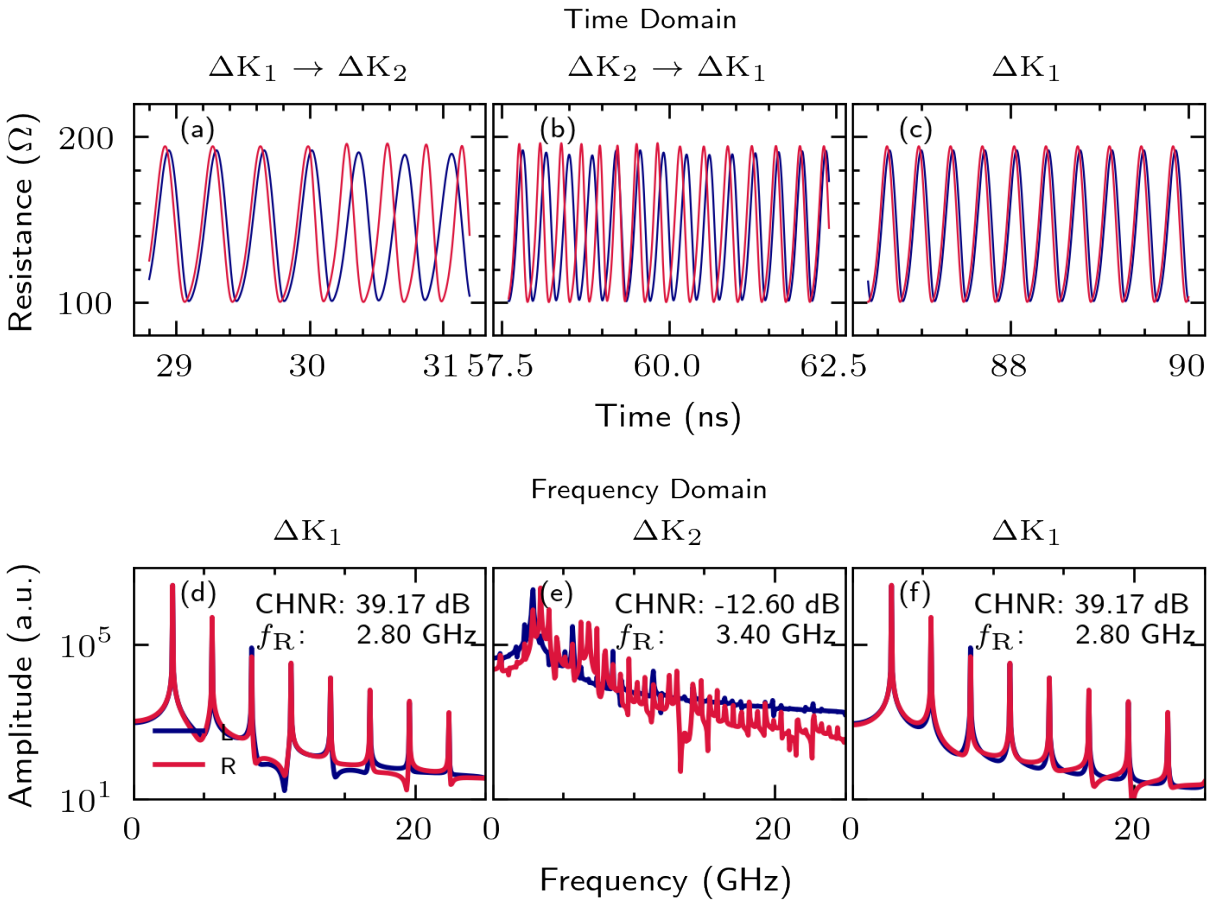

Figure 49: Reproduction of Fig.27 from the Numerical modelling of electrical in-series coupling, but with strict preservation of KCL, with j_{total}. $\chi = 0.1$, all the remaining parameters as in the original figure.

Additional Tools and Interfaces for CMTJ

For a description of the full range of CMTJ, together with comprehensive simulated examples, the reader is encouraged to visit the package documentation at https://lemurpwned.github.io/cmtj/. In this section, we briefly discuss some of the additional tooling that enhances the CMTJ library.

Web interface

Built with the Streamlit framework, the web interface enables quick and intuitive parameter fitting using standard measurement techniques such as VSD or PIMM. It offers a user-friendly interface, specifically designed for experimentalists who might have limited experience with simulation software. Users can access the application directly from the Web browser at https://cmtj-app.streamlit.app and run simulations without requiring software installation or dependency management. The interface allows users to adjust the number of layers and their basic magnetic and geometric parameters, change the system's excitation type, and modify field or frequency scanning parameters.

Agentic package helper

In addition to the WebUI, we also provide a large language model (LLM) agentic system that can help the user navigate the world of macrospin simulations. The code is available at https://github.com/LemurPwned/cmtj-cursor. Fig.50 shows the high-level overview of the agent with four categories of nodes: standard non-LLM nodes (blue), LLM nodes (green), tool nodes (red), and data nodes (purple). As the user query enters the flow, it is first classified – the system determines whether the user asks for code or asks a general question about simulations or spintronics. If the input is classified as a question, the subquery generator node produces up to three additional questions to broaden the search scope. Then a vector search is performed on the local index of the spintronics literature. Optionally, web search results can be included, but the article search is always preferred by the response synthesis model. If the user input asks for code, the flow is transferred to a planning agent that has access to a range of tools: *code search*, *documentation search*, and *code validation*. The code search is performed on the CMTJ repository and a set of curated simulation examples. *Docstring search* is a special index that parses function signatures and class documentation. Such a search enables partial keyword matching across the parsed fields. Finally, there is a code validation and fixing loop, where the *Validate code* first compiles and runs the code and the *Fix code* attempts to fix any simple errors before handing it over to the main agent again for further processing. When the code agent completes the generation, it calls the LLM to prepare the final user-friendly response. The code generation agent with tool calling

benefits most from reasoning models, whereas the remaining LLM nodes do not require such capabilities.

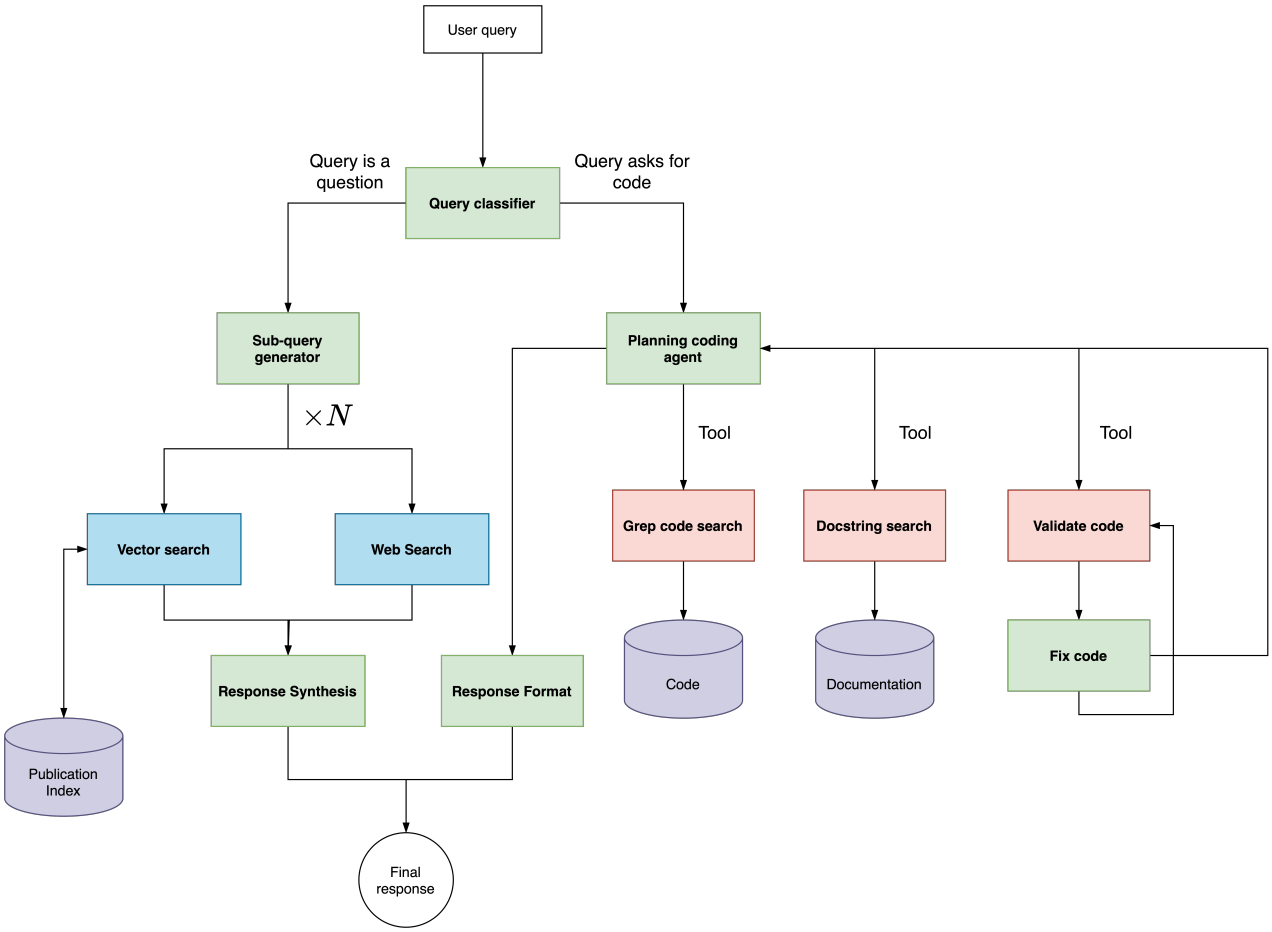

Figure 50: A layout of the LLM Q&A and code agent. Green denotes LLM nodes, blue non-LLM nodes, red denotes the *tool* nodes, and document databases are shown in purple.

Magnetization dynamics driven by displacement currents across an MTJ

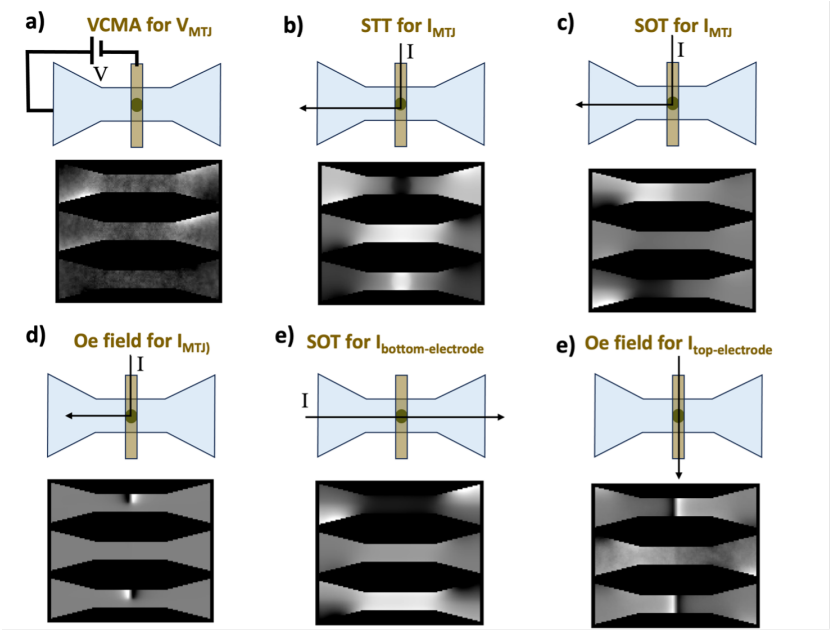

Figure 51: 'Micromagnetic simulation showing the expected magnetization dynamics in the bottom electrode if (a) voltage across MTJ leads to VCMA, (b) current through MTJ gives STT, (c) SOT generated at bottom electrode region where the current flows, (d) Oersted field generated from the top electrode region where the current flows, (e) the current is applied through only bottom electrode generates SOT at the entire bottom electrode, and (f) the current is applied only through top electrode leading opposite Oersted field along both sides of the top electrode. For each case, the top panel shows the current or voltage configuration, and bottom image consists of 3 snapshots of simulated magnetization dynamics at time=maximum, minimum and zero nodes. The black and white contrast corresponds to magnetization variation along +Z and -Z directions respectively'. Figure sourced from appendix of Safeer, C., Keatley, P. S., (Aug. 2024). "Magnetization dynamics driven by displacement currents across a magnetic tunnel junction". In: *Physical Review Applied* 22.2, p. 024019.

Although relevant to the topics discussed in this dissertation, we placed the description of the simulations from Safeer et al.[180] in the Appendix due to their micromagnetic nature. The structure described in that work consists of an MTJ pillar (CoFeB/MgO/CoFeB) placed atop a W substrate. The purpose of the simulations was to explain the origin of the magnetisation dynamics observed in the experiment. In total, six alternatives were considered: excitation via the VCMA across MTJ leads (mostly, through the top layer), the STT through the MTJ, the SOT generated in the bottom electrode (W) or top electrode (Pt), the Oersted field from the top electrode (Pt), and bottom electrode (W). All of these options are shown in the top diagrams of Fig.51. We simulated the corresponding cases with Mumax3[181], taking the approximate magnetic parameters from the work. The particular strip geometry was replicated in the simulation using cutout geometry, we set the cell size at 2 nm, $A = 13\,\mathrm{pJ\,m^{-1}}$. The following is an excerpt from the publication that describes in detail the simulations conducted to pinpoint the mechanism responsible for the magnetisation dynamics patterns observed in the experiment.

> At first, we induce magnetization saturation by applying an in-plane field, By = 75 mT. For each excitation type, we use the RF signal in the GHz range 3-9GHz (depending on what the system responds best to) and take snapshot at maximum, minimum and zero nodes as shown in Fig.51. In the VCMA

[180] Safeer, Keatley, et al., "Magnetization dynamics driven by displacement currents across a magnetic tunnel junction".

[181] Vansteenkiste, Leliaert, et al., "The design and verification of MuMax3".

simulation, we lower the By field to 1 mT, and increase the anisotropy to better capture the excitation via the RF signal. In the STT and VCMA simulations (Fig.51 a-b), we excite the system exclusively in the center, where the circular MTJ pillar meets the FM layer. Similarly, for the case (c, bottom), where the system is excited with the current flowing through the top electrode and then through the pillar, we model SOT excitation only in the left half of the geometry.

Following the results of the simulation, the conclusion was reached that the Oersted field (as shown in Fig.51e) best replicates the experimental observation.

Sample fabrication process

For completeness sake, we include a short mention of the fabrication techniques of the spintronic devices in question. Most of the multilayer thin film samples, of which numerical fits are presented in this work, were prepared by Singulus, the Advanced Institute of Industrial Science and Technology (AIST) and the Institute Molecular Physics of the Polish Academy of Sciences. In most cases, samples were deposited using the magnetron sputtering technique on thermally oxidised silicon wafers. The samples were then patterned in the cleanrooms of the AGH Academic Centre for Materials and Nanotechnology.

The deposition method depends on the target type; most commonly, metallic layers are stacked onto an oxidised silicon wafer using magnetron sputtering. In this technique[182], a gas[183] is pumped into a vacuum chamber where the target material is located in the cathode and the substrate in the anode. The magnetrons create shaping magnetic fields that, combined with a high electric field, trap electrons into circular paths close to the target. This process increases the ionisation efficiency of the gas and leads to the creation of high-density plasma regions at the cathode. Consequently, a high kinetic impact of the ions knocks out the target material particles that eventually deposit at the substrate. Quite often, as a method of streamlining the measurement process, the sample is prepared in the form of a wedge with varying thicknesses of critical elements in the stack. For instance, later sections discuss the Co/Pt/Co interfaces, where the Pt thickness is varied. This is achieved by slowly moving the wafer at a constant deceleration rate under the sputtering target and at a constant deposition rate[184]. Other techniques such as MBE[185,186] are also common in the MTJ fabrication process. MBE is based on the epitaxial growth of deposited vapour particles released from so-called K cells[187] that contain the target material. Usually, the growth rate and its quality can be monitored using the accompanying RHEED[188] technique. Alternatively, AFM targets such as NiO can be deposited using PLD[189], wherein a strong pulse-gated laser beam incident on the target causes the plasma plume to be kinetically ejected towards the substrate and film growth.

After the deposition process, micro- and nanofabrication is performed at the Academic Centre for Materials and Technology of AGH University using optical or electron lithography, ion-beam milling, and the lift-off process. The first of those steps involves coating the sample with a negative photoresist[190] – this usually occurs by means of a spin coating, with the photoresist uniformly spreads on the substrate as a result of a high but constant spinning rate of the sample. After the sample is annealed, the lithography mask is imprinted, for example, using an adapted SEM[191] and then etched, often with the ion milling method[192]. After the etching stage, the Ti/Au contact layers are deposited and then, during the lift-off process, the positive photoresist is removed along with the redundant conducting layers atop.

[182] Swann, "Magnetron sputtering".

[183] usually a noble gas such as Argon or Xenon

[184] as an example, given 6 cm distance between the target and the substrate, the deposition rate of wolfram at 4 W is about $0.01\,\mathrm{nm\,s^{-1}}$

[185] molecular beam epitaxy

[186] Singh, Bhardwaj, et al., "Fabrication of Magnetic Tunnel Junctions".

[187] Knudsen cells

[188] reflection high energy electron diffraction

[189] Pulsed Laser Deposition

[190] a negative photoresist hardens after exposure to the UV light, making it resistant to etching. In contrast, a positive photoresist becomes easily solvable in the etching solution after it has been exposed to UV light

[191] scanning electron microscope

[192] dry etching process in which high energy ions kinetically knock off the unmasked material. Plasma is usually generated using a strong RF field

Numerical model of harmonic Hall voltage detection for spintronic devices

Sławomir Ziętek,[1,*] Jakub Mojsiejuk,[1,†] Krzysztof Grochot,[1,2] Stanisław Łazarski,[1] Witold Skowroński,[1] and Tomasz Stobiecki[1,2]

[1]*Institute of Electronics, AGH University of Science and Technology, Aleja Adama Mickiewicza 30, 30-059 Kraków, Poland*

[2]*Faculty of Physics and Applied Computer Science, AGH University of Science and Technology, Aleja Adama Mickiewicza 30, 30-059 Kraków, Poland*

(Received 2 February 2022; revised 28 May 2022; accepted 10 June 2022; published 5 July 2022)

We present a numerical macrospin model for harmonic voltage detection in multilayer spintronic devices. The core of the computational backend is based on the Landau-Lifshitz-Gilbert-Slonczewski equation, which combines high performance and satisfactory agreement with the experimental results in large-scale applications. We compare the simulations with the experimental findings in a Ta/CoFeB bilayer system for angular- and magnetic-field-dependent resistance measurements, electrically detected magnetization dynamics, and harmonic Hall voltage detection. Using simulated scans of the selected system parameters such as the polar angle θ, magnetization saturation ($\mu_0 M_s$), or uniaxial magnetic anisotropy (K_u), we show the resultant changes in the harmonic Hall voltage, demonstrating the dominating influence of the $\mu_0 M_s$ on the first and second harmonics. In the spin-diode ferromagnetic resonance method, the ($\mu_0 M_s$, K_u) parameter space may be optimized numerically to obtain a set of viable curves that fit the experimental data.

DOI: 10.1103/PhysRevB.106.024403

I. INTRODUCTION

The development of novel electronic devices utilizing electron spin for their operation has become an increasingly important branch of science and engineering in the past decade [1–4]. Specifically, taking advantage of both the electron spin and charge creates an opportunity for further miniaturization and increase in the energy efficiency [5] of the electronic devices. However, experimental investigations typically require expensive and time-consuming fabrication processes as well as a unique measurement methodology. Computer-aided optimization of spintronics devices, coupled with the prediction of their electric and magnetic properties, vastly reduces the number of experimental iterations and allows a faster and more efficient prototype device development. In addition, modeling of multilayer devices enables the extraction of parameters that are typically hard to obtain from experiments.

After the experimental discovery of the so-called spin-orbit torque (SOT) [6–12], there have been numerous studies on spin current generation in nonmagnetic materials with high spin-orbit coupling additionally improved by interfacial effects [13,14]. Utilizing SOT may lead to fast magnetization switching [15] and more durable magnetic memory design [16]. To quantify the efficiency of the effect, typically called the spin-Hall angle, one computes the ratio of the spin current to the charge current. In recent years, there has been a sprout in the development of spin-Hall angle measurement techniques such as spin-torque ferromagnetic resonance (ST-FMR) [17], magnetization switching induced by current [18], and harmonic Hall voltage detection [19,20]. The latter method does not require a sophisticated fabrication protocol, nor the determination of additional thermal or high-frequency effects, and allows for the extraction of dampinglike and fieldlike effective fields, from which the spin-Hall efficiencies may be calculated.

In this work, we employ the SOT effect as a basis for the electrical model that simulates the harmonic Hall voltage technique using fieldlike (FL) and dampinglike (DL) SOT torques. Furthermore, we present highly efficient macrospin modeling software for the electrical detection of static and dynamic magnetic properties in multilayer spintronic devices. The software numerically solves the Landau-Lifshitz-Gilbert-Slonczewski (LLGS) equation using a dedicated c++ engine and enables simulations of the magnetization, magnetoresistance, ferromagnetic resonance, and harmonic Hall voltage measurements of the multilayer system simultaneously as a function of the magnetic field amplitude and angle with respect to the anisotropy axis direction. Our model demonstrates good agreement with the experimental data and provides additional insights into different aspects of magnetization dynamics and harmonic Hall measurement.

Moreover, we show the dependence of magnetization, saturation, and anisotropy on the harmonic Hall voltage detection, with the former having a much stronger impact on the final result. The model package, called CMTJ (C++ Magnetic Tunnel Junctions), is provided in both c++ and PYTHON interfaces, along with the hereby described postprocessing steps. As a demonstration of the ease of use and the speed of the model, all simulations conducted in this article may be reproduced within a half-hour on a modern laptop. The simulation scripts along with the simulation package itself are open source; see Ref. [21].

*zietek@agh.edu.pl
†mojsieju@agh.edu.pl

II. NUMERICAL MODEL OF ELECTRICAL DETECTION

A. Theoretical background

First, we present a theoretical model of the magnetization dynamics together with the electrical detection methodology. We adapt the standard Landau-Lifshitz-Gilbert-Slonczewski (LLGS) equation, like presented in, e.g., Nguyen *et al.* [22], into LL form [6], such that it may be implemented in the numerical engine. The LLGS equation itself is given in the form

$$\frac{d\mathbf{m}}{dt} = -\gamma_0 \mathbf{m} \times \mathbf{H}_{\text{eff}} + \alpha_{\text{G}} \mathbf{m} \times \frac{d\mathbf{m}}{dt} - \gamma_0 |H_{\text{FL}}| (\mathbf{m} \times \mathbf{p}) - \gamma_0 |H_{\text{DL}}| (\mathbf{m} \times \mathbf{m} \times \mathbf{p}), \quad (1)$$

where $\mathbf{m} = \frac{\mathbf{M}}{\mu_0 M_{\text{s}}}$ is the normalized magnetization vector with $\mu_0 M_{\text{s}}$ as the magnetization saturation, α_{G} is the dimensionless Gilbert damping parameter, $\mathbf{H}_{\text{eff}}$ is the effective field vector, $\mathbf{p}$ is the polarization vector, and γ_0 is the gyromagnetic factor. The terms representing the magnitude of the H_{FL} (fieldlike) and H_{DL} (dampinglike) torque fields have a concrete connection with the spin-Hall angle and correspond to the DL and FL SOT. See the Appendix for more details on the transition from the LLGS form to the numerically viable LL form. The effective field vector $\mathbf{H}_{\text{eff}}$ is usually composed of various field contributions, which, depending on the context of the simulation, may be added or disabled. The simulation package in question already provides a range of such contributions, including the interlayer exchange coupling (IEC), dipole and demagnetization interactions, magnetic anisotropy, and external magnetic field contribution. In the experimental data, presented in the following sections, we investigate a bilayer (heavy metal/ferromagnet) structure, and thus we may omit IEC and dipole interactions in our simulations. For numeric integration, we employ the higher-order Runge-Kutta method. After each integration step, the $\mathbf{m}$ vectors are normalized to avoid cumulative numerical error. In deciding on the value of the integration step, we usually compromise the computation time and the stability of the numerical solution. For the majority of the simulations, this parameter is in the range of a femtosecond or lower. As a good rule of thumb, it is better to start at a lower value (around 10^{-13} s) and steadily increase it, verifying that the obtained results are still consistent.

B. Modeling of magnetoresistance effects

In our simulations, we can easily compute longitudinal (R_{xx}) and transverse (R_{xy}) magnetoresistance loops for current in-plane (CIP) and current perpendicular to the plane (CPP) configurations [see Figs. 1(d) and 1(e)], as a function of the magnetic field magnitude or angle. To obtain R_{xx} and R_{xy} loops, we adopt a model from [23], given by Eqs. (2) and (3),

$$R_{\text{xx}} = R_{\text{xx0}} + \left(\Delta R_{\text{AMR}} m_x^2 + \Delta R_{\text{SMR}} m_y^2\right), \quad (2)$$

$$R_{\text{xy}} = R_{\text{xy0}} + \frac{1}{2}\Delta R_{\text{AHE}} m_z + \frac{w}{l}(\Delta R_{\text{SMR}} + \Delta R_{\text{AMR}}) m_x m_y, \quad (3)$$

where ΔR_{AMR} and ΔR_{SMR} are the magnitudes of the anisotropic (AMR) and spin-Hall (SMR) magnetoresistances (both in Ω) in the R_{xx} configuration. ΔR_{AHE} is the magnitude of the anomalous Hall effect (AHE) (also in ohms), l is the length, and w is the width of the sample. In the dynamic state, the resistance is calculated as a function of time and then used for the calculation of ST-FMR and harmonic Hall voltages.

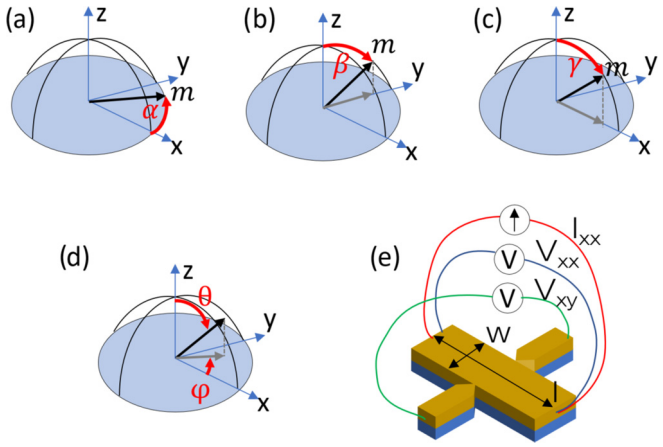

FIG. 1. The reference diagram for measurement arrangements used in this work. (a)–(c) The angles α, β, γ used in simulations and experiment in the saturating field. The angle θ is taken to be the polar angle and ϕ is the azimuthal angle (d). (e) The application of the voltmeter in the measurement.

C. Spin-diode ferromagnetic resonance (SD-FMR)

In addition to the inductive and optical magnetometry methods, SD-FMR has proven to be a powerful experimental tool in the study of magnetization dynamics in microwave spintronic devices such as oscillators or detectors [24]. When the alternating current (AC) is passed through a magnetoresistive element, it generates small changes of magnetization driven by secondary effects of the Oersted field, spin transfer torque (STT), or SOT, which finally lead to the oscillations of resistance [25]. Mixing of the AC and oscillating resistance gives rise to the mixing voltage, which has both direct current (DC) and AC components at the first ($f' = f$) and second ($f' = 2f$) harmonic frequency. Those components may be extracted with different filters in the postprocessing step. For SD-FMR, this DC component is called the V_{DC} voltage and, in the experiment, it is separated from the AC components using a bias-T filter [26,27].

In the simulation setup, we compute V_{DC} analogously to the experiment: a sinusoidal current I_{RF} with microwave frequency f is applied along the x axis, which in turn generates a tangent Oersted field H_{Oe}. This guides oscillations of the magnetization and time-varying resistance, $R_{\text{xx}}(t)$ and $R_{\text{xy}}(t)$. Multiplying the sinusoidal current excitation and the resistance produces a voltage $V(t)$, that akin to experiment, has the DC and AC components. To separate the DC component, we filter the voltage signal with a digital low pass filter (LPF). Taking a mean of the LPF-filtered voltage signal yields one V_{DC} value for each magnetic field and frequency.

D. Harmonic Hall voltage detection

We determine the spin torque components with harmonic Hall voltage measurements in the low-frequency regime. The

established methods use either magnetic field dependence [19] or angular dependence [28] to analyze the first and second harmonic Hall voltage signals under AC (below the resonance frequency) excitation. CMTJ simulates these two approaches by extending the previously described SD-FMR method with a simple computation of phase and amplitude in the first and second harmonic, for the R_{xy} configuration. For low-frequency regimes, when the magnetization vector does not undergo large-angle variations, the results happen to be sufficiently close.

In our simulations, we follow the SOT formulation as described in Eq. (1). At a low frequency, below the resonance, we perform a field scan, where at each field step the system is excited with a sinusoidal torque signal, with separate amplitudes for damping- and fieldlike torques. We compute the R_{xy} magnetoresistance using Eq. (3), and calculate the fast Fourier transform (FFT) of the mixing voltage signal to obtain the amplitude and phase. We remove the offset from the experiment and simulation data for the first harmonic, and we convert the second harmonic phase from radian to voltage. Then, following the lock-in [29] operation, we first take the cosine of the simulated phase and then multiply by the amplitude of the signal at that second harmonic. In such a way, we obtain the amplitudes consistent with what we get from the experiment, while keeping all simulation parameters realistic (layer parameters, applied current density, and torques come well within the range observed during the experiment measurement).

III. RESULTS

We now turn to a comparison of numerical simulations conducted using CMTJ with the experimental results obtained on the Ta(5)/CoFeB(1.45)/MgO(2)/Ta(1) structure (thickness in nanometers). The system has been patterned into Hall bars, enabling both static and low-frequency longitudinal and transverse resistance measurements as well as magnetization dynamics characterization using the SD-FMR technique. The Ta underlayer was chosen such that it generates significant SOT and SMR [30]. The selected CoFeB thickness results in net perpendicular anisotropy induced by the dominating interfacial anisotropy component. For low-frequency R_{xx} and R_{xy} measurements, the excitation voltage was fixed to 1 V. High-frequency measurements were performed with the radio frequency (rf) signal of power $P = 16$ dBm. The details of the sample fabrication are presented in Ref. [31].

The process of numerical harmonic detection is composed of several steps. First, we compute the magnetoresistance parameters that will serve as a basis for our further simulations. In particular, we use our model to fit the magnetoresistance parameters using the angular dependencies of the resistance in the saturating magnetic field. This permits us to determine the resistance values: AMR, SMR, and AHE. Then, we obtain the magnetization, saturation, and magnetic anisotropy from the R-H loops. In the next step, we simulate the SD-FMR maps for the R_{xx} and R_{xy} configurations using previously determined parameters. We compare them with the dispersion relations from the SD-FMR measurements for those two electrical configurations. Finally, using all the parameters that were determined in the previous steps, we reproduce the first and second harmonics measurements.

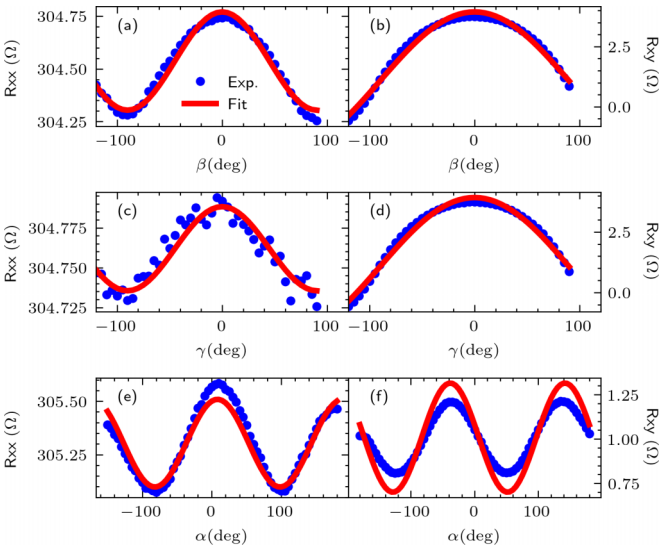

FIG. 2. Comparison measurements and simulations for (a),(c),(e) R_{xx} and (b),(d),(f) R_{xy} at the rotations of the saturating magnetic field in α, β, and γ angles. Experimental results are marked with blue dots; red lines represent simulation.

A. Resistance measurement

To determine the magnetoresistance and magnetic parameters of the investigated sample, we perform a series of angular measurements in the saturating magnetic field and field scans at preset directions. Angular dependencies of R_{xx} and R_{xy} measured at magnetic field of 1 T sweeping at α, β, and γ angles are shown in Fig. 2. The red line represents the results obtained from the numerical model, with electrical parameters listed in Table I. A small discrepancy from a perfect sine waveform may be caused due to the FM layer being not fully saturated.

Figure 3 shows the experimental results of R_{xx} and R_{xy} as a function of magnetic field applied along an xy plane at 0° and 45°. Corresponding simulations reproduced by CMTJ are depicted as red lines in the same figure. The higher switching field in the simulated loops observed for the $R_{xy}(H)$ dependency may be explained by the thermally activated magnetic domain switching [32] that we did not take into account in this version of the model. The following parameters

TABLE I. Optimal parameters used in the simulations.

Parameter	Value	Unit
$\mu_0 M_s$	0.525	T
K_u	0.154	MJ/m^3
α_G	0.03	
t_{FM}	1.45	nm
ΔR_{SMR}	−0.464	Ω
ΔR_{AMR}	−0.053	Ω
ΔR_{AHE}	−5.71	Ω
w	30	μm
l	20	μm
$\lvert H_{DL}\rvert$	420	A/m
$\lvert H_{FL}\rvert$	574	A/m

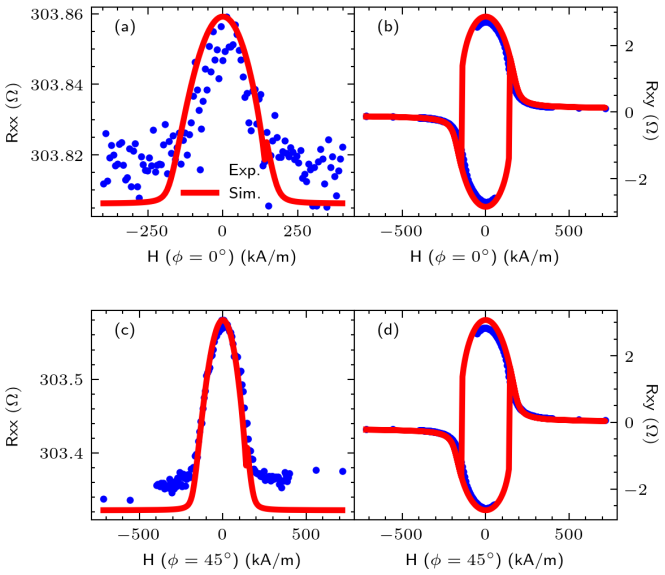

FIG. 3. Comparison measurements' data points and simulations for (a),(c) R_{xx} and (b),(d) R_{xy} at sweeps of the in-plane ($\theta = 90^\circ$) magnetic field at $\phi = 0^\circ$ and 45°. Blue connected dots indicate the experimental results, whereas the solid red line represents simulation results obtained with CMTJ.

reproduce experimental findings to a good degree of precision: the saturation magnetization $\mu_0 M_s = 0.525\,\mathrm{T}$, the nominal thickness of CoFeB (t_{FM}) of 1.45 nm, the magnetic perpendicular anisotropy $K_u = 0.154\,\mathrm{MJ/m^3}$, and resistance parameters of $\Delta R_{AMR} = -0.053\,\Omega$, $\Delta R_{SMR} = -0.464\,\Omega$, and $\Delta R_{AHE} = -5.71\,\Omega$, all summarized in Table I for convenience.

B. Magnetization dynamics

The magnetization dynamics was measured using the SD-FMR technique with a fixed RF power of 16 dBm, frequency between 1 and 18 GHz, and a magnetic field swept between 0 and 600 kA/m. An example of the measured and simulated spectra for the transverse and longitudinal magnetoresistance measurement configurations is presented in Fig. 4. In Fig. 4, we also plot the individual resonance modes of both configurations (R_{xx} and R_{xy}) in a selected range of higher frequencies (12–16 GHz), then depicted for the whole frequency range in the form of dispersion relations in Fig. 5. Generally, the half widths as well as the resonance peaks of the simulated runs (the dashed red line) remain in good agreement with the experiment marked with colored dots. The colored lines represent the Lorentz fit, which was computed with the following formula:

$$V_{DC}(H) = A_S L + A_A D, \tag{4}$$

$$L = \frac{\Delta H^2}{(H - H_r)^2 + \Delta H^2}, \quad D = \frac{\Delta H (H - H_r)}{(H - H_r)^2 + \Delta H^2}, \tag{5}$$

where A_S and A_A are amplitudes of the symmetric and antisymmetric components of the resonance line, H_r is the resonance field, and ΔH is the linewidth.

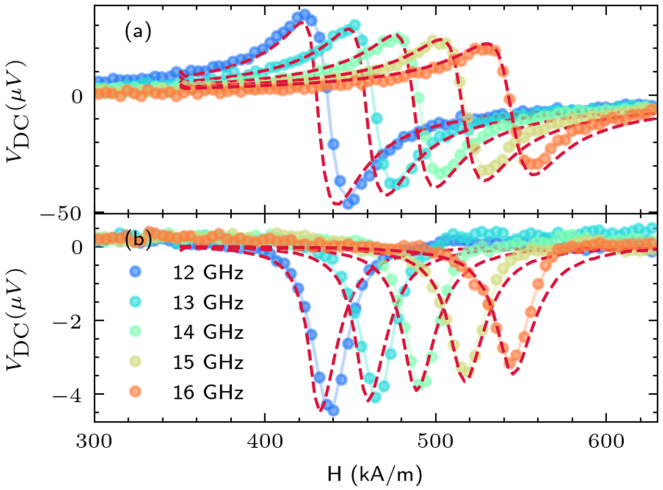

FIG. 4. Examples of V_{DC} voltage measured as a function of external magnetic field applied in plane ($\theta = 90^\circ$) measured at (a) R_{xy} (H applied at $\phi = 0^\circ$) and (b) R_{xx} (H applied at $\phi = 45^\circ$) electrical configuration for frequencies ranging from 12 to 16 GHz. Colored points are experimental data; the Lorentz fits to (4) are marked with a solid line of the same color. Simulations corresponding to each frequency are marked with red dashed lines; for the R_{xx} configuration, the current was 0.4 mA, while for the R_{xy} one, the current was 0.75 mA. Finally, we get the best agreement with $\alpha_G = 0.03$, and the other simulation parameters follow Table I.

C. Harmonic Hall detection

In the experimental setup, we are primarily interested in measuring the effective torque efficiencies (ξ), for both the DL and FL. Those efficiencies may be easily calculated given the values of H_{DL} and H_{FL} fields at a current density j_e [22],

$$\xi_{DL/FL} = \frac{2e\mu_0 M_s}{\hbar} \frac{t_{FM} H_{DL/FL}}{j_e}, \tag{6}$$

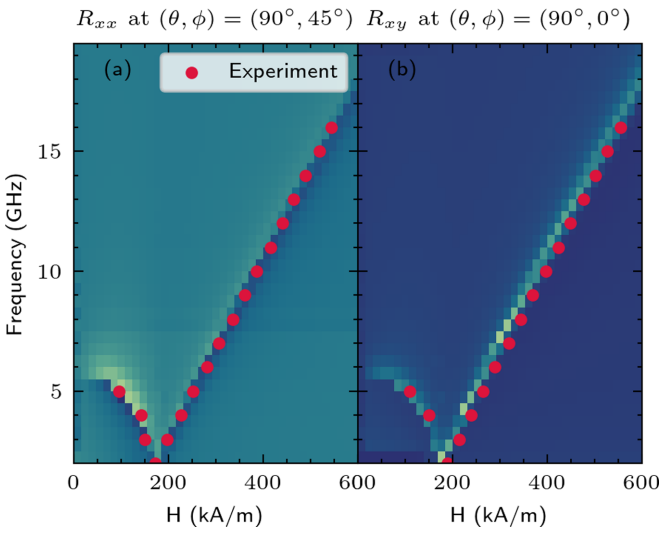

FIG. 5. Dispersion relations of SD-FMR measurements for (a) longitudinal and (b) transverse. Red dots represent the experimental relations of the dispersion obtained for both configurations.

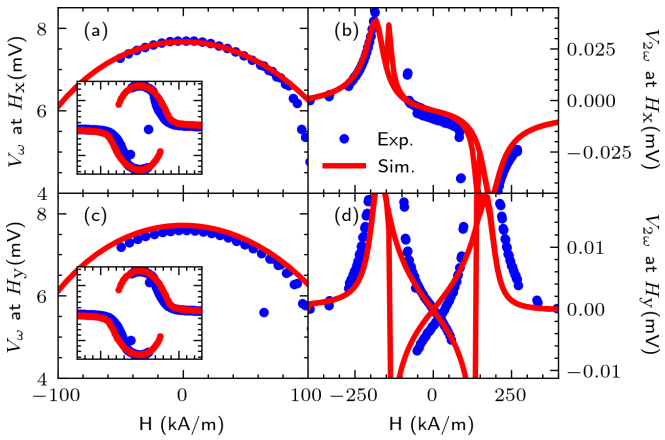

FIG. 6. The best fit for first and second harmonics in the following arrangements: (a),(b) H_x with $\theta = 90^\circ, \phi = 0^\circ$ and (c),(d) H_y with $\theta = 90^\circ, \phi = 90^\circ$. Blue dots represent the experimental data, and the red lines depict the simulation results from CMTJ. (a),(c) The first harmonic response; (b),(d) the second harmonic response. The primary fitting variables are the curvature of the quadratic region in the first harmonics and the slope in the linear section in the second harmonic curve. Inset: the complete view of the first harmonic voltage in the field range from -400 to 400 k$\frac{A}{m}$.

where $\mu_0 M_s$ is the magnetization saturation and t_{FM} is the thickness of the ferromagnetic layer. The H_{DL} and H_{FL} fields may be computed from the first V_ω and and second $V_{2\omega}$ harmonic responses in two arrangements: longitudinal (L), later called H_x, and transversal (T), marked H_y. For instance, one can obtain H_{DL} with the following formula:

$$H_{DL} = -\frac{2}{\zeta}\frac{\rho_L \pm 2\kappa\rho_T}{1-4\kappa^2}, \tag{7}$$

where κ is the ratio of planar Hall effect (PHE) and AHE resistance and $\rho_{L/T} = \partial V_{2\omega}/\partial H_{ext}^{L/T}$ for the longitudinal L and transverse T arrangement, respectively. In the H_x (longitudinal) setting, we apply the external field at $\phi = 0^\circ$ and $\theta = 90^\circ$, whereas for the H_y (transverse) arrangement, we have $\phi = 90^\circ$ and $\theta = 90^\circ$. The parameter $\zeta = \partial^2 V_\omega/\partial H_{ext}^2$ is obtained by fitting the low-regime region of the first harmonic, V_ω to a quadratic function. The $V_{2\omega}$ should resemble a linear function in the same low-field regime as in the case of the first harmonic. We fit that region to obtain the function slope ρ for both H_x and H_y arrangements. Interchanging the subscripts L and T in Eq. (7) yields the value of H_{FL}.

The parameters $\mu_0 M_s$ and K_u were not adjusted in this step and the values of the torques were determined from the experimental data using Eq. (7). We show the results of the best fit to the experimental data in Fig. 6. The computed torque fields are $|H_{DL}| = 420\ \frac{A}{m}$ and $|H_{FL}| = 574\ \frac{A}{m}$ at 5 mA current, with the remaining parameters of the simulated structure taken from Table I. As the experimental rotations may have a slight angular error, we emulate that in the simulation by allowing for the θ and ϕ (as per Fig. 1) angle to deviate from the ideal up to $\approx 3^\circ$.

IV. PARAMETRIC ANALYSIS

Finally, after introduction of the model and presentation of the best fits to the experimental results, we turn to the discussion of the parametric analysis. Specifically, we performed the analysis of $\mu_0 M_s$, K_u, and θ by scanning each within a $\pm 5\%$ margin respective to the value of the best fit to the experimental data (Fig. 7). The deviations of the polar angle cause little effect for the second harmonics in the region of interest (the linear region in the low-field regime), but may contribute to large changes in the first harmonic at higher field magnitudes. From contrasting $\mu_0 M_s$ and K_u scans, we see that the former has a much greater impact on both harmonic Hall voltage components than the latter—specifically, much greater widening/stretching of the quadratic region in the first harmonic and the significant increase/decrease of the slope in the second harmonics in both arrangements. Furthermore, manipulating $\mu_0 M_s$ has an inverse effect of that of K_u. Namely, an increase in $\mu_0 M_s$ may potentially be compensated by the adequate decrease of the K_u.

We then turn to the analysis of the behavior of the FL and DL torques when their values are being varied while all other parameters stay constant (note that the magnitude of change is now $\pm 20\%$). Figure 8 depicts this attempt at evaluating the influence of torque modifications across different applied field arrangements. First, we observe little to no change in the first harmonic response under either FL- or DL-torque variation. Altering the DL torque yields a significant deviation of the slope of the linear region in the longitudinal arrangement towards lower field regimes. However, manipulating with the DL torque causes no visible alterations in the transverse arrangement. The situation flips when the FL torque is varied while the DL torque is kept constant—we notice a visible decrease in the slope values over the crossing linear regions in the H_y arrangements, but no remarkable changes in the H_x setting. Together with the analysis of Fig. 7, we may posit that in our experiments, the first harmonic was entirely affected by the values of θ, $\mu_0 M_s$, or K_u. The inspection of the second harmonic components becomes more involved, as the linear regions may be compensated by manipulating with $\mu_0 M_s$, K_u, but also the corresponding torque component and, to a lesser degree, the θ angle also. Fortunately, we can fix either $\mu_0 M_s$ or K_u by fitting to the dispersion relation first, thus reducing the initial problem of the second harmonic to exclusively tailoring H_{FL} or H_{DL} components.

In Fig. 9, we plot the mean-squared error (MSE) between the parameters taken from Table I and other simulations with parameters taken within some neighborhood of the optimal ones. The color indicates the magnitude of the MSE, with brighter regions corresponding to a lower MSE. In Fig. 9(a), we see that there is a line of minimal MSE for a range of $(\mu_0 M_s, K_u)$ pairs. For a small variation of the K_u, as is the case in Fig. 9(b), we may calculate the corresponding $\mu_0 M_s$ values based on a linear model. Then, we overlay several SD-FMR lines computed based on those pairs to obtain Fig. 9(a). We see that within a good approximation, the $(\mu_0 M_s, K_u)$ pairs produce the same SD-FMR line, which supports the idea that there are several families of parameters that may be eligible for a fit. Hence, it is of primary importance to cross-check those values against the dispersion relation, as presented in

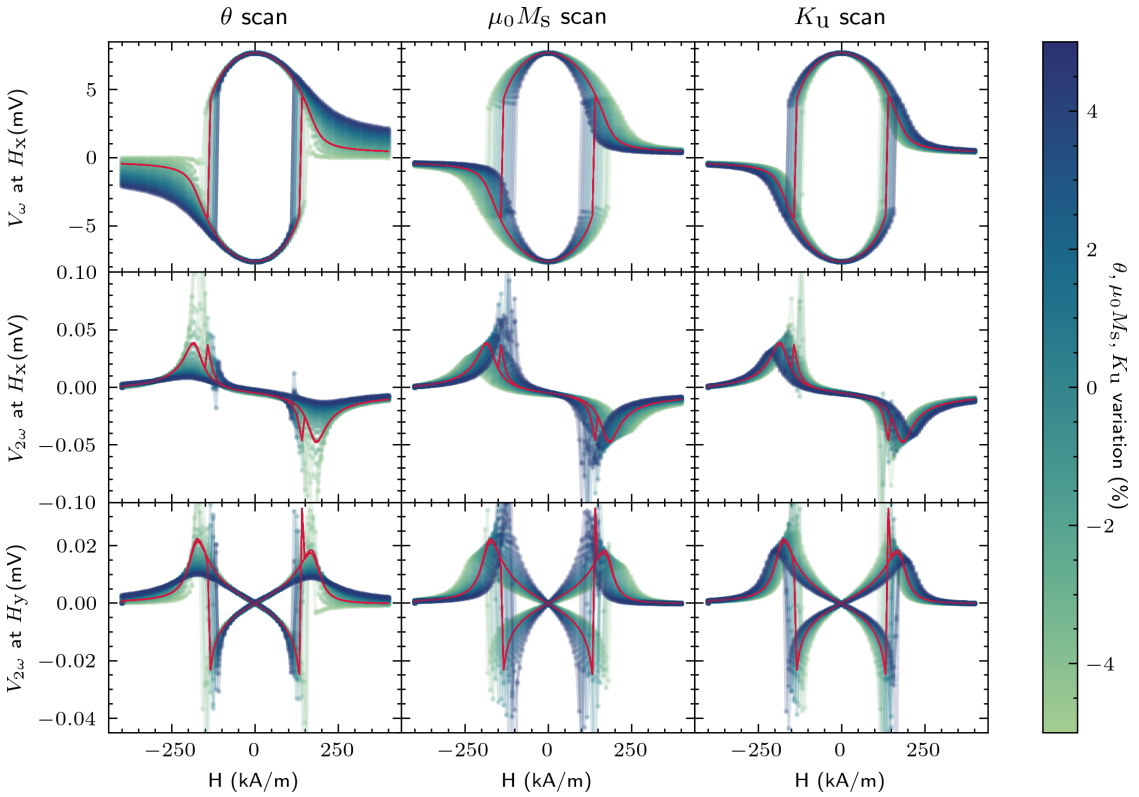

FIG. 7. The figure presents the influence of parameters $\mu_0 M_s$, K_u, and θ on the first and second harmonic scans. Red lines represent the original curve simulated with the parameters from Table I. We simulated the system by varying the selected parameter, but keeping the rest fixed. We see that increasing $\mu_0 M_s$ reveals an inverse effect to increasing K_u, but the rate of change for the latter is much smaller than the one for the former. The range of the θ scan was centered around $94.8^\circ \pm 5\%$; for the $\mu_0 M_s$, K_u scans, the default angle was $\theta = 92^\circ$.

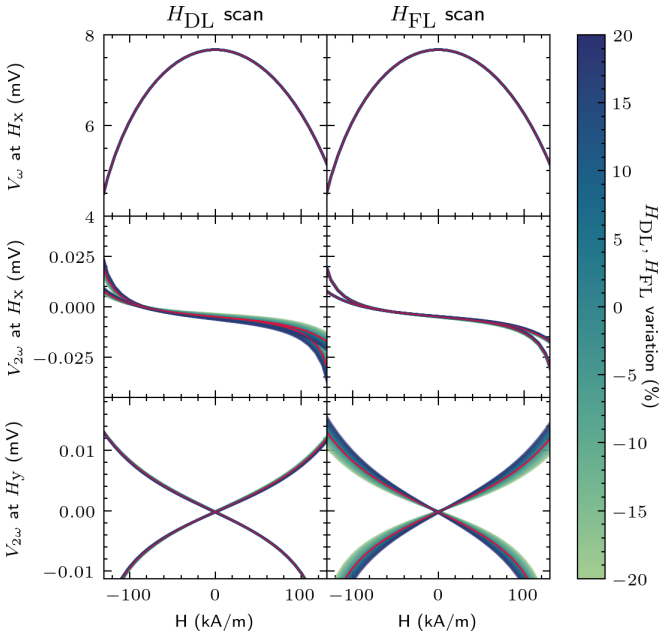

FIG. 8. The torque variation at different field arrangements. Clearly, H_{DL} influences only the second harmonic at the H_x setting, but has no strong effect when the sample is subjected to field at H_y. Conversely, H_{FL} has a strong impact on the angle of line crossing in the H_y arrangement, but causes little changes in the H_x setup. Neither of the torque contributions significantly affects the first harmonic components.

Fig. 5. A good approximation of $\mu_0 M_s$ from, e.g., vibrating sample magnetometer (VSM) measurements, helps to reduce the exhaustive search and narrow the range of feasible values of the K_u parameter. To sum up, the parametric analysis specficially shows that even a small variation of the saturation

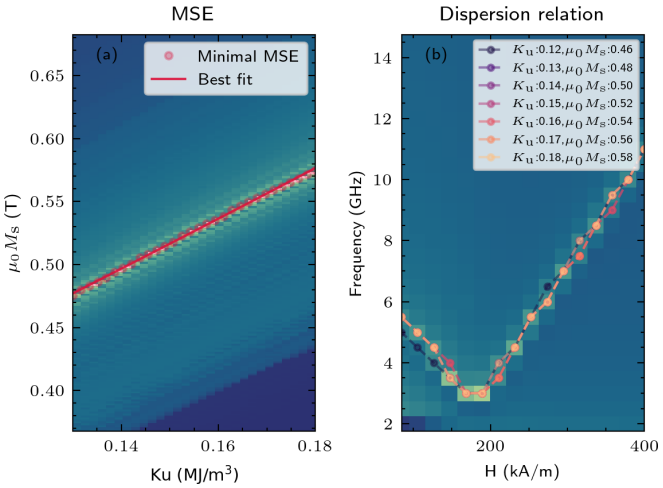

FIG. 9. (a) The map of the MSE respective to the SD-FMR generated with Table I. The brighter the color, the better the minimum (smaller distance between two curves). (b) The resulting dispersion relation for a range of K_u (in MJ/m^3) parameters and respective $\mu_0 M_s$ (in T) values computed from the fitted function in the right panel.

magnetization may lead to significant over- or underestimation of the SOT parameters.

Combining the observations made regarding Fig. 8 and Fig. 7, one may try to optimize for an optimal effective spin-Hall angle. By knowing how the change in the $(\mu_0 M_s, K_u)$ pair affects the quadratic region of the first harmonic and the linear region of the second harmonic, it is possible to relate that change to the dependency from Fig. 8 and thus conclude the effective impact on the spin-Hall angle, as computed in Eq. (6).

V. CONCLUSIONS

To conclude, we demonstrated a stable, reproducible method for modeling a wide spectrum of static and dynamic experimental techniques using the macrospin numerical model. All parameters obtained from the experimental angular and field dependencies are consistent with magnetoresistance dependencies, SD-FMR, and harmonics detection measurements. Furthermore, we performed scans of parameters such as $\mu_0 M_s$, K_u, and θ, each within $\pm 5\%$, to gain insight into the effect that those parameters have on the shape of the harmonics. From that, we show a strong dependency of both V_ω and $V_{2\omega}$ curves on $\mu_0 M_s$, much more potent than that of K_u, which may have a significant bearing on the resultant Hall angle. However, here we presented only a small portion of the functionality offered by our model. Primarily, we focused on the determination of spin-torque effective fields H_{DL} and H_{FL}, which has become an important problem in practical spintronics applications over recent years. CMTJ has more to offer in modeling multilayer spintronic devices and spintronics circuits, where several devices are coupled to each other via the mechanism of either electric or dipole coupling. Future work may also focus on automatic fitting parameters with Bayesian optimization, significantly reducing the need for manual supervision of fit quality. Specifically, an interesting direction of research is optimizing for minimizing the switching current in STT- or SOT-based devices with a given set of parameters such as spin-Hall angle, magnetization saturation, and anisotropy. Furthermore, with the CMTJ package, one can also try to minimize the microwave oscillation linewidth and maximize the oscillation power of STT- or SOT-based nano-oscillators by proposing a set of realistic magnetic parameters of the multilayer system.

ACKNOWLEDGMENTS

We would like to thank P. Ogrodnik and J. Chęcinski for a fruitful discussion. S.Ł., K.G., and T.S. acknowledge the National Science Centre, Poland, Grant No. Spinorbitronics UMO-2016/23/B/ST3/01430. W.S. acknowledges the National Science Centre, Poland, Grant No. UMO-2015/17/D/ST3/00500. Research project partly supported by the program "Excellence initiative research university" for the AGH University of Science and Technology.

APPENDIX: REFORMULATING LLGS EQUATION TO THE LL FORM

In this section, we outline the steps to obtain the numerically useful LL form of the LLGS equation, wherein there is no implicit $\frac{d\mathbf{m}}{dt}$,

$$\frac{d\mathbf{m}}{dt} = -\gamma_0 \mathbf{m} \times \mathbf{H}_{\text{eff}} + \alpha_G \mathbf{m} \times \frac{d\mathbf{m}}{dt} - \gamma_0 |H_{FL}| \mathbf{m} \times \mathbf{p} - \gamma_0 |H_{DL}| \mathbf{m} \times \mathbf{m} \times \mathbf{p}. \tag{A1}$$

We follow [33]. First, applying $\mathbf{m}\times$ to Eq. (A1) yields

$$\mathbf{m} \times \frac{d\mathbf{m}}{dt} = -\gamma_0 \mathbf{m} \times \mathbf{m} \times \mathbf{H}_{\text{eff}} + \alpha_G \mathbf{m} \times \mathbf{m} \times \frac{d\mathbf{m}}{dt} - \gamma_0 |H_{FL}| \mathbf{m} \times \mathbf{m} \times \mathbf{p} - \gamma_0 |H_{DL}| \mathbf{m} \times \mathbf{m} \times \mathbf{m} \times \mathbf{p}. \tag{A2}$$

After some simplification of (A2), we obtain

$$\mathbf{m} \times \frac{d\mathbf{m}}{dt} = -\gamma_0 \mathbf{m} \times \mathbf{m} \times \mathbf{H}_{\text{eff}} - \alpha_G \frac{d\mathbf{m}}{dt} - \gamma_0 |H_{FL}| \mathbf{m} \times \mathbf{m} \times \mathbf{p} + \gamma_0 |H_{DL}| \mathbf{m} \times \mathbf{p}. \tag{A3}$$

Substituting the right-hand side of (A3) into (A1) in lieu of the $\mathbf{m} \times \frac{d\mathbf{m}}{dt}$ term leads to

$$\frac{d\mathbf{m}}{dt} = -\gamma_0 \mathbf{m} \times \mathbf{H}_{\text{eff}} + \alpha_G \Big[-\gamma_0 \mathbf{m} \times \mathbf{m} \times \mathbf{H}_{\text{eff}} - \alpha_G \frac{d\mathbf{m}}{dt} - \gamma_0 |H_{FL}| \mathbf{m} \times \mathbf{m} \times \mathbf{p} + \gamma_0 |H_{DL}| \mathbf{m} \times \mathbf{p} \Big] - \gamma_0 |H_{FL}| \mathbf{m} \times \mathbf{p} - \gamma_0 |H_{DL}| \mathbf{m} \times \mathbf{m} \times \mathbf{p}.$$

Gathering all the $\frac{d\mathbf{m}}{dt}$ terms produces

$$\frac{d\mathbf{m}}{dt}(1+\alpha_G^2) = -\gamma_0 \mathbf{m} \times \mathbf{H}_{\text{eff}} - \alpha_G \gamma_0 \mathbf{m} \times \mathbf{m} \times \mathbf{H}_{\text{eff}} - \gamma_0 |H_{FL}| [\mathbf{m} \times \mathbf{p} + \alpha_G \mathbf{m} \times \mathbf{m} \times \mathbf{p}] - \gamma_0 |H_{DL}| [\mathbf{m} \times \mathbf{m} \times \mathbf{p} - \alpha_G \mathbf{m} \times \mathbf{p}].$$

Rearranging the torque terms gives

$$\frac{d\mathbf{m}}{dt} = \frac{-\gamma_0}{1+\alpha_G^2} [\mathbf{m} \times \mathbf{H}_{\text{eff}} + \alpha_G \mathbf{m} \times \mathbf{m} \times \mathbf{H}_{\text{eff}}] + \frac{-\gamma_0}{1+\alpha_G^2} [|H_{FL}| [\mathbf{m} \times \mathbf{p} + \alpha_G \mathbf{m} \times \mathbf{m} \times \mathbf{p}] + |H_{DL}| [\mathbf{m} \times \mathbf{m} \times \mathbf{p} - \alpha_G \mathbf{m} \times \mathbf{p}]].$$

The last part of Eq. (A4) can be rearranged to

$$\frac{d\mathbf{m}}{dt} = \frac{-\gamma_0}{1+\alpha_G^2} [\mathbf{m} \times \mathbf{H}_{\text{eff}} + \alpha_G \mathbf{m} \times \mathbf{m} \times \mathbf{H}_{\text{eff}}] + \frac{-\gamma_0}{1+\alpha_G^2} [\mathbf{m} \times \mathbf{p}(|H_{FL}| - \alpha_G |H_{DL}|) + \mathbf{m} \times \mathbf{m} \times \mathbf{p}(|H_{DL}| + \alpha_G |H_{FL}|)]. \tag{A4}$$

What becomes evident in this LL form of the LLG equation is the mixing of the torques with damping as the scaling factor. The fieldlike term, for instance, becomes $|H_{\mathrm{FL}}| - \alpha|H_{\mathrm{DL}}|$. We may neglect the second part of that term for small values of $|H_{\mathrm{FL}}| \gg \alpha|H_{\mathrm{DL}}|$. For numerical computation, we use Eq. (A4).

[1] B. Dieny, I. L. Prejbeanu, K. Garello, P. Gambardella, P. Freitas, R. Lehndorff, W. Raberg, U. Ebels, S. O. Demokritov, J. Akerman, A. Deac, P. Pirro, C. Adelmann, A. Anane, A. V. Chumak, A. Hirohata, S. Mangin, S. O. Valenzuela, M. C. Onbaşlı, M. d'Aquino, G. Prenat, G. Finocchio, L. Lopez-Diaz, R. Chantrell, O. Chubykalo-Fesenko, and P. Bortolotti, Opportunities and challenges for spintronics in the microelectronics industry, Nat. Electron. **3**, 446 (2020).

[2] S. Bhatti, R. Sbiaa, A. Hirohata, H. Ohno, S. Fukami, and S. Piramanayagam, Spintronics based random access memory: A review, Mater. Today **20**, 530 (2017).

[3] S. Ikegawa, F. B. Mancoff, J. Janesky, and S. Aggarwal, Magnetoresistive random access memory: Present and future, IEEE Trans. Electron Devices **67**, 1407 (2020).

[4] A. Hirohata, K. Yamada, Y. Nakatani, I.-L. Prejbeanu, B. Diény, P. Pirro, and B. Hillebrands, Review on spintronics: Principles and device applications, J. Magn. Magn. Mater. **509**, 166711 (2020).

[5] S. Manipatruni, D. E. Nikonov, C.-C. Lin, T. A. Gosavi, H. Liu, B. Prasad, Y.-L. Huang, E. Bonturim, R. Ramesh, and I. A. Young, Scalable energy-efficient magnetoelectric spin–orbit logic, Nature (London) **565**, 35 (2019).

[6] D. Ralph and M. Stiles, Spin transfer torques, J. Magn. Magn. Mater. **320**, 1190 (2008).

[7] A. Brataas, A. D. Kent, and H. Ohno, Current-induced torques in magnetic materials, Nat. Mater. **11**, 372 (2012).

[8] A. Manchon, J. Železný, I. M. Miron, T. Jungwirth, J. Sinova, A. Thiaville, K. Garello, and P. Gambardella, Current-induced spin-orbit torques in ferromagnetic and antiferromagnetic systems, Rev. Mod. Phys. **91**, 035004 (2019).

[9] C. Zhang, Y. Takeuchi, S. Fukami, and H. Ohno, Field-free and sub-ns magnetization switching of magnetic tunnel junctions by combining spin-transfer torque and spin–orbit torque, Appl. Phys. Lett. **118**, 092406 (2021).

[10] Z. Chen, C. Pan, N. Wang, M. Qiu, T. Lin, J. Liu, S. Li, P. Han, J. Shi, K. Ando *et al.*, Manipulation of perpendicular exchange bias and spin-orbit torques via mgo in pt/co/mgo films, J. Magn. Magn. Mater. **507**, 166822 (2020).

[11] L. Liu, C.-F. Pai, Y. Li, H. Tseng, D. Ralph, and R. Buhrman, Spin-torque switching with the giant spin Hall effect of tantalum, Science **336**, 555 (2012).

[12] C. Song, R. Zhang, L. Liao, Y. Zhou, X. Zhou, R. Chen, Y. You, X. Chen, and F. Pan, Spin-orbit torques: Materials, mechanisms, performances, and potential applications, Prog. Mater. Sci. **118**, 100761 (2021).

[13] W. Skowroński, Ł. Karwacki, S. Zietek, J. Kanak, S. Łazarski, K. Grochot, T. Stobiecki, P. Kuświk, F. Stobiecki, and J. Barnaś, Determination of Spin Hall Angle in Heavy-Metal/co- fe- b-Based Heterostructures with Interfacial Spin-Orbit Fields, Phys. Rev. Applied **11**, 024039 (2019).

[14] P. Ogrodnik, K. Grochot, Ł. Karwacki, J. Kanak, M. Prokop, J. Chęciński, W. Skowroński, S. Ziętek, and T. Stobiecki, Study of spin-orbit interactions and interlayer ferromagnetic coupling in co/pt/co trilayers in wide range of heavy metal thickness, ACS Appl. Mater. Interfaces **13**, 47019 (2021).

[15] E. Grimaldi, V. Krizakova, G. Sala, F. Yasin, S. Couet, G. S. Kar, K. Garello, and P. Gambardella, Single-shot dynamics of spin–orbit torque and spin transfer torque switching in three-terminal magnetic tunnel junctions, Nat. Nanotechnol. **15**, 111 (2020).

[16] H. Zhou, C. Wang, Z. Li, Z. Wang, T. Liu, B. Wu, and W. Zhao, Design of an erasable spintronics memory based on current-path-dependent field-free spin orbit torque, AIP Adv. **10**, 015317 (2020).

[17] L. Liu, T. Moriyama, D. C. Ralph, and R. A. Buhrman, Spin-Torque Ferromagnetic Resonance Induced By the Spin Hall Effect, Phys. Rev. Lett. **106**, 036601 (2011).

[18] Q. Hao and G. Xiao, Giant Spin Hall Effect and Switching Induced By Spin-Transfer Torque in a w/co 40 fe 40 b 20/mgo Structure With Perpendicular Magnetic Anisotropy, Phys. Rev. Applied **3**, 034009 (2015).

[19] M. Hayashi, J. Kim, M. Yamanouchi, and H. Ohno, Quantitative characterization of the spin-orbit torque using harmonic hall voltage measurements, Phys. Rev. B **89**, 144425 (2014).

[20] J. Kim, J. Sinha, M. Hayashi, M. Yamanouchi, S. Fukami, T. Suzuki, S. Mitani, and H. Ohno, Layer thickness dependence of the current-induced effective field vector in ta| cofeb| mgo, Nat. Mater. **12**, 240 (2013).

[21] https://github.com/LemurPwned/cmtj.

[22] M.-H. Nguyen and C.-F. Pai, Spin–orbit torque characterization in a nutshell, APL Mater. **9**, 030902 (2021).

[23] J. Kim, P. Sheng, S. Takahashi, S. Mitani, and M. Hayashi, Spin Hall Magnetoresistance in Metallic Bilayers, Phys. Rev. Lett. **116**, 097201 (2016).

[24] N. Locatelli, V. Cros, and J. Grollier, Spin-torque building blocks, Nat. Mater. **13**, 11 (2014).

[25] A. A. Tulapurkar, Y. Suzuki, A. Fukushima, H. Kubota, H. Maehara, K. Tsunekawa, D. D. Djayaprawira, N. Watanabe, and S. Yuasa, Spin-torque diode effect in magnetic tunnel junctions, Nature (London) **438**, 339 (2005).

[26] J. C. Sankey, Y.-T. Cui, J. Z. Sun, J. C. Slonczewski, R. A. Buhrman, and D. C. Ralph, Measurement of the spin-transfer-torque vector in magnetic tunnel junctions, Nat. Phys. **4**, 67 (2008).

[27] S. Ziętek, P. Ogrodnik, M. Frankowski, J. Chęciński, P. Wiśniowski, W. Skowroński, J. Wrona, T. Stobiecki, A. Żywczak, and J. Barnaś, Rectification of radio-frequency current in a giant-magnetoresistance spin valve, Phys. Rev. B **91**, 014430 (2015).

[28] C. O. Avci, K. Garello, M. Gabureac, A. Ghosh, A. Fuhrer, S. F. Alvarado, and P. Gambardella, Interplay of spin-orbit torque and thermoelectric effects in ferromagnet/normal-metal bilayers, Phys. Rev. B **90**, 224427 (2014).

[29] Sr830 dsp lock-in amplifier manual, Stanford Research Systems (2011), https://www.thinksrs.com/downloads/pdfs/manuals/SR830m.pdf.

[30] M. Cecot, Ł. Karwacki, W. Skowroński, J. Kanak, J. Wrona, A. Żywczak, L. Yao, S. van Dijken, J. Barnaś, and T. Stobiecki, Influence of intermixing at the ta/cofeb interface on spin Hall angle in ta/cofeb/mgo heterostructures, Sci. Rep. **7**, 968 (2017).

[31] S. Łazarski, W. Skowroński, K. Grochot, W. Powroźnik, J. Kanak, M. Schmidt, and T. Stobiecki, Spin-orbit torque induced magnetization dynamics and switching in a cofeb/ta/cofeb system with mixed magnetic anisotropy, Phys. Rev. B **103**, 134421 (2021).

[32] M. Czapkiewicz, T. Stobiecki, and S. van Dijken, Thermally activated magnetization reversal in exchange-biased [pt/ co] 3/ pt/ ir mn multilayers, Phys. Rev. B **77**, 024416 (2008).

[33] J.-V. Kim, Spin-torque oscillators, in *Solid State Physics*, Vol. 63, edited by R. E. Camley and R. L. Stamps (Academic Press, San Diego, 2012), Chap. 4, pp. 217–294.

npj computational materials

www.nature.com/npjcompumats

ARTICLE OPEN

Check for updates

CMTJ: Simulation package for analysis of multilayer spintronic devices

Jakub Mojsiejuk[1]✉, Sławomir Ziętek[1]✉, Krzysztof Grochot[1,2], Witold Skowroński[1] and Tomasz Stobiecki[1,2]

We present CMTJ—a simulation package for large-scale macrospin analysis of multilayer spintronics devices. Apart from conventional simulations, such as magnetoresistance and magnetisation hysteresis loops, CMTJ implements a mathematical model of dynamic experimental techniques commonly used for spintronics devices characterisation, for instance: spin diode ferromagnetic resonance, pulse-induced microwave magnetometry, or harmonic Hall voltage measurements. We find that macrospin simulations offer a satisfactory level of agreement, demonstrated by a variety of examples. As a unified simulation package, CMTJ aims to accelerate wide-range parameter search in the process of optimising spintronics devices.

npj Computational Materials (2023)9:54 ; https://doi.org/10.1038/s41524-023-01002-x

INTRODUCTION

Modern development of spintronic devices[1] requires careful design and a time-consuming fabrication process, a preparation of which is often carried out with the help of simulations. The use of magnetic materials and multilayer structures with certain material parameters enables the creation of a spintronic device with optimal functionality, depending on the application: good memory is characterised by high endurance and energy-efficient write operations[2], sensor development usually focuses on high sensitivity and low inherent noise[3], and in devices with a high-frequency component, we aim to maximise the quality factor while retaining low energy consumption[4]. To simulate such a variety of use cases, we need an extensive simulation toolkit. As we climb from the macromagnetic models, steadily increasing the resolution of the phenomena in atomistic simulations, and finally reaching the ab initio simulations, we do so with increasing computational cost. This computational cost is closely correlated with the number and complexity of the simulation parameters and may hamper the speed of prototyping. Consequently, we are facing the dilemma of choosing between a slower, but accurate approach and a faster, but not as precise method.

Micromagnetic packages, such as MUMAX3[5] and OOMMF[6], offer a lot of plasticity in modelling magnetic interactions of complex structures while maintaining an acceptable computational cost. On the other side of the spectrum, VASP[7] and QUANTUM ESPRESSO[8,9] lead the way as recognised self-consistent solvers. Between them, there are tools for atomistic magnetic simulations such as VAMPIRE[10] or SPIRIT[11] that, in addition to dynamics solvers, can also employ Monte Carlo methods for time-independent processes. In the micromagnetic regime, a notable research direction was devoted to creating magnetic tunnel junction (MTJ) behavioural models in Verilog, for example, in the work of R. Garg et al.[12] or T. Chen et al.[13,14]. Such models attempt to capture the electronic nature of spintronics devices, describing them as discrete elements or electronic elements in a circuit, making it easy to prototype devices composed of discrete components.

In this article, we seek to fill a gap in the magnetic simulation hierarchy by providing an open-source, computationally efficient standardised Python package, CMTJ, for rapid prototyping, large-scale parameter search, and macrospin simulation of multilayer systems. CMTJ is capable of simulating, for example, current-induced magnetisation dynamics calculations originating from spin transfer torque (STT)[15,16] such as spin torque oscillator (STO)[17], STT-induced magnetisation switching[18] or voltage-controlled magnetic anisotropy (VCMA) phenomena[19]. Some of those motivating examples are shown in Fig. 1. In the text, we first discuss the structure of the simulation in the CMTJ and its driver systems. Then we present some of the more advanced simulations where CMTJ provides valuable information, showing its ability to verify experimental setups that include, but are not limited to, static and dynamic characteristics of spin valves or magnetic tunnel junctions (MTJ).

RESULTS

Simulation design

The core of CMTJ is based on the Landau–Lifschitz–Gilbert–Slonczewski (LLGS) macrospin equation implemented in C++, with a simple header-only library interface. If the user wishes to benefit from the provided PYTHON interface, the setup involves a standard PIP installation process. The scope of the PYTHON interface covers all basic functionalities of the C++ core library, exposing the functions using the open-source solution PYBIND11[20]. In addition, the PYTHON package offers utility functions that complement frequently used operations such as unit conversions, parallelism, parameter sweep, filtering, energy and resistance calculations, or template procedures for spin-diode ferromagnetic resonance (SD-FMR) or pulse-induced microwave magnetometry (PIMM). The library is composed of a couple of classes, mainly the *Junction* and *Layer* classes that define a basic magnetic component in the MTJ simulation and the *Driver* class that contains definitions of various excitations that influence the magnetisation dynamics of the system. We briefly discuss them in the following paragraphs, but detailed descriptions of key CMTJ functionality, as well as implementation details, can be found in the library documentation (https://lemurpwned.github.io/cmtj/).

The input to each simulation is the programmatic description of the system and its dynamic stimuli, which may vary over the simulation runtime. The result of a simulation holds the evolution

[1]Institute of Electronics, AGH University of Science and Technology, Al. Mickiewicza 30, Kraków 30-059, Poland. [2]Faculty of Physics and Applied Computer Science, AGH University of Science and Technology, Al. Mickiewicza 30, Kraków 30-059, Poland. ✉email: mojsieju@agh.edu.pl; zietek@agh.edu.pl

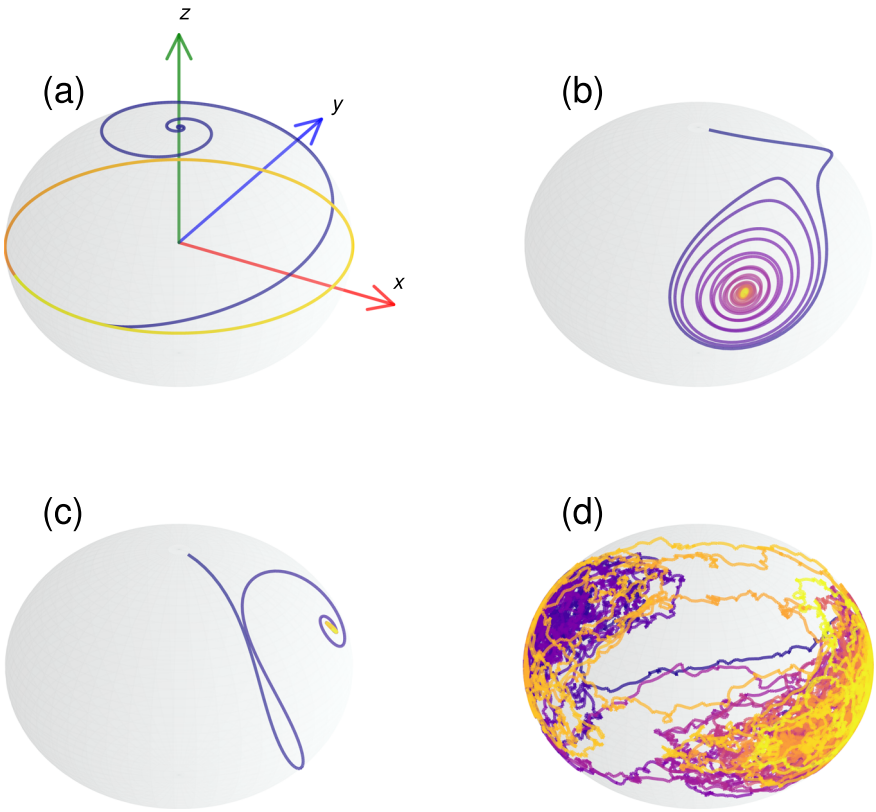

Fig. 1 Example trajectories extracted by simulating a single ferromagnetic layer with different parameters and excitations. a Depicts a stable oscillator trajectory under a constant current density. **b** Demonstrates a trajectory obtained with exciting the magnetisation with VCMA. In **c** we see a trajectory under a pulse excitation of the Oersted field. Finally, **d** is a thin, bilayer ferromagnetic system with a low-energy barrier that changes states from parallel to anti-parallel under thermal noise.

of the magnetisation vector for each layer at each time step, and if the user chooses so, additional time-dependent metadata such as different flavours of magnetoresistance[21] or field contributions. All simulations in CMTJ are conceptually divided into three levels of abstraction: single-layer simulations, multilayer simulations, and stacked device simulations. The first of those levels are designed to provide a basic interface of the ferromagnetic (FM) layer, which is represented by a time-dependent magnetisation vector, as dictated by a macrospin model. Layers in CMTJ are created using the *Layer* class, for example:

```
# define the tensor using cmtj C++ binding class called CVector
demagTensor = [
        CVector(0.0002, 2.7139e-10, 5.9550e-14),
        CVector(2.7139e-10, 0.0001, 1.3250e-14),
        CVector(5.95503e-14, 1.3250e-14, 0.9995)
]
# create a simple layer
free_layer = Layer(
            id="free",
        mag=CVector(0, 0, 1),
        anis=CVector(0, 0., 1),
        Ms=1.6,
        thickness=2e-9,
        cellSurface=surface,
        damping=5e-3,
        demagTensor=demagTensor,
)
```

which defines a layer that can be later referred to by its 'free' id, with perpendicular anisotropy axis, initial magnetisation along the *z*-axis, magnetisation saturation, M_s, of 1.6 T, the thickness of 2 nm, Gilbert damping constant of $\alpha_G = 0.005$ and a demagnetisation tensor under variable name *demagTensor* (see the "Methods" section for an explanation how those parameters influence the simulation). Multilayer simulation applications revolve most commonly around simple bilayer structures consisting of heavy metal (HM) and FM layers, or MTJs composed of FM layers, each separated by a thin tunnel barrier (TB). Non-ferromagnetic layers, such as HM, are not simulated in the package, but their inclusion in the experiment has direct consequences in the simulation. For example, between two FM layers separated by TB, there is an interlayer exchange coupling (IEC) that varies with thickness[22,23]. Similarly, layers can be coupled in the multilayer system via a longer-range dipole interaction. HMs are typically simulated indirectly with the addition of STT or SOT terms[24,25]. It is also possible to save computing time by including pinned layers, experimentally obtained by the exchange-bias structure enforced by the presence of an antiferromagnet. In such a case, the solver is not run for a pinned/reference layer, but the effects of SOT or STT are still modelled via a constant reference vector.

To create a multilayer device in CMTJ, the user needs to create at least one FM layer. Layers are then composed into a single *Junction* that represents a discrete multilayer system. A two-layer *Junction* can be defined as follows:

```
# Create MTJ composed of two FM layers created earlier
# Rap - anti-parallel, Rp - parallel resistance
mtj=Junction([free_layer, reference_layer], Rp=100, Rap=200)
```

Wrapping multiple layers into a single object provides an additional level of control; for instance, the same magnetic field or excitation may be applied to all members of the *Junction* with a single function instead of to each layer individually.

For some simulations, two or more junctions can be combined into a *Stack* of type *Parallel* or *Series*, which alters the resistance calculation. However, the main consequence of composing a *Stack*

device is the electrical coupling by a current passing through. The model for this kind of coupling follows the work of Taniguchi et al.[26]. For a parallel or series stack of two junctions, the current depends on the free magnetisations **m** and the pinning layers **p** of the junctions i and $i+1$:

$$I(t) = I_0(t) + \chi I_0(t)(\mathbf{m}_i \cdot \mathbf{p}_i + \mathbf{m}_{i+1} \cdot \mathbf{p}_{i+1}) \quad \text{(series)} \tag{1}$$

$$I(t) = I_0(t) + \chi I_0(t)(\mathbf{m}_i \cdot \mathbf{p}_i - \mathbf{m}_{i+1} \cdot \mathbf{p}_{i+1}) \quad \text{(parallel)} \tag{2}$$

where $I_0(t)$ represents the value of the uncoupled current. The coupling strength χ can be positive or negative, most of the time strictly much <1 in absolute value. Creating a stack is simple; for example, setting a current density of $I_0 = 60\,\text{GA/m}^2$ through the stack with the coupling strength of 0.1 reduces to the following:

```
# create a parallel connection of junction1 and junction 1
stack=ParallelStack([junction1, junction2])
# set the constant current density fed into the system
stack.setCoupledCurrentDriver(ScalarDri-
ver.getConstantDriver(6e10))
# set coupling strength
stack.setCouplingStrength(0.1)
```

Excitation drivers

The dynamic pathway to excite any system in CMTJ takes place through the driver system. The user can define any excitation in the form of a driver, an adequate *Scalar* driver, or a vector (*Axial*) driver. The latter are just compositions of the former along each dimension (the x, y, and z axes independently). Each driver component is calculated at each time step and influences the selected effective field contributions. For instance, one may define a sinusoidal driver and use it as a driving excitation of the anisotropy, leading to stimulation of the VCMA effect:

```
# Junction called mtj was created earlier
# reference the free layer from 'mtj` using the Junction interface,
mtj.setLayerAnisotropyDriver("free",
    # arguments for the anisotropy sine driver are:
    # offset (J/m^3), amplitude (J/m^3), frequency (GHz), phase
    ScalarDriver.getSineDriver(
        K1, 1e3, 7e9, 0
    ))
```

Similarly, an externally applied magnetic field can be added through the *AxialDriver* class by specifying field contributions along each axis. For example, setting a constant field of 5 kA m^{-1} along the y-axis can happen by using a simple function call:

```
# reference all layers in the junction
mtj.setLayerExternalFieldDriver("all",
        AxialDriver(
            NullDriver(), # x, does nothing
            ScalarDriver.getConstantDri-
            ver(5e3), # y,
            NullDriver())) # z, does nothing
```

All mechanisms described in this section offer great flexibility in designing an experiment. Since drivers act as input to a state machine, the simulation may be paused, modified, and resumed without having to restart. The output is saved online in a native PYTHON dictionary object that assumes seamless integration with other common numerical, plotting, or machine-learning packages available in that language.

In the consecutive sections section, we focus on reproducing selected interesting experiments and, where possible, comparing the simulation result with the experimental data and analytical functions. The examples are arranged by the level of complexity, starting from the simplest towards more advanced ones. We decided to showcase the following techniques: standard $M(H)$ and $R(H)$ loops in the section "$M(H)$ and $R(H)$ loops", magnetoresistance (MR) based SD-FMR and PIMM in the section "Spin valve dynamics", harmonic Hall voltage detection, an angular variant in the section "Angular harmonic Hall detection", current-induced magnetisation switching (CIMS) in Sect. "CIMS", electrical coupling of two MTJs in the section "Electrical coupling". These examples can be reproduced by running the JUPYTER notebooks from the GITHUB repository of the CMTJ package.

$M(H)$ and $R(H)$ loops

The $M(H)$ and $R(H)$ are the basic magnetic characterisation methods that allow the determination of various material parameters of the multilayer system, such as magnetisation saturation, magnetic anisotropy, or magnetoresistance ratio. The $M(H)$ loop simulates magnetometry measurements, such as a vibrating sample magnetometer (VSM) or magnetooptical Kerr effect (MOKE), whereas the $R(H)$ loops are indispensable in adjusting the magnetoresistance magnitude. By performing angular sweep simulations in different planes, one can also determine a type of magnetoresistance, because anisotropic MR (AMR), anomalous Hall effect MR (AHE), giant MR (GMR)/tunnelling MR (TMR) and spin-Hall MR (SMR) are characterised by different angular dependencies[21,27,28]. Other magnetoresistance flavours, such as those presented, for example, in the works by Avci et al. and Vélez et al.[29,30], may be easily added after the magnetisation dynamics have been computed by CMTJ.

In the case of $M(H)$ and $R(H)$ loop simulation, we replicated the experimental method by extending the simulation time and collecting the magnetisation or resistance vector at the steady state for each magnitude of the swept magnetic field. As an example, magnetic-field-dependent simulations of the Co(4 nm)/Ru(0.65 nm)/Co(4 nm) system are presented in Fig. 2a–f. The data for this example come from, yet unpublished, wider research on the Co/Ru/Co trilayers. A similar setup may be found in ref. [31]. In the simulations, increasing H along the y direction leads to a scissor-shaped magnetisation vector alignment, which saturates at around 600 kA m^{-1}. This becomes particularly clear in the loop $M(H)$ for m_y component illustrated in Fig. 2b, with the remaining m_x and m_z having very small amplitudes. Furthermore, the simulation reveals that, due to antiferromagnetic coupling (AFM), the two layers oscillate in antiphase in a certain region, as depicted in Fig. 3. The experimental points for this sample were collected from SD-FMR measurement, with an external field applied at 45° angle respective to the long axis of the stripe, and an RF signal power of 16 dBm. The DC voltage originating from the mixing between oscillating resistance and the in-phase current

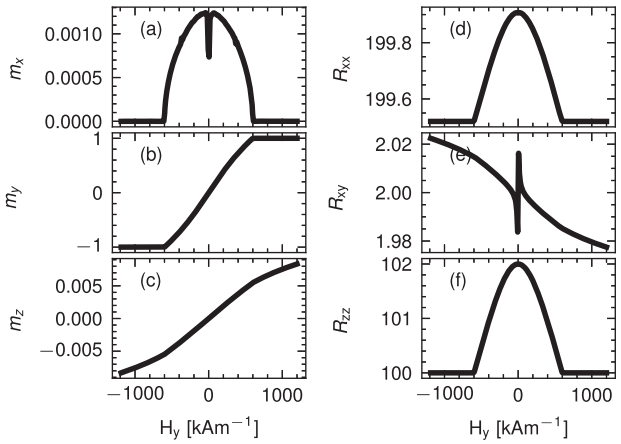

Fig. 2 Steady-state simulations of the Co/Ru/Co system with the transverse applied field. $M(H)$ **a**–**c** and $R(H)$ **d**–**f** loops simulated with parameters taken from Supplementary Table 1. The magnetic moment is normalised to unity, whereas the SMR, AMR, and GMR magnitudes are set to −0.24, −0.045, and 2 Ω, respectively (note that m_y and m_z components show very little variation with the applied field).

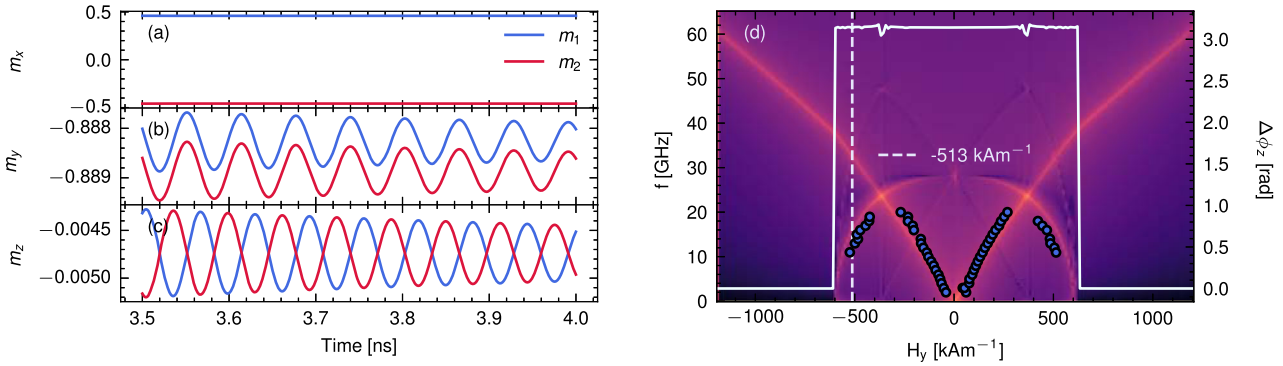

Fig. 3 Co(4 nm)/Ru(0.65 nm)/Co(4 nm) system with both linear and quadratic components of the IEC. a–c magnetisation trajectory components for a $H_{ext} = 513$ kA m^{-1}, marked with the dashed white line in (**d**). Colour denotes a layer, blue for the top and red for the bottom layer. **c** Shows that the m_z components of the two layers oscillate in antiphase. **d** Kittel dispersion relation obtained from PIMM (described in the section "Spin valve dynamics"), with experimental points from SD-FMR (given by blue dots), and phase difference $\Delta\phi_z$ between m_z components of two layers (solid white line) across the external magnetic field range. The region between approximately −600 and 600 kA m^{-1}, where the optical branch is visible, exhibits antiphase oscillation of m_z components. Parameters are taken from Supplementary Table 1.

was obtained using Hall-bar system by a lock-in amplifier synchronised to an amplitude-modulated RF source.

Spin valve dynamics

A more complex example begins with a study of a CoFe(2.1 nm)/Cu(1.9–2.37 nm)/CoFe(1 nm)/NiFe(5 nm) spin valve sample with variable thickness of the Cu spacer layer. This system exhibits characteristic oscillatory coupling varying with spacer thickness, which is well described in terms of the Rudermann–Kittel–Kasyua–Yosida (RKKY) interaction between the magnetisations of the reference and the free layers[32]. Resulting GMR, $R(\theta)$, is calculated with respect to resistances in parallel (R_P) and antiparallel states (R_{AP}):

$$R(\theta) = R_P + \frac{1}{2}(R_{AP} - R_P)(1 - \mathbf{m}_{free} \cdot \mathbf{m}_{reference}) \quad (3)$$

where θ is the angle between the magnetisation vectors of the free and reference layer, $\mathbf{m}_{free}$ is the magnetisation of the free layer, and $\mathbf{m}_{reference}$ is the magnetisation of the reference layer. Using the parameters for the system from the papers[32,33], also summarised in Supplementary Table 2, we perform SD-FMR and PIMM simulations.

Experimentally SD-FMR methods involve supplying AC current, I_{AC}, in a given frequency range, typically between 2 and 40 GHz, while sweeping with an external magnetic field. As a result, the DC mixing voltage V_{mix} arises, which is essentially a function of both the frequency and the magnitude of the external magnetic field[34]. Thus, SD-FMR allows for the calculation of the ferromagnetic resonance frequency for a given set of system parameters in the form of a Kittel dispersion relation. Furthermore, analysis of the shape of the simulated signal can be used to determine the spin torque values, in the current perpendicular to the plane STT[35] and in-plane SOT geometries[24]. In the simulation setup, a representation of SD-FMR is modelled with a 2D map, where V_{mix}, the mixing voltage of $R(\theta)$ and I_{AC} at a frequency f, is plotted against a range of applied external field, H. For each field and frequency, the I_{AC} time series is multiplied by a magnetoresistance time series and then passed through a low-pass filter. Finally, the mixing voltage is extracted as a means of that signal. The results are presented in Fig. 4 with bright green hollow circles as experimental points for comparison. In simple cases, a known analytical relation, in the form of the Kittel dispersion function[36], produces the main resonance mode of the system:

$$f = \frac{\gamma_e}{2\pi}\sqrt{B(B + \mu_0 M_s)} \quad (4)$$

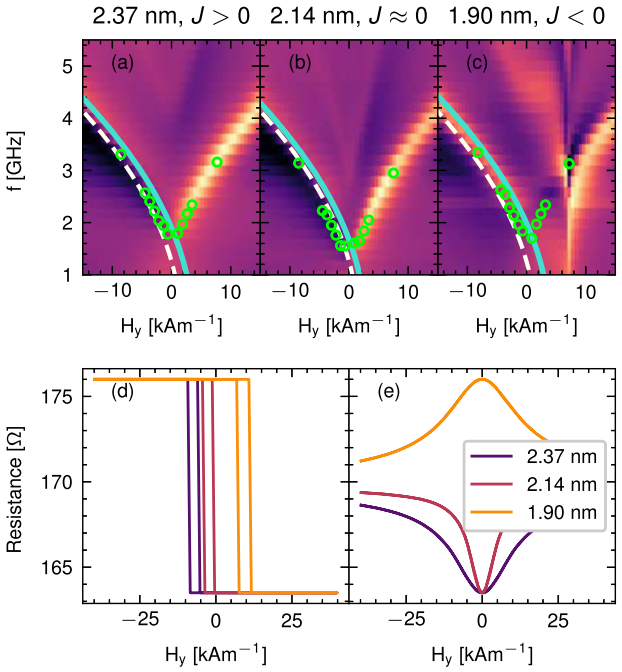

Fig. 4 Spin valve simulations of CoFe(2.1 nm)/Cu(1.9–2.37 nm)/CoFe(1 nm)/NiFe(5 nm) sample for three different values of Cu thickness which result in different IEC magnitudes. a–c Kittel dispersion relations, with the blue dots marking the experimental data. Resistance loops at $\phi_H = 90°$ (**d**) and at $\phi_H = 0°$ (**e**) applied external magnetic field with ϕ denoting the polar angle. Solid turquoise lines mark the fit to Kittel's formula, Eq. (4) and ivory dashed line represents simulated data from the free-energy Smit–Beljers model. Discrepancies between Kittel and Smit–Beljers model may come from the fact that the latter is better suited to multilayer systems. Parameters of the system may be found in Supplementary Table 2.

where the $\frac{\gamma_e}{2\pi}$ factor is ≈ 28,024 MHz T^{-1}, and the B field is composed of an external magnetic field, an interlayer exchange coupling field, and an anisotropy field, respectively: $B = \mu_0(H_{ext} + H_{IEC} + H_K)$ (see the section "Field contributions" for more details on how they are computed macro magnetically). We plot the fit to Eq. (4) in Fig. 4 with the solid turquoise line. In addition to Kittel's model, we included the free-energy model

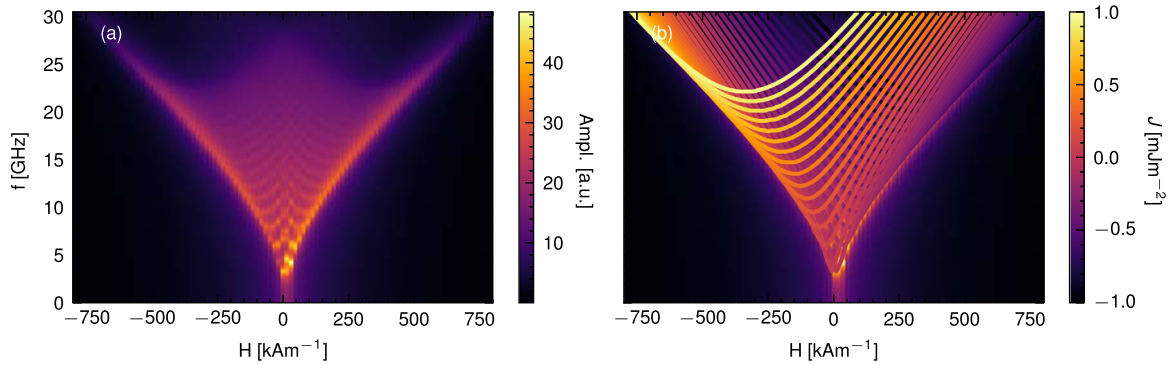

Fig. 5 PIMM scans of the CoFe(2.1 nm)/Cu(1.9–2.37 nm)/CoFe(1 nm)/NiFe(5 nm) system in the function of IEC constant J_{linear}. **a** spectrum of multiple IEC values in (−1,1 mJ m^{-2}) was combined into a single map. The colour indicates the total frequency amplitude summed over all PIMM simulations. **b** Illustrates the same PIMM, but with a marked maximum amplitude resonance line for each J_{linear} value mapped accordingly to the colour scale. The colour scale attached represents different IEC values, from −1 to 1 mJ m^{-2}. We observe the shift of the resonance curve towards the centre for smaller absolute IEC values. Note that at $H = 0$ the system still exhibits non-zero oscillation. Parameters used for simulation can be found in Supplementary Table 2. Field applied along at 45° angle between x and y axes.

based on the Smit–Beljers model[37] (dashed ivory line), which yields more precise results for a multilayer case. The key effect modelled in Fig. 4a–c is the increase of the zero-field oscillation frequency when the IEC increases with absolute value. In Fig. 4d the simulation captures the shift of the resistance loop at $\phi_H = 90°$ and the widening of the resistance curve peak at $\phi_H = 45°$ in Fig. 4e, all respectively, for the case where $J \approx 0$. In any case, macromagnetic simulation, being a dynamic process, can model the experimental data more accurately for that particular experiment. A further advantage of computing the dynamics is that we obtain the full SD-FMR map, rather than the individual resonance modes, as is the case with the Smit–Beljers model.

Apart from the SD-FMR method described above, magnetisation dynamics can also be investigated by analysing the magnetisation response to picosecond magnetic field pulses. In the experiment, this time domain method is performed indirectly using PIMM[38–40]. From the simulation perspective, PIMM is simulated as an analysis of the free oscillations induced by a short magnetic field pulse, contrary to the dynamics caused by the alternating signal input, as is the case for the FMR. Specifically, we measure the response to a step excitation of a short-lived (2–3 ps), small-amplitude (usually about 50–100 Oe) Oersted field pulse along the z-axis. This corresponds to the experimental setup where a short DC pulse is injected into the system. If the FFT computation of the pulse response for each value of the applied magnetic field from the sweep is repeated, one can obtain a spectrogram representing the dispersion relation, where each pixel denotes the FFT magnitude for a given frequency and magnetic field. For the spin valve system, multiple PIMM simulations are performed for a range of different IEC values and then overlayed, resulting in Fig. 5a, b. Similarly as in the case of the SD-FMR experiment, when the magnitude of the IEC coupling increases, the resonance curve shifts away from the zero fields.

Angular harmonic Hall voltage detection

There are several experimental methods that lead to the determination of the SOT components: SOT-FMR line[41] and line width analysis[42], the SOT switching current analysis[43], or field-dependent harmonic Hall voltage techniques[44]. Another approach, less susceptible to various artefacts, such as the anomalous Nernst effect, is called the angular harmonic Hall voltage[45]. Our model has been thoroughly verified using the field-dependent method[46], here we present a simplified angular variation of the harmonic Hall voltage detection. The standard

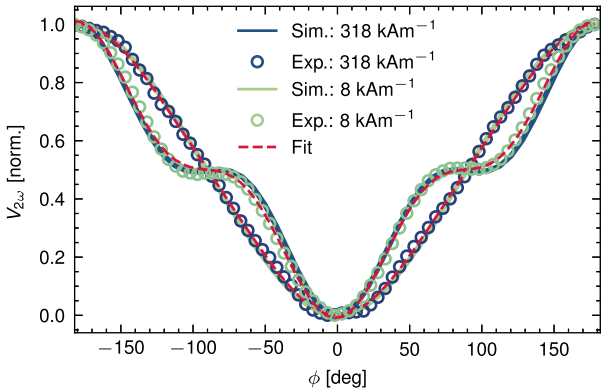

Fig. 6 Second Harmonic Hall voltage detection in angular variation. Hollow dots represent the experiment, solid lines mark the simulation data and a dashed red line denotes the fit to Eq. (5). The y-axis is normalised. Measurement data was collected from Pt(4.3 nm)/FeCoB(2 nm) device, for two example magnitudes of the external magnetic field.

process for obtaining torque amplitudes $H_{DL/FL}$ in the angular variation of harmonic Hall voltage detection follows the model of Avcii et al.[47,48]:

$$V_{2\omega} = \left(-\frac{H_{FL}}{H_{ext}} V_P \cos 2\phi - \frac{1}{2}\frac{H_{DL}}{H_{eff}} V_A + V_{ANE} \right) \cos\phi \quad (5)$$

where ϕ is the angle in the plane between the long axis of the Hall bar and magnetisation. The effective field H_{eff} includes the external field H_{ext} and the anisotropy field, H_K. V_P and V_A are the planar and anomalous Hall voltages, respectively. V_{ANE} is a contribution of the anomalous Nerst effect. We show the simulation result, along with the experimental results for the corresponding Pt(4.3 nm)/FeCoB(2 nm) sample[49], in Fig. 6. Each line is produced by sweeping with the azimuth angle $\phi \in [-180°, 180°]$ at the frequency f of the AC current and measuring the second harmonic output in the mixing voltage of the input current (for details of the experimental setup, see ref. [49]). The parameters for this system can be found in Supplementary Table 3. The signal consists of one part proportional to the damping-like field with a $\cos\phi \cos 2\phi$ dependence and another, related to the field-like term. The former dominates in small magnetic fields because it is scaled by an external field alone, unlike the latter, which is scaled by the effective field (which also includes anisotropy and

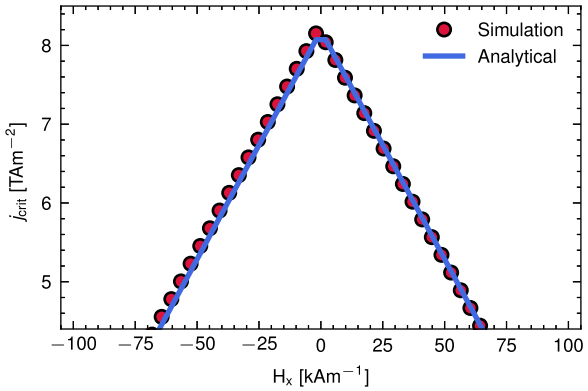

Fig. 7 Critical switching current densities as a function of external field H_x for Pt(4 nm)/Co(1 nm)/MgO SOT device. Fit to analytical formula is represented as a solid blue line and red dots depict the simulated result.

demagnetising fields). In Fig. 6, this torque causes an inflexion in the curve at large ϕ angles.

CIMS

Next, we discuss an example of SOT-induced magnetisation switching in the HM/FM bilayer. The experimental data were obtained in the multilayer system: Pt(4 nm)/Co(1 nm)/MgO (A1) from the work of Grochot et al.[50]. In this case, we reproduce the theoretical switching behaviour of the system using the field-like and damping-like SOT, and magnetic parameters obtained from the experiment. The result is shown in Fig. 7. We approximated the critical current density analytically using a formula from Lee et al.[51]:

$$j_{sw} \approx \frac{2e\mu_0 M_s t_{FM}}{\hbar\theta_{SH}}\left(\frac{H_K}{2} - \frac{H_x}{\sqrt{2}}\right) \quad (6)$$

where e is the electron charge, μ_0 is the magnetic permeability in a vacuum, M_s is the magnetisation saturation, $\hbar$ is the reduced Planck constant, θ_{SH} is the effective spin Hall angle, H_K is the effective perpendicular anisotropy value, and H_x is the applied field along the x direction.

For simulations, we used the trapezoidal impulse shape, with a rising and falling edge of 1 ns and a flat edge of 3 ns. We also normalised the damping- and field-like torque magnitudes obtained from the experiment by the current density with which they were measured. Under the current density sweep, they will scale proportionally, giving the correct values of H_{DL} and H_{FL} at each step.

Electrical coupling

Using this example, we illustrate how electric coupling can be simulated with CMTJ. First, we created two MTJs with slightly different magnetic and resistance parameters, emulating a typical experimental dispersion. Then, using the interface of the *Stack* class (see the section "Simulation design"), we couple them in a parallel connection, setting the coupling value χ. We sweep the external magnetic field at the azimuthal angle of 5° and measure the frequency response of the stack to constant current density excitation. For larger values of the applied external magnetic field and negative coupling constant χ, we observe how two main resonance lines, each corresponding to a separate MTJ, converge towards a common resonance mode. Ultimately, around 250 kA m^{-1}, the two MTJs desynchronise and their resonance lines separate again. The result of the electric synchronisation of two MTJs is depicted in Fig. 8a, while Fig. 8b and c illustrate a situation with a positive coupling coefficient and coupling disabled, respectively. This example shows that the software

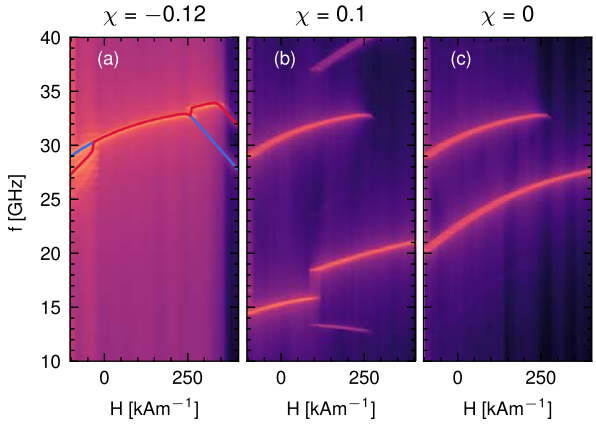

Fig. 8 The electric synchronisation of two MTJs. Electric coupling constant was set to $\chi = -0.12$ (**a**) and $\chi = 0.1$ (**b**). Solid blue and red lines in (**a**) indicate the primary resonance modes of individual MTJs from the stack. **c** Shows the same device with no coupling present.

presented can also be used in more complex systems, for example, for the analysis of neural computing platforms[52]. The parameters of the coupled system have been collected in Supplementary Table 4.

DISCUSSION

In this article, we presented CMTJ, fast modelling software for macrospin simulation of magnetic heterostructures. Its core is grounded in the LLGS equation, and the package is capable of calculating both the static and dynamic characteristics of spintronic devices. However, macrospin simulations are inherently limited in modelling any sort of spin wave or materials with non-uniform magnetisation and therefore are not a suitable method in cases where those effects play a key role. Yet, many experimental setups in electrical detection are, in principle, averaged pictures of reality. For instance, in measurements such as $M(H)$ or $R(H)$, we observe only a mean value of multi-domain behaviour of magnetisation or resistance. Therefore, in such use cases, the use of macrospin modelling can be justified and, as shown in the previous sections, results obtained from CMTJ agree well with the experimental data.

The key benefit of using macrospin over micromagnetic frameworks is the speed of computation. Additionally, with the Python bindings CMTJ provides, the package can be used directly in common parameter search procedures that involve Bayesian optimisation processes or neural network training. The combination of those two advantages, performance and integration with native Python code, hints at the intended use of CMTJ, which lies in large-scale sweeps over multidimensional parameter spaces. Such an application plays an interesting role in understanding how different magnetic parameters influence the dynamics of the spintronic device.

Finally, in the spirit of the modern modular development approach suggested, for example, in refs. [53,54], CMTJ expands its usability to connect multiple spintronic structures using the *Junction* or *Stack* system. Future extensions based on the modular approach may involve the addition of a separate structure, such as a reservoir, where an array of thin-layer spintronics devices is dynamically coupled through dipole interaction[55,56].

METHODS

Magnetisation dynamics

The pivotal equation for magnetic macrospin simulations is called Landau–Lifshitz–Gilbert–Slonczewski (LLGS)[15,45,57–59]. In the

simulation, we use the numerically solvable LL-form of that equation. A formulation with SOT torques included in the package has the following form:

$$\frac{d\mathbf{m}}{dt} = \frac{-\gamma_0}{1+\alpha_G^2}[\mathbf{m}\times\mathbf{H}_{eff} + \alpha_G\mathbf{m}\times\mathbf{m}\times\mathbf{H}_{eff}] + \frac{-\gamma_0}{1+\alpha_G^2}[\mathbf{m}\times\mathbf{p}(H_{FL} - \alpha_G H_{DL}) + \mathbf{m}\times\mathbf{m}\times\mathbf{p}(H_{DL} + \alpha_G H_{FL})] \quad (7)$$

where $\mathbf{m} = \frac{\mathbf{M}}{M_s}$ is a normalised magnetisation vector, with M_s as the magnetisation saturation, $\mathbf{H}_{eff}$ as the effective field, α_G as the dimensionless Gilbert damping parameter, $\mathbf{p}$ is the polarisation vector, and γ_0 is the gyromagnetic factor. Factors H_{DL} and H_{FL} are the so-called damping and field-like torque amplitudes, respectively. Usually, for small values of α_G, compared to the torque value, the torque mixing can be omitted in the last two terms in this form of the equation.

For structures where the spin current is injected through HM, the values of the SOT torques are usually taken from the experiment. For example, in the harmonic Hall voltage measurement[45], their values can be computed with the following equation:

$$H_{DL} = -\frac{2}{\zeta}\frac{\rho_L \pm 2\kappa\rho_T}{1-4\kappa^2} \quad (8)$$

where κ is the ratio of the planar Hall effect and the resistance of the anomalous Hall effect and $\rho_{L/T} = \partial V_{2\omega}/\partial H_{ext}^{L/T}$ for the longitudinal arrangement L, when an external magnetic field is applied along the length of the sample, and the transverse arrangement T, when the field is applied along the width of the sample. The parameter $\zeta = \partial^2 V_\omega/\partial H_{ext}^2$ is obtained by fitting the low-field regime of the first harmonic response, V_ω to a quadratic function. Substituting the subscripts L and T produces torque H_{FL}. The voltage in the experiment arises as a response to the low-frequency AC current in longitudinal and transverse arrangements, but in the simulations, we often model it as an Oersted field excitation along the y direction. More details can be found in ref. [46]. For simulations more suited to the STT model, we assume the following LL form of the LLGS equation:

$$\frac{d\mathbf{m}}{dt} = \frac{-\gamma_0}{1+\alpha_G^2}[\mathbf{m}\times\mathbf{H}_{eff} + \alpha_G\mathbf{m}\times\mathbf{m}\times\mathbf{H}_{eff}] + \frac{-\gamma_0}{1+\alpha_G^2}[a_j\varepsilon\beta(\mathbf{m}\times\mathbf{p}) + a_j\varepsilon(\mathbf{m}\times\mathbf{m}\times\mathbf{p})] \quad (9)$$

with β as the secondary parameter that describes the torque (usually set to 0 or equal to the damping parameter α_G). The variable a_j is defined in terms of current density j:

$$a_j = \frac{\hbar j}{eM_s t_{FM}} \quad (10)$$

where $\hbar$ is the reduced Planck constant and e is the electron charge. Furthermore, the variable ε depends on λ, the parameter of the spacer layer derived by Slonczewski, and η, the efficiency of the spin current polarisation ($0 \le \eta \le 1$):

$$\varepsilon = \frac{\eta\lambda^2}{\lambda^2 + 1 + (\lambda^2 - 1)\mathbf{m}\cdot\mathbf{p}} \quad (11)$$

Often, λ is set to 1, which consequently removes the dependence of torque magnitudes on $\mathbf{m}\cdot\mathbf{p}$.

Field contributions

In this section, we describe in detail the methods for computing field contributions. The effective field vector $\mathbf{H}_{eff}$ is usually composed of various field contributions that, depending on the context of the simulation, may be added or disabled. CMTJ provides a range of such contributions:

$$\mathbf{H}_{eff} = \mathbf{H}_{ext} + \mathbf{H}_{IEC} + \mathbf{H}_{Oe} + \mathbf{H}_K + \mathbf{H}_{demag} + \mathbf{H}_{dipole} + \mathbf{H}_{th}^* + \mathbf{H}_{1/f}^* \quad (12)$$

where each component corresponds, respectively, to the applied external field, interlayer exchange coupling (IEC), Oersted field, anisotropy field, demagnetising, dipole, thermal, and $1/f$ noise field[60] (all expressed in $A\,m^{-1}$). Contributions marked with * require a stochastic solver. Each of the contributions that constitute $\mathbf{H}_{eff}$ may be varied over time using a driver system, as laid out in the section "Excitation drivers".

Anisotropy field. In CMTJ, the anisotropy contribution has two parameters—the axis **a** which determines a uniaxial anisotropy vector and the scalar value K_u which determines the amplitude of the anisotropy field. The axis parameter is passed in the layer constructor function. However, the scalar value can be driven dynamically using a *Driver* mechanism using the *Layer* or *Junction* API. The formula we use in CMTJ is as follows:

$$\mathbf{H}_K = \frac{2K_u}{\mu_0 M_s}(\mathbf{m}\cdot\mathbf{a})\mathbf{a} \quad (13)$$

Interlayer exchange coupling field. The interlayer exchange coupling governs the RKKY-like interaction between neighbouring FM layers separated by a metallic spacer[61]. In CMTJ we include both linear (J_{linear}) and quadratic (J_{quad}) contributions. The contribution enters the effective field of layer i as a result of the interaction with layer j in the form:

$$\mathbf{H}_{IEC,i} = \frac{1}{\mu_0 M_s t_{FM}}[J_{linear}\mathbf{m}_j + 2J_{quad}(\mathbf{m}_i\cdot\mathbf{m}_j)\mathbf{m}_j] \quad (14)$$

If a given FM layer is sandwiched between two other FM layers, then the engine will compute the IEC contribution from the top and bottom layers separately and then add them both to the effective field.

Demagnetisation and dipole fields. The demagnetisation interaction has a source in the geometry of the sample. On the other hand, the dipole interaction is a long-range interaction that originates from coupling with other FM layers. Both demagnetisation and dipole fields can be calculated from the tool linked in the repository CMTJ (https://github.com/pawelkulig1/Demagnetization-Tensor-Tool). The tool computes a dipole and demagnetising tensor based on the finite difference method and analytical calculations derived in refs. [62–64]. These tensors can be set directly in the simulation. Specifically, the demagnetisation tensor is passed through the constructor of a *Layer*. The dipole is set using *setBottomDipoleTensor* if the interaction originates from the top layers relative to the current layers or *setTopDipoleTensor* if the dipole interaction originates from the FM layers underneath. The field contribution of dipole and demagnetisation hence takes the form:

$$\mathbf{H}_{dipole/demag} = -M_s\mathbf{N}\mathbf{m} \quad (15)$$

where $\mathbf{N}$ is the dipole or demagnetisation tensor and $\mathbf{m}$ is the magnetisation of the current layer (demagnetisation) or the coupled layer (dipole). Often the demagnetisation tensor may be approximated by its diagonal when the off-diagonal terms become negligible compared to the diagonal ones.

Oersted field. The Oersted field is statically modelled in CMTJ, which means that users can dynamically change it during simulation, but it is not precomputed based on the input current. Obtaining a value of the Oersted field in an element may be a complicated problem. For simple FM/HM bilayer systems[41], the Oersted field can be calculated from a simple relation: $H_{Oe} = jt_{HM}/2$ where t_{HM} is the thickness of the HM. In more involved cases, numerical integration or variations of finite-difference methods are required to obtain a precise result.

Table 1. Example of serial execution times and the number of steps per experiment.

Benchmark	Steps [10^6]	Time [s]	Steps per s [10^3 per s]
M(H), R(H), PIMM	50	42	1190
CIMS	187.5	823	228
Spin valve VSD	1872	748	2503
Spin valve PIMM	360	315	1143
Stack synchronisation	120	62	1935

The number of steps summarises all sweeps over parameters, fields, frequencies, and the number of iterations during the simulation time. The timing was done on a MacBook Pro 2020 with an Apple M1 processor and 16 GB of RAM. Some experiments, such as, for instance, CIMS, involve more parameter scanning than individual simulation steps, so they are less efficient than simulations with longer in-simulation time, such as VSD for the spin valve system.

1/f field. The amplitude of the noise field 1/*f* is calculated using a modified Voss–McCartney–Trammel (VMT) algorithm[60]. Being a stochastic contribution, it has the following form:

$$\mathbf{H}_{1/f} = c\eta_{\mathrm{VMT}}\mathrm{d}\mathbf{W_t} \tag{16}$$

where c is the scaling parameter, η_{VMT} is generated from the VMT algorithm, and $\mathrm{d}\mathbf{W_t}$ is the random unit vector. The user specifies a number of generating sources k, and a Bernoulli distribution bias parameter p. At each generation step, k numbers are drawn from the Bernoulli distribution, each representing a source active in that step. For each unique index, a random float is generated, contributing to the total amplitude of the 1/*f* noise, η_{VMT}.

Solver methods

The core solver for most of the systems in CMTJ is the Runge–Kutta 4 (RK4) algorithm, as it balances decent convergence with speed. However, if the user specifies a temperature component for the system, CMTJ switches to the stochastic solver, using the Euler–Heun or Heun method, and solves the Stratonovich form of the LLG equation[65]:

$$\mathrm{d}\mathbf{m}(t) = \mathbf{f}(\mathbf{m}(t), t)\Delta t + \mathbf{g}(\mathbf{m}(t), t) \circ \mathrm{d}\mathbf{W_t}\sqrt{\Delta t} \tag{17}$$

where the non-stochastic part $\mathbf{f}(\mathbf{m}(t), t)$ is the LL form of the LLG equation, while the stochastic part, $\mathbf{g}(\mathbf{m}(t), t)$ contains thermal and other stochastic contributions. Δt is the integration step of the numerical method. For example, in the Langevin thermal field, we have the following:

$$\mathbf{g}(\mathbf{m}_t, t) \circ \mathrm{d}\mathbf{W_t} = -\frac{\sigma\gamma}{1+\alpha^2}\left[\mathbf{m}\times\mathrm{d}\mathbf{W_t} + \alpha\mathbf{m}\times(\mathbf{m}\times\mathrm{d}\mathbf{W_t})\right] \tag{18}$$

where $\mathrm{d}\mathbf{W_t}$ is the random unit vector whose components are sampled from the normal distribution with zero mean, $\mathcal{N}(0,1)$, σ is the standard deviation of thermal noise[66,67]. From our experience, an optimal integration time should be of the order of at least a picosecond, or tenths of a picosecond, for either type of solver, which was verified experimentally. In cases involving strong IEC coupling or larger stochastic excitation, even shorter integration times may be required. In cases involving strong IEC coupling or larger stochastic excitation, much lower integration times may be required.

Magnetoresistance

Apart from tunnelling and giant magnetoresistance, which are calculated as per Eq. (3), we also include methods to compute longitudinal R_{xx} and transverse R_{xy} magnetoresistance[21], expressed in terms of magnetisation vector components:

$$R_{xx} = R_{xx0} + \left(\Delta R_{\mathrm{AMR}} m_x^2 + \Delta R_{\mathrm{SMR}} m_y^2\right) \tag{19}$$

$$R_{xy} = R_{xy0} + \frac{1}{2}\Delta R_{\mathrm{AHE}} m_z + \frac{w}{l}(\Delta R_{\mathrm{SMR}} + \Delta R_{\mathrm{AMR}}) m_x m_y \tag{20}$$

where w and l are the width and length of the sample. ΔR_{SMR}, ΔR_{AMR}, ΔR_{AHE} are the magnitudes of the spin-Hall, anisotropic, and Anomalous Hall Effect resistances, respectively. R_{xx0} and R_{xy0} are base longitudinal and transverse resistances.

Benchmarks

The CMTJ is meant to run on personal computers as well. In Table 1 we present example execution times for more computationally challenging examples described in the sections "*M*(*H*) and *R*(*H*) loops, Spin valve dynamics, Angular harmonic Hall voltage detection, CIMS, and Electrical coupling". The runtimes were recorded on a typical 2020 MacBook Pro with Apple Silicon M1 with 16 GB RAM. In the table, the step column designates the number of RK4 steps. For example, in the spin valve VSD experiment, we scan with a field for every frequency; therefore, the total number of steps is frequency steps × field steps × (simulation time/integration time). The measured times in Table 1 are given for a serial execution of each experiment. However, the CMTJ library also includes additional helper functions that allow for easy parallelism, designed for simulations performed across multiple parameter spaces.

DATA AVAILABILITY

The data supporting the findings of this study are available from the corresponding author on a reasonable request.

CODE AVAILABILITY

Code used in this work is open source and can be accessed free of charge under the following webpage https://github.com/LemurPwned/cmtj (the release version for this article is marked as 1.3.0). The examples section in the repository contains the code required to reproduce the results presented in this manuscript.

Received: 11 August 2022; Accepted: 16 March 2023;
Published online: 06 April 2023

REFERENCES

1. Dieny, B. et al. Opportunities and challenges for spintronics in the microelectronics industry. *Nat. Electron.* **3**, 446–459 (2020).
2. Ikegawa, S., Mancoff, F. B., Janesky, J. & Aggarwal, S. Magnetoresistive random access memory: present and future. *IEEE Trans. Electron Devices* **67**, 1407–1419 (2020).
3. Xu, Y., Yang, Y., Luo, Z., Xu, B. & Wu, Y. Macro-spin modeling and experimental study of spin–orbit torque biased magnetic sensors. *J. Appl. Phys.* **122**, 193904 (2017).
4. Hirohata, A. et al. Review on spintronics: principles and device applications. *J. Magn. Magn. Mater.* **509**, 166711 (2020).
5. Vansteenkiste, A. et al. The design and verification of MuMax3. *AIP Adv.* **4**, 107133 (2014).
6. Donahue, M. J. & Porter, D. G. *OOMMF User's Guide, Version 1.0* (National Institute of Standards and Technology (NIST), 1999). https://doi.org/10.6028/NIST.IR.6376.
7. Kresse, G. & Hafner, J. Ab initio molecular dynamics for liquid metals. *Phys. Rev. B* **47**, 558–561 (1993).
8. Giannozzi, P. et al. QUANTUM ESPRESSO: a modular and open-source software project for quantum simulations of materials. *J. Phys. Condens. Matter* **21**, 395502 (2009).
9. Giannozzi, P. et al. Advanced capabilities for materials modelling with quantum ESPRESSO. *J. Phys. Condens. Matter* **29**, 465901 (2017).
10. Evans, R. F. L. et al. Atomistic spin model simulations of magnetic nanomaterials. *J. Phys. Condens. Matter* **26**, 103202 (2014).

11. Müller, G. P. et al. *Spirit*: multifunctional framework for atomistic spin simulations. *Phys. Rev. B* **99**, 224414 (2019).
12. Garg, R., Kumar, D., Jindal, N., Negi, N. & Ahuja, C. Behavioural model of spin torque transfer magnetic tunnel junction, using Verilog-A. *Int. J. Adv. Res. Technol.* **1**, 36–42 (2012).
13. Chen, T. et al. Comprehensive and macrospin-based magnetic tunnel junction spin torque oscillator model—Part II: Verilog-A model implementation. *IEEE Trans. Electron Devices* **62**, 1045–1051 (2015).
14. Chen, T. et al. Comprehensive and macrospin-based magnetic tunnel junction spin torque oscillator model—Part I: analytical model of the MTJ STO. *IEEE Trans. Electron Devices* **62**, 1037–1044 (2015).
15. Slonczewski, J. Current-driven excitation of magnetic multilayers. *J. Magn. Magn. Mater.* **159**, L1–L7 (1996).
16. Ogrodnik, P. et al. Study of spin–orbit interactions and interlayer ferromagnetic coupling in Co/Pt/Co trilayers in a wide range of heavy-metal thickness. *ACS Appl. Mater. Interfaces* **13**, 47019–47032 (2021).
17. Kiselev, S. I. et al. Microwave oscillations of a nanomagnet driven by a spin-polarized current. *Nature* **425**, 380–383 (2003).
18. Myers, E. B., Ralph, D. C., Katine, J. A., Louie, R. N. & Buhrman, R. A. Current-induced switching of domains in magnetic multilayer devices. *Science* **285**, 867–870 (1999).
19. Nozaki, T. et al. Electric-field-induced ferromagnetic resonance excitation in an ultrathin ferromagnetic metal layer. *Nat. Phys.* **8**, 491 (2012).
20. Wenzel, J., Rhinelander, J. & Moldovan, D. pybind11 — Seamless operability between C++11 and Python. https://github.com/pybind/pybind11 (2017).
21. Kim, J., Sheng, P., Takahashi, S., Mitani, S. & Hayashi, M. Spin Hall magnetoresistance in metallic bilayers. *Phys. Rev. Lett.* **116**, 097201 (2016).
22. Katayama, T. et al. Interlayer exchange coupling in Fe/MgO/Fe magnetic tunnel junctions. *Appl. Phys. Lett.* **89**, 112503 (2006).
23. Kozioł-Rachwał, A. et al. Interlayer exchange coupling, dipolar coupling and magnetoresistance in Fe/MgO/Fe trilayers with a subnanometer MgO barrier. *J. Magn. Magn. Mater.* **424**, 189–193 (2017).
24. Liu, L. et al. Spin-torque switching with the giant spin Hall effect of tantalum. *Science* **336**, 555–558 (2012).
25. Miron, I. M. et al. Perpendicular switching of a single ferromagnetic layer induced by in-plane current injection. *Nature* **476**, 189–193 (2011).
26. Taniguchi, T., Tsunegi, S. & Kubota, H. Mutual synchronization of spin-torque oscillators consisting of perpendicularly magnetized free layers and in-plane magnetized pinned layers. *Appl. Phys. Express* **11**, 013005 (2018).
27. Cho, S., Baek, S.-hC., Lee, K.-D., Jo, Y. & Park, B.-G. Large spin Hall magnetoresistance and its correlation to the spin–orbit torque in W/CoFeB/MgO structures. *Sci. Rep.* **5**, 14668 (2015).
28. Rzeszut, P., Skowroński, W., Ziętek, S., Ogrodnik, P. & Stobiecki, T. Biaxial magnetic-field setup for angular-dependent measurements of magnetic thin films and spintronic nanodevices. *IEEE Trans. Magn.* **54**, 1–7 (2018).
29. Avci, C. O. et al. Unidirectional spin Hall magnetoresistance in ferromagnet/normal metal bilayers. *Nat. Phys.* **11**, 570–575 (2015).
30. Vélez, S. et al. Hanle magnetoresistance in thin metal films with strong spin–orbit coupling. *Phys. Rev. Lett.* **116**, 016603 (2016).
31. McKinnon, T., Heinrich, B. & Girt, E. Spacer layer thickness and temperature dependence of interlayer exchange coupling in Co/Ru/Co trilayer structures. *Phys. Rev. B* **104**, 024422 (2021).
32. Ziętek, S. et al. The influence of interlayer exchange coupling in giant-magnetoresistive devices on spin diode effect in wide frequency range. *Appl. Phys. Lett.* **107**, 122410 (2015).
33. Ziętek, S. et al. Rectification of radio frequency current in giant magnetoresistance spin valve. *Phys. Rev. B* **91**, 014430 (2015).
34. Tulapurkar, A. A. et al. Spin-torque diode effect in magnetic tunnel junctions. *Nature* **438**, 339–342 (2005).
35. Sankey, J. C. et al. Measurement of the spin-transfer-torque vector in magnetic tunnel junctions. *Nat. Phys.* **4**, 67–71 (2008).
36. Kittel, C. On the theory of ferromagnetic resonance absorption. *Phys. Rev.* **73**, 155–161 (1948).
37. Baselgia, L. et al. Derivation of the resonance frequency from the free energy of ferromagnets. *Phys. Rev. B* **38**, 2237–2242 (1988).
38. Silva, T. J., Lee, C. S., Crawford, T. M. & Rogers, C. T. Inductive measurement of ultrafast magnetization dynamics in thin-film permalloy. *J. Appl. Phys.* **85**, 7849–7862 (1999).
39. Serrano-Guisan, S. et al. Inductive determination of the optimum tunnel barrier thickness in magnetic tunneling junction stacks for spin torque memory applications. *J. Appl. Phys.* **110**, 023906 (2011).
40. Banasik, M. et al. Magnetic properties and magnetization dynamics of magnetic tunnel junction bottom electrode with different buffer layers. *IEEE Trans. Magn.* **51**, 1–4 (2015).
41. Liu, L., Moriyama, T., Ralph, D. C. & Buhrman, R. A. Spin-torque ferromagnetic resonance induced by the spin Hall effect. *Phys. Rev. Lett.* **106**, 036601 (2011).
42. Pai, C.-F. et al. Spin transfer torque devices utilizing the giant spin Hall effect of tungsten. *Appl. Phys. Lett.* **101**, 122404 (2012).
43. Hao, Q. & Xiao, G. Giant spin Hall effect and switching induced by spin-transfer torque in a W/Co40Fe40B20/MgO structure with perpendicular magnetic anisotropy. *Phys. Rev. Appl.* **3**, 034009 (2015).
44. Kim, J. et al. Layer thickness dependence of the current-induced effective field vector in Ta|CoFeB|MgO. *Nat. Mater.* **12**, 240–245 (2013).
45. Nguyen, M.-H. & Pai, C.-F. Spin–orbit torque characterization in a nutshell. *APL Mater.* **9**, 030902 (2021).
46. Ziętek, S. et al. Numerical model of harmonic Hall voltage detection for spintronic devices. *Phys. Rev. B* **106**, 024403 (2022).
47. Avci, C. O. et al. Interplay of spin–orbit torque and thermoelectric effects in ferromagnet/normal-metal bilayers. *Phys. Rev. B* **90**, 224427 (2014).
48. Fritz, K., Wimmer, S., Ebert, H. & Meinert, M. Large spin Hall effect in an amorphous binary alloy. *Phys. Rev. B* **98**, 094433 (2018).
49. Skowroński, W. et al. Angular harmonic Hall voltage and magnetoresistance measurements of Pt/FeCoB and Pt-Ti/FeCoB bilayers for spin Hall conductivity determination. *IEEE Trans. Electron Devices* **68**, 6379–6385 (2021).
50. Grochot, K. et al. Current-induced magnetization switching of exchange-biased NiO heterostructures characterized by spin–orbit torque. *Phys. Rev. Appl.* **15**, 014017 (2021).
51. Lee, K.-S., Lee, S.-W., Min, B.-C. & Lee, K.-J. Threshold current for switching of a perpendicular magnetic layer induced by spin Hall effect. *Appl. Phys. Lett.* **102**, 112410 (2013).
52. Romera, M. et al. Binding events through the mutual synchronization of spintronic nano-neurons. *Nat. Commun.* **13**, 883 (2022).
53. Locatelli, N., Cros, V. & Grollier, J. Spin-torque building blocks. *Nat. Mater.* **13**, 11–20 (2014).
54. Camsari, K. Y., Ganguly, S. & Datta, S. Modular approach to spintronics. *Sci. Rep.* **5**, 10571 (2015).
55. Nomura, H. et al. Reservoir computing with dipole-coupled nanomagnets. *Jpn. J. Appl. Phys.* **58**, 070901 (2019).
56. Akashi, N. et al. A Coupled spintronics neuromorphic approach for high-performance reservoir computing. *Adv. Intell. Syst.* **4**, 2200123 (2022).
57. Gilbert, T. Classics in magnetics: a phenomenological theory of damping in ferromagnetic materials. *IEEE Trans. Magn.* **40**, 3443–3449 (2004).
58. Ralph, D. & Stiles, M. Spin transfer torques. *J. Magn. Magn. Mater.* **320**, 1190–1216 (2008).
59. Ament, S., Rangarajan, N., Parthasarathy, A. & Rakheja, S. Solving the stochastic Landau–Lifshitz–Gilbert–Slonczewski equation for monodomain nanomagnets: a survey and analysis of numerical techniques. Preprint at http://arxiv.org/abs/1607.04596 (2017).
60. Voss, R. F. "1/*f* noise" in music: music from 1/*f* noise. *J. Acoust. Soc. Am.* **63**, 258 (1978).
61. Parkin, S. S. P. Systematic variation of the strength and oscillation period of indirect magnetic exchange coupling through the 3*d*, 4*d*, and 5*d* transition metals. *Phys. Rev. Lett.* **67**, 3598–3601 (1991).
62. Schabes, M. & Aharoni, A. Magnetostatic interaction fields for a three-dimensional array of ferromagnetic cubes. *IEEE Trans. Magn.* **23**, 3882–3888 (1987).
63. Newell, A. J., Williams, W. & Dunlop, D. J. A generalization of the demagnetizing tensor for nonuniform magnetization. *J. Geophys. Res.* **98**, 9551 (1993).
64. Fukushima, H., Nakatani, Y. & Hayashi, N. Volume average demagnetizing tensor of rectangular prisms. *IEEE Trans. Magn.* **34**, 193–198 (1998).
65. Bertotti, G., Mayergoyz, I. D. & Serpico, C. in *Chapter 10—Stochastic Magnetization Dynamics* (eds Bertotti, G., Mayergoyz, I. D. & Serpico, C.) *Nonlinear Magnetization Dynamics in Nanosystems* Elsevier Series in Electromagnetism 271–357 (Elsevier, Oxford, 2009).
66. Brown, W. F. Thermal fluctuations of a single-domain particle. *Phys. Rev.* **130**, 1677–1686 (1963).
67. Kubo, R. & Hashitsume, N. Brownian motion of spins. *Prog. Theor. Exp. Phys.* **46**, 210–220 (1970).

ACKNOWLEDGEMENTS

We thank P. Ogrodnik for a fruitful and insightful discussion. The research project is partially supported by the National Science Centre, Poland project no.2021/40/Q/ST5/00209 (Sheng), the Excellence initiative-research university programme of the AGH University of Science and Technology and by the Polish Ministry of Education and Science under subvention funds for the Institute of Electronics AGH. T.S. and K.G. were supported by the National Science Centre, Poland, Grant No. UMO-2016/23/B/ST3/01430 (SPINORBITRONICS). For the purpose of Open Access, the author has applied a CC-BY public copyright licence to any Author Accepted Manuscript (AAM) version arising from this submission.

AUTHOR CONTRIBUTIONS

J.M. developed the simulation software. S.Z. and J.M. contributed to the model, analysed results and wrote the article. K.G., W.S. and T.S. provided experimental data and extensive feedback on the article.

COMPETING INTERESTS

The authors declare no competing interests.

ADDITIONAL INFORMATION

Supplementary information The online version contains supplementary material available at https://doi.org/10.1038/s41524-023-01002-x.

Correspondence and requests for materials should be addressed to Jakub Mojsiejuk or Sławomir Ziętek.

Reprints and permission information is available at http://www.nature.com/reprints

Publisher's note Springer Nature remains neutral with regard to jurisdictional claims in published maps and institutional affiliations.

Reinforcement learning for spin torque oscillator tasks

J. Mojsiejuk, S. Ziętek and W. Skowroński

Institute of Electronics, AGH University of Kraków, Kraków, Poland

E-mail: mojsieju@agh.edu.pl

Abstract. We address the problem of automatic synchronisation of the spintronic oscillator (STO) by means of reinforcement learning (RL). A numerical solution of the macrospin Landau-Lifschitz-Gilbert-Slonczewski equation is used to simulate the STO and we train the two types of RL agents to synchronise with a target frequency within a fixed number of steps. We explore modifications to this base task and show an improvement in both convergence and energy efficiency of the synchronisation that can be easily achieved in the simulated environment.

1 Introduction

Spintronic oscillators (STO) [1] come in many forms and shapes and appear in a number of interesting technical applications, such as magnetic field sensors [2], or in wireless communication [3]. More recently, a greater focus has been placed on neuromorphic applications that employ multiple oscillators, usually electrically connected [4, 5, 6]. Many of the aforementioned uses of STOs are based on the consistent fabrication of oscillators and tuning of the mutual frequencies using current, and some even require real-time control. In the wake of rapidly arising interest in reinforcement learning (RL) applications, one avenue is to pretrain an RL controller (an agent) on a simulated environment, then tune it and deploy in a real environment. This approach, using the actor-critic model, has been demonstrated to work well in some physical applications, such as plasma control [7, 8]. From an experimental point of view, the main advantage is that, in a simulation, an RL agent can observe more unique events on a shorter time scale for a wide range of parameters.

This study addresses the challenge of adapting control inputs to a magnetic tunnel junction (MTJ) optimised for STO operation to reach the desired frequency efficiently, starting from randomly chosen magnetic parameters. To achieve that, we apply two RL algorithms and train the models to converge to a desired target frequency in a smooth fashion. The advantage of using RL, compared to conventional methods known from control theory, such as proportional-integral-derivative (PID) controllers, is that an RL agent can implicitly learn the complex dependency of device parameters on the frequency spectra and, once trained, operates on devices with a wide parameter spread without the need for re-tuning. In addition, RL frameworks provide versatility in the design of a reward system, facilitating an intuitive definition of the optimisation objective, which is also investigated in this study.

2 Theoretical background

We employ a numerical solution of the Landau-Lifschitz-Gilbert-Slonczewski (LLGS) macrospin equation using the Runge-Kutta 4th order method as the main basis of our simulation [9, 10, 11, 12]. This approach enables time-series analysis which is close to what can be expected in the experimental setup. We define an operator $\tilde{\mathbf{M}}$ acting on some effective field term $\mathbf{H}_{\text{eff}}$:

$$\tilde{\mathbf{M}}(\mathbf{H}_{\text{eff}}, \eta_1, \eta_2) = \eta_1 \mathbf{m} \times \mathbf{H}_{\text{eff}} + \eta_2 \mathbf{m} \times \mathbf{m} \times \mathbf{H}_{\text{eff}} \tag{1}$$

where $\mathbf{m}$ is the magnetisation at time t, and η_1, η_2 are field-like and damping-like weighting terms respectively. The magnetisation dynamics is then described by the LLGS equation of the following form:

$$\frac{\mathrm{d}\mathbf{m}}{\mathrm{dt}} = \frac{-\gamma_0}{1+\alpha_\mathrm{G}^2}[\tilde{\mathbf{M}}(\mathbf{H}_\mathrm{eff}, 1, \alpha_\mathrm{G}) + \tilde{\mathbf{M}}(\boldsymbol{\sigma}, -\eta_\mathrm{FL}, \eta_\mathrm{DL})] \tag{2}$$

where $\boldsymbol{\sigma}$ denotes the fixed polarisation vector that depends on the MTJ configuration, α_G is Gilbert's damping term, $\eta_\mathrm{DL} = a_j\epsilon$ is the damping-like torque, and $\eta_\mathrm{FL} = \beta\eta_\mathrm{DL}$ is the field-like torque. a_j is defined as:

$$a_j = \frac{\hbar j_e}{e\mu_0 \mathrm{M_s} t_\mathrm{FM}} \tag{3}$$

and ϵ is:

$$\epsilon = \frac{P\lambda^2}{\lambda^2 + 1 + (\lambda^2 - 1)(\mathbf{m}\cdot\boldsymbol{\sigma})} \tag{4}$$

where j_e is the current density, $\mu_0\mathrm{M_s}$ is the magnetisation saturation, $\hbar$ is Planck's constant, e is the electron charge, t_FM is the thickness of the ferromagnetic layer, P is the spin current polarisation efficiency, λ is the angular parameter. β is used as a scaling term for the field-like torque.

In our simulations, we assume that fixed layer polarisation is a unit vector along the x axis, that is, $\boldsymbol{\sigma} = \hat{\mathbf{e}}_x$. In the effective field $\mathbf{H}_\mathrm{eff}$ term we account for the external, applied magnetic field, $\mathbf{H}_\mathrm{ext}$, the anisotropy field, $\mathbf{H}_\mathrm{anis}$, and the demagnetizing field, $\mathbf{H}_\mathrm{demag}$:

$$\mathbf{H}_\mathrm{eff} = \mathbf{H}_\mathrm{ext} + \mathbf{H}_\mathrm{anis} + \mathbf{H}_\mathrm{demag} \tag{5}$$

Details on the implementation of the effective field contributions can be found in [13]. Training successful RL agents requires many iterations and therefore the speed of the simulation is important, hence we use macrospin models from the CMTJ library [13], although the steps described here can also be reproduced with micromagnetic packages, for example MUMAX3 [14].

3 Environment design

Often, the key part of constructing a successful RL system lies in the design of the environment. In our basic setting, we mimic an experimental measurement setup of an STO, as pictured in Fig.1a). A trilayer CoFeB/MgO/CoFeB-like MTJ is placed in an external magnetic field generated by an electromagnet. An adjustable direct current (DC) source is connected to the MTJ via the inductive terminal of the bias tee. The spin torque exerted on the free layer via the STT effect induces the precession of the free layer $\mathbf{m}$, which in turn leads to the oscillating voltage signal picked up on the capacitive terminal of the bias tee. Both the direction and the magnitude of the external magnetic field as well as the magnitude of the DC supply are assumed to be controlled by a black-box controller.

We allow the field to vary between 50 and 1200 kA/m, and both polar (θ) and azimuthal (ϕ) lie in the $(0, \pi/2)$ range. The controller can adjust the current density j_e between $\sim 10^{10}$-$10^{11}\mathrm{A/m^2}$ [16]. Together, they form an action tuple $(j_e, H_\mathrm{ext}, \theta, \phi)$ and are passed to an RL algorithm in a normalised way, with values bounded $[-1, 1]$. The MTJ itself is modelled magnetically primarily using two parameters: the magnetic perpendicular anisotropy constant $\mathrm{K_u}$ and the magnetisation saturation $\mu_0\mathrm{M_s}$. Given an action, i.e. the input from the controller, we can configure a simulation with corresponding current density and magnetic field values. To ensure rapid training, we set the integration time at 1 ps and the simulation time at about 10 ns, which are sufficiently large to have a good resolution of the resonance spectrum for this system. For more complicated systems, a smaller integration step is required. In this example, the simulation solves the LLGS model (2) with preset STT parameters ($\lambda = 0.69, \beta = \alpha_\mathrm{G}, P = 1$), because the device will operate in a subswitching regime [10]. At each step, the magnetisation of the agent is first reset to the same initial, semi-stable condition to avoid numerical issues, specifically non-harmonic oscillations in the spectrum resulting from sudden change of the input. In principle, the simulation can be extended and a couple of initial nanoseconds of the run can be discarded to approximate a stable state, but that would increase the cost and time of the simulation, without much added generality. In the experiment, the pause between actions provides enough relaxation time, so the concept of restarting the initial conditions does not exist.

Another component of the RL setup is the observation space. As illustrated in Fig.1a), in the experiment we can only observe the oscillating magnetisation $\mathbf{m}$ indirectly through a resistance measurement. In our setup, we rely on tunnelling magnetoresistance (TMR) calculation, as per formula [17]:

$$R(\mathbf{m}, \boldsymbol{\sigma}) = R_\mathrm{P} + \frac{1}{2}(R_\mathrm{AP} - R_\mathrm{P})(1 - \mathbf{m}\cdot\boldsymbol{\sigma}) \tag{6}$$

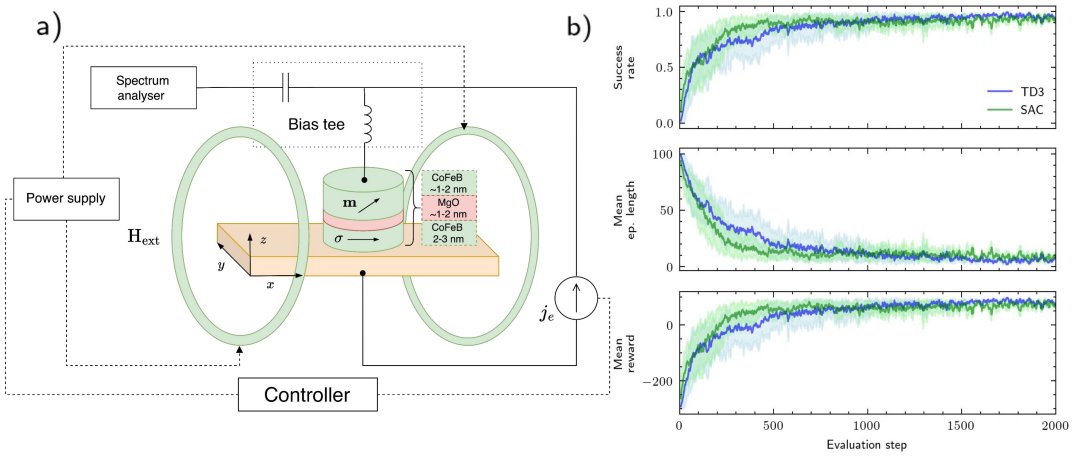

Figure 1: System schematics and training results. (a) The design of a synchronisation task setup which corresponds to a typical experimental setup used for spintronic oscillators [15]. Green solenoids represent an electromagnet producing the external magnetic field, in which the sample can be rotated. In the simulation we rotated the field instead of the sample, but those two designs are equivalent. The controller manipulates the sample (field) rotation, the field magnitude and the magnitude of the current fed into the sample. A typical experimental structure consists of a trilayer stack CoFeB(1-2 nm)/MgO(1-2 nn)/CoFeB(2-3 nm). (b) Success rate for a SAC and TD3 agent for the oscillator tuning environment, averaged across 8 runs. After reaching about 1500 evaluation steps the agents achieve almost 100% success rate of synchronising a randomly sampled MTJ to a desired frequency within limited number of steps. The imperfect score results derive from synchronisation achieved beyond the designated number of steps and the boundary target frequency sampling.

where R_{P} denotes the resistance in the parallel state and R_{AP} denotes the resistance in the anti-parallel state. From the measured time series of the resistance, we extract its frequency spectrum with FFT, after allowing first $1-2$ns for relaxation to avoid aharmonic frequencies in the output spectrum. Thus, the observation feature consists of the peak frequency of STO, $f_{\max}$, the difference between the target frequency and the peak frequency: $\varepsilon^* = |f_{\max} - f^*|$, the difference between the peak frequency in the previous step $(t-1)$ and the current step t, $f_{\mathrm{diff}} = f_{\max}^{t-1} - f_{\max}^{t}$, the rate of change of the frequency with respect to the current, f_{diff}/dj, and with respect to the field, f_{diff}/dh, or any of the field angles, $f_{\mathrm{diff}}/d\theta$, $f_{\mathrm{diff}}/d\phi$. In the end, similarly to the action input, the observation feature is normalised to $[-1, 1]$, using some sensible limiting values, such as the maximum possible frequency of oscillation given the magnetic parameters. Normalisation of the action and the observation space is critical to the proper operation of network-based algorithms, as spurious inputs result in likewise spurious gradients, which worsen both the convergence and the stability of training.

4 Simulation results

In our tests, the best results were given by the twin delayed deep-deterministic gradient (TD3) [18] and soft actor-critic (SAC) [19] algorithms. The baseline reward engineering assumes a fixed small negative reward for each step where the STO frequency is not sufficiently close to the target frequency, that is, $\varepsilon^* > \varepsilon_0$. If $\varepsilon^* < \varepsilon_0$, a large positive reward, $\hat{\mathcal{R}}_{\mathrm{sync}}$, is ascribed and the episode is terminated. Each episode is capped with a maximum number of steps; in our case, we set it to either 50 or 100 attempts at synchronisation. Fig.1b) presents the average of 8 runs in TD3 and SAC for the baseline simulation. At the beginning of each episode, we randomly sample the device $(\mu_0 \mathrm{M_s}, \mathrm{K_u})$ and the target frequency f^* such that the frequency target falls within the achievable frequency range under specified action limits. In our experiments, we generally used a constant learning rate of about 0.002, the discount factor of 0.98, and small actor feedforward networks [64, 64], where 64 is the number of hidden units per layer.

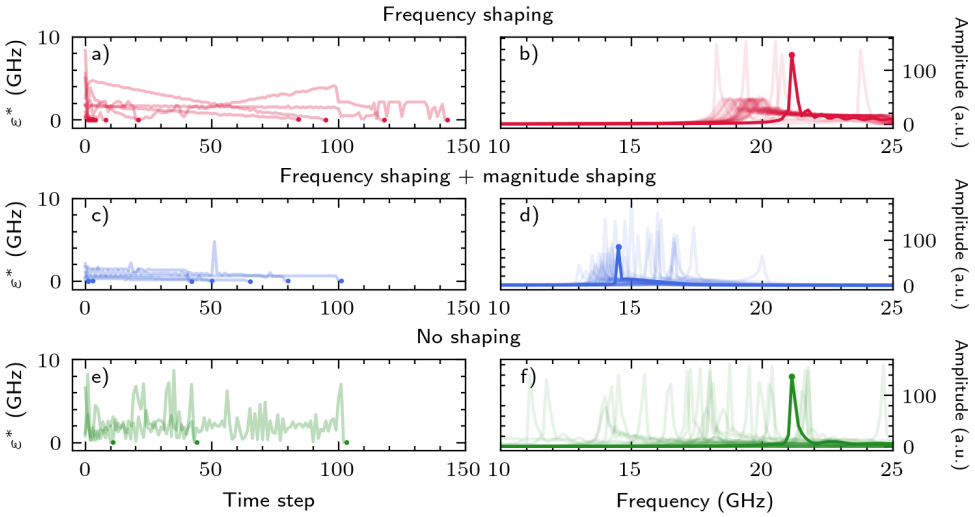

Figure 2: The effect of the reward shaping strategies on the sample trajectories. (a) shows the RL agent with plain frequency reward shaping depending on the ε^*, (c) frequency reward shaping and a punishment on the magnitude of the action derivative, and (e) presents baseline with a fixed punishment for each step taken, with no reward signal on neither action derivative magnitude nor ε^*. (b, d, f) show a sample trajectory from an agent with frequency reward shaping, frequency reward shaping and punishment on the magnitude of action derivative, and no shaping respectively. Synchronised state is given in the most opaque colour. As seen in (f), the agent with no shaping is more eager to explore a wider range of frequencies which may lead to the sample deterioration due to drastic changes in applied field or current.

4.1 Reward shaping

In the following, we describe the influence of different changes to the reward system on the controller's ability to smoothly synchronise to a desired frequency. In reward shaping, the punishment applied at each step when the STO is not synchronised to the desired frequency is proportional to the difference between the target and the achieved frequency:

$$\mathcal{R}_{\delta \mathrm{f}} = |\varepsilon^* - \varepsilon_0|. \tag{7}$$

Secondly, we consider energy optimisation and smoothness of the transition. Drastic changes in the current density and field magnitude result in a greater amount of energy being used and may be detrimental to the devices under test. Thus, it is desirable to reduce the magnitude of the action derivatives taken at each step as much as possible. We compute the square of the normalised action derivative vector and assign an additional weighted punishment to the agent proportional to its magnitude:

$$\mathcal{R}_{\delta \mathrm{a}} = (a_t - a_{t-1})^2 \tag{8}$$

where a_t denotes normalised action taken at time t. The results showing the impact of $\mathcal{R}_{\delta \mathrm{f}}$ and $\mathcal{R}_{\delta \mathrm{a}}$ are shown in Fig.2. Introducing reward shaping (7) causes smoother exploration of the action space and, thus, results in less chaotic convergence overall. Punishment on the magnitude of the action derivative (8) produces even smoother convergence, where each action parameter was slightly tweaked, rather than being rotated by larger values. Because we limit the action to sensible values, the agent necessarily must use values of the external field or current density that should not destroy the sample.

Finally, we may wish to synchronise with a greatest possible Q-factor. To that end, we employ the normalised Q-factor definition:

$$\hat{\mathcal{R}}_{\mathrm{Q}^*} = \frac{\mathcal{A}_r}{\Delta f} \tag{9}$$

where $\mathcal{A}_r$ is the amplitude at the oscillating frequency and Δf is the bandwidth defined as the width at full width at half maximum. We prefer this definition because it does not promote a behaviour that

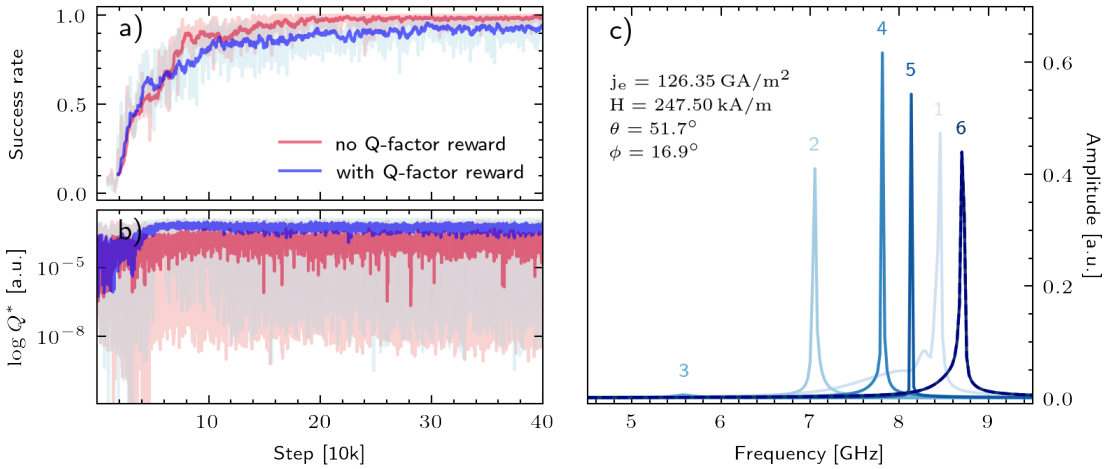

Figure 3: The effect of the Q-factor reward shaping, averaged over 8 runs per each variant. (a-b) present the success rate and Q-factor values over time for SAC with Q factor reward enabled (blue) and disabled (red). (b) the agent with Q-factor reward does not promote lowering the amplitude when searching for target frequency, though this may result in longer synchronisation times (a), as more steps may be required to arrive at the desired state with sufficiently large Q-factor. (c) a sample agent trajectory with Q-reward, completed in 6 steps. Though the final state is not necessarily the highest Q-factor among other, unsynchronised states, a relatively large Q-factor is retained in the final state nevertheless. Sampled device had the following parameters: $\mu_0 M_s = 0.98\,T$ and $K_u = 305.93\,kJ/m^3$. Final control values are listed in (c).

selects higher oscillating frequencies and instead supports larger amplitudes. In the reward function we modify the reward on successful synchronisation event by appending a weighted Q^* value, so that the final reward has the form of:

$$\mathcal{R} = \zeta_1 \mathcal{R}_{\delta f} + \zeta_2 \mathcal{R}_{\delta a} + \hat{\mathcal{R}}_{\text{synch}} + \zeta_3 \hat{\mathcal{R}}_{Q^*} \tag{10}$$

with $\zeta_1, \zeta_2, \zeta_3$ denoting weighting for each of the reward functions. $\hat{\mathcal{R}}$ rewards are applied only on the synchronisation event. Combined with derivative magnitude shaping, $\hat{\mathcal{R}}_{Q^*}$ has the side effect that the agent needs a larger number of steps for synchronisation, as seen in Fig.3, but helps in generating higher-quality oscillations.

5 Outlook

Automatic synchronisation of the STO to a desired frequency poses many challenges revolving around smooth arrival to the synchronised state or achieving a large, energy-efficient Q-factor. We show that using relatively straightforward methods, some of those challenges can be addressed in the simulation setup. It should be noted that the framework presented here can be extended to the control of other devices such as voltage controlled magnetic anisotropy (VCMA) [20] field sensors [21] where field noise must be balanced against the sensor sensitivity parameters [22]. In this case, the control parameters are the applied voltage, controlling the magnitude of the VCMA effect, thus the sensitivity, and the bias current supplied to the MTJ which affects both the noise magnitude and the sensitivity.

Acknowledgements

We acknowledge funding from the National Science Centre, Poland project no.2021/40/Q/ST5/00209 (Sheng) and the Excellence initiative-research university programme (IDUB) of the AGH University of Krakow.

References

[1] J.-V. Kim. "Chapter Four - Spin-Torque Oscillators". Ed. by R. E. Camley and R. L. Stamps. Vol. 63. Solid State Physics. ISSN: 0081-1947. Academic Press, 2012, pp. 217–294.

[2] D. Suess et al. "Topologically protected vortex structures for low-noise magnetic sensors with high linear range". *Nature Electronics* **1** 6 (2018), pp. 362–370.

[3] H. S. Choi et al. "Spin nano–oscillator–based wireless communication". *Scientific Reports* **4** 1 (2014), p. 5486.

[4] S. Tsunegi et al. "Scaling up electrically synchronized spin torque oscillator networks". *Scientific Reports* **8** 1 (2018), p. 13475.

[5] M. Romera et al. "Vowel recognition with four coupled spin-torque nano-oscillators". *Nature* **563** 7730 (2018), pp. 230–234.

[6] M. Romera et al. "Binding events through the mutual synchronization of spintronic nano-neurons". *Nature Communications* **13** 1 (2022), p. 883.

[7] J. Degrave et al. "Magnetic control of tokamak plasmas through deep reinforcement learning". *Nature* **602** 7897 (2022), pp. 414–419.

[8] J. Seo et al. "Avoiding fusion plasma tearing instability with deep reinforcement learning". *Nature* **626** 8000 (2024), pp. 746–751.

[9] T. Gilbert. "Classics in Magnetics A Phenomenological Theory of Damping in Ferromagnetic Materials". *IEEE Transactions on Magnetics* **40** 6 (2004), pp. 3443–3449.

[10] D. Ralph and M. Stiles. "Spin transfer torques". *Journal of Magnetism and Magnetic Materials* **320** 7 (2008), pp. 1190–1216.

[11] J. Slonczewski. "Current-driven excitation of magnetic multilayers". *Journal of Magnetism and Magnetic Materials* **159** 1-2 (1996), pp. L1–L7.

[12] J. Slonczewski. "Currents and torques in metallic magnetic multilayers". *Journal of Magnetism and Magnetic Materials* **247** 3 (2002), pp. 324–338.

[13] J. Mojsiejuk et al. "cmtj: Simulation package for analysis of multilayer spintronic devices". *npj Computational Materials* **9** 1 (2023), p. 54.

[14] A. Vansteenkiste et al. "The design and verification of MuMax3". *AIP Advances* **4** 10 (2014), p. 107133.

[15] S. Tamaru et al. "Analysis of phase noise in a spin torque oscillator stabilized by phase locked loop". *Applied Physics Express* **9** 5 (2016), p. 053005.

[16] T. Chen et al. "Spin-Torque and Spin-Hall Nano-Oscillators". *Proceedings of the IEEE* **104** 10 (2016), pp. 1919–1945.

[17] M. Harder, Y. Gui, and C.-M. Hu. "Electrical detection of magnetization dynamics via spin rectification effects". *Physics Reports* **661** (2016), pp. 1–59.

[18] S. Fujimoto, H. van Hoof, and D. Meger. *Addressing Function Approximation Error in Actor-Critic Methods*. arXiv:1802.09477 [cs, stat]. 2018.

[19] T. Haarnoja et al. *Soft Actor-Critic: Off-Policy Maximum Entropy Deep Reinforcement Learning with a Stochastic Actor*. arXiv:1801.01290 [cs, stat]. 2018.

[20] T. Nozaki et al. "Voltage-induced perpendicular magnetic anisotropy change in magnetic tunnel junctions". *Applied Physics Letters* **96** 2 (2010), p. 022506.

[21] W. Skowroński et al. "Magnetic field sensor with voltage-tunable sensing properties". *Applied Physics Letters* **101** 19 (2012), p. 192401.

[22] P. Wisniowski et al. "Effect of CoFeB electrode compositions on low frequency magnetic noise in tunneling magnetoresistance sensors". *Journal of Applied Physics* **122** 21 (2017), p. 213906.

Bibliography

The list below follows the order of first appearance in the text.

Zhang, X., Ezawa, M., Zhou, Y., (Mar. 2015). "Magnetic skyrmion logic gates: conversion, duplication and merging of skyrmions". In: *Scientific Reports* 5.1, p. 9400 (cit. on p. 15).

Zhang, W. (Sept. 2014). "Voltage-driven spintronic logic gates in graphene nanoribbons". In: *Scientific Reports* 4.1, p. 6320 (cit. on p. 15).

Papp, Á., Kiechle, M., Mendisch, S., Ahrens, V., Sahin, L., Seitner, L., Porod, W., Csaba, G., Becherer, M., (Dec. 2021). "Experimental demonstration of a concave grating for spin waves in the Rowland arrangement". In: *Scientific Reports* 11.1, p. 14239 (cit. on p. 15).

Huang, W., Xia, X., Zhu, C., Steichen, P., Quan, W., Mao, W., Yang, J., Chu, L., Li, X., (Dec. 2021). "Memristive Artificial Synapses for Neuromorphic Computing". In: *Nano-Micro Letters* 13.1, p. 85 (cit. on p. 15).

Chanthbouala, A., Garcia, V., Cherifi, R. O., Bouzehouane, K., Fusil, S., Moya, X., Xavier, S., Yamada, H., Deranlot, C., Mathur, N. D., Bibes, M., Barthélémy, A., Grollier, J., (Oct. 2012). "A ferroelectric memristor". In: *Nature Materials* 11.10, pp. 860–864 (cit. on p. 15).

Houshang, A., Zahedinejad, M., Muralidhar, S., Chęciński, J., Khymyn, R., Rajabali, M., Fulara, H., Awad, A. A., Dvornik, M., Åkerman, J., (Jan. 2022). "Phase-Binarized Spin Hall Nano-Oscillator Arrays: Towards Spin Hall Ising Machines". In: *Physical Review Applied* 17.1, p. 014003 (cit. on p. 15).

Torrejon, J., Riou, M., Araujo, F. A., Tsunegi, S., Khalsa, G., Querlioz, D., Bortolotti, P., Cros, V., Yakushiji, K., Fukushima, A., Kubota, H., Yuasa, S., Stiles, M. D., Grollier, J., (July 2017). "Neuromorphic computing with nanoscale spintronic oscillators". In: *Nature* 547.7664, pp. 428–431 (cit. on p. 15).

Nomura, H., Furuta, T., Tsujimoto, K., Kuwabiraki, Y., Peper, F., Tamura, E., Miwa, S., Goto, M., Nakatani, R., Suzuki, Y., (July 2019). "Reservoir

computing with dipole-coupled nanomagnets". In: *Japanese Journal of Applied Physics* 58.7, p. 070901 (cit. on pp. 15, 64, 73).

Taniguchi, T., Utsumi, Y., Imamura, H., (Dec. 2013). "Thermally activated switching rate of a nanomagnet in the presence of spin torque". In: *Physical Review B* 88.21, p. 214414 (cit. on p. 15).

Hayakawa, K., Kanai, S., Funatsu, T., Igarashi, J., Jinnai, B., Borders, W. A., Ohno, H., Fukami, S., (Mar. 2021). "Nanosecond Random Telegraph Noise in In-Plane Magnetic Tunnel Junctions". In: *Physical Review Letters* 126.11, p. 117202 (cit. on p. 15).

Kaiser, J., Datta, S., (Oct. 2021). "Probabilistic computing with p-bits". In: *Applied Physics Letters* 119.15, p. 150503 (cit. on p. 15).

Camsari, K. Y., Sutton, B. M., Datta, S., (Mar. 2019). "p-Bits for Probabilistic Spin Logic". In: *Applied Physics Reviews* 6.1. arXiv: 1809.04028, p. 011305 (cit. on p. 15).

Kurenkov, A., Fukami, S., Ohno, H., (July 2020). "Neuromorphic computing with antiferromagnetic spintronics". In: *Journal of Applied Physics* 128.1, p. 010902 (cit. on p. 15).

Taniguchi, T., Ogihara, A., Utsumi, Y., Tsunegi, S., (Dec. 2022). "Spintronic reservoir computing without driving current or magnetic field". In: *Scientific Reports* 12.1, p. 10627 (cit. on p. 15).

Hafner, J., Kresse, G., (1997). "The Vienna AB-Initio Simulation Program VASP: An Efficient and Versatile Tool for Studying the Structural, Dynamic, and Electronic Properties of Materials". In: *Properties of Complex Inorganic Solids*. Ed. by A. Gonis, A. Meike, and P. E. A. Turchi. Boston, MA: Springer US, pp. 69–82 (cit. on p. 16).

Giannozzi, P., Andreussi, O., Brumme, T., Bunau, O., Nardelli, M. B., Calandra, M., Car, R., Cavazzoni, C., Ceresoli, D., Cococcioni, M., Colonna, N., Carnimeo, I., Corso, A. D., Gironcoli, S. d., Delugas, P., DiStasio, R. A., Ferretti, A., Floris, A., Fratesi, G., Fugallo, G., Gebauer, R., Gerstmann, U., Giustino, F., Gorni, T., Jia, J., Kawamura, M., Ko, H.-Y., Kokalj, A., Küçükbenli, E., Lazzeri, M., Marsili, M., Marzari, N., Mauri, F., Nguyen, N. L., Nguyen, H.-V., Otero-de-la-Roza, A., Paulatto, L., Poncé, S., Rocca, D., Sabatini, R., Santra, B., Schlipf, M., Seitsonen, A. P., Smogunov, A., Timrov, I., Thonhauser, T., Umari, P., Vast, N., Wu, X., Baroni, S., (Oct. 2017). "Advanced capabilities for materials modelling with Quantum ESPRESSO". in: *Journal of Physics: Condensed Matter* 29.46. Publisher: IOP Publishing, p. 465901 (cit. on p. 16).

Müller, G. P., Hoffmann, M., Dißelkamp, C., Schürhoff, D., Mavros, S., Sallermann, M., Kiselev, N. S., Jónsson, H., Blügel, S., (June 2019). "Spirit: Multifunctional framework for atomistic spin simulations". In:

Physical Review B 99.22, p. 224414 (cit. on p. 16).

Donahue, M. J., Porter, D. G., (Sept. 1999). *OOMMF User's Guide, Version 1.0*. URL: http://math.nist.gov/oommf/ (cit. on p. 16).

Vansteenkiste, A., Leliaert, J., Dvornik, M., Helsen, M., Garcia-Sanchez, F., Van Waeyenberge, B., (Oct. 2014). "The design and verification of MuMax3". In: *AIP Advances* 4.10, p. 107133 (cit. on pp. 16, 111).

Xiao, J., Zangwill, A., Stiles, M. D., (July 2005). "Macrospin models of spin transfer dynamics". In: *Physical Review B* 72.1, p. 014446 (cit. on p. 16).

Mojsiejuk, J., Ziętek, S., Grochot, K., Skowroński, W., Stobiecki, T., (Apr. 2023). "cmtj: Simulation package for analysis of multilayer spintronic devices". In: *npj Computational Materials* 9.1, p. 54 (cit. on pp. 16–18, 103).

Grochot, K., Ogrodnik, P., **Mojsiejuk, J.**, Mazalski, P., Guzowska, U., Skowroński, W., Stobiecki, T., (Apr. 2024). "Influence of ferromagnetic interlayer exchange coupling on current-induced magnetization switching and Dzyaloshinskii–Moriya interaction in Co/Pt/Co multilayer system". In: *Scientific Reports* 14.1, p. 9938 (cit. on pp. 17, 18, 39, 46, 51, 53–55, 57).

Ziętek, S., **Mojsiejuk, J.**, Grochot, K., Łazarski, S., Skowroński, W., Stobiecki, T., (July 2022). "Numerical model of harmonic Hall voltage detection for spintronic devices". In: *Physical Review B* 106.2, p. 024403 (cit. on pp. 17, 18, 103).

Rzeszut, P., **Mojsiejuk, J.**, Skowroński, W., Tsunegi, S., Kubota, H., Yuasa, S., (June 2023). "Towards mutual synchronization of serially connected Spin Torque Oscillators based on magnetic tunnel junctions". In: arXiv:2306.11608 [physics] (cit. on pp. 17, 18, 65, 68, 70, 72, 73, 89).

Mojsiejuk, J., Ziętek, S., Skowroński, W., (Sept. 2025). "Reinforcement learning for spin torque oscillator tasks". In: arXiv:2509.10057 [physics] (cit. on pp. 17, 19).

Skowroński, W., Łazarski, S., **Mojsiejuk, J.**, Chęciński, J., Frankowski, M., Nozaki, T., Yakushiji, K., Yuasa, S., (Aug. 2019). "High frequency voltage-induced ferromagnetic resonance in magnetic tunnel junctions". In: *Applied Physics Letters* 115.7, p. 072401 (cit. on p. 18).

Mojsiejuk, J., Kulig, P., Chęciński, J., Frankowski, M., (Feb. 2020). "Visualization for Micromagnetics With Synchronized Plotting". In: *IEEE Transactions on Magnetics* 56.2, pp. 1–6 (cit. on pp. 18, 37).

Safeer, C., Keatley, P. S., Skowroński, W., **Mojsiejuk, J.**, Yakushiji, K., Fukushima, A., Yuasa, S., Bedau, D., Casanova, F., Hueso, L. E., Hicken, R. J., Pinna, D., Van Der Laan, G., Hesjedal, T., (Aug. 2024). "Magneti-

zation dynamics driven by displacement currents across a magnetic tunnel junction". In: *Physical Review Applied* 22.2, p. 024019 (cit. on pp. 18, 111).

Landau, L., Lifshitz, E., (1935). "On the Theory of the Dispersion of Magnetic Permeability in Ferromagnetic Bodies". In: *Physikalische Zeitschrift der Sowjetunion* 8, p. 9 (cit. on p. 21).

Lakshmanan, M. (Mar. 2011). "The fascinating world of the Landau-Lifshitz-Gilbert equation: an overview". In: *Philosophical Transactions of the Royal Society A: Mathematical, Physical and Engineering Sciences* 369.1939, pp. 1280–1300 (cit. on p. 21).

Gilbert, T. (Nov. 2004). "Classics in Magnetics A Phenomenological Theory of Damping in Ferromagnetic Materials". In: *IEEE Transactions on Magnetics* 40.6, pp. 3443–3449 (cit. on pp. 22, 35).

Slonczewski, J. (June 1996). "Current-driven excitation of magnetic multilayers". In: *Journal of Magnetism and Magnetic Materials* 159.1-2, pp. L1–L7 (cit. on pp. 22, 25).

Berger, L. (Oct. 1996). "Emission of spin waves by a magnetic multilayer traversed by a current". In: *Phys. Rev. B* 54.13, pp. 9353–9358 (cit. on pp. 22, 26).

Arun, R., Gopal, R., Chandrasekar, V. K., M. Lakshmanan, (Sept. 2020). "Influence of Field-Like Torque in Synchronization of Spin Torque Oscillators". In: *IEEE Transactions on Magnetics* 56.9, pp. 1–10 (cit. on pp. 22, 67, 71).

Nguyen, M.-H., Pai, C.-F., (Mar. 2021). "Spin–orbit torque characterization in a nutshell". In: *APL Materials* 9.3, p. 030902 (cit. on pp. 22, 46).

Strelkov, N., Timopheev, A., Sousa, R. C., Chshiev, M., Buda-Prejbeanu, L. D., Dieny, B., (May 2017). "Stability phase diagram of a perpendicular magnetic tunnel junction in noncollinear geometry". In: *Physical Review B* 95.18, p. 184409 (cit. on pp. 23, 47, 48).

Donahue, M., Porter, D., (Jan. 2004). "Exchange energy formulations for 3D micromagnetics". In: *Physica B: Condensed Matter* 343.1-4, pp. 177–183 (cit. on p. 24).

Newell, A. J., Williams, W., Dunlop, D. J., (1993). "A generalization of the demagnetizing tensor for nonuniform magnetization". In: *Journal of Geophysical Research* 98.B6, p. 9551 (cit. on p. 24).

Abert, C., Bruckner, F., Vogler, C., Windl, R., Thanhoffer, R., Suess, D., (Aug. 2015). "A full-fledged micromagnetic code in fewer than 70 lines of NumPy". In: *Journal of Magnetism and Magnetic Materials* 387, pp. 13–18 (cit. on p. 24).

Miltat, J. E., Donahue, M. J., (July 2007). “Numerical Micromagnetics: Finite Difference Methods”. In: *Handbook of Magnetism and Advanced Magnetic Materials*. Ed. by H. Kronmüller and S. Parkin. 1st ed. Wiley (cit. on p. 24).

Tsymbal, E. Y., Žutić, I., (2020). *Spintronics handbook. Volume 2: Semiconductor spintronics*. Second edition, first issued in paperback. Boca Raton London New York: CRC Press (cit. on p. 24).

Stiles, M. (2005). “Interlayer Exchange Coupling”. In: *Ultrathin Magnetic Structures III*. ed. by J. A. C. Bland and B. Heinrich. Berlin/Heidelberg: Springer-Verlag, pp. 99–142 (cit. on p. 24).

Bruno, P. (Dec. 2004). “Interlayer Exchange Interactions in Magnetic Multilayers”. In: *Magnetism: Molecules to Materials*. Ed. by J. S. Miller and M. Drillon. 1st ed. Wiley, pp. 329–353 (cit. on p. 24).

Ralph, D., Stiles, M., (Apr. 2008). “Spin transfer torques”. In: *Journal of Magnetism and Magnetic Materials* 320.7, pp. 1190–1216 (cit. on p. 25).

Inoue, J., Ohno, H., (Sept. 2005). “Taking the Hall Effect for a Spin”. In: *Science* 309.5743, pp. 2004–2005 (cit. on p. 26).

Sinova, J., Valenzuela, S. O., Wunderlich, J., Back, C. H., Jungwirth, T., (Oct. 2015). “Spin Hall effects”. In: *Reviews of Modern Physics* 87.4, pp. 1213–1260 (cit. on pp. 26, 27).

Hirsch, J. E. (Aug. 1999). “Spin Hall Effect”. In: *Physical Review Letters* 83.9, pp. 1834–1837 (cit. on p. 26).

Dyakonov, M., Perel, V., (July 1971). “Current-induced spin orientation of electrons in semiconductors”. In: *Physics Letters A* 35.6, pp. 459–460 (cit. on p. 26).

Smit, J. (Jan. 1958). “The spontaneous hall effect in ferromagnetics II”. in: *Physica* 24.1-5, pp. 39–51 (cit. on p. 26).

Amin, V. P., Stiles, M. D., (Sept. 2016). “Spin transport at interfaces with spin-orbit coupling: Phenomenology”. In: *Physical Review B* 94.10, p. 104420 (cit. on p. 27).

Qiu, X., Narayanapillai, K., Wu, Y., Deorani, P., Yang, D.-H., Noh, W.-S., Park, J.-H., Lee, K.-J., Lee, H.-W., Yang, H., (Apr. 2015). “Spin–orbit-torque engineering via oxygen manipulation”. In: *Nature Nanotechnology* 10.4, pp. 333–338 (cit. on p. 27).

An, H., Kageyama, Y., Kanno, Y., Enishi, N., Ando, K., (Oct. 2016). “Spin–torque generator engineered by natural oxidation of Cu”. In: *Nature Communications* 7.1, p. 13069 (cit. on p. 27).

Evans, R. F. L., Fan, W. J., Chureemart, P., Ostler, T. A., Ellis, M. O. A., Chantrell, R. W., (Mar. 2014). “Atomistic spin model simulations of magnetic nanomaterials”. In: *Journal of Physics: Condensed Matter* 26.10, p. 103202 (cit. on p. 28).

Dormand, J., Prince, P., (Mar. 1980). “A family of embedded Runge-Kutta formulae”. In: *Journal of Computational and Applied Mathematics* 6.1, pp. 19–26 (cit. on p. 28).

Mackevičius, V. (Aug. 2011). *Introduction to Stochastic Analysis: Integrals and Differential Equations*. 1st ed. Wiley (cit. on p. 29).

Rößler, A. (2010). “Runge-Kutta Methods for the Strong Approximation of Solutions of Stochastic Differential Equations”. In: *SIAM Journal on Numerical Analysis* 48.3, pp. 922–952 (cit. on p. 29).

Ament, S., Rangarajan, N., Parthasarathy, A., Rakheja, S., (Jan. 2017). “Solving the stochastic Landau-Lifshitz-Gilbert-Slonczewski equation for monodomain nanomagnets : A survey and analysis of numerical techniques”. In: *arXiv:1607.04596 [cs]*. arXiv: 1607.04596 (cit. on p. 29).

Brown, W. F. (June 1963). “Thermal Fluctuations of a Single-Domain Particle”. In: *Physical Review* 130.5, pp. 1677–1686 (cit. on p. 30).

Kubo, R., Hashitsume, N., (1970). “Brownian Motion of Spins”. In: *Progress of Theoretical Physics Supplement* 46, pp. 210–220 (cit. on p. 30).

Baselgia, L., Warden, M., Waldner, F., Hutton, S. L., Drumheller, J. E., He, Y. Q., Wigen, P. E., Maryško, M., (Aug. 1988). “Derivation of the resonance frequency from the free energy of ferromagnets”. In: *Physical Review B* 38.4, pp. 2237–2242 (cit. on p. 31).

Rodríguez-Suárez, R. L., Rezende, S. M., Azevedo, A., (June 2005). “Ferromagnetic resonance investigation of the residual coupling in spin-valve systems”. In: *Physical Review B* 71.22, p. 224406 (cit. on p. 31).

Arregi, J. A., Riego, P., Berger, A., Vedmedenko, E. Y., (Oct. 2023). “Large interlayer Dzyaloshinskii-Moriya interactions across Ag-layers”. In: *Nature Communications* 14.1, p. 6927 (cit. on p. 32).

Kingma, D. P., Ba, J., (Jan. 2017). *Adam: A Method for Stochastic Optimization*. arXiv:1412.6980 [cs]. URL: http://arxiv.org/abs/1412.6980 (cit. on p. 32).

Boyd, S. P., Vandenberghe, L., (2004). *Convex optimization*. Cambridge, UK: Cambridge University Press (cit. on p. 33).

More, J. J., Garbow, B. S., Kenneth E. Hillstrom, (2023). *User Guide for MINPACK-1*. URL: https://cds.cern.ch/record/126569/files/CM-P00068642.pdf?version=1 (cit. on p. 33).

Virtanen, P., Gommers, R., Oliphant, T. E., Haberland, M., Reddy, T., Cournapeau, D., Burovski, E., Peterson, P., Weckesser, W., Bright, J., Van Der Walt, S. J., Brett, M., Wilson, J., Millman, K. J., Mayorov, N., Nelson, A. R. J., Jones, E., Kern, R., Larson, E., Carey, C. J., Polat, İ., Feng, Y., Moore, E. W., VanderPlas, J., Laxalde, D., Perktold, J., Cimrman, R., Henriksen, I., Quintero, E. A., Harris, C. R., Archibald, A. M., Ribeiro, A. H., Pedregosa, F., Van Mulbregt, P., SciPy 1.0 Contributors, Vijaykumar, A., Bardelli, A. P., Rothberg, A., Hilboll, A., Kloeckner, A., Scopatz, A., Lee, A., Rokem, A., Woods, C. N., Fulton, C., Masson, C., Häggström, C., Fitzgerald, C., Nicholson, D. A., Hagen, D. R., Pasechnik, D. V., Olivetti, E., Martin, E., Wieser, E., Silva, F., Lenders, F., Wilhelm, F., Young, G., Price, G. A., Ingold, G.-L., Allen, G. E., Lee, G. R., Audren, H., Probst, I., Dietrich, J. P., Silterra, J., Webber, J. T., Slavič, J., Nothman, J., Buchner, J., Kulick, J., Schönberger, J. L., De Miranda Cardoso, J. V., Reimer, J., Harrington, J., Rodríguez, J. L. C., Nunez-Iglesias, J., Kuczynski, J., Tritz, K., Thoma, M., Newville, M., Kümmerer, M., Bolingbroke, M., Tartre, M., Pak, M., Smith, N. J., Nowaczyk, N., Shebanov, N., Pavlyk, O., Brodtkorb, P. A., Lee, P., McGibbon, R. T., Feldbauer, R., Lewis, S., Tygier, S., Sievert, S., Vigna, S., Peterson, S., More, S., Pudlik, T., Oshima, T., Pingel, T. J., Robitaille, T. P., Spura, T., Jones, T. R., Cera, T., Leslie, T., Zito, T., Krauss, T., Upadhyay, U., Halchenko, Y. O., Vázquez-Baeza, Y., (Mar. 2020). “SciPy 1.0: fundamental algorithms for scientific computing in Python”. In: *Nature Methods* 17.3, pp. 261–272 (cit. on p. 33).

Ogrodnik, P., Grochot, K., Karwacki, L., Kanak, J., Prokop, M., Chęciński, J., Skowroński, W., Ziętek, S., Stobiecki, T., (Oct. 2021). “Study of Spin–Orbit Interactions and Interlayer Ferromagnetic Coupling in Co/Pt/Co Trilayers in a Wide Range of Heavy-Metal Thickness”. In: *ACS Applied Materials & Interfaces* 13.39, pp. 47019–47032 (cit. on pp. 35, 39, 51–53, 57).

Ogrodnik, P., Antonio Vetrò, F., Frankowski, M., Chęciński, J., Stobiecki, T., Barnaś, J., Ansermet, J.-P., (Feb. 2019). “Field- and temperature-modulated spin diode effect in a GMR nanowire with dipolar coupling”. In: *Journal of Physics D: Applied Physics* 52.6, p. 065002 (cit. on p. 35).

Nozaki, T., Shiota, Y., Miwa, S., Murakami, S., Bonell, F., Ishibashi, S., Kubota, H., Yakushiji, K., Saruya, T., Fukushima, A., Yuasa, S., Shinjo, T., Suzuki, Y., (June 2012). “Electric-field-induced ferromagnetic resonance excitation in an ultrathin ferromagnetic metal layer”. In: *Nature Physics* 8.6, pp. 491–496 (cit. on p. 35).

Döring, W. (July 1948). “Über die Trägheit der Wände zwischen Weißschen Bezirken”. In: *Zeitschrift für Naturforschung A* 3.7, pp. 373–379 (cit. on p. 35).

Thiaville, A., Rohart, S., Jué, É., Cros, V., Fert, A., (Dec. 2012). “Dynamics of Dzyaloshinskii domain walls in ultrathin magnetic films”. In: *EPL (Europhysics Letters)* 100.5, p. 57002 (cit. on p. 36).

Martinez, E., Emori, S., Perez, N., Torres, L., Beach, G. S. D., (June 2014). “Current-driven dynamics of Dzyaloshinskii domain walls in the presence of in-plane fields: Full micromagnetic and one-dimensional analysis”. In: *Journal of Applied Physics* 115.21, p. 213909 (cit. on p. 36).

Alejos, O., Raposo, V., Sanchez-Tejerina, L., Tomasello, R., Finocchio, G., Martinez, E., (Jan. 2018). “Current-driven domain wall dynamics in ferromagnetic layers synthetically exchange-coupled by a spacer: A micromagnetic study”. In: *Journal of Applied Physics* 123.1, p. 013901 (cit. on p. 36).

Yang, S.-H., Parkin, S., (Aug. 2017). “Novel domain wall dynamics in synthetic antiferromagnets”. In: *Journal of Physics: Condensed Matter* 29.30, p. 303001 (cit. on p. 36).

Harris, C. R., Millman, K. J., Van Der Walt, S. J., Gommers, R., Virtanen, P., Cournapeau, D., Wieser, E., Taylor, J., Berg, S., Smith, N. J., Kern, R., Picus, M., Hoyer, S., Van Kerkwijk, M. H., Brett, M., Haldane, A., Del Río, J. F., Wiebe, M., Peterson, P., Gérard-Marchant, P., Sheppard, K., Reddy, T., Weckesser, W., Abbasi, H., Gohlke, C., Oliphant, T. E., (Sept. 2020). “Array programming with NumPy”. In: *Nature* 585.7825, pp. 357–362 (cit. on p. 37).

Martin, R. C., ed. (2009). *Clean code: a handbook of agile software craftsmanship*. Upper Saddle River, NJ: Prentice Hall (cit. on p. 37).

Boost C++ Libraries (2024). URL: https://www.boost.org/ (cit. on p. 37).

PyQt5 Reference Guide — PyQt Documentation v5.15.7 (2024). URL: https://www.riverbankcomputing.com/static/Docs/PyQt5/ (cit. on p. 37).

Kim, J., Sinha, J., Hayashi, M., Yamanouchi, M., Fukami, S., Suzuki, T., Mitani, S., Ohno, H., (Mar. 2013). “Layer thickness dependence of the current-induced effective field vector in Ta|CoFeB|MgO”. in: *Nature Materials* 12.3, pp. 240–245 (cit. on p. 40).

Saitoh, E., Ueda, M., Miyajima, H., Tatara, G., (May 2006). “Conversion of spin current into charge current at room temperature: Inverse spin-Hall effect”. In: *Applied Physics Letters* 88.18, p. 182509 (cit. on p. 40).

Taniguchi, T. (Nov. 2016). “Magnetoresistance generated from charge-spin conversion by anomalous Hall effect in metallic ferromagnetic/nonmagnetic bilayers”. In: *Physical Review B* 94.17, p. 174440 (cit. on p. 40).

Ziętek, S., Cecot, M., Skowroński, W., Stobiecki, T., (May 2016). "Magnetization dynamics of NiFe film and anisotropic magnetoresistance device: Comparison of microwave detection methods". In: *2016 21st International Conference on Microwave, Radar and Wireless Communications (MIKON)*. Kraków, Poland: IEEE, pp. 1–4 (cit. on p. 41).

Brochu, E., Cora, V. M., Freitas, N., (Dec. 2010). *A Tutorial on Bayesian Optimization of Expensive Cost Functions, with Application to Active User Modeling and Hierarchical Reinforcement Learning*. arXiv:1012.2599 [cs]. URL: http://arxiv.org/abs/1012.2599 (cit. on p. 42).

Bishop, C. M. (2006). *Pattern recognition and machine learning*. Information science and statistics. New York: Springer (cit. on p. 43).

Cowen-Rivers, A. I., Lyu, W., Tutunov, R., Wang, Z., Grosnit, A., Griffiths, R. R., Maraval, A. M., Jianye, H., Wang, J., Peters, J., Ammar, H. B., (May 2022). *HEBO Pushing The Limits of Sample-Efficient Hyperparameter Optimisation*. arXiv:2012.03826 [cs, math]. URL: http://arxiv.org/abs/2012.03826 (cit. on p. 43).

Skowroński, W., Karwacki, Ł., Ziętek, S., Kanak, J., Łazarski, S., Grochot, K., Stobiecki, T., Kuświk, P., Stobiecki, F., Barnaś, J., (Feb. 2019). "Determination of Spin Hall Angle in Heavy-Metal/ Co − Fe − B -Based Heterostructures with Interfacial Spin-Orbit Fields". In: *Physical Review Applied* 11.2, p. 024039 (cit. on p. 46).

Timopheev, A. A., Sousa, R., Chshiev, M., Buda-Prejbeanu, L. D., Dieny, B., (Sept. 2015). "Respective influence of in-plane and out-of-plane spin-transfer torques in magnetization switching of perpendicular magnetic tunnel junctions". In: *Physical Review B* 92.10, p. 104430 (cit. on p. 47).

Wilczyński, M., Barnaś, J., Świrkowicz, R., (Feb. 2008). "Free-electron model of current-induced spin-transfer torque in magnetic tunnel junctions". In: *Physical Review B* 77.5, p. 054434 (cit. on p. 48).

Chshiev, M., Manchon, A., Kalitsov, A., Ryzhanova, N., Vedyayev, A., Strelkov, N., Butler, W. H., Dieny, B., (Sept. 2015). "Analytical description of ballistic spin currents and torques in magnetic tunnel junctions". In: *Physical Review B* 92.10, p. 104422 (cit. on p. 48).

Lee, K.-S., Lee, S.-W., Min, B.-C., Lee, K.-J., (Mar. 2013). "Threshold current for switching of a perpendicular magnetic layer induced by spin Hall effect". In: *Applied Physics Letters* 102.11, p. 112410 (cit. on pp. 48, 49, 55, 98).

Cierpiał, M., Grochot, K., **Mojsiejuk, J.**, Wrona, J., Vafaee, M., Nan, T., Skowroński, W., (May 2024). "Spin-Orbit torque in α-W-Based Magnetic Tunnel Junction". In: *2024 IEEE International Magnetic Conference - Short papers (INTERMAG Short papers)*. Rio de Janeiro, Brazil: IEEE,

pp. 1–2 (cit. on p. 49).

Kim, J., Sheng, P., Takahashi, S., Mitani, S., Hayashi, M., (Feb. 2016). “Spin Hall Magnetoresistance in Metallic Bilayers”. In: *Physical Review Letters* 116.9, p. 097201 (cit. on p. 55).

Kuepferling, M., Casiraghi, A., Soares, G., Durin, G., Garcia-Sanchez, F., Chen, L., Back, C. H., Marrows, C. H., Tacchi, S., Carlotti, G., (Mar. 2023). “Measuring interfacial Dzyaloshinskii-Moriya interaction in ultrathin magnetic films”. In: *Reviews of Modern Physics* 95.1, p. 015003 (cit. on p. 56).

Rzeszut, P., Skowroński, W., Ziętek, S., Wrona, J., Stobiecki, T., (June 2019). “Multi-bit MRAM storage cells utilizing serially connected perpendicular magnetic tunnel junctions”. In: *Journal of Applied Physics* 125.22, p. 223907 (cit. on p. 60).

Butler, W. H., Zhang, X.-G., Schulthess, T. C., MacLaren, J. M., (Jan. 2001). “Spin-dependent tunneling conductance of Fe | MgO | Fe sandwiches”. In: *Physical Review B* 63.5, p. 054416 (cit. on p. 61).

Miyazaki, T., Tezuka, N., (Jan. 1995). “Giant magnetic tunneling effect in Fe/Al2O3/Fe junction”. In: *Journal of Magnetism and Magnetic Materials* 139.3, pp. L231–L234 (cit. on p. 62).

Parkin, S. S. P., Kaiser, C., Panchula, A., Rice, P. M., Hughes, B., Samant, M., Yang, S.-H., (Dec. 2004). “Giant tunnelling magnetoresistance at room temperature with MgO (100) tunnel barriers”. In: *Nature Materials* 3.12, pp. 862–867 (cit. on p. 62).

Yuasa, S., Nagahama, T., Fukushima, A., Suzuki, Y., Ando, K., (Dec. 2004). “Giant room-temperature magnetoresistance in single-crystal Fe/MgO/Fe magnetic tunnel junctions”. In: *Nature Materials* 3.12, pp. 868–871 (cit. on p. 62).

Ikeda, S., Hayakawa, J., Ashizawa, Y., Lee, Y. M., Miura, K., Hasegawa, H., Tsunoda, M., Matsukura, F., Ohno, H., (Aug. 2008). “Tunnel magnetoresistance of 604% at 300K by suppression of Ta diffusion in CoFeB/MgO/CoFeB pseudo-spin-valves annealed at high temperature”. In: *Applied Physics Letters* 93.8, p. 082508 (cit. on p. 62).

Ikeda, S., Miura, K., Yamamoto, H., Mizunuma, K., Gan, H. D., Endo, M., Kanai, S., Hayakawa, J., Matsukura, F., Ohno, H., (Sept. 2010). “A perpendicular-anisotropy CoFeB–MgO magnetic tunnel junction”. In: *Nature Materials* 9.9, pp. 721–724 (cit. on pp. 62, 63).

Yakata, S., Kubota, H., Suzuki, Y., Yakushiji, K., Fukushima, A., Yuasa, S., Ando, K., (Apr. 2009). “Influence of perpendicular magnetic anisotropy on spin-transfer switching current in CoFeB/MgO/CoFeB magnetic tunnel junctions”. In: *Journal of Applied Physics* 105.7, p. 07D131 (cit. on

p. 62).

Igarashi, J., Jinnai, B., Desbuis, V., Mangin, S., Fukami, S., Ohno, H., (Jan. 2021). "Temperature dependence of the energy barrier in X/1X nm shape-anisotropy magnetic tunnel junctions". In: *Applied Physics Letters* 118.1, p. 012409 (cit. on pp. 62, 63).

Hayakawa, J., Ikeda, S., Lee, Y. M., Sasaki, R., Meguro, T., Matsukura, F., Takahashi, H., Ohno, H., (Sept. 2005). "Current-Driven Magnetization Switching in CoFeB/MgO/CoFeB Magnetic Tunnel Junctions". In: *Japanese Journal of Applied Physics* 44.9L, p. L1267 (cit. on p. 62).

Jinnai, B., Watanabe, K., Fukami, S., Ohno, H., (Apr. 2020). "Scaling magnetic tunnel junction down to single-digit nanometers—Challenges and prospects". In: *Applied Physics Letters* 116.16, p. 160501 (cit. on p. 63).

Kanai, S., Hayakawa, K., Ohno, H., Fukami, S., (Mar. 2021). "Theory of relaxation time of stochastic nanomagnets". In: *Physical Review B* 103.9, p. 094423 (cit. on p. 63).

Skowroński, W., Stobiecki, T., Wrona, J., Reiss, G., Dijken, S. v., (May 2012). "Zero-Field Spin Torque Oscillator Based on Magnetic Tunnel Junctions with a Tilted CoFeB Free Layer". In: *Applied Physics Express* 5.6, p. 063005 (cit. on p. 63).

Fang, B., Feng, J., Gan, H., Malmhall, R., Huai, Y., Xiong, R., Wei, H., Han, X., Zhang, B., Zeng, Z., (Dec. 2016). "Zero-field spin transfer oscillators based on magnetic tunnel junction having perpendicular polarizer and planar free layer". In: *AIP Advances* 6.12, p. 125305 (cit. on p. 63).

Taniguchi, T., Arai, H., Kubota, H., Imamura, H., (Jan. 2014). "Theoretical Study of Spin-Torque Oscillator with Perpendicularly Magnetized Free Layer". In: *IEEE Transactions on Magnetics* 50.1, pp. 1–4 (cit. on p. 64).

Tsunegi, S., Taniguchi, T., Lebrun, R., Yakushiji, K., Cros, V., Grollier, J., Fukushima, A., Yuasa, S., Kubota, H., (Dec. 2018). "Scaling up electrically synchronized spin torque oscillator networks". In: *Scientific Reports* 8.1, p. 13475 (cit. on p. 64).

Sharma, R., Mishra, R., Ngo, T., Guo, Y.-X., Fukami, S., Sato, H., Ohno, H., Yang, H., (May 2021). "Electrically connected spin-torque oscillators array for 2.4 GHz WiFi band transmission and energy harvesting". In: *Nature Communications* 12.1, p. 2924 (cit. on p. 64).

Gibeault, S., Adeyeye, T. N., Pocher, L. A., Lathrop, D. P., Daniels, M. W., Stiles, M. D., McClelland, J. J., Borders, W. A., Ryan, J. T., Talatchian, P., Ebels, U., Madhavan, A., (Mar. 2024). "Programmable electrical coupling between stochastic magnetic tunnel junctions". In: *Physical Review Applied* 21.3, p. 034064 (cit. on p. 64).

Romera, M., Talatchian, P., Tsunegi, S., Yakushiji, K., Fukushima, A., Kubota, H., Yuasa, S., Cros, V., Bortolotti, P., Ernoult, M., Querlioz, D., Grollier, J., (Dec. 2022). “Binding events through the mutual synchronization of spintronic nano-neurons”. In: *Nature Communications* 13.1, p. 883 (cit. on p. 64).

Yun, S. J., Lee, K.-J., Lim, S. H., (Nov. 2017). “Critical switching current density induced by spin Hall effect in magnetic structures with first- and second-order perpendicular magnetic anisotropy”. In: *Scientific Reports* 7.1, p. 15314 (cit. on p. 64).

Kanao, T., Suto, H., Mizushima, K., Goto, H., Tanamoto, T., Nagasawa, T., (Aug. 2019). “Reservoir Computing on Spin-Torque Oscillator Array”. In: *Physical Review Applied* 12.2, p. 024052 (cit. on pp. 64, 70, 73).

Nomura, H., Furuta, T., Tsujimoto, K., Kuwabiraki, Y., Samura, N., Tamura, E., Goto, M., Nakatani, R., Kubota, H., Suzuki, Y., (Feb. 2020). “Randomly generated node-state-update procedure for dipole-coupled magnetic reservoir computing with voltage control of the magnetism”. In: *Journal of Physics D: Applied Physics* 53.9, p. 094001 (cit. on p. 64).

Kubota, H., Ishibashi, S., Saruya, T., Nozaki, T., Fukushima, A., Yakushiji, K., Ando, K., Suzuki, Y., Yuasa, S., (Apr. 2012). “Enhancement of perpendicular magnetic anisotropy in FeB free layers using a thin MgO cap layer”. In: *Journal of Applied Physics* 111.7, p. 07C723 (cit. on p. 65).

Dieny, B., Chshiev, M., (June 2017). “Perpendicular magnetic anisotropy at transition metal/oxide interfaces and applications”. In: *Reviews of Modern Physics* 89.2. Publisher: American Physical Society, p. 025008 (cit. on p. 65).

Skowroński, W., Chęciński, J., Ziętek, S., Yakushiji, K., Yuasa, S., (Dec. 2019). “Microwave magnetic field modulation of spin torque oscillator based on perpendicular magnetic tunnel junctions”. In: *Scientific Reports* 9.1, p. 19091 (cit. on p. 65).

Slavin, A., Tiberkevich, V., (Apr. 2009). “Nonlinear Auto-Oscillator Theory of Microwave Generation by Spin-Polarized Current”. In: *IEEE Transactions on Magnetics* 45.4, pp. 1875–1918 (cit. on p. 65).

Taniguchi, T., Tsunegi, S., Kubota, H., (Jan. 2018). “Mutual synchronization of spin-torque oscillators consisting of perpendicularly magnetized free layers and in-plane magnetized pinned layers”. In: *Applied Physics Express* 11.1, p. 013005 (cit. on p. 67).

Acebrón, J. A., Bonilla, L. L., Pérez Vicente, C. J., Ritort, F., Spigler, R., (Apr. 2005). “The Kuramoto model: A simple paradigm for synchronization phenomena (PREVIEW)”. in: *Reviews of Modern Physics* 77.1, pp. 137–185 (cit. on p. 70).

Liu, L., Pai, C.-F., Ralph, D. C., Buhrman, R. A., (Oct. 2012). “Magnetic Oscillations Driven by the Spin Hall Effect in 3-Terminal Magnetic Tunnel Junction Devices”. In: *Physical Review Letters* 109.18, p. 186602 (cit. on p. 73).

Bauer, U., Yao, L., Tan, A. J., Agrawal, P., Emori, S., Tuller, H. L., Van Dijken, S., Beach, G. S. D., (Feb. 2015). “Magneto-ionic control of interfacial magnetism”. In: *Nature Materials* 14.2, pp. 174–181 (cit. on p. 73).

Shiota, Y., Nozaki, T., Bonell, F., Murakami, S., Shinjo, T., Suzuki, Y., (Jan. 2012). “Induction of coherent magnetization switching in a few atomic layers of FeCo using voltage pulses”. In: *Nature Materials* 11.1, pp. 39–43 (cit. on p. 73).

Skowroński, W., Nozaki, T., Shiota, Y., Tamaru, S., Yakushiji, K., Kubota, H., Fukushima, A., Yuasa, S., Suzuki, Y., (May 2015). “Perpendicular magnetic anisotropy of Ir/CoFeB/MgO trilayer system tuned by electric fields”. In: *Applied Physics Express* 8.5, p. 053003 (cit. on p. 73).

Nomura, H., Tsujimoto, K., Goto, M., Samura, N., Nakatani, R., Suzuki, Y., (Apr. 2020). “Reservoir computing with two-bit input task using dipole-coupled nanomagnet array”. In: *Japanese Journal of Applied Physics* 59.SE, SEEG02 (cit. on p. 73).

Chęciński, J., Wiśniowski, P., Frankowski, M., Stobiecki, T., (Sept. 2018). “Magnetic Noise Prediction and Evaluation in Tunneling Magnetoresistance Sensors”. In: *Sensors* 18.9, p. 3055 (cit. on p. 76).

Stoyanov, M., Gunzburger, M., Burkardt, J., (2011). “Pink Noise, 1/f noise, and their effect on solutions of differential equations”. In: *International Journal for Uncertainty Quantification* 1.3, pp. 257–278 (cit. on pp. 76, 80).

Sauer, T. (Sept. 2013). “Computational solution of stochastic differential equations”. In: *WIREs Computational Statistics* 5.5, pp. 362–371 (cit. on p. 77).

Jiang, L., Nowak, E. R., Scott, P. E., Johnson, J., Slaughter, J. M., Sun, J. J., Dave, R. W., (Feb. 2004). “Low-frequency magnetic and resistance noise in magnetic tunnel junctions”. In: *Physical Review B* 69.5, p. 054407 (cit. on p. 77).

Nowak, E. R., Weissman, M. B., Parkin, S. S. P., (Jan. 1999). “Electrical noise in hysteretic ferromagnet–insulator–ferromagnet tunnel junctions”. In: *Applied Physics Letters* 74.4, pp. 600–602 (cit. on p. 77).

Ozbay, A., Gokce, A., Flanagan, T., Stearrett, R. A., Nowak, E. R., Nordman, C., (May 2009). “Low frequency magnetoresistive noise in spin-valve structures”. In: *Applied Physics Letters* 94.20, p. 202506 (cit. on p. 77).

Egelhoff, W., Pong, P., Unguris, J., McMichael, R., Nowak, E., Edelstein, A., Burnette, J., Fischer, G., (Oct. 2009). “Critical challenges for picoTesla magnetic-tunnel-junction sensors”. In: *Sensors and Actuators A: Physical* 155.2, pp. 217–225 (cit. on p. 77).

Wisniowski, P., Dabek, M., Wrona, J., Cardoso, S., Freitas, P. P., (Dec. 2017). “Effect of CoFeB electrode compositions on low frequency magnetic noise in tunneling magnetoresistance sensors”. In: *Journal of Applied Physics* 122.21, p. 213906 (cit. on pp. 78, 86).

Voss, R. F. (1978). “”1/f noise” in music: Music from 1/f noise”. In: *The Journal of the Acoustical Society of America* 63.1, p. 258 (cit. on p. 80).

Kasdin, N. (May 1995). “Discrete simulation of colored noise and stochastic processes and 1/f^alpha power law noise generation”. In: *Proceedings of the IEEE* 83.5, pp. 802–827 (cit. on p. 80).

Hosking, J. R. M. (1981). “Fractional differencing”. In: *Biometrika* 68.1, pp. 165–176 (cit. on p. 80).

Carpena, P., Coronado, A. V., (Apr. 2022). “On the Autocorrelation Function of 1/f Noises”. In: *Mathematics* 10.9, p. 1416 (cit. on p. 83).

Kirchner, J. W. (June 2005). “Aliasing in 1/f^alpha noise spectra: Origins, consequences, and remedies”. In: *Physical Review E* 71.6, p. 066110 (cit. on p. 84).

Haarnoja, T., Zhou, A., Abbeel, P., Levine, S., (Aug. 2018). *Soft Actor-Critic: Off-Policy Maximum Entropy Deep Reinforcement Learning with a Stochastic Actor*. arXiv:1801.01290 [cs, stat]. URL: http://arxiv.org/abs/1801.01290 (cit. on p. 92).

Fujimoto, S., Hoof, H., Meger, D., (Oct. 2018). *Addressing Function Approximation Error in Actor-Critic Methods*. arXiv:1802.09477 [cs, stat]. URL: http://arxiv.org/abs/1802.09477 (cit. on p. 92).

Schulman, J., Wolski, F., Dhariwal, P., Radford, A., Klimov, O., (Aug. 2017). *Proximal Policy Optimization Algorithms*. arXiv:1707.06347 [cs]. URL: http://arxiv.org/abs/1707.06347 (cit. on p. 92).

Sutton, R. S., Barto, A. G., (2018). *Reinforcement learning: An introduction.* 2nd Edition. Adaptive computation and machine learning. Cambridge, Mass: MIT Press (cit. on pp. 92, 95).

Degrave, J., Felici, F., Buchli, J., Neunert, M., Tracey, B., Carpanese, F., Ewalds, T., Hafner, R., Abdolmaleki, A., Casas, D., Donner, C., Fritz, L., Galperti, C., Huber, A., Keeling, J., Tsimpoukelli, M., Kay, J., Merle, A., Moret, J.-M., Noury, S., Pesamosca, F., Pfau, D., Sauter, O., Sommariva, C., Coda, S., Duval, B., Fasoli, A., Kohli, P., Kavukcuoglu, K., Hassabis, D., Riedmiller, M., (Feb. 2022). “Magnetic control of tokamak plasmas

through deep reinforcement learning". In: *Nature* 602.7897, pp. 414–419 (cit. on p. 92).

Schulman, J., Levine, S., Moritz, P., Jordan, M. I., Abbeel, P., (Apr. 2017). *Trust Region Policy Optimization*. arXiv:1502.05477 [cs]. URL: http://arxiv.org/abs/1502.05477 (cit. on p. 92).

Lillicrap, T. P., Hunt, J. J., Pritzel, A., Heess, N., Erez, T., Tassa, Y., Silver, D., Wierstra, D., (July 2019). *Continuous control with deep reinforcement learning*. arXiv:1509.02971 [cs, stat]. URL: http://arxiv.org/abs/1509.02971 (cit. on p. 92).

Schulman, J., Moritz, P., Levine, S., Jordan, M., Abbeel, P., (Oct. 2018). *High-Dimensional Continuous Control Using Generalized Advantage Estimation*. arXiv:1506.02438 [cs]. URL: http://arxiv.org/abs/1506.02438 (cit. on p. 93).

Raffin, A., Hill, A., Gleave, A., Kanervisto, A., Ernestus, M., Dormann, N., (Nov. 2021). "Stable-Baselines3: Reliable Reinforcement Learning Implementations". In: *Journal of Machine Learning Research* 22.268, pp. 1–8 (cit. on p. 93).

Achiam, J. (2023). *Spinning Up documentation*. URL: https://spinningup.openai.com/en/latest/index.html (cit. on p. 93).

Ender, J., De Orio, R., Fiorentini, S., Selberherr, S., Goes, W., Sverdlov, V., (Nov. 2021). "Improving failure rates in pulsed SOT-MRAM switching by reinforcement learning". In: *Microelectronics Reliability* 126, p. 114231 (cit. on p. 97).

Ender, J., Lacerda De Orio, R., Fiorentini, S., Selberherr, S., Goes, W., Sverdlov, V., (Aug. 2022). "Reinforcement learning to reduce failures in SOT-MRAM switching". In: *Microelectronics Reliability* 135, p. 114570 (cit. on pp. 97, 102).

Swann, S. (Mar. 1988). "Magnetron sputtering". In: *Physics in Technology* 19.2, pp. 67–75 (cit. on p. 113).

Singh, J. P., Bhardwaj, R., Sharma, A., Kaur, B., Won, S. O., Gautam, S., Chae, K. H., (2019). "Fabrication of Magnetic Tunnel Junctions". In: *Advanced Applications in Manufacturing Enginering*. Elsevier, pp. 53–77 (cit. on p. 113).